A Thesis Submitted for the Degree of PhD at the University of Warwick

Permanent WRAP URL:
http://wrap.warwick.ac.uk/95551

Measurement of non-linear elastic properties of metals using non-contact methods

by

Yavor Emilov Arnaudov

Thesis

Submitted to the University of Warwick

for the degree of

Doctor of Philosophy

Department of Physics

September 2016

THE UNIVERSITY OF
WARWICK

Contents

List of Figures

Acknowledgments

Firstly, I would like to thank my supervisor, Professor Steve Dixon, for giving me the opportunity to work on such a great project, and for giving me the support and guidance I needed so that I could finish the PhD. I would also like to thank the rest of my colleagues in the Warwick Ultrasound group. Thanks go to Charley Fan for all his EMAT wisdom, discussions of impossible EMAT designs and his invaluable help with electronics theory. I would like to thank Lei Kang and Zhichao Li for the long and productive discussions. Thanks also go to Matthew Clough and William Blackmore for the regular office breaks and the immersion experience of the weird and strange bits of the British culture. I am thankful for the fun sessions in the teaching laboratory of Doctor Rachel Edwards, which kept my mind from worrying too much and provided much-needed laughter. Thanks to everyone else I have failed to name - there are just too many people to mention.

I also want to express my deepest gratitude to both my parents for all their support and encouragement - I would not be where I am without you, Mum and Dad. Thanks also to my sister, Diliyana, and the rest of the family for helping me keep my sanity. Thanks also go to all my close friend from the Bulgarian Society, which provided the much needed emotional support throughout my seven years at Warwick University.

Lastly, I would like to acknowledge the funding provided by the Research Centre of Nondestructive Evaluation (RCNDE) which made this work possible.

Declarations

I declare that the work presented in this thesis is my own except where stated otherwise, and was carried out entirely at the University of Warwick during the period between October 2012 and October 2016, under the supervision of Prof. Steve Dixon. The research reported here has not been submitted, either wholly or in part, in this or any other academic institution, for admission to a higher degree. Parts of this work, and other work not reported in this thesis, have appeared in other forms, listed here.

Abstract

Nonlinear ultrasonic techniques have the potential to allow for earlier detection of material degradation. Recent advances in the area show promising results, but the methods used are often impractical outside laboratory conditions. Non-contact methods have the potential to address some of the current measurement limitations. Electromagnetic acoustic transducers (EMAT) are one potential candidate for non-contact, nonlinear measurements in metals. The EMAT ultrasonic wave generation process is complex and requires an in-depth understanding of the electro-mechanical coupling phenomena. The potential of EMAT transducers as generators and detectors has been evaluated for multiple nonlinear measurement techniques.

The ultrasonic wave, generated by the interaction of the dynamically generated magnetic field and the eddy currents within the sample surface, called the self-field Lorentz force, have a significant impact on generated nonlinearity and must always be considered. For longitudinal wave measurements, the ultrasonic wave generated by the self-field Lorentz force has a similar amplitude and behaviour to the second harmonic wave generated by the material nonlinearity, thus making the measurements impractical. For shear waves, the third harmonic nonlinear ultrasonic generation shows inconclusive results with regards to microstructural change. Additionally, shear wave, nonclassical nonlinear ultrasonics show no significant change during the fatigue lifetime for aluminium alloy. Ultrasonic measurements of the temperature dependence of the sound velocity and of the coefficient of temperature expansion show a promising new field of study where EMAT application is well suited.

Meanderline EMATs have a great potential as receivers, but not as ultrasonic transmitters for nonlinear Rayleigh waves. The ultrasonic Rayleigh waves generated by the self-field Lorentz force, have similar amplitude and behaviour to the nonlinear ultrasonic Rayleigh waves. Optimised PPM (periodic permanent magnet) EMATs are used for entirely non-contact, nonlinear measurement of third harmonic shear horizontal waves and show great potential.

A new method to study and minimise experimental system nonlinearity is proposed. Measuring the ultrasonic waves generated from an artificially added harmonic distortion to the generation signal can provide a method to separate the effects of the system and the material nonlinearities.

Abbreviations

AFG	Arbitrary function generator
CAN	Contact acoustic nonlinearity
EMAR	Electromagnetic acoustic resonance
EMAT	Electromagnetic acoustic transducer
FEM	Finite element modelling
FFT	Fast Fourier transform
FWHM	Full width half maximum
LF	Line focusing
MFR	Magnet filling ratio
NDT	Non-destructive testing
NLU	Nonlinear ultrasonics
NRUS	Nonlinear resonance ultrasonic spectroscopy
NWMS	Nonlinear wave modulation spectroscopy
PCB	Printer circuit board
PPM	Periodic permanent magnet
PSB	Persistent slip band
RWWSI	Ratio of wire width to spacing interval
SH	Shear horizontal
SHG	Second harmonic generation
STFT	Short time Fourier transform
SWSH	Shear wave second harmonic
TOEC	Third order elastic constants

Chapter 1

Background

1.1 Research motivation

The aim of this thesis is to investigate the potential of electromagnetic acoustic transducers (EMATs) to measure nonlinear elastic parameters of metals. Two separate applications have been considered to assess EMATs capability to measure nonlinear ultrasound parameters. The first project uses Nonlinear Ultrasound Resonance Spectroscopy (NRUS) [2; 197] combined with Electromagnetic Acoustic Resonance (EMAR) [153] to measure changes of nonlinear parameters in fatigued aluminium samples. The second project focuses on determining the practical limitations of measuring surface wave nonlinearity using EMAT transducers. Development of a system for practical measurement of the nonlinear parameter is needed to allow industrial application of the nonlinear acoustic methods.

The primary objective of NDT is to detect damage at the earliest stage and to reduce further failure risk. Introducing practical means of using nonlinear ultrasonics can provide an early indication of accumulating damage, allowing condition-based maintenance as opposed to a schedule-based methodology. The current detection limit of conventional NDT methods only covers the latest part of the macroscale damage that leads to failure, see fig 1.1. The focus is based on crack detection and crack growth monitoring and remaining life prognosis. By improving the detection limit, measurements of microstructural evolution can allow degradation predictions at an earlier stage of the fatigue life [112]. This significantly reduces the failure probability by moving away from the crack-growth regime.

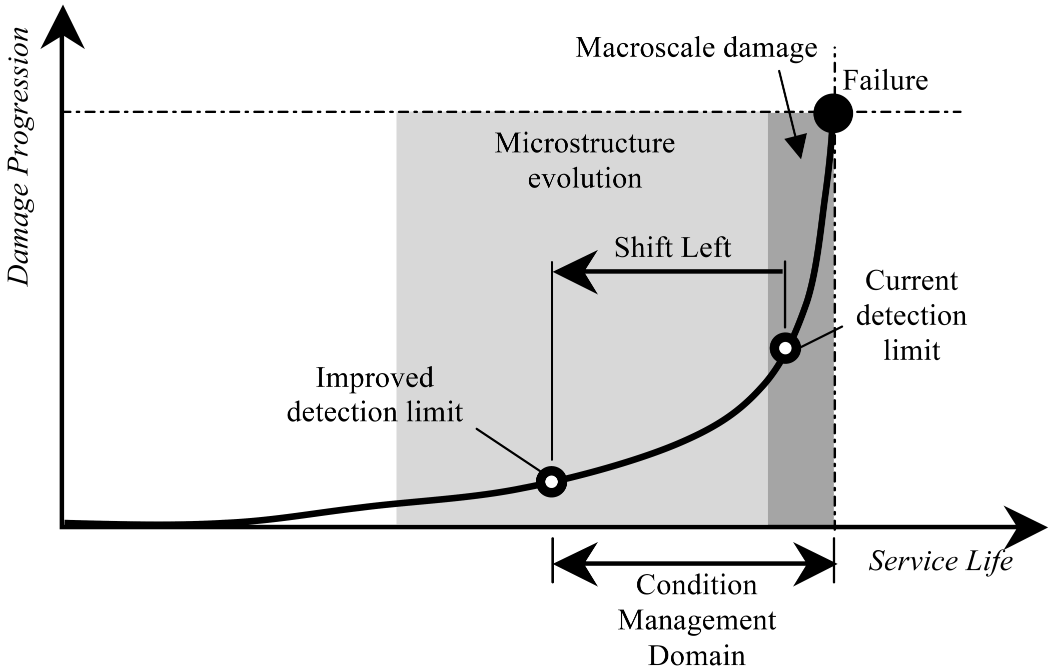

Figure 1.1: Nonlinear ultrasonics has the potential to improve the current detection limit. NLU allows measurements of microstructural evolution and precrack conditions. Adapted from Lissenden [112].

1.2 Thesis outline

Chapter 1 introduces the basic concepts of contact and non-contact ultrasonic measurements. Additionally, brief descriptions of different nonlinear techniques and EMAT nonlinear studies in the literature are presented. In Chapter 2, the theoretical framework of nonlinear ultrasonic (NLU) theory is summarised, including both classical and nonclassical nonlinear ultrasonics. Analysis of the NLU contributions from microstructural defects, as well as their generation, evolution and alternative dislocation density measurement techniques are also shown. Chapter 3 summarises the available research literature on EMAT transducers. Descriptions of the electromechanical coupling phenomena, multiple EMAT designs and the supporting EMAT electronics are presented. A review of the nonlinear ultrasonic techniques available in the literature is presented in Chapter 4. Chapter 5 explores NLU techniques, which employ EMAT transducers, and their results. Analysis of the available EMAT techniques for NLU is also included.

The experimental details for the nonlinear bulk wave measurements, employing EMAT transducers, are detailed in Chapter 6. Analysis of the nonlinearity contributions from the supporting electronics is included. Also, simulations of the ultrasonic generation forces and the resultant diffraction pattern are presented. Finally, the shear wave resonance technique for frequency shift and higher harmonic measurement is described. The results from the nonlinear bulk wave measurements are presented in Chapter 7. Experimental measurements of the ultrasonic displacement profile are used to confirm the simulated results for shear wave EMAT transduction. Additionally, a new method for system nonlinearity compensation, using artificial higher harmonic signals, is examined. Investigation of the effect of liftoff to the self-field Lorentz force is also shown. Results for the measured classical and nonclassical nonlinear ultrasonic parameter, employing bulk wave techniques, are analysed. A new ultrasonic method is proposed for measuring the temperature dependence of the velocity and coefficient of thermal expansion, as a function of the fatigue life of the specimen.

Descriptions of the experimental details for guided wave nonlinear measurements, employing EMAT transducers, are presented in Chapter 8. The EMAT Rayleigh wave generation for nonlinear ultrasonics is analysed. Also, the experimental configuration of an angled wedge piezoelectric transducer used for ultrasonic generation is described. Measurements of the nonlinear Rayleigh wave parameter are presented for the angled wedge - EMAT transducer pair. The experimental details for shear horizontal nonlinear ultrasonic wave measurements are also detailed. In Chapter 9, the results of the nonlinear Rayleigh wave measurements are presented and analysed. Furthermore, simulations of an optimised shear horizontal periodic permanent magnet (PPM) EMAT are shown. Experimental measurements of the third harmonic nonlinear shear horizontal wave using the improved PPM EMAT design are presented. Chapter 10 contains a summary of the experimental results and conclusions.

1.3 Non-destructive evaluation

Non-destructive testing or non-destructive evaluation is a discipline combining multiple methods of inspecting components without damaging them [19; 75; 213]. These methods can be classified into categories by the physical principles involved in the inspection: Visual Inspection, Thermography, Ultrasound, Radiography, Electromagnetic [17; 160; 200] or by the parameter/feature inspected such as residual stress, flaw detection, material characterization. Each method will possess its advantages and limitations, making it necessary to select the best technique for the particular application. This thesis will discuss multiple parameters, extracted from ultrasonic measurements of metal components and assess their ability to characterise fatigue lifetime.

1.4 Ultrasonic inspection

Ultrasonic methods use high frequency mechanical vibrations propagating through the material in order to probe the material. The methods require energy transfer of a driving electrical signal by an acoustic transducer, which generates the sound waves. Signals are received by the same transducer or a second transducer and are analysed to determine material parameters. Measurements of linear parameters such as time of flight or attenuation can be used to determine the size, position, and shape of a flaw in the material. Similar techniques can be used to measure material thickness or changes in the material properties such as composition or geometry. The use of different ultrasonic wave modes is required to inspect the bulk or surface of the component, each requiring individually selected transducers. These can employ two different acoustic transfer characteristics: contact or non-contact. Contact ultrasonic methods typically use couplant medium or water to achieve the acoustic transfer between the transducer and material. Non-contact ultrasound methods use transducers that transfer energy to the material without directly contacting the surface of the component.

1.4.1 Contact transducers

Piezoelectric transducers

Piezoelectric transducers are the most common type of ultrasonic transducer in industry. The high electromechanical efficiency is their main advantage, allowing for simple implementation of ultrasonic inspections. Piezoelectric transducers require good surface contact with the sample by the use of couplant, which can reduce its practical applications: hostile environments (elevated temperatures, chemical composition) or when rapid surface scanning is required. The application of couplant can be a major source of inconsistency when precise amplitude measurements are needed. A wedge can be employed in transducers to allow for a variety of wave modes to be generated, although couplant is still required for transmission and detection of ultrasonic waves. Performing contact measurements can be time consuming and can suffer from significant variations, due to inconsistent contact conditions.

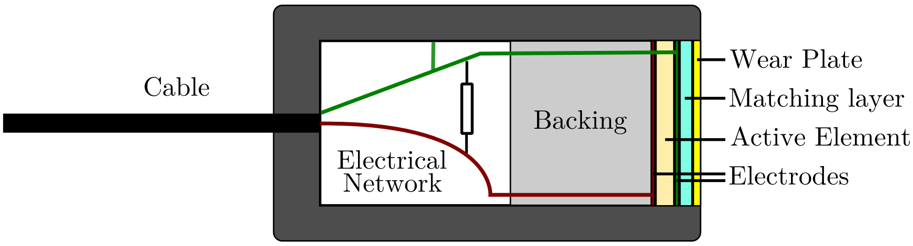

Figure 1.2: Schematic diagram of a piezoelectric transducer. It consists of multiple layers: Wear plate - it protects the active element from mechanical shocks. Matching layer - provides acoustic impedance matching. Active elements electrically coated on both faces - transforms the electrical signal to mechanical vibrations. Backing layer - suppresses ringing and absorbs backward going waves. Electrical network - provides electrical impedance matching.

The construction of a piezoelectric transducer consists of a wear plate, matching layer, active piezoelectric element, backing, electrodes and casing, see fig 1.2. A scratch resistant wear plate protects the inner layers from damage. A matching layer can be installed beneath it, to improve the power transfer between the mismatched media and piezoelement [105]. The thickness of the layer is selected to be a quarter of the wavelength $\lambda/4$ and to have an acoustic impedance equal to the geometric mean between the impedance of the active element and the material under test. The piezoelectric element has a thickness $\lambda/2$, which is the fundamental through thickness resonant mode of the element and specifies the sensors centre frequency. The backing material influences greatly the damping characteristics and hence the transducer bandwidth.

Magnetostrictive transducers

The magnetostrictive transducer consists of a thin foil of highly magnetostrictive material in contact with the sample, a magnet and a meanderline electric coil, as shown in figure 1.3. The meander spacing specifies the wavelength and in combination with the frequency of the driving current, different wave modes can be excited. By using different configurations of magnets and polarizations particular elastic waves can be generated. Magnetostrictive transducers have been used to generate shear horizontal (SH) waves. For improved generation efficiency, the static magnetic field should be parallel to the induced eddy currents in the sample. To achieve good acoustic transduction and improve the signal-to-noise ratio, surface preparation is required.

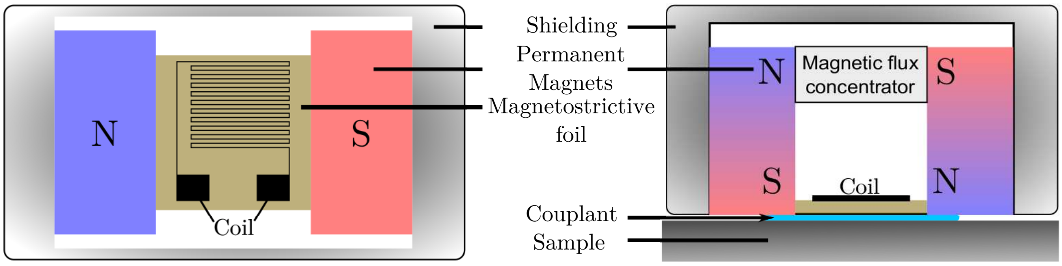

Figure 1.3: Schematic diagram of a magnetostrictive transducer

1.4.2 Non-contact ultrasonic evaluation

Non-contact ultrasound generation can be achieved by using air-coupled, laser and electromagnetically coupled methods.

Air coupled transducers

Air-coupled transducers transmit sound waves across multiple air-material interfaces. The proportion of energy transferred depends on the acoustic impedance matching between the materials. Typically, much less than 1% of the sound energy is transmitted at each interface due to the very low acoustic impedance of air. The total path loss of four transitions may induce loss of 100dB or higher. To maximize the performance of air-coupled transducers piezoelectric elements, with a suitable acoustic matching layer attached, are excited with toneburst signals. However, due to the high acoustic impedance of metals in comparison to air, the performance of air-coupled transducers is generally very inefficient. However, air-coupled receivers can be used to reduce the variations due to inconstant coupling conditions in contact methods [182].

Laser ultrasonics

Laser ultrasonics can be separated into generation and detection. The physical principles behind the ultrasound generation from lasers are thermoelastic and ablative [176]. In the thermoelastic regime, short pulses ($\sim$ 1 ms - 100 ns) from a high power laser beam induce sudden thermal expansion in small surface area, while in the ablative regime laser energy generates a plasma at the surface of the material that can arise from vaporisation of the surface of the sample or by breakdown of the air above the sample. The amplitude of the generated ultrasonic waves can be orders of magnitude higher than contact methods. The acoustic generation of ultrasound by laser beams is broadband and depends on the material that is tested and the experimental conditions. Laser generation results in multiple ultrasonic modes, making analysis and determination of waveforms complicated. Laser detection techniques allow for high sensitivity, broadband non-contact acoustic measurements. The most common laser-based ultrasound detectors use interferometric or amplitude variation principles [125].

Electromagnetic acoustic transducers

The electromagnetic acoustic transducer (EMAT) is a non-contact transducer typically composed of an electrically conducting coil and a source of strong magnetic field, both placed in close proximity to the sample, as shown in figure 1.4. Pulsed alternating electrical current is passed through the coil, which induces a dynamic electromagnetic field in the surface region of the conductive material. Three different mechanisms can be involved in the EMAT acoustic energy transfer: The Lorentz mechanism, magnetostriction or the magnetisation force, which allow for the non-contact ultrasonic generation. Chapter 3 contains more detailed information about the physical principles involved in the electromagnetic acoustic coupling.

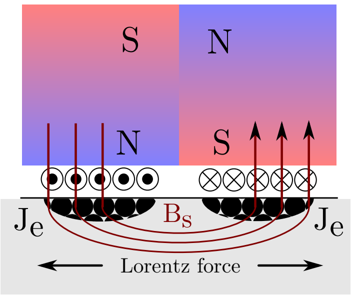

Figure 1.4: Schematic diagram of an electromagnetic acoustic transducer. Two strong $NdFeB$ magnets with opposing field direction provide the static magnetic field B_S. Racetrack coil placed near the sample surface induces eddy currents J_e. Lorentz force excites the acoustic vibration in the surface layer of a conductive material.

1.5 Acoustic nonlinearity background

Linear ultrasonic methods are widely used for thickness measurements, and also provide excellent sensitivity to macroscale features such as: fatigue cracks, surface corrosion, etc. However these features occur shortly before the end of the components life cycle. Therefore, linear ultrasonics have limited application for conditional monitoring purposes. Nonlinear ultrasonics allows the evaluation of primary damage precursors in principle, which can characterise material degradation and detect changes in material structural integrity earlier in the material lifetime. Nonlinear ultrasonic methods are sensitive to microstructural features that are orders of magnitudes smaller in size than the ultrasonic wavelength. However, these methods cannot distinguish individual features, such as single monopole dislocations or dislocation slip bands, but measure the cumulative effect of the microstructural features within the interaction volume of the ultrasonic wave path.

Nonlinear acoustics effects are reported as early as the 19th century [57]. Applications of nonlinear acoustics using underwater methods have been investigated in detail from the 1960s to the 1970s [12; 209; 210]. The earliest attempt to summarise different nonlinear acoustic applications, is produced by Zheng [224]. These aspects cover fields from acousto-optics, Earth studies, biophysics, non-destructive testing or acoustic microscopy. In all these applications, nonlinear effects have proven much more sensitive than using linear parameters [13; 57; 106]. The most promising use of nonlinear acoustic methods is the material characterisation of early stage damage. As the ultrasonic parameters are directly probing properties of the material, nonlinear acoustic methods are capable of inspecting microcracks and degradation over the sound wave propagation volume.

The principle difference between linear and nonlinear ultrasound is that the latter characterises defects by measuring acoustic signals whose frequency differs from that of the generating signal. Classical nonlinear ultrasonics is focused on measurements of the higher harmonics or sub-harmonic components of the fundamental frequency, or the mixed frequency response from multiple acoustic generation sources. The nonclassical nonlinear ultrasonic methods exploit the hysteretic properties of the materials to measure frequency shifts caused by a change in the stress state of the material. The nonclassical elasticity theory defines the elastic constants as functions of the maximum applied stress from the previous load cycle. The different hysteretic curves of the elastic constants cause the observed nonlinear behaviour, see figure 1.5. The nonclassical nonlinear methods have been widely used in geophysics to study the hysteretic behaviour of rocks and their mesoscopic elasticity [121]. These methods have been adopted by NDT to test materials with typically small elastic hysteresis - such as metallic alloys and ceramics [58], also see section 1.5.2.

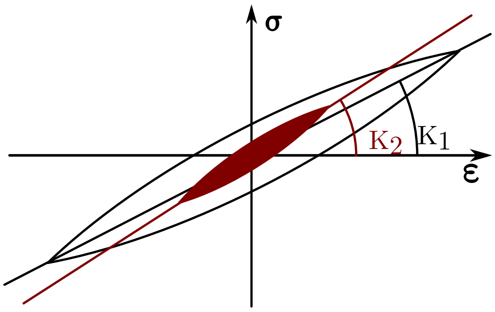

Figure 1.5: Stress strain curve for two different excitation levels adapted from [122]. The generated sine wave for the lower excitation level describes a hysteresis curve with an average elastic modulus of K_2, while the higher excitation level describes a larger hysteresis loop with an average elastic modulus of K_1.

1.5.1 Classical acoustic nonlinearity

Early second harmonic generation investigations were reported by Hikata [63] and Thompson[18; 183]. The response of single crystal aluminium to finite amplitude sinusoidal acoustic waves has been recorded over the fatigue lifetime [52], showing a correlation between the damage state and nonlinear parameter.

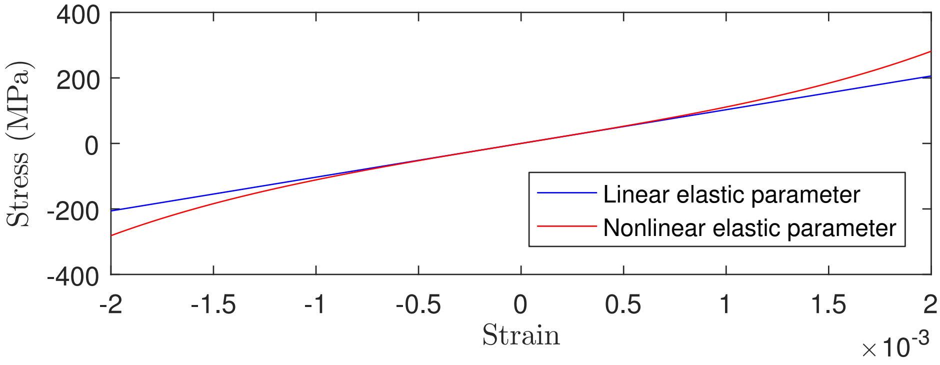

Figure 1.6: Stress-strain relation: linear elastic model vs. nonlinear elastic model

By using Taylor series expansion, the linear stress-strain relation is expanded to higher order elastic constants, as shown in figure 1.6. By substitution for the stress expression and a pure sinusoidal function in the wave equation, an approximate solution for the nonlinear second order partial differential equation (PDE) can be obtained. Using an iteration method to solve the PDE expression for the nonlinearity, an expression for the second harmonic amplitude is acquired [63]. Contributions to the second harmonic generation (SHG) are from lattice and dislocations. This allows for the assessment of the state of degradation of the material by measuring the amplitudes of the higher harmonic components, see figure 1.7. Multiple parameters are shown to have an effect on the nonlinear parameter such as dislocation density, dislocation loop length and applied stress.

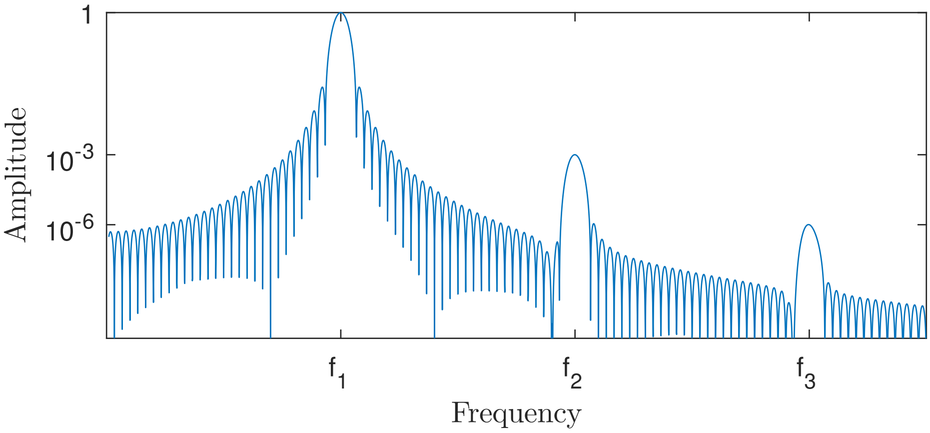

Figure 1.7: Predicted FFT spectrum of a nonlinear ultrasonic signal. Ultrasonic wave with frequency f_1 is expected to generate higher harmonic components at f_2, f_3 due to material nonlinearity. Amplitudes of the higher harmonics are expected to be orders of magnitude smaller $\sim -60\,dB$.

Contributions from more complex dislocation structures have been summarized in Cantrell [21]. Interactions of ultrasonic waves with edge dislocations and dislocation dipoles have been quantified. In-situ measurements of the second harmonic amplitude over the duration of a full specimen lifetime have been taken by Frouin [50] to confirm a monotonic increment in nonlinear parameter, and to provide useful data about dislocation generation stages. Liu [178] had investigated the effects of different experimental parameters on the measured nonlinearity parameter.

The nonlinear ultrasonic techniques reviewed by Jhang [78] ,based on a previously published review of material characterization by Zheng [224], cover multiple areas of nonlinear methods. Nonlinear acoustic phenomena are categorized into four different groups: higher harmonics, sub-harmonics, shift of resonance frequency and mixed frequency acoustic response. The article strongly supports the finding that observed significant changes in the nonlinear parameter occur over the fatigue lifetime. The SHG is reviewed for different wave modes in [119], suggesting a complicated experimental setup and the necessity of improved apparatus sensitivity for the case of surface or Lamb waves.

1.5.2 Non-classical acoustic nonlinearity

Further techniques were analysed by Abeele [2; 197] to evaluate fatigue damage. Nonlinear wave modulation spectroscopy (NWMS) simultaneously applies two sinusoidal ultrasonic waves of different frequencies f_a and f_b. Changes in the amplitudes of the side bands of those two frequencies are observed - $2f_a, 2f_b, f_a + f_b, f_b - f_a$, see figure 1.8. The article concludes that by interacting with cracks and deformations of the materials, mono-frequency ultrasonic waves experience nonlinear perturbations to the stress-strain relation, and that higher harmonics are generated with contributions from those perturbations.

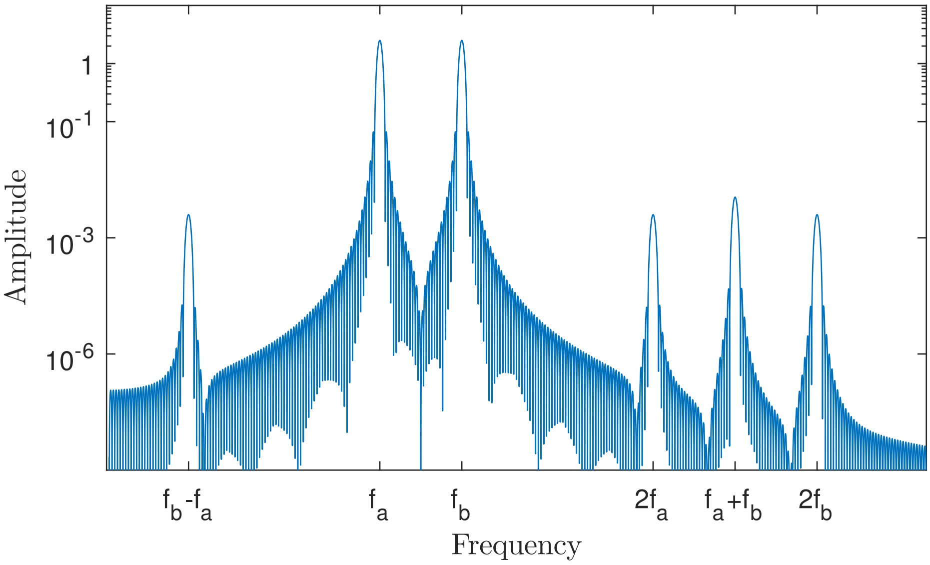

Figure 1.8: Expected FFT spectrum of the nonlinear modulation from two ultrasonic waves with frequencies f_a, f_b. Resulting spectrum includes higher harmonics at $2f_a, 2f_b$ and nonlinear wave interactions at side-bands $f_b - f_a, f_b + f_a$. The side-band amplitudes provide information about the material nonlinear parameters.

Nonlinear resonance ultrasonic spectroscopy (NRUS) is an experimental technique that uses sample geometry to generate signals within the sample's mechanical resonance frequencies [149; 150; 157; 197]. From the output frequency, an amplitude signature is extracted. By varying the excitation amplitude of the fundamental mode, as shown on 1.9 , the resonant frequency experiences a shift Δf, while the higher harmonics increase in amplitude. As materials degrade, the frequency shift $|\Delta f|/f_0$ increases in magnitude. NRUS methods have been evaluated to have higher sensitivity to the accumulated macroscopic damage compared to linear acoustic techniques or classical nonlinearity methods [133; 142].

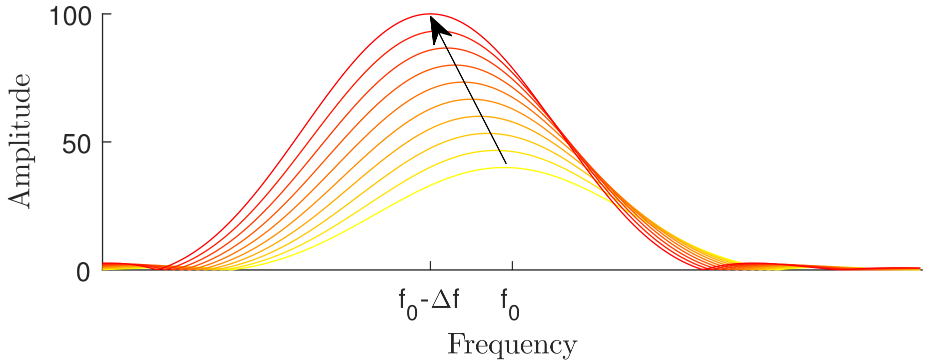

Figure 1.9: Typical frequency spectra of an NRUS measured signals. The frequency of the ultrasonic signal shifts with the amplitude of the excitation signal. The change of the frequency shift (Δf) is proportional to the damage state of the measured material.

1.6 Nonlinear ultrasonics using EMATs

Electromagnetic acoustic transducers (EMAT) have lower generation efficiency compared to contact methods. The small amplitude of the fundamental frequency signal may prevent the generation of an observable second harmonic component. However, EMATs have wideband operation range, which allows generation and detection of multiple harmonic components using a single transducer. To overcome limitations of EMATs generation and receiving processes, an investigation is required with regard to nonlinear methods.

1.6.1 Electromagnetic acoustic resonance

Electromagnetic acoustic resonance method (EMAR) uses the samples geometrical resonance to increase the amplitude of the driving signal. The method has been adopted by Ohtani [153] to measure the changes in attenuation during fatigue steel. Additionally, changes in the ultrasound wave velocity are measured, in terms of resonance frequency shifts. The non-contact nature of the transducers allows for high sensitivity continuous measurements during the fatigue process.

Measurements combining EMAR technique and NRUS method have been reported by Ohtani [152] on Cr-Mo-V steel. Surface waves are pulsed synchronously at $\frac{f_1}{2}$ - half the fundamental geometric resonance frequency of a cylindrical sample, as shown in figure 1.10. As a result, the high amplitude driving signal does not satisfy the resonance conditions and only lasts for a short time due to interference. The generated second harmonic component matches the resonance conditions and is accumulated over time. Shear surface wave magnetostrictive non-contact transducers have been used. This reduces the system nonlinearity as it avoids using couplants. Correlation between the change of the attenuation and the nonlinearity coefficients is drawn.

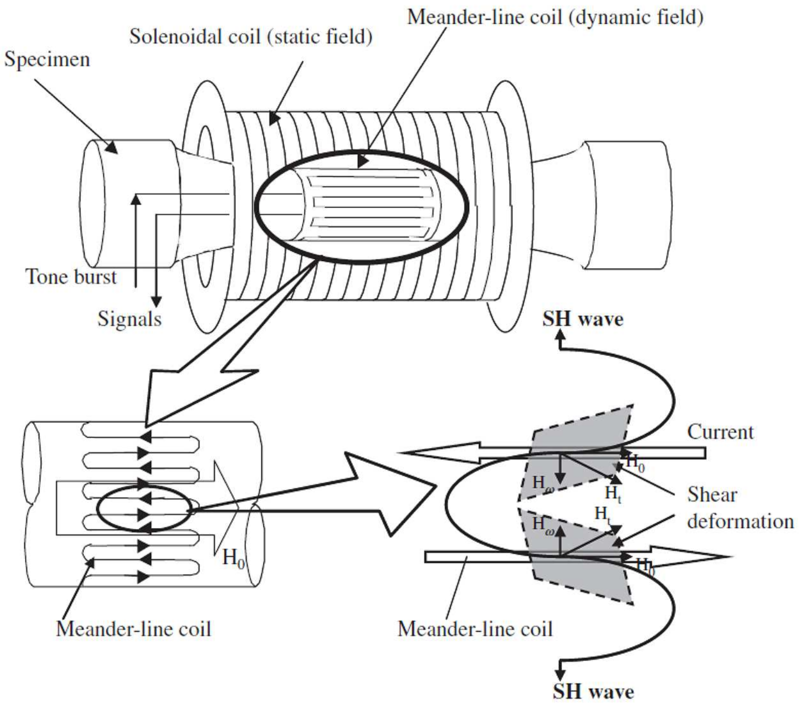

Figure 1.10: Axial-shear-wave EMAT: Solenoid coil is providing the static magnetic field. Meanderline coil surrounding the cylindrical surface generates a dynamic magnetic field. The magnetostrictive force generates axial surface SH waves. This figure is reproduced from [152].

NRUS measurements were taken of pure copper [149] and austenitic steel [151] using EMAT transducers. Changes in the nonlinearity frequency coefficient are shown to have a correlation with the fatigue progress. Non-contact three wave mixing measurements have been reported by Ohtani [148]. In Ohtani's study, shown in figure 1.11, two EMAT transmitters were used to generate synchronised toneburst wave packages which interact within the sample. Changes in the three-wave nonlinear acoustic parameters and frequency shift were presented as the result of creep damage. More detailed analysis of Ohtani's results will be presented in chapter 4.

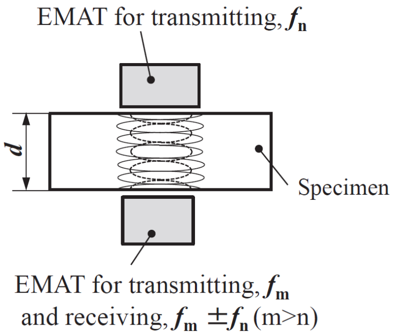

Figure 1.11: Dual EMAT configuration: Two shear wave transducers positioned on opposite sides of the sample, generate acoustic signals of different frequencies f_n and f_m. Nonlinear interaction within the specimen volume generates multiple sideband signals. This figure is reproduced from [148].

1.6.2 EMAT guided waves

Measurements on nonlinear guided waves generated by EMATs have been reported by Murayama [135; 136] and Cobb [35]. Murayama evaluated EMATs for nonlinear measurements of the S_0-Lamb and SH_0 shear horizontal waves during the fatigue lifecycle of low carbon steel. EMATs have been used for both transmission and reception of the ultrasonic waves. However, conclusive results were not drawn from the data obtained. Cobb's [35] interrupted fatigue tests were conducted on stainless steel samples and measurements of the nonlinear Rayleigh wave parameter are taken at regular stages of the fatigue lifetime. Cobb's study used EMATs for both transmission and reception, but the measured results were inconclusive. The potential of EMATs to measure the nonlinear ultrasonic parameter may allow for single sided ultrasonic measurements of the material surface damage state. The application of EMATs will permit for a field deployable measurement method.

Chapter 2

Nonlinear ultrasonics

2.1 Classical nonlinear ultrasonics

2.1.1 Wave equations

Infinitesimal amplitude waves

A mathematical description of a one-dimensional wave propagating in ideal media is given by the wave equation [169]:

$$\frac{\partial^2 U}{\partial t^2} = c_0^2 \frac{\partial^2 U}{\partial x^2} \tag{2.1}$$

where the $x, t, U(x,t), c_0$ are the position coordinate, time variable, the wave displacement in the one-dimensional system and the velocity of the wave in non-disturbed media. For linear ultrasonics, the forces between the particles are described by Hook's law:

$$F = -k\Delta x \tag{2.2}$$

where F is the returning force, k is the spring constant and Δx is the displacement from the equilibrium position. This description assumes linear interactions between particles and ignores any dependence on the amplitude of the oscillation. Such approximations can be made for waves of infinitesimal amplitudes.

Nonlinear ultrasound waves

Nonlinear ultrasound has the unique capability of detecting damage precursors prior to any macroscopic crack formation. As such, it has the potential to become a method for condition health monitoring for metallic structures. Using a variety of different nonlinear acoustic effects the approach can provide applications for safe and efficient operation of ageing infrastructure. Several measurement methods have been developed based on the nonlinear effect. The next sections will summarise the different sources of nonlinearity and nonlinear ultrasound interactions.

2.1.2 Lattice anharmonicity

Finite amplitude ultrasonic waves would experience an additional nonquadratic interatomic potential. When the amplitude of oscillation of the ultrasonic wave becomes of significance, at amplitudes ~ 200 nm [141], the elastic response of the lattice deviates significantly from the linear Hooke's law.

The potential energy wells generated from the lattice are described to a good approximation by the Lennard-Jones potential equation [87]:

$$V(r) = 4W\left[\left(\frac{q}{r}\right)^{12} - \left(\frac{q}{r}\right)^{6}\right] \tag{2.3}$$

where $V(r)$ is the interatomic potential between two neighbouring atoms, W is the depth of the potential well, q is the distance of minimum interatomic potential and r is the distance separation between two adjacent particles. Due to the simplicity and computational efficiency of the equation, it is heavily used in simulations and basic calculations regarding lattice parameters and effects. A better model to describe the lattice atomic forces is using the Morse potential [1]. The forces on each individual atom can be approximated to a good agreement by differentiating the atomic potential, see figure 2.1. Ultrasonic waves, with amplitudes higher than 200 nm, can generate displacements between neighbouring atoms in the lattice of approximately 0.001Å. Similar displacement levels are required to enter the nonlinear elastic regime:

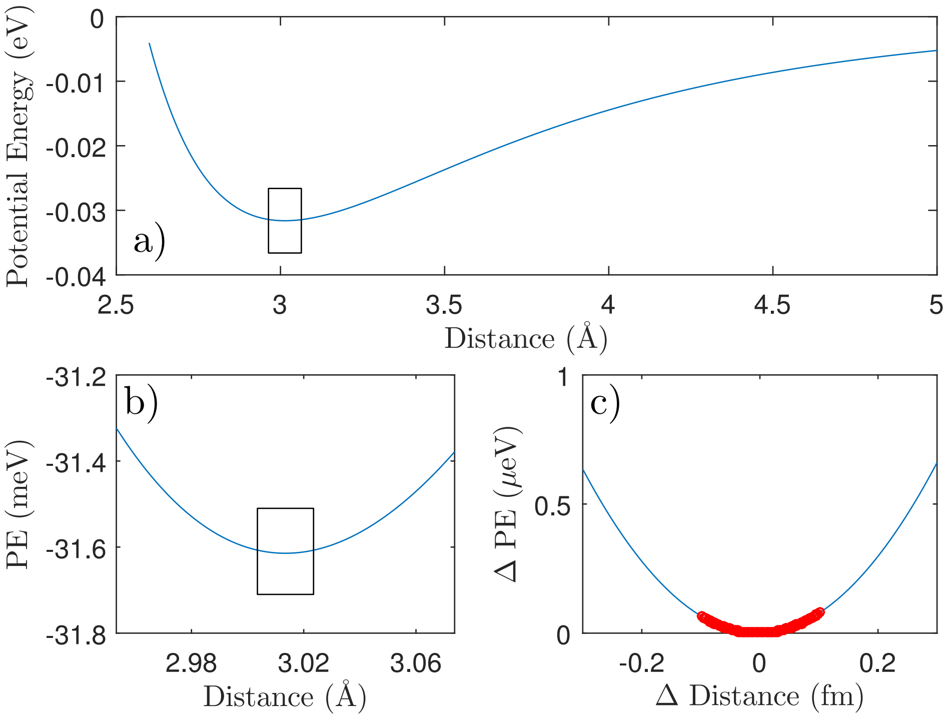

Figure 2.1: Interatomic potential energy for aluminium lattice (a,b) [5]. The potential well is positioned around 3.01Å(c). The linear elastic regime (red) is limited around the equilibrium position.

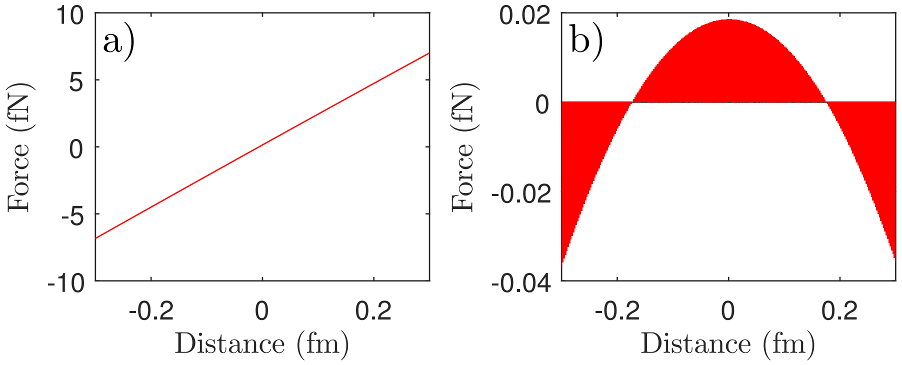

Figure 2.2: Atomic spring force for aluminium single crystal (a) [5]. Linear fit to the ultrasonic elastic regime and plot of the residual errors to the linear fit (b).

The returning force from the lattice potential wells shown in figure 2.2 is only linear across a small range of displacements. The linear fit shows deviation of the returning force from the expected infinitesimal amplitude wave assumption. For a more complete mathematical description of the material response to elastic waves, consider a nonlinear spring connecting each pair of atoms. Cantrell has summarised the set of fundamental principles of nonlinear ultrasonics to describe acoustoelasticity and harmonic generation [21]. The model defines the lattice motion in discrete displacements for each atom. Each atom is described as a point with mass m which is separated from adjacent points by a distance d. Each point p is described by y_p - displacement from its equilibrium position. The system assumes a Lagrangian (material) reference system. When taking into account the inter-particle interactions, the potential energy V_{PE} of the system can be expressed as an infinite series:

$$V_{PE} = (V_{PE})_0 + \sum_p k_1(y_{p+1} - y_p) + \sum_p \frac{1}{2!} k_2 (y_{p+1} - y_p)^2 + \sum_p \frac{1}{3!} k_3 (y_{p+1} - y_p)^3 + \dots \tag{2.4}$$

Where $(V_{PE})_0$ is a constant, k_1, k_2, k_3 are first, second and third order spring constants which simulate the forces between two adjacent particles. The force applied to the nth particle can be expressed as:

$$F_n = -\frac{dV_{PE}}{dy_n} = -k_1 \sum_p \left(\frac{dy_{p+1}}{dy_n} - \frac{dy_p}{dy_n} \right) - \frac{1}{2} k_2 \sum_p \left(\frac{dy_{p+1}}{dy_n} - \frac{dy_p}{dy_n} \right)^2 - \dots \tag{2.5}$$

Consideration should be taken only for the cases $dy_p/dy_n = \delta_{pn}$, therefore after the summation the expression can be reduced to:

$$F_n = m\frac{d^2U}{dt^2} = k_2 \left[(y_{n+1} - y_n) - (y_n - y_{n-1}) \right] + \frac{1}{2} k_3 \left[(y_{n+1} - y_n)^2 - (y_n - y_{n-1})^2 \right] \tag{2.6}$$

Where the linear term involving k_1 is cancelled. Taking the continuum limit of the above equation with respect to the x-dimension over a finite small area cross-section δS, a construction for the left side of equation (2.1) can be obtained:

$$\rho \frac{\partial^2 U}{\partial t^2} = \frac{1}{\delta S} \frac{\partial F_n}{\partial x} = \frac{\partial \sigma}{\partial x} = A_{11} \frac{\partial^2 U}{\partial x^2} + A_{111} \frac{\partial U}{\partial x} \frac{\partial^2 U}{\partial x^2} + \dots \tag{2.7}$$

where σ, A_{11} and A_{111} are respectively the stress along the propagation direction, second and third order Huang coefficients [68]. Using only the first two terms, the expansion can be rewritten as:

$$\frac{\partial^2 U}{\partial t^2} = c_1^2 \left(1 - \tilde{\beta}_l \frac{\partial U}{\partial x} \right) \left(\frac{\partial^2 U}{\partial x^2} \right) \tag{2.8}$$

Where $c_1^2 = A_{11}/\rho$ is the infinitesimal amplitude longitudinal speed and $\tilde{\beta}_l = -A_{111}/A_{11}$ is defined as the longitudinal acoustic nonlinearity parameter using the

Voigt notation. When $\tilde{\beta}_l$ tends to zero the solution reduces to the linear wave equation (2.1). The relationship between the stress and the observed displacements can be obtained from equation (2.7):

$$\sigma = A_1 + A_{11}\frac{dU}{dx} + \frac{1}{2}A_{111}\left(\frac{dU}{dx}\right)^2 \tag{2.9}$$

This single dimensional expansion can be obtained for three dimensional space using Voigt notation [21]:

$$\rho\frac{\partial^2 u_i}{\partial t^2} = \left(A_{ijkl} + A_{ijklmn}\frac{\partial u_m}{\partial x_n}\right)\frac{\partial^2 u_k}{\partial x_j \partial x_l} \tag{2.10}$$

where A_{ijkl} and A_{ijklmn} are second and third order Huang coefficients and x_i is the continuum of Lagrangian three dimensional coordinates.

2.2 Harmonic generation

2.2.1 Second harmonic generation

The wave equation can be expressed in perturbation terms:

$$U = u_{(1)} + u_{(2)} \tag{2.11}$$

Where $u_{(1)}$ is the plane wave solution and $u_{(2)}$ is the perturbation term. Suppose $u_{(1)}$ is a plane wave solution in the form:

$$u_{(1)} = P_1 \cos(kx - \omega t) \tag{2.12}$$

Where P_1 is the amplitude of a plane wave traveling in the x-axis, with angular frequency ω and wave number k. For $u_{(1)}$ to be a solution to (2.8) it needs to satisfy the boundary condition, where the wave is launched in the material at x = 0:

$$U(0,t) = P_1 cos(\omega t) = P_1 cos(-\omega t) \tag{2.13}$$

The solution to equation (2.8) is obtained by adding the perturbation from $u_{(2)}$. For full derivation refer to Cantrell [21] :

$$\frac{\partial^2 u_{(2)}}{\partial t^2} = c^2\frac{\partial u_{(2)}^2}{\partial x^2} - \frac{1}{2}\tilde{\beta}c^2k^2P_1^2 \sin 2(wt - kx) \tag{2.14}$$

Subject to boundary conditions (2.13), equation (2.14) gives the general solution the form of:

$$U = P_1 \cos(kx - \omega t) - \frac{1}{8}\tilde{\beta} c^2 k^3 P_1^2 \sin(2(kx - \omega t)) \tag{2.15}$$

From this it can be concluded that the nonlinear parameter can be related to the amplitudes of the first P_1 and second P_2 harmonic:

$$\tilde{\beta}_{HG} = \frac{8}{xk^2}\frac{P_2}{P_1^2} \tag{2.16}$$

Where $\tilde{\beta}_{HG}$ is the nonlinear parameter for a 1D sinusoidal wave propagating in an ideal material without attenuation.

2.2.2 Attenuation of finite amplitude waves

By adjusting the solution (2.12) to the wave equation (2.8) to incorporate attenuation from scattering, diffraction and absorption:

$$\rho \frac{\partial^2 u_{(1)}}{\partial t^2} = c^2 \frac{\partial^2 u_{(1)}}{\partial x^2} + \lambda_{dis} \frac{\partial^3 u_{(1)}}{\partial t \partial x^2} \tag{2.17}$$

The solution for the fundamental wave is modified to $\partial u_{(1)}/\partial x = \alpha_{(1)} u_{(1)}$. The attenuation of the second harmonic is expressed in the same form, assuming it is unaffected by the attenuation of the fundamental wave $\alpha_{(1)}$:

$$\left(\frac{\partial P_2}{\partial x}\right)_{attn} = -\alpha_{(2)} u_{(2)} \tag{2.18}$$

From (2.16):

$$\left(\frac{\partial P_2}{\partial x}\right)_{HG} = \frac{1}{8}\tilde{\beta}_{HG} k^2 P_1^2 \tag{2.19}$$

Combining the two equations (2.18) and (2.19):

$$\tilde{\beta}_{abs} = \tilde{\beta}_{HG} \frac{x(\alpha_2 - 2\alpha_1)}{1 - exp[-(\alpha_2 - 2\alpha_1)x]} \tag{2.20}$$

Therefore the measured nonlinearity has to be compensated for the attenuation, so that the material properties can be extracted. Measurements of the nonlinear parameter without the compensation for diffraction, attenuation, transfer functions of the transducers can only provide relative values of the nonlinear parameter for that exact experimental configuration. Such measurements can be used to show trends within a single experiment and cannot be used as comparison across the literature. In this thesis, all measurements of the nonlinear parameter are non-normalised. Within this thesis, theoretically defined expressions for the absolute value of the nonlinear parameter are labelled with $\tilde{\beta}$, while relative values for the nonlinear parameter have no accents.

2.2.3 Sources of nonlinear ultrasonic waves

Nonlinear ultrasonic wave interactions can result from lattice anharmonicity, deviating from a non-quadratic interatomic potential, or from nonlinearities involving defects, microstructural features, or other disruptions in the lattice structure of the material. Two different models are available in the literature [26]: Cantrell [22; 23] and Kim et al [99]. Cantrell's model considers contributions to the nonlinear parameter separately: lattice anharmonicity, dislocation sources and cracks. This model requires detailed information about the dislocation densities, loop length, dipole heights, volume fractions. This makes the predictions accurate, but experimentally tedious. The model of Kim et al. aggregate all the nonlinearity contributions induced during fatigue damage into the third order elastic constants of the material, assuming the other parameters contribute very little to the increase of β. This allows for more practical predictions for the variance of the nonlinear parameter, but the model fails to acknowledge the plastic deformations introduced by the acoustic wave and makes the wrong assumptions about the contributions of third order elastic coefficients (TOEC). Therefore the introduction in this thesis will focus on Cantrell's predictive model. For simplicity, the following equations are given for one-dimensional longitudinal ultrasonic waves. The corresponding set of equations in 2D and 3D are given in Cantrell [21].

Anharmonicity of lattice

Considering the approximation of interactions (spring constants), the lattice contribution to the nonlinear parameter $\tilde{\beta}_{lattice}$, can be expressed in the following terms, where the Huang coefficients are defined in section 2.2.7:

$$\tilde{\beta}_{lattice} = -\frac{A_{111}}{A_{11}} \tag{2.21}$$

Dislocation monopoles - Hikata model

From Cantrell [21] and Hikata [63] the contribution from monopole dislocations can be taken as:

$$\tilde{\beta}_{mp} = \frac{24}{5}\frac{\Omega\Lambda_{mp}L^4R^3}{\mu^3b^2}|\sigma_{initial}| \tag{2.22}$$

Where Ω is the conversion factor between shear strain and longitudinal strain, Λ_{mp} is the monopole dislocation density, L is the dislocation loop length, R is the resolving factor of the shear to longitudinal stress, b is the Burgers vector and μ is the shear modulus. It is worth noting that the contribution from dislocation monopoles requires the application of stress to the structures. The formula is derived considering a longitudinal wave passing through the material, which drives the self-interaction of a bowing dislocation line, under a quasistatic load.

Dislocation monopoles - Cash and Cai model

Recent research [27] has reported a more accurate formulation for the dislocation contribution to the acoustic nonlinearity. Dislocation dynamics (DD) simulations are used to evaluate the analytical model for both pure screw or edge dislocations. For a Poisson's ratio in the range of 0.2 to 0.4, the constant line-tension Hikata model can no longer be considered valid. The contributions from edge and screw dislocations show different behaviour with an increase of the line energy of the dislocation. The model shows that there are possible negative values of β for materials with large Poisson's ratios ν, and containing predominantly edge dislocations. These materials include a large portion of the fcc engineering metals. The result for the nonlinear parameter of an edge monopole dislocations is:

$$\begin{aligned}\frac{\tilde{\beta}^{e}_{mp}}{\Lambda_{mp} b^2} &= \frac{24(1-4\nu)(1-\nu)^3 \Omega R^3}{5(1-2\nu)^4} \left(\frac{L}{b}\right)^4 \left(\frac{\sigma}{\mu}\right) \\ &+ \frac{240(1-8\nu+20\nu^2)(1-2\nu^7)\Omega R^5}{7(1+\nu)^7} \left(\frac{L}{b}\right)^6 \left(\frac{\sigma}{\mu}\right)^3\end{aligned} \tag{2.23}$$

which allows for a negative contribution to the nonlinear parameter. This effect can play a significant role in the early stages of fatigue damage, as the ultrasound measurements can only measure the amplitude, but not the sign. Further research is required to confirm the dislocation monopole interaction with ultrasonic waves under small applied stresses.

Dislocation dipoles

From Cantrell [21], the contributions from dislocation dipoles can be expressed as:

$$\tilde{\beta}_{dp} = \frac{16\pi^2 \Omega R^2 \Lambda_{dp} h^3 (1-\nu)}{\mu b} \tag{2.24}$$

where h is the dislocation dipole height, ν is the Poissons ratio and Λ_{dp} is the dipole dislocation density. Dipoles inside the material form by forming dislocation pairs of edge dislocation of opposite polarity. The nonlinearity contribution from dipole dislocation structures does not depend on the applied/residual stresses introduced to the material. The dipoles interact with each other forming more complex structures. From Hull [70] the force between two pairs of dislocations can be expressed by:

$$F = -\frac{\mu b^2}{2\pi(1-\nu)} \frac{x(x^2-y^2)}{x^2+y^2} \tag{2.25}$$

where, (x, y) are the Cartesian coordinates of one dislocation in the dipole pair, relative to the coordinates of the second dislocation (0,0). Cash and Cai [28] have improved the model for dislocation dipoles using DD simulations. The nonlinear dipole contribution $\tilde{\beta}_{dp}$ is shown to depend on stress, which previously was neglected. The spatial arrangement of the dislocations also affects the total contribution. It is proposed that only single isolated dipoles contribute to a non-zero β at zero stress, while larger structures have no contribution at zero stress. When cycled stress is applied to the structure, the formation of persistent slip bands (PSB) occur. Those are often situated at grain boundaries or around secondary phase precipitates and contribute to the overall nonlinear parameter due to their multipolar structures. It is important to understand the ultrasonic interaction of more realistic dislocation microstructures during fatigue to predict acoustic nonlinearity parameters.

Precipitates

For polycrystalline alloys the distribution of precipitates must be considered. They have no direct contribution to the β parameter, but they interact with the dislocations. The precipitate is incorporated in the material matrix and creates a local stress field, which can bow a dislocation in the vicinity. This may lead to significant change in the magnitude of the measured nonlinear parameter.

Microcracks

Microcracks can generate higher harmonics due to contact acoustic nonlinearity (CAN) mechanisms. The elastic waves can cause the microcrack surfaces to close or open - clapping mechanism. For longitudinal waves, during the compression cycle the material elasticity is higher than that during the tensile part of the cycle. For shear waves, the elastic wave generates additional sub-harmonics and higher harmonics, due to surface-to-surface friction of the semi open microcrack. Similar behaviour can be observed in the early stages of delaminated composite materials or in corrosion generated cracks. At larger damage scales such as macroscopic cracking, linear ultrasonics provide better options for damage detection.

2.2.4 Shear wave harmonic generation

Earlier derivations have considered mostly longitudinal wave propagation. For a transverse wave, the lattice contribution to the nonlinearity cancels due to symmetry for almost all polycrystalline configurations. To express the self-interaction of a shear wave, it would require one to formulate the stresses in three dimensions using the Piola-Kirchhoff stress tensor $\boldsymbol{P}$. To express the equation of motion (2.1) in terms of the first Piola-Kirchhoff stress tensor:

$$\rho \ddot{u} = \nabla \boldsymbol{P} \tag{2.26}$$

Expanding the equation in terms of displacements and third-order elastic constants and splitting the terms into linear (red) and nonlinear (blue) contributions:

$$\begin{aligned}
\boldsymbol{P}^{L}_{ij} + \boldsymbol{P}^{NL}_{ij} &= \lambda \frac{\partial u_k}{\partial x_k}\delta_{ij} + \mu\left(\frac{\partial u_i}{\partial x_j} + \frac{\partial u_j}{\partial x_i}\right) \\
&+ \left(\frac{\lambda}{2}\frac{\partial u_k}{\partial x_l}\frac{\partial u_k}{\partial x_l} + \mathcal{C}\frac{\partial u_k}{\partial x_k}\frac{\partial u_l}{\partial x_l}\right)\delta_{ij} + \mathcal{B}\frac{\partial u_k}{\partial x_k}\frac{\partial u_i}{\partial x_j} + \frac{\mathcal{A}}{4}\frac{\partial u_i}{\partial x_k}\frac{\partial u_k}{\partial x_j} \\
&+ \frac{\mathcal{B}}{2}\left(\frac{\partial u_k}{\partial x_l}\frac{\partial u_k}{\partial x_l} + \frac{\partial u_k}{\partial x_l}\frac{\partial u_l}{\partial x_k}\right)\delta_{ij} + (\lambda + \mathcal{B})\frac{\partial u_k}{\partial x_k}\frac{\partial u_j}{\partial x_i} \\
&+ \left(\mu + \frac{\mathcal{A}}{4}\right)\left(\frac{\partial u_j}{\partial x_k}\frac{\partial u_i}{\partial x_k} + \frac{\partial u_k}{\partial x_j}\frac{\partial u_l}{\partial x_i} + \frac{\partial u_j}{\partial x_k}\frac{\partial u_k}{\partial x_i}\right)
\end{aligned} \tag{2.27}$$

where $(\mathcal{A})$, $(\mathcal{B})$, $(\mathcal{C})$ are TOEC as introduced by Landau [109]. By using the perturbation method as in Bender [9], the self-interaction of a wave is described by:

$$\begin{aligned}
\nabla \boldsymbol{P}^{NL} =& j\left[\left(\lambda + 2\mu + \frac{\mathcal{A}}{2} + \mathcal{B}\right)(U_I \cdot U_I)(k_I \cdot k_I)k_I\right. \\
&+ (2\lambda + 4\mu + \mathcal{A} + 2\mathcal{B})(U_I \cdot k_I)(k_I \cdot k_I)U_I \\
&+ \left.\left(\frac{\mathcal{A}}{2} + 3\mathcal{B} + 2\mathcal{C}\right)(U_I \cdot k_I)(U_I \cdot k_I)k_I\right]\frac{1}{2}e^{j(2\omega t - 2k_I x \sin\theta - 2k_I z \cos\theta)}
\end{aligned} \tag{2.28}$$

where U_I is the amplitude of the wave and k_I is the wave number. By considering shear wave interactions:

$$U_I = U_S \begin{bmatrix} \cos\theta \\ 0 \\ \sin\theta \end{bmatrix}, k_I = k_S \begin{bmatrix} \sin\theta \\ 0 \\ \cos\theta \end{bmatrix} \tag{2.29}$$

Equation (2.28) simplifies to:

$$\nabla \boldsymbol{P}^{NL} = jk_S^3 \left(\lambda + 2\mu \; + \frac{\mathcal{A}}{2} + \mathcal{B} \right) U_S^2 \begin{bmatrix} \sin\theta \\ 0 \\ \cos\theta \end{bmatrix} \frac{1}{2} e^{j(2\omega t - 2k_S x \sin\theta - 2k_S z \cos\theta)} \tag{2.30}$$

Self-interaction of shear waves in the bulk generate longitudinal wave harmonics. Due to the mismatch of the propagation velocity of the intrinsic transverse waves and the generated compressive second harmonics, there is no cumulative generation. No coherent contribution to the shear wave nonlinearity from lattice anharmonicity is allowed in an polycrystalline material under no-stress condition. In specific single crystal orientations second harmonic generation is permitted due to anisotropy of the elastic tensor. As stated in Jiang [85] there are limitations to the research done on shear wave interaction with dislocations: self-interaction of shear waves are prohibited in isotropic media and there is no reported method to measure the absolute amplitude of shear waves. The later statement made by Jiang [85], is refuted in Monchalin [126]. Monchalin has used optical heterodyne interferometry to measure surface in-plane and out-of-plane displacements. However, such experimental measurement requires complex laser path configuration.

2.2.5 Third harmonic generation

Third harmonics generation is a result of a symmetric nonlinear stress strain relation [63]. Due to the symmetric elastic relation no external stress is required to activate the dislocation contributions to the nonlinear acoustic generation. In the case of third harmonic generation, as opposed to second harmonic generation, the contribution from the lattice parameters is found to be an order of magnitude smaller than that from dislocations. This allows easier study of dislocation generation and motion during the fatigue cycle, without the contribution from the lattice anharmonicity.

An expression for the third harmonic parameter β_3 can be derived as in section 2.2.1.

$$\beta_3 \propto \frac{8}{k^3 x}\left(\frac{A_3}{A_1^3}\right) \tag{2.31}$$

where A_1, A_3 are the amplitudes of the fundamental and third harmonics. Third harmonic generation from the self-interaction is allowed for both transverse and longitudinal waves due the symmetric stress-strain relation.

2.2.6 Guided waves

For guided waves nonlinear generation becomes more complex. Ultrasonic waves in the bulk have non-dispersive behaviour, which allows for cumulative generation of measurable harmonic signals. When constricted by the geometric boundaries of a structure, the acoustic waves are limited to certain wave modes. These modes have dispersive nature and complex power flux. Specific conditions must be met to cumulatively generate second harmonics when measuring using guided waves.

Lamb waves

Lamb wave are guided waves, which propagate in plates. They consist of compressional and transverse waves that are reflected at the plate boundaries, as seen in the schematic diagram in Fig. 2.3. Due to mode conversion at those multiple reflections, a standing wave interference patterns is formed. As a result, a wave will propagate in certain directions guided by the geometry. A complete description of the Rayleigh-Lamb frequency equation can be found in Rose [169].

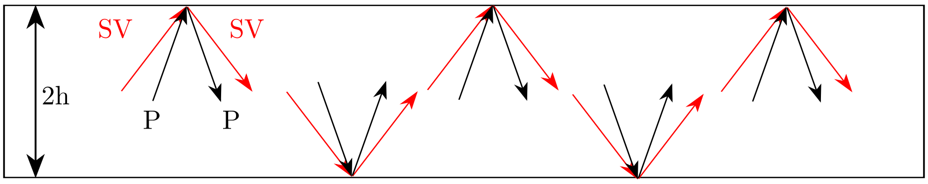

Figure 2.3: Wave reflections in a waveguide

To model the complex behaviour of the Lamb waves, one needs to split the wave potentials in two expressions.

$$\phi = \Phi(y)e^{i(kx-\omega t)} \qquad \psi = \Psi(y)e^{i(kx-\omega t)} \tag{2.32}$$

For a plate of thickness $2h$, the solutions for the Rayleigh-Lamb frequency equations, assuming stress-free boundaries, are expressed as [3]:

$$\frac{tan(qh)}{tan(ph)} = -\frac{4k^2pq}{(q^2-k^2)^2} \qquad \frac{tan(qh)}{tan(ph)} = -\frac{(q^2-k^2)^2}{4k^2pq} \tag{2.33}$$

Where:

$$p^2 = \frac{\omega^2}{c_L^2} - k^2 \qquad q^2 = \frac{\omega^2}{c_T^2} - k^2 \tag{2.34}$$

Solutions to (2.33) can be divided into symmetric and antisymmetric Lamb wave groups. This definition describes the amplitude distribution over the plate thickness. Solutions to the equations require numerical computations. Each of the modes defined by (2.33) propagates with frequency ω and a phase velocity $c_{ph} = \frac{\omega}{k}$. Group velocity $c_g(f)$ is defined as partial numerical derivative with respect to the wavenumber k applied to the solutions for (f, k).

$$c_g(f) = 2\pi\frac{\partial f}{\partial k} \tag{2.35}$$

Phase and group velocities for each of the modes, change with frequency, which makes the Lamb wave's propagation dispersive in nature, as shown in figure 2.4. Additional to the velocity dispersion, the mechanical displacement through thickness profile for each mode also changes with frequency. Due to this dispersive nature, for nonlinear Lamb wave generation, certain additional conditions must be met: phase velocity matching, group velocity matching and non-zero power flux to higher harmonics. More advanced discussion will be provided later in section 4.1.2

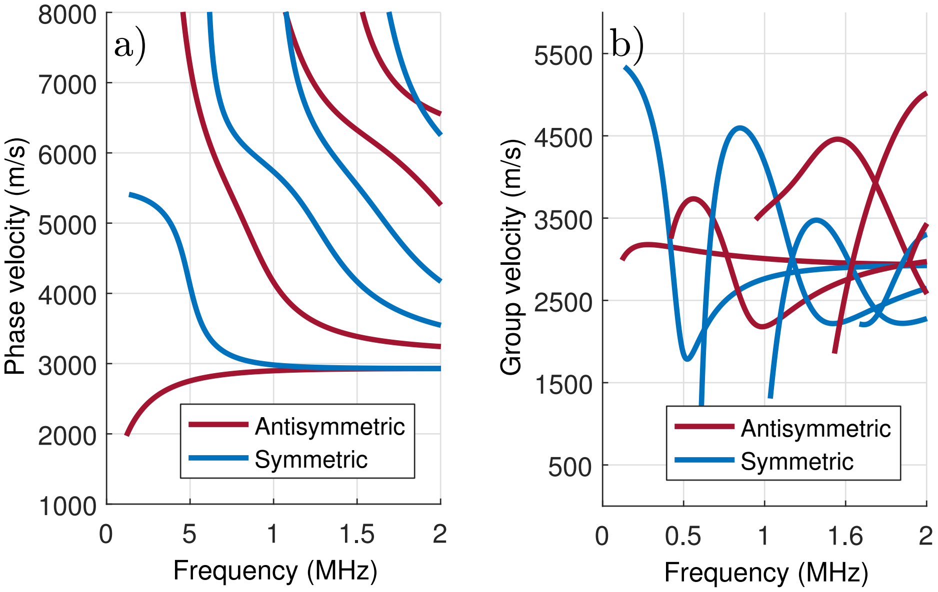

Figure 2.4: Dispersion curves for a Lamb wave in a 4.76 mm thick aluminium plate (AL6061).

Rayleigh waves

Rayleigh waves are surface waves travelling along a stress-free boundary. The energy concentration of the wave is limited to the surface of the elastic material. The wave displacement decays exponentially with the depth. The surface wave is composed of longitudinal and shear components. As previously discussed, the acoustic nonlinearity for the transverse wave in isotropic materials vanishes due to symmetry. Therefore, only the longitudinal component of the Rayleigh wave contributes to the nonlinear wave generation. As derived in Herrmann [61], the nonlinear Rayleigh parameter $\tilde{\beta}_R$ can be expressed as:

$$\tilde{\beta}_R = \frac{8iA_2^z}{k_l^2 x (A_1^z)^2} \frac{p}{k_R} \left(1 - \frac{2k_R^2}{k_R^2 + s^2}\right) \tag{2.36}$$

where A_1^z, A_2^z, k_R, k_l, k_s are the amplitude of the out-of-plane displacement at the surface of the fundamental and second harmonics and the wavenumbers for Rayleigh, longitudinal and shear waves. Also p and s are defined as:

$$p^2 = k_R^2 - k_l^2 \qquad s^2 = k_R^2 - k_s^2 \tag{2.37}$$

Higher order harmonic guided wave generation is discussed in Chillara [33]. A summary of the possible higher order nonlinear interactions will be presented in section 4.1.2.

Shear horizontal waves

Shear horizontal waves are a mode of ultrasonic guided wave with a polarised displacement, perpendicular to the direction of travel, and in-plane with the boundary interfaces. The shear horizontal waves can classified as symmetric and antisymmetric, relating to their through thickness displacement profiles. As with the Lamb-Rayleigh guided wave family, shear horizontal guided waves exhibit frequency dependence for both phase and group velocities, see figure 2.5. An exception to this is the SH0 mode, which is a symmetric dispersionless mode, which has a speed equal to the bulk wave shear speed. Due to symmetry conditions, shear horizontal waves are allowed to generate: second harmonic longitudinal guided waves, as proved earlier in section 2.2.4, and third harmonic shear horizontal waves.

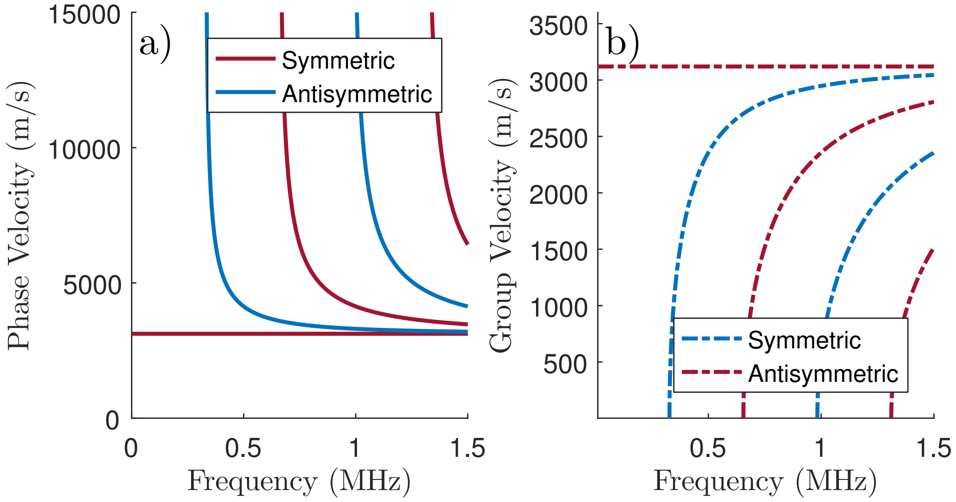

Figure 2.5: Dispersion curves for shear horizontal modes in a 4.76 mm thick aluminium plate (AL6061).

2.2.7 Second and third order elastic coefficients

Second order elastic coefficients

Using Voigt notation and Brugger constants the second-order elastic coefficients for cubic crystals, which have the highest number of symmetries, can be reduced to:

$$\lambda + 2\mu = C_{11} = C_{22} = C_{33} \tag{2.38}$$

$$\lambda = C_{12} = C_{13} = C_{23} = C_{21} = C_{31} = C_{32} \tag{2.39}$$

$$\mu = C_{44} = C_{55} = C_{66} \tag{2.40}$$

Where λ and μ are the Lames constants.

Third order elastic coefficients

A few different sets of notation exist, but are all compatible with the total of 3 independent constants to complete all third order coefficients. The earlier mentioned elastic constants can be expressed as:

$$A_{111} = 3C_{11} + C_{111} \tag{2.41}$$

$$A_{11} = \sigma(x) + C_{11} \tag{2.42}$$

2.2.8 Velocities dependence on TOEC

Sound velocity changes when stress is applied to the structure, as described by (2.8). Additional velocity changes can be introduced by variance of the nonlinear parameter. Contributions to the latter will also depend on stress. Using Murnaghan constants l, m, n [137] and Lames constants λ, μ, the wave velocities can be expressed as a function of the stress applied:

$$\rho_0 c_{L\|}^2 = \lambda + 2\mu - \frac{\sigma}{3K_0}\left[2l + \lambda + \frac{\lambda + \mu}{\mu}(4m + 4\lambda + 10\mu)\right] \tag{2.43}$$

$$\rho_0 c_{L\perp}^2 = \lambda + 2\mu - \frac{\sigma}{3K_0}\left[2l - \frac{2\lambda}{\mu}(m + \lambda + 2\mu)\right] \tag{2.44}$$

$$\rho_0 c_{S\|}^2 = \mu - \frac{\sigma}{3K_0}\left[m + \frac{\lambda n}{4\mu} + 4\lambda + 4\mu)\right] \tag{2.45}$$

$$\rho_0 c_{S\perp\|}^2 = \mu - \frac{\sigma}{3K_0}\left[m + \frac{\lambda n}{\mu} + \lambda + 2\mu\right] \tag{2.46}$$

$$\rho_0 c_{S\perp\perp}^2 = \mu - \frac{\sigma}{3K_0}\left[m - \frac{\lambda + \mu}{2\mu}n - 2\lambda\right] \tag{2.47}$$

Where $K_0 = \lambda + \frac{2\mu}{3}$ and $c_{\alpha\beta\gamma}$ is the wave velocity of a wave of type α with wave propagating in the β direction with respect to the stress, and with particle oscillating in the γ orientation with respect to the stress.

2.3 Non-classical nonlinear ultrasonics

In non-classical nonlinearity the mesoscopic elastic behaviour of materials give rise to a complex dynamic hysteretic response. At high wave amplitudes the classical Landau theory [109] does not describe the experimentally measured wave behaviour. The observed scaling of harmonics and frequency peak shifts require a revised nonlinear ultrasonic theory. Using Green's function and Preisach-Mayergoyz space, McCall and Guyer [120; 121] have derived a theory that describes the elastic behaviour of solids at higher ranges of dynamic strain. The nonlinear stress-strain relationship is expressed as:

$$\sigma(\epsilon, \dot{\epsilon}) = K_0 \left\{ (\epsilon - \beta\epsilon^2 - \delta\epsilon^3 - \ldots) + \frac{\alpha}{2}\left[2(\Delta\epsilon)\epsilon - sign(\dot{\epsilon})((\Delta\epsilon)^2 - \epsilon^2) \right] \right\} \tag{2.48}$$

where K_0, σ, ϵ, $\dot{\epsilon}$, $\Delta\epsilon$, α are the linear modulus, the stress, the strain, the time derivative of the strain, the amplitude of strain over the entire wave cycle and the hysteretic nonlinear parameter respectively. β and δ are the classical Landau nonlinear parameters. The hysteretic elastic behaviour is explained as a result of intrinsic damage such as micro-cracks, dislocation interactions and grain boundary effects.

The nonlinear stress strain relation in micro-inhomogeneous media changes with damage, which allows for promising applications in NDT. Multiple techniques have been used to measure non-classical components in rocks, concrete and metal. Two of them are going to be discussed here, to present their analytical formulation.

2.3.1 Nonlinear resonance ultrasonic spectroscopy

Nonlinear resonance ultrasonic spectroscopy (NRUS) is a resonance method, measuring variations in the hysteretic nonlinear acoustic parameter α and attenuation. The high amplitude of the ultrasonic waves leads to changes in the average elastic modulus K. In Fig. 2.6 the average elastic modulus for two different excitations amplitudes are drawn. The area enclosed by the hysteresis loop, causes a reduction in the ultrasonic signal. This reduction varies with the amplitude of the excitation signals, which leads to both changes in the attenuation and the frequency of the ultrasonic waves. NRUS uses geometrical resonance modes to create a high amplitude wave, capable of exhibiting nonlinear behaviour. The material is excited with a sine wave with different amplitudes. The technique measures changes in the frequencies of a resonance mode for different excitation amplitudes. The NRUS frequency shift Δf has been reported to be highly sensitive to the damage magnitude. It can be expressed as:

$$\frac{\Delta f}{f_0} = \frac{f_0 - f}{f_0} = C_\alpha \Delta\epsilon \qquad (2.49)$$

where C_α is a hysteretic coefficient proportional to β, and $\Delta\epsilon$ is the local strain amplitude for the previous period.

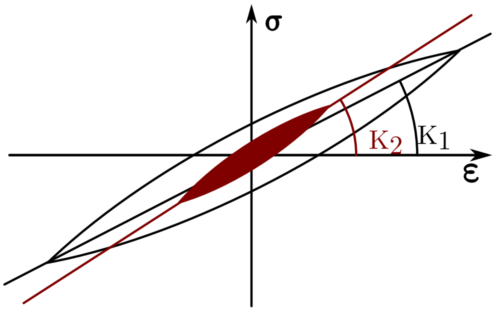

Figure 2.6: Stress strain curve for two different excitation levels adapted from [122]. The generated sine wave for the lower excitation level describes a hysteresis curve with an average elastic modulus of K_2, while the higher excitation level describes a larger hysteresis loop with an average elastic modulus of K_1.

2.3.2 Nonlinear wave modulation spectroscopy

In nonlinear wave modulation spectroscopy (NWMS) continuous acoustic waves are applied to a sample at two different frequencies and their interaction is measured. Under linear elastic propagation, the input frequency spectrum should not generate any new frequencies. Material damage such as cracks, delamination and microscopic defects give rise to increased nonclassical nonlinearity effects, corresponding to the material hysteretical behaviour. At higher damaged states, the nonlinear stress-strain response permits a higher frequency f_1 to be modulated at the low frequency f_2. This generates additional frequencies within the measured signals, such as combination of input frequencies - first and second order sidebands $f_1 \pm f_2$, $f_1 \pm 2f_2$ and the complimentary higher harmonics. Damage detection is measured as a ratio between the combined frequency output amplitude $A(f_1 + f_2)$ to the applied input amplitudes

$A(f_1)$, $A(f_2)$, and can be expressed as:

$$\tilde{\beta}(f_1+f_2) = \frac{A(f_1+f_2)}{A(f_1)A(f_2)} \tag{2.50}$$

Under certain conditions this allows for wave-mixing of non-collinear waves [36]. This can be a combination of two shear waves or a shear wave and a longitudinal wave, resulting in both cases in the generation of a longitudinal wave of the summed frequencies. A schematic diagram of the wave interaction is presented in Fig. 2.7. Further discussion regarding this method can be found in 4.2.

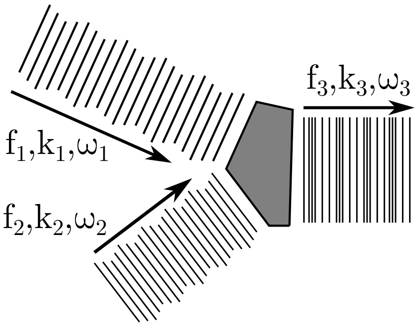

Figure 2.7: Schematic diagram of non-collinear wave-mixing configuration. Two incident waves interact within a small volume within the material and generate a third wave of their combined frequencies and wavenumbers. The amplitude of the generated third wave is proportional to the the nonlinear elastic properties within the interaction volume.

Conditions must be met to allow the nonlinear wave modulation:

$$k_3 = k_1 + k_2 \qquad \omega_3 = \omega_1 + \omega_2 \tag{2.51}$$

Where k_1, k_2 and ω_1, ω_2 are the wavenumbers and angular frequencies respectively of the input signals and k_3, ω_3 are the wavenumber and angular frequency of the combined nonlinear response. For collinear propagation this allows for cumulative generation of nonlinear signals when both the input waves are of the same type, as their velocities are equal.

2.4 Dislocation generation

During the plastic deformation of crystalline materials the dislocation density drastically increases. In most polycrystalline metal materials this leads to work-hardening due to dislocation entangling and formation of cell or subgrain walls. Different models have been proposed to explain the generation mechanisms for dislocation generation, such as: the Frank-Read source [49], the double-cross slip mechanism [103]. As such, the dislocation density can be related directly to the fatigue lifetime.

2.4.1 Dislocations in materials

Dislocations are line imperfections in the regular arrangement of an atomic crystal lattice. They disturb the local properties of crystalline solids. Defects in crystals can be categorised as point, line, surface and volume groups, although the behaviour of the latter can be described as a cumulative interaction between more primitive structures.

Dislocation movement depends on the bonding energy of the crystal structure. For metal materials, the close-packed non-directional bonding reduces the force required to move a dislocation, known as Peierl's stress. For ceramic materials this force is higher due to angular and/or ionic bonding, and restricts any dislocation movement.

Dislocation movement is strongly connected to plastic deformation. Such motion requires the breaking and reinstating of lattice bonds. The plane at which one crystal block from the atomic structure slides over another crystal block is called the slip plane. An understanding of the slip plane interactions with applied stress allows predictions for the velocity of the dislocations. Dislocation movement depends on the applied shear stress, temperature, crystal purity and the dislocation type. Concepts of dislocation glide motion are summarised in [70]. Such movement must be reduced in order to increase the strength of polycrystalline metals. Three different methods can provide strengthening: reduction of grain size, precipitates and cold work (dislocation entanglement). Grain size reduction decreases the length a slip can travel before it reaches a grain boundary, which prevents any further travel. This can be done by anisotropic deformation, affecting the orientation, shape and cross-section of individual grains. The introduction of precipitates or impurities generates local shear fields which increases the local Peierls stress. This produces a barrier for any dislocation motion opposing the local shear stress. During room temperature deformation - cold work - the material undergoes forming operations changing its cross-sectional area. The process generates new dislocations which interact with each other and hinder any further movement. Due to the low temperature no recrystallization is allowed during the cold working process.

Annealing is a heat treatment process which reverses the effects of cold working. Depending on the treatment duration, the process can be split into three stages: recovery, recrystallization and grain growth. At the recovery stage dislocations density is greatly reduced by annihilation of opposite dislocations. Further reduction of the dislocation density occurs when previously deformed crystal grains form new undeformed grains, during the recrystallization phase. In the final phase of the annealing process, smaller grains are consumed by larger grains, therefore reducing grain boundary areas.

2.4.2 Dislocation density measurements

Traditionally there are three methods to observe the generation of dislocations: line broadening of X-ray electron backscatter diffraction (EBSD) lines, etch-pit density and transmission electron microscopy (TEM) [70].

Chemical etching involves the application of a destructive substance which interacts with the crystal surface. The core of the dislocation interacts more rapidly than the surrounding crystal. This generates etch pits measurable by optical microscopes or scanning electron microscopy (SEM). An example of an pit-etch treated surface can be seen in Fig. 2.8. This technique allows one to measure atomic scale dislocation density with readily available apparatus. However, due to its destructive nature it will alter the material state irreversibly.

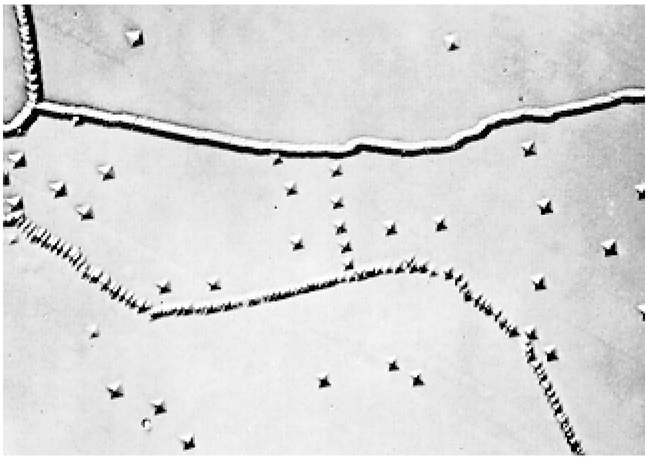

Figure 2.8: Pit-etch treated surface of a LiF crystal. Dark lines represent grain boundaries and the individual pyramids correspond to single dislocations [76].

TEM images can produce a measurement of dislocation density of thin foils typically less than 200 nm thick [70]. TEM uses focused electron beams in a similar technique to the optical microscopes. A high energy electron beam, typically over 100 keV, is emitted and passes through the thin specimen. Electrons are diffracted, scatter or transmitted by the crystalline material and are refocused on a screen. Dislocations reduce the intensity of the transmitted electrons by altering the Bragg diffraction conditions of the electron beam surrounding the core of the dislocation. This allows the dislocation to be be directly observed as a dark line on a bright-field image. High resolution TEM allows one to image dislocation processes including their motion, generation and interaction with grain boundaries on the atomic level [89]. This method provides high accuracy results within the limit of a nanoscale area and the statistical representation. A snapshot from a video referred in Kacher [89], is shown on Fig. 2.9. The dark lines represent dislocation gliding from a persistent slip bands (PSB) source.

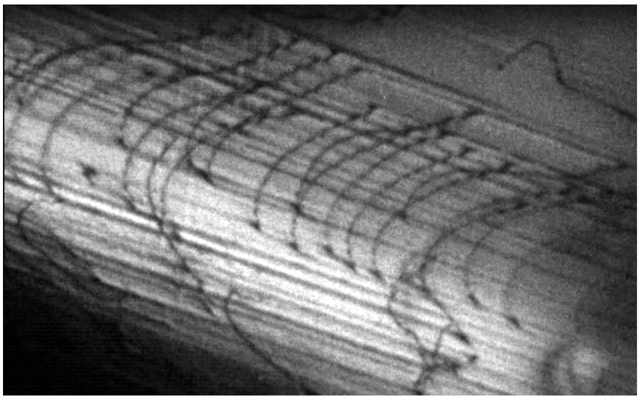

Figure 2.9: Dislocation glide during in-situ measurement of 304 stainless steel using TEM from [89].

Electron backscatter diffraction, when compared to TEM, has a greatly reduced resolution. The method measures an estimate of the dislocation density from the shape of the diffraction peaks. Models of dislocation distribution are used to assess the crystal, while no information is provided for the topology of the dislocation structures. This does not allow for accurate measurement of the dislocation density for small crystalline size metals [30].

2.4.3 Fatigue and creep damage

Fatigue is caused by the repeated application of stress to metals. It measures the material's probability of failure due to fracture when subjected to cyclic stress. Creep damage occurs when the material is exposed to static loads at elevated temperatures for prolonged durations. Both of those failure mechanisms are considered in structural engineering designs, which provides life assurance for mechanical parts.

Fatigue SN curves

Fatigue failure consists of three stages. Initially a crack originates at the surface, where precursors can exist, such as scratches, inclusions, dislocation build-up or other stress concentrators. With increasing load cycles the crack gradually propagates and grows. Finally when the reduced cross-section of the component cannot support the applied load, fracture occurs. To model this behaviour fatigue data is presented in Stress - Number of Cycles (S-N) curves. The S-N curve for aluminium alloy AL6061 is shown in Fig. 2.10 for the case of fully reverse tensile stress. These contain information about the probability of the current material failing under the specific test conditions. These conditions are expressed as a combination of stress amplitude σ_a, stress ratio R, stress range σ_r and/or mean stress σ_m. These parameters are selected with respect to the yield point σ_y. Permanent irreversible plastic deformation occurs at stress levels above the yield stress, also defined as the elastic limit.

$$\sigma_m = \frac{\sigma_{max} + \sigma_{min}}{2} \qquad \sigma_r = \sigma_{max} - \sigma_{min} \tag{2.52}$$

$$\sigma_a = \frac{\sigma_{max} - \sigma_{min}}{2} \qquad R = \frac{\sigma_{max}}{\sigma_{min}} \tag{2.53}$$

The cyclic loading can be performed with non-zero mean stress. As the mean stress σ_m increases, the stress amplitude must be reduced for the material to tolerate the applied stress and stay within the elastic limit. Approximations for non-zero stress amplitude σ_a are expressed by the Goodman relation [54]:

$$\sigma_a = \sigma_{fat} \left[1 - \frac{\sigma_m}{\sigma_{UTS}} \right] \tag{2.54}$$

where σ_{fat} is the desired zero-mean fatigue limit and σ_{UTS} is the ultimate tensile strength limit. For certain types of ferritic steels, the S-N curves become horizontal below a certain stress level - endurance limit, and failure is not expected to occur.

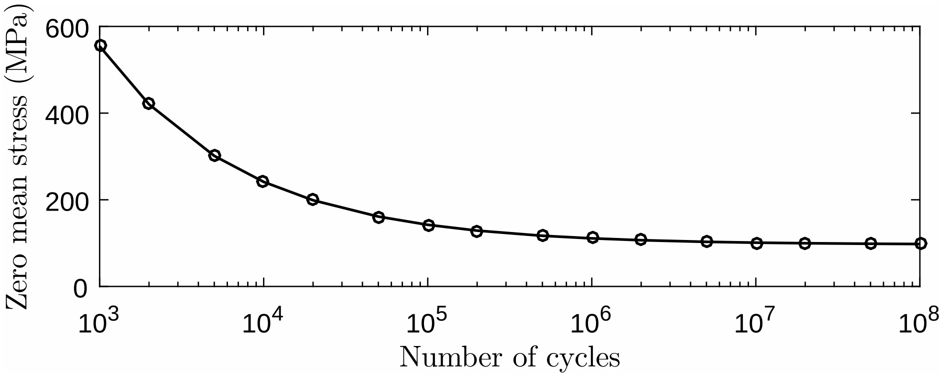

Figure 2.10: SN curve for fully reversed tensile test based on 6061 fatigue data [215].

Fatigue testing can be accomplished using different types of stresses: axial, flexural or torsional. The strength of the materials can be reduced by environmental factors, for example exposure to corrosive chemicals. Corrosion enhances the crack propagation and this causes the materials to fail below their yield strength. This can be prevented by the application of corrosion preventive coatings.

Alternatively, the material can be exposed to elevated temperatures, whilst under constant stress - creep fatigue. The increased temperature causes an increase in the amount of free energy in the system. This allows the dislocations to glide past previously obstructing barriers. During this process, cold-work hardened materials lose some of their strength.

Chapter 3

EMAT introduction

Electromagnetic acoustic transducers (EMAT) have been studied for applications which require non-contact generation and detection of ultrasound waves in electrically conductive materials since the early 1970s [48; 185–187; 189]. Further studies have been conducted, and a summary of EMAT applications is available in Hirao and Ogi [67]. EMAT transducers have advantages over contact methods within certain applications such as: high speed scanning across a surface [46], elevated temperature measurements [60], generation and detection of ultrasound waves with no additional surface loading [67], wide bandwidth transduction [67] and the ability to generate and detect many different wave modes [67]. This chapter will introduce the physical principles behind the operation of EMATs, discuss the multiple transducer designs, force generation patterns, supporting electronics and signal processing.

3.1 Electromagnetic acoustic forces

EMAT are transducers which convert electrical signals to mechanical vibrations in the surface of a sample by means of electromagnetic coupling. Similar to piezoelectric ultrasonic transducers, electromagnetic acoustic transducers can be used to receive and generate ultrasound signals using the same sensor, although the physical coupling mechanisms involved in the two processes may differ. Piezoelectric transducers require physical coupling to achieve high electromechanical transfer, while EMATs have non-contact transduction.

EMAT force generation process involves multiple EM mechanisms: Lorentz force, magnetostriction force, magnetisation force and self-field force. The principles involved depend on the tested material and its physical characteristics. EMATs use the interaction of a dynamic magnetic field B_D, produced by a time varying current flowing through an electrical coil, with the eddy currents within a conducting sample in order to generate force within the sample's surface [67]. In electrically conducting materials this dynamic magnetic field induces image eddy currents in the surface, defined by Lenz's law [217], which then interact with other electromagnetic potentials.

3.1.1 Lorentz force

The Lorentz force mechanism is present in all EMAT applications using electrically conducting materials, where, in generation, it creates a body force due to the interaction of the current flow in the sample and an applied magnetic field [217].

$$\vec{F}_{Lorentz} = q\left(\vec{E} + \vec{v} \times \vec{B}\right) \tag{3.1}$$

where $\vec{E}$ is the electric field vector, $\vec{v}$ is the velocity of the electrical charge particles, q is the charge of the particle and $\vec{B}$ is the density of the magnetic flux. For EMAT applications, there is no direct electric field $\vec{E}$ contribution to the Lorentz force, so the term can be neglected. The moving charge q are the electrons driven by the eddy image currents $\vec{J}_{eddy}$ on the sample surface. As presented in Kawashima [94], the charge and velocity terms can be combined and expressed as the eddy current density $\vec{J}_{eddy}$. The magnetic field $\vec{B}$ is in general a combination of an applied magnetic field $\vec{B}_S$ (from a permanent or electromagnet, for example) and the dynamic magnetic field $\vec{B}_D$ from the EMAT coil that generates the eddy current in the sample. The expression for the force can be defined in these terms as:

$$\vec{F}_{Lorentz} = \vec{J}_{eddy} \times (\vec{B}_D + \vec{B}_S) \tag{3.2}$$

The contribution from each of the forces depends on the magnitude of their respective magnetic fields. The static magnetic field B_S can be applied using strong static magnets ($NdFeB$, $SmCo$), an electromagnet or a pulsed solenoid [60]. The applied magnetic field is either static or is changing very slowly relative to the eddy current, and so can be thought of as a static field for the purpose of this analysis. The directivity of the external field can be varied to match the required force direction. The direction of the self-field force is independent of the applied external magnetic field and generates repulsive body forces in the sample surface [83], see Fig. 3.1.

The frequency of the ultrasound generated using the static magnetic field is equal to the frequency ω of the electrical signal in the EMAT coil. The dynamic magnetic field $\vec{B}_D$ also fluctuates at the same frequency, but at a $\pi/2$ phase offset to the $\vec{J}_{Eddy}$ [101]. For a sinusoidal electrical driving signal of amplitude J_0:

$$\left|\vec{J}_{Eddy}\right| \propto J_0 sin(\omega t) \tag{3.3}$$

From Maxwell's equations [217] the generated dynamic magnetic field is then:

$$\left|\vec{B_D}\right| \propto J_0 sin(\omega t) \tag{3.4}$$

Applying Maxwell's equations once more, the eddy current generation is defined as:

$$\left|\vec{J}_{Eddy}\right| \propto \frac{d\left|\vec{B_D}\right|}{dt} \propto J_0 \omega cos(\omega t) \tag{3.5}$$

Combining equations 3.2, 3.4 and 3.5:

$$\left|\vec{F}_D\right| \propto \omega sin(\omega t) cos(\omega t) = J_0^2 \omega sin(2\omega t)/2 \tag{3.6}$$

The frequency of the force generated by the dynamic field is twice the excitation signal frequency. The ultrasonic amplitude generated by the dynamic field force increases quadratically with excitation signal amplitude [203; 205]. At high currents the dynamic force can generate ultrasonic waves without a permanent magnet [80; 83].

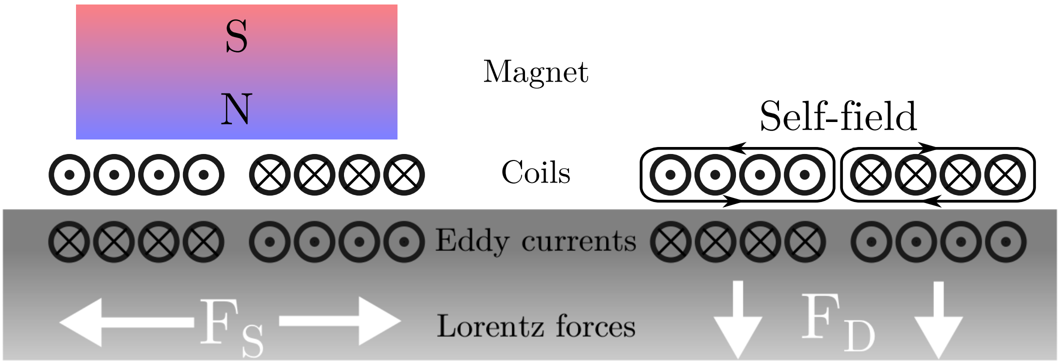

Figure 3.1: EMAT Lorentz Force due to static external magnetic field and dynamic self-field using simplified eddy current depiction.

Skin effect

Electromagnetic coupling effect is limited to a small volume at the sample surface - skin depth [71]. The current density for conducting material is defined as [211]:

$$\left|\vec{J}_{Eddy}\right| = J_0 e^{(-z/\delta)} \tag{3.7}$$

where J_0, δ, z are the current density at the surface, skin depth of the material and depth from the surface. The skin depth is a function of frequency and electrical properties of the material:

$$\delta = \sqrt{\frac{2\rho}{\omega \mu_r \mu_0}} \tag{3.8}$$

where ρ, μ_r, μ_0 are the material resistivity, relative magnetic permeability and free space permeability. The skin effect also causes depth dependant phase delay to eddy currents [211].

$$\vec{J}_{Eddy} = \vec{J_0} e^{(-z/\delta)} e^{i(\omega t - z/\delta)} \tag{3.9}$$

A large portion, 63%, of the induced current is concentrated within one skin depth of the sample surface. The total induced image current can be treated as a single current with a phase lag of $\pi/4$ relative to the surface induced current:

$$\vec{J}_{Total} = \int_0^\infty \vec{J}_{Eddy} dz = \vec{J_0} e^{i\omega t} \int_0^\infty e^{(1+i)z/\delta} dz = \vec{J_0} e^{i\omega t} \frac{\delta}{1+i} \tag{3.10}$$

For aluminium the skin depth is $82\,\mu m$ at 1 MHz and $59\,\mu m$ at 2 MHz. The shear wave wavelengths at those frequencies are 3.1 mm and 1.5 mm. The Lorentz force can be approximated to a surface force, as the skin depth is two orders of magnitude smaller than the acoustic wavelength.

Lorentz force acoustic coupling

The EMAT ultrasonic wave generation is a complex mechanism [67]. Current in the driving coil generates mirror image current in the sample surface. These eddy currents interact with the magnetic field and a Lorentz force acts on the moving charge carriers - electrons. The motion of electrons in the metallic sample causes electron-ion collisions which transfer some of the momentum to the acoustic wave carriers - ions. The electron equation of motion is:

$$m_e \frac{d\vec{v_e}}{dt} = -e(\vec{E} + \vec{v_e} \times \vec{B} - \frac{m_e \vec{v_e}}{\tau}) \tag{3.11}$$

where m_e, ev_e are the mass, charge and mean velocity of the electron and τ is the mean time of electron-ion collisions. The average relaxation time τ is of order 10^{-14} s [67], which is orders of magnitude smaller than the period of oscillation of the electric field. Therefore, the electron-ion collision momentum transfer can be viewed as a continuous process [67; 97]. Assuming a sample with neutral charge, equal electrons and ion density, the force per unit volume can be expressed as:

$$\vec{F}_{Lorentz} = -n\, e\, \vec{v_e} \times \vec{B} = \vec{J_e} \times \vec{B} \tag{3.12}$$

where n is the electron density.

Lorentz force detection

The receiving process for the Lorentz force based EMATs is different from the generation process. The ultrasonic vibrations cause the material to oscillate, with both ions and electrons in motion. In the presence of an external magnetic field, Lorentz force acts on both types of charge carriers. Due to their smaller mass, the electrons exhibit much higher acceleration than the ions. The deflected electrons' motion give rise to electromagnetic fields that will induce a surface current, measurable by the EMATs coil [42; 67]. EMATs are velocity sensors, as presented in [96] and generalised by Dixon [38]. The magnitude fast Fourier transform (FFT) for the velocity signal is enhanced by a factor of ω with respect to the FFT displacement magnitude.

The displacement $\vec{u}(z,t)$ of an ultrasonic wave travelling to the surface of a semi-infinite space can be described as:

$$\vec{u}(z,t) = u_0 e^{i(\omega t - kz)}\hat{z} \tag{3.13}$$

where $\hat{z}$ is a unit vector perpendicular to the plane of the semi-infinite space. At the interface of the space the ultrasonic wave is reflected and the resultant surface displacement vector $\vec{\xi}$ from the incoming and reflected signal can be described as:

$$\vec{\xi} = u_0\, e^{i\omega t}(e^{ikz} + e^{-ikz})\hat{z} = 2u_0\, cos(kz)\, e^{i\omega t}\hat{z} \tag{3.14}$$

The motion of electrons in the static magnetic field, generates a dynamic electric field [42; 67; 97]:

$$\vec{E_d} = \frac{\partial \vec{\xi}}{\partial t} \times \vec{B} \tag{3.15}$$

Assuming the magnetic field and displacement field are perpendicular, the magnitude of the induced surface current density is given by:

$$\left|\vec{J}\right| = 2i\omega\, \sigma\, u_0\, cos(kz)\, e^{i\omega t} \left|\vec{B}\right| \tag{3.16}$$

The result is integrated for the skin depth δ:

$$J = \frac{1}{\delta}\int_0^{\delta} 2i\omega\,\sigma\,u_0\,cos(kz)\,e^{i\omega t}\left|\vec{B}\right| dz = \frac{2i\omega\sigma}{k\delta}u_0 e^{i\omega t}\left|\vec{B}\right| sin(kz) \tag{3.17}$$

As the ultrasonic wavelength is much smaller than the skin depth, the small angle approximation can reduce the expression to:

$$J = 2i\omega\,\sigma u_0\,e^{i\omega t}\,\left|\vec{B}\right| = 2\sigma\left|\vec{B}\right|\frac{\partial u(0,t)}{\partial t} \tag{3.18}$$

Therefore, EMATs are velocity sensors and the transducer coil measures the temporal derivative of the wave displacement at the surface by detecting the surface current density [42].

3.1.2 Magnetisation force

In addition to the Lorentz force, magnetoelastic mechanisms can generate ultrasound in ferromagnetic materials, such as magnetostriction and magnetisation force [67; 100; 143; 192]. The magnetisation force arises in a ferromagnetic material exposed to an external magnetic field [67]. This phenomenon occurs when the external electromagnetic field interacts with the magnetic dipoles within the material. The magnetisation force causes reorientation of the dipoles [188]. The magnetisation force $\vec{F}_{MH}$ can be expressed in terms of volume and surface components [190]:

$$\vec{F}_{MH} = \vec{F}_v + \vec{F}_s = \int_v (\vec{M}\cdot\nabla)\vec{H}d\hat{x}^3 + \frac{1}{2}\mu_0\int_s \vec{M}_n^2\hat{n}d\hat{x}^2 \tag{3.19}$$

where $\vec{M}$, $\vec{H}$ are the magnetisation and magnetic field strength. In an electrical conductor when the static magnetic force is tangentially oriented, the normal component of the Lorentz and magnetisation forces act in opposite directions. Therefore, longitudinal wave mode generation in ferromagnetic materials is reduced [67; 143; 188]. The magnetisation force has been shown to have a smaller contribution to the generation of shear waves and therefore is neglected in calculations and measurements [67; 188].

3.1.3 Magnetostriction force

The magnetostriction force is generated when an external magnetic field is applied and the magnetic domains want to realign, which leads to mechanical strain [143] - the Joule effect [88]. The reverse process of magnetic field generation from applied stress is the Villari effect [199]. If the magnetic field oscillates, the ferromagnetic material vibrates and ultrasonic waves are generated. In polycrystalline materials, the magnetostrictive effect is highly nonlinear [67]. The relationship between the applied magnetic field $\vec{H}$ and the resulting strain $\Delta L/L$, as shown in figure 3.2, is symmetrical with respect to the zero magnetic field. Due to this symmetry, if an oscillating magnetic field $\vec{H}_d$ with frequency ω is applied by itself, the resulting mechanical wave would have frequency 2ω. To reduce nonlinear effects of the magnetostrictive curve, a static magnetic field $\vec{H}_s$ is applied to offset the operation range. The static field is carefully selected to centre the operational range over the most linear part of the magnetostrictive curve. The amplitude of the applied dynamic field $\Delta\vec{H}$ must be sufficiently smaller than $\vec{H}_s$ to ensure linear behaviour of the resultant strain. The strength of the magnetostrictive mechanism in low carbon steel have been compared to that of the Lorentz force by Ribichini [165; 166]. At low bias field strengths, in these samples the contribution from the magnetostrictive force dominates the ultrasonic wave generation, and as the field increases, the magnetostrictive force saturates, and the Lorentz force becomes dominant.

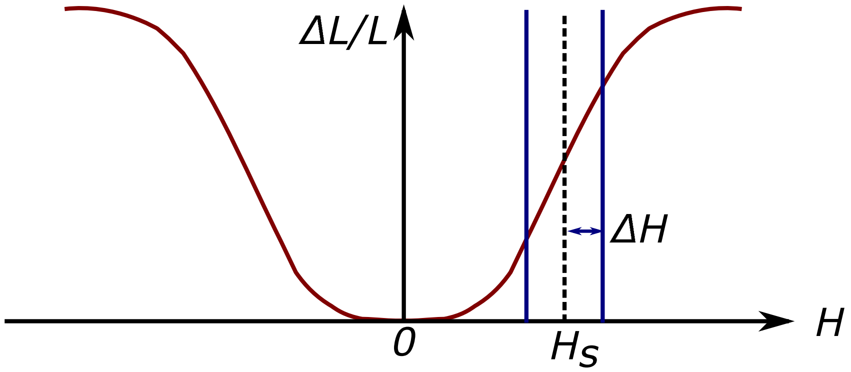

Figure 3.2: Typical magnetostrictive curve: Strain $\Delta L/L$ and magnetic field H. Bias magnetic field H_s offsets the range of operation. An oscillating dynamic magnetic field with amplitude $2\Delta H$ generates mechanical vibrations using Joule's effect.

For contact magnetostrictive transducers a thin magnetostrictive foil is fixed to the sample surface. Ultrasonic vibration is induced in the thin foil and is mechanically transferred to the sample surface. Contact methods using magnetostrictive patches have been used to measure elastic nonlinearity by Lissenden [111] and Liu [116]. Kim [100] has written a review of magnetostrictive patch transducers, which has detailed information regarding their applications and different modes of operation. Ferromagnetic materials are not the focus of this thesis, therefore contributions from the magnetostrictive force will be ignored. Magnetostrictive EMAT transducers can be contact or non-contact.

3.1.4 Effect of the EMAT's lift-off

The three electromechanical coupling mechanisms described in sections 3.1.1 , 3.1.2 , 3.1.3 allow for non-contact ultrasonic measurements to be performed. The distance between the sample and the EMAT transducer (lift-off), greatly influences the efficiency of the electromagnetic coupling. The amplitude of the electromagnetic field decreases approximately exponentially with increased lift-off, therefore limiting the operational range of EMATs to several millimetres [47; 144; 184]. Analytical solutions for EMATs coupling have been derived by Dodd [43] and Kawashima[95] and others [81; 82]. These provide good theoretical understanding of the effect of different experimental parameters. Lift-off performance and coil separation have been studied experimentally by Fan [47]. The results show improved lift-off performance for a ferrite-backed Rayleigh wave transducer and exponential decrease of amplitude with lift-off. Non-contact ultrasonic wave transduction allows for several potential applications. EMATs can be used in automated high speed scans as they do not require contact with the sample. As no coupling agent is required, measurements have improved repeatability, and mechanical loading from the sensor applied to the sample surface is minimised [188]. This gives EMATs great potential to reduce measurement uncertainty, have more repeatable coupling to the sample, and improve linear measurement techniques such as attenuation measurements [146]. However, stand-off greatly influences EMAT transducers, reducing greatly the transduction efficiency. EMATs can be used in high temperature applications [60], solving the problems associated with liquid couplants and cooling [177]. Another advantage of non-contact coupling is the possibility to measure conductive materials covered in non-conductive protective coatings, as well as providing information on the coating thickness [41; 66].

3.2 Types of EMATs

Various types of EMAT transducers have been developed for different wave modes. A summary of the more popular EMAT designs will be presented in this section. Advantages and limitations of these designs with regards to nonlinear ultrasonic applications will be presented in chapter 4. EMAT transducer designs can be classified into several categories depending on wave mode: bulk shear waves, bulk longitudinal waves, Lamb-Rayleigh guided waves and shear horizontal guided waves. Multiple EMAT designs are available for each of these ultrasonic wave modes. Magnet configurations and coils can vary in shape, size and pattern to generate specific force distributions on the sample surface. All of the designs described consider contributions from the Lorentz force only, unless specifically stated. A summary and references for magnetostrictive EMAT designs and their applications can be found in Kim [100] and the works of Hirao,Ogi and Ribichini [67; 144; 165; 166]. In all EMAT designs, a longitudinal component, normal to the surface, is generated by the self-field Lorentz force. The cumulative contribution, from each current carrying wire, generates a repulsive out of surface normal, piston-like, force acting on the specimen surface [81]. The self-field force distributions closely match that of the pattern of the EMAT coil. It is important to note that the amplitude of this effect increases quadratically with the magnitude of the driving current in the coil. Typically, the self-field force has much smaller amplitude than that arising from the magnetic field applied to the sample.

3.2.1 Bulk shear waves

EMATs can generate and receive bulk propagating shear waves with different oscillation polarisations. Multiple designs are available with different magnet configurations and coil patterns. Three coil designs will be presented and compared with respect to their force distribution.

The most basic EMAT design consists of a planar spiral coil and a single permanent magnet - spiral EMAT, as shown on figure 3.3. The magnetic field, produced by the permanent magnet, has normal and radial components, which interact with the induced eddy currents. The Lorentz force generated from the static magnetic field has both shear and longitudinal components. The shear horizontal (SH) transverse wave is radially polarised and propagates normal to the sample surface. Edge effects from the coil and the radial component of the magnetic field generate small amplitude longitudinal waves. Traction force discontinuities also contribute to the generation of longitudinal ultrasonic waves [73; 123]. This assumption is valid for all shear wave EMAT configurations. This additional compressional wave component must be considered when measurements contain mode-converted signals. The effects of the ratio between the width of the magnet W_{Magnet} and the diameter of coil D_{Coil} on the amplitude of the generated shear waves has been investigated by Mirkhani and Zhai [123; 220]. Increasing the magnet size collimates and increases the strength of the magnetic field. The amplitude increases up to a ratio of $W_{Magnet}/D_{Coil} = 1.20$, after which no significant further improvement is observed.

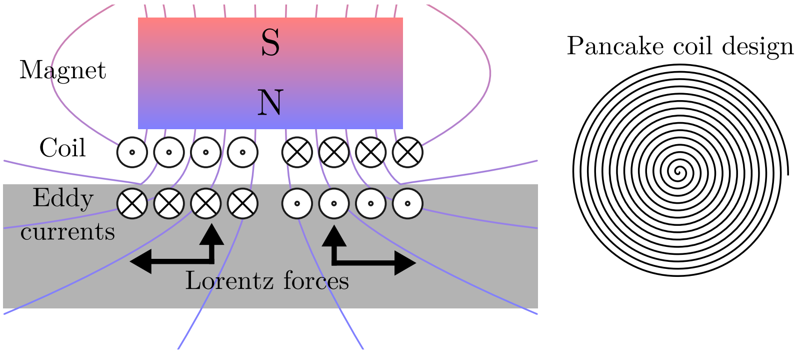

Figure 3.3: Radially polarized bulk shear wave EMAT design using single magnet and pancake coil.

An alternative design combining twin-magnet and racetrack coil can be used to generate linearly polarised shear horizontal SH waves - Racetrack SH EMAT, see Fig. 3.4. Static magnetic field Lorentz forces under both magnets act in the parallel direction, contributing to the shear wave generation. The magnetic field between the two magnets generates compressional waves with opposite directions, depending on the direction of the image current.

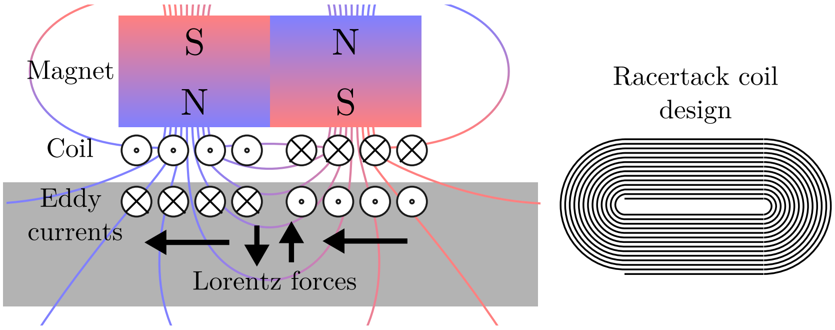

Figure 3.4: Linear polarized bulk shear wave EMAT design using twin magnet and racetrack coil.

The third SH EMAT design is constructed using single magnet and double-spiral (butterfly) coil. The schematic diagram for the butterfly SH EMAT is shown in Fig. 3.5. The coil pattern generates linearly polarised shear waves with minimal longitudinal components.

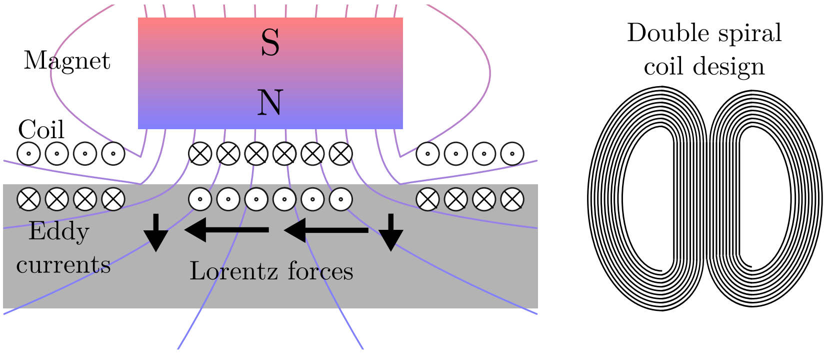

Figure 3.5: Linear polarized bulk shear wave EMAT design using single magnet and double spiral coil.

Wang [204] has analysed the ultrasonic radiation patterns of the three coil designs discussed, see Fig. 3.6. The article presents simulation results and experimental measurements that are in good agreement. The amplitudes generated from racetrack and double-spiral coils have almost equal value, but the divergence angle of the double-spiral coil is smaller. From the three designs, pancake coils have the worst performance with respect to the ultrasonic wave beam profile. They generate the smallest amplitude signal and have the largest angle of divergence.

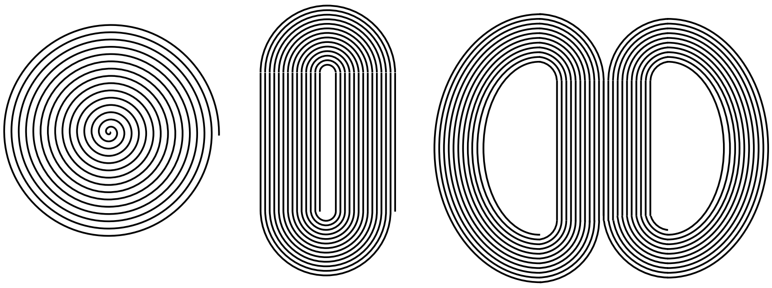

Figure 3.6: Three bulk shear wave EMAT coil designs discussed in Wang [204].

3.2.2 Line-focusing shear EMAT

Line focusing (LF) EMATs use complex meanderline coil patterns with variable coil spacing to generate focused shear ultrasonic waves, see Fig. 3.7. The radiation pattern and the directivity of LF EMATs depend on the selected frequency and the coil spacing. An optimised LF EMAT has an improved directivity when compared to the equally spaced meander coils [147]. Applications of the latter configuration will be discussed in 3.2.4.

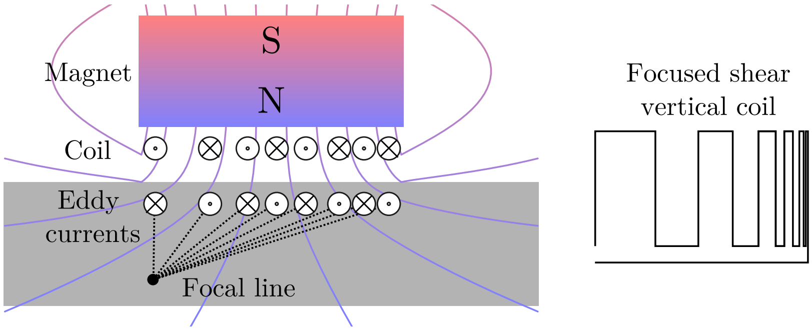

Figure 3.7: Shear vertical wave EMAT with a permanent magnet block and a meander-line coil with variable spacing.

Magnetic field

The amplitude of ultrasonic waves generated by the Lorentz force is linearly proportional to the strength of the magnetic field. Dutton [44; 45] has modelled an enhanced EMAT design arranging two magnets with parallel polarities in close proximity. The magnetic field compression configuration improves overall EMAT performance by reducing the physical size of the coils. Further research on optimizing the magnetic field for shear wave EMATs has been conducted by Isla [73]. Magnet designs using ferromagnetic flux concentrators or multiple magnets arranged in repelling configuration, have been analysed with regard to maximising the generated ultrasonic amplitude.

The proposed capped cone flux concentrator [73; 102] has been proven to increase the intensity of the magnetic flux, as the flux concentrator provides a high permeability path in close proximity to the sample surface. The effect is significantly reduced with lift-off. The magnetic field strength underneath the flux concentrator decreases sharply with distance, as the magnetic field lines try to reach the opposing pole. It is concluded that the performance of a ferromagnetic caped spiral EMAT is worse than that of a single magnet transducer.

The core-magnet arrangement has been analysed by Isla [73]. Multiple magnets are arranged in repulsive configuration, with a central flux concentrator core, to intensify the magnetic field strength. A high bias magnetic field has been achieved, ~ 2.4 T, and fields of strength ~ 3 T have been proposed for a hollow cylindrical magnet with radial magnetization. Single magnet configurations are limited by the physical properties of rare-earth magnets such as $NdFeB$, which can provide magnetic field strengths of ~ 1 T.

3.2.3 Longitudinal bulk EMAT

EMAT configurations for longitudinal bulk wave generation and detection have rarely been used [15; 190]. Their efficiency is lower compared to that of shear wave generating EMATs [158]. The magnetic field strength is significantly reduced due to the increased distance between the magnets. The efficiency is further decreased by inefficient coil design, which has a small ratio of active coil area to total coil area. The basic longitudinal EMAT design consists of a double spiral coil and two magnets, see Fig. 3.8. The magnets are separated by a finite distance and have opposite polarisation. Such a configuration produces a magnetic field parallel to the sample's surface. A magnetic flux guide can connect the poles, that face away from the sample, to close the upper magnetic field loop, and therefore improve the magnetic flux concentration. The linear centre part of a double spiral coil generates eddy currents in a perpendicular direction to the tangential magnetic field. The produced Lorentz force is in the out-of-plane direction to the sample surface. The resulting compressional waves travel normal to the surface plane.

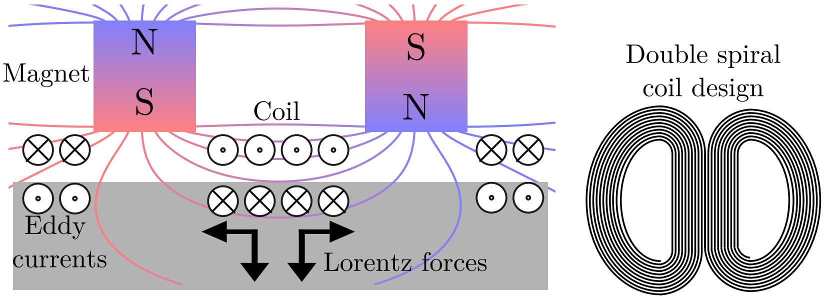

Figure 3.8: Traditional longitudinal EMAT configuration: A tangential magnetic field is provided from spaced magnets with opposing poles. The linear part of a double spiral coil generates eddy currents perpendicular to the applied magnetic field. Longitudinal waves are generated normal to the sample surface. [190]

The longitudinal EMAT transducer developed by Kawashima [94; 95] and analysed by Pereira Da Cunha [158] is shown to have improved transduction performance. The design increases the strength of the tangential magnetic field by reducing the distance between the opposing magnets and increases the efficient coil area, see Fig. 3.9.

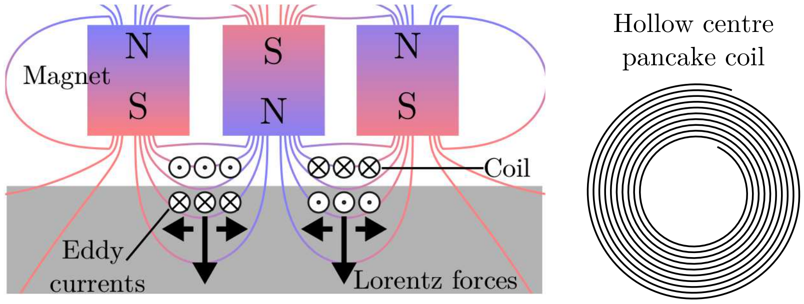

Figure 3.9: Improved longitudinal EMAT constructed from a cylindrical hollow magnet and magnetic rod. The middle magnet can be substituted for a magnetic flux guide [158]. A spiral coil, with inner radius equal or greater than the radius of the magnetic core, is located within the volume of the tangential magnetic field.

3.2.4 Guided waves

EMAT transducers have the ability to generate guided waves in plate and plate-like structures. Two different types of plate guided waves can be generated and measured using EMATs: Lamb-Rayleigh waves and shear horizontal waves. A detailed summary of the principles and applications of guided wave EMATs can be found in Huang [69].

Lamb-Rayleigh wave meanderline coil designs

Designs for Lamb and Rayleigh wave EMATs were developed by Thompson [186; 191; 193]. Lamb wave EMAT design have been optimised [93] and numerically modelled [203]. The transducer design consists of a meanderline coil and single magnet, see Fig. 3.10. The meander spacing D defines the periodicity of the force distribution pattern, which also defines the ultrasonic wavelength of a surface wave.

$$D = \lambda = c/f \tag{3.20}$$

Dispersion phenomena have been studied for Lamb waves and multiple techniques have been used to reduce their effect [4; 56; 59; 127; 155; 169; 198; 212]. Due to the guided nature of Lamb waves, multiple ultrasonic wave modes exist within a small frequency range, which requires careful selection of the transducers design [169; 170]. The frequency of the driving signal combined with the wavelength, defined by the coil spacing, improves the mode-selectivity of the Lamb EMATs [93; 219].

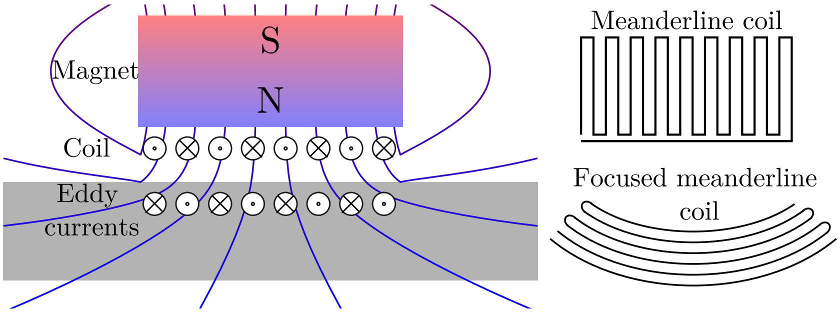

Figure 3.10: Lamb wave EMAT: A single magnet provides uniform magnetic field, whilst a meander-line coil with equal spacing generates the force radiation pattern. Additionally, the meander coil can be focussed to improve resolution and increase the generation amplitude.

The complete model of the forces generating ultrasound in Rayleigh-Lamb wave EMATs have been simulated and analysed by Wang [203]. The Lorentz force generated by the self-field interaction has a different periodicity than the force generated by the static magnetic field, as each coil wire generates a repulsive force beneath itself due to the self-field force, see Fig. 3.11. The contribution from the dynamic field force was shown to increase rapidly with current and plays a significant role typically when excitation currents are in order of 100 A or higher. The ratio of wire width to spacing interval between neighbouring wires (RWWSI) has a significant effect on the vibration amplitude and the divergence of the ultrasound beam [205]. As RWWSI converges to unity the contribution to the generating force from the dynamic Lorentz force is minimised, while the static field force contribution is reduced by 30%.

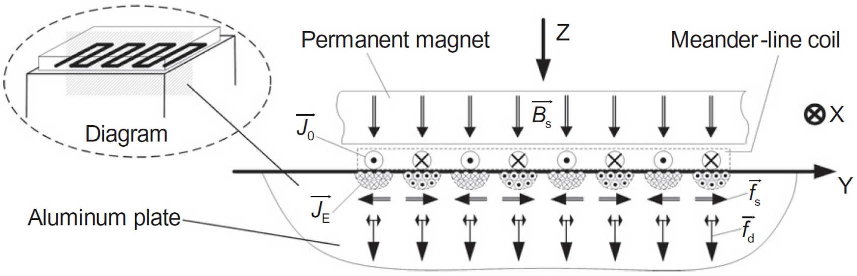

Figure 3.11: Force patterns of meanderline EMAT, including contributions from the static magnetic field $\vec{f}_s$ and the self-generated magnetic field $\vec{f}_d$ from [203].

Excitation performance of Lamb wave EMATs can be improved significantly by reducing lift-off and increasing excitation current [90; 93]. Other factors that affect the amplitude of the static field Lorentz force are: the thickness of the magnet, width of the coil conductors and the ratio between the size of magnet and coil [90; 108]. The effect of the coil's conductor on the receiving efficiency has been analysed by Wang [206]. Two types of meander line EMATs were simulated and experimentally tested: printed circuit board (PCB) and enamelled copper wires. The analysis shows wider single layer coils have better signal to noise ratio (SNR) compared to multi-layered or narrow coils. The SNR improves with the number of wires in one layer of the meander line.

Focussed surface wave EMATs have been developed to improve the resolution and increase the amplitude of the generated surface ultrasonic waves [195]. Meander-line coils with variable wire length have been tested to reduce the amplitude of the side lobes [214]. The use of two driving signals with 90° phase offset and variable meander coil spacing can allow for unidirectional surface or bulk shear wave EMAT [207].

Shear horizontal waves

Lorentz force shear horizontal EMATs typically use periodic permanent magnet (PPM) arrays [66; 156; 192]. The alternating polarity of the magnets generate an alternating Lorentz force parallel to the sample surface, see Fig. 3.12. The wavelength of the generated ultrasonic wave depends on the periodicity of the magnetic array, see Fig. 3.13. The magnet width and the gap between neighbouring magnets define the PPM array pitch and the lift-off performance of the EMAT [65].

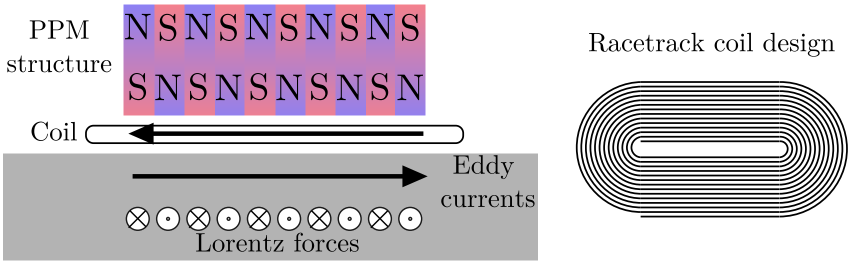

Figure 3.12: SH PPM EMAT: A periodic permanent magnet array is placed on top of racetrack coil. The ultrasonic wavelength equals twice the pitch of the magnetic array. Alternating Lorentz forces in the skin depth generate polarized shear wave travelling parallel to the surface.

PPM EMATs can also generate angled bulk shear waves [65; 128; 190]. The periodicity of the magnetic array creates interference patterns. Constructive interference at specific angles is achieved by applying a narrowband driving signal. The angle depends on the magnetic pitch and the ultrasonic wavelength [40; 64].

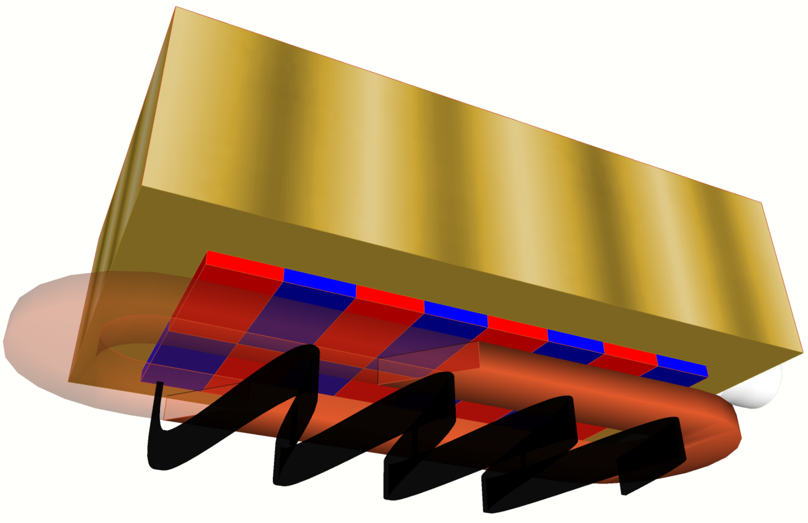

Figure 3.13: Shear horizontal wave generated by PPM EMAT.

3.3 Pulsed electromagnet

The magnetic field for EMATs can alternatively be provided by pulsed electromagnets. Pulsed electromagnet EMAT systems have been shown to produce large amplitude signals in ferritic steel and aluminium samples [154]. The pulsed electromagnets can have air or iron core solenoid structures [221], as the latter provide higher magnetic flux densities. A high current pulse, typically of the order of 100 A or higher, is supplied by a high voltage capacitor discharge. The pulsed magnet can generate a stronger magnetic field, compared to that of a permanent magnet and allows for high temperature measurements [60; 154]. Rare earth magnets such as NdFeB, SmCo have low Curie temperatures between 310 °C and 800 °C. These can operate at temperatures below 300 °C [154], and have limited efficiency at elevated temperatures. Water cooled systems have been tested, but require constant flow which reduces their practical advantage [60].

3.4 EMAT electronics

EMATs do not require contact with the specimen, which is an important advantage over piezoelectric transducers. The main disadvantage of non-contact electromechanical coupling is its low transduction efficiency. To address this problem suitable electronics are required in EMAT transmission and detection. In summary, this requires careful electrical matching of all electrical components, the use of high gain, low noise amplifiers on detection EMATs and high current electrical drivers on generation EMATs.

3.4.1 Impedance matching

To maximise the power transfer of EMAT coils, matching networks are often used. Resonant LC circuits at the desired frequency are designed to ensure that the driving source can transfer the maximum amount of power into the EMAT coil, and the receiver signal has improved impedance matching [67]. The components used in the matching network and any additional electronics, such as cables or filters, will affect the EMAT coil lift-off and bandwidth performance [44; 74]. Each coil can be individually optimised for the particular application by adding capacitive loads in series and parallel. Values for these passive components can be derived by measuring and designing equivalent electronic circuit as described in Hirao [67]. LC circuit impedance matching is frequency selective and improved transduction efficiency comes as a trade-off to reduced bandwidth.

3.4.2 Amplification

The EMAT low transduction efficiency requires suitable analog amplifying receiver electronics [67]. Signals received by EMAT transducers are often less than 100 μV [92]. Ultra low noise amplifiers are used with gains of 40-60 dB. To further improve the signal to noise ratio (SNR) of EMAT, specifically designed pre-amplifiers are used to match the coils low impedance. Johnson noise from the coil resistance contributes the majority of the random noise [118]. EMATs are also highly sensitive to surrounding electromagnetic noise.

3.4.3 Generation of the signals

Due to the lower transduction efficiency of EMATs, high power driving currents are required to generate ultrasonic waves. High voltage capacitor discharge is typically used for pulsed signal generation, while toneburst or continuous waves are generated by high power linear amplifiers. When power amplifiers are used, a matching output transformer is required to lower the impedance of the driving circuit to match the low impedance inductive load of the EMAT coil, see Fig. 3.14. This is an important consideration when using EMATs for nonlinear ultrasonic experiments. The hysteresis of the ferromagnetic core and the harmonic distortion of the power

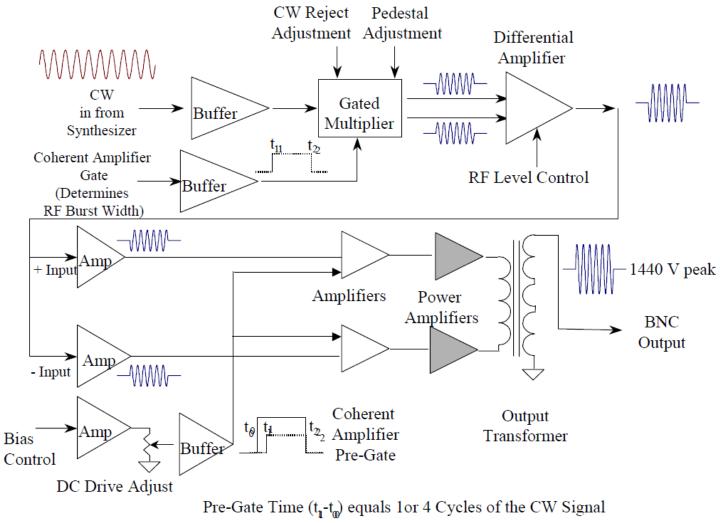

Figure 3.14: Block diagram of RITEC gated amplifier module, adapted from RITEC [167].

amplifiers introduce high levels of harmonic components in the output signal, see Fig. 3.15. Such high power systems require passive filtering and matching networks to reduce the total harmonic content.

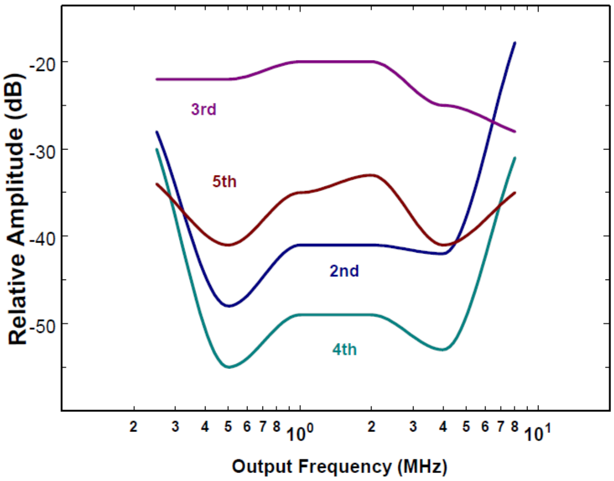

Figure 3.15: Harmonic content of the high power amplifier output as a function of driving frequency (from [167]).

EMAT applications using lower powered drivers have been investigated [91], to reduce the requirement of bulky apparatus and make EMAT systems practicable for field measurements.

Chapter 4

Review of nonlinear techniques

Nonlinear ultrasonic methods have been researched since the early 1960's. Hikata [63] and Suzuki [181] provided theoretical background for ultrasonic-dislocation interactions. With the improvement of material knowledge and electronic apparatus, multiple nonlinear ultrasonic NDE techniques have been researched. Zheng [224] wrote the first comprehensive summary of nonlinear acoustic techniques, providing information regarding theoretical and experimental considerations for nonlinear applications in solids and fluids, including attenuation, diffraction, dispersion and hysteretic elasticity. The nonlinear measurement methods discussed include: acoustoelasticity, finite-amplitude harmonic generation, resonance frequency and contact acoustic nonlinearity techniques. Sensitivity and limitations of different transducer types are discussed with respect to their suitability for higher harmonic generation techniques. The article provides an extensive list of experimental configurations for various nonlinear techniques.

Jhang [78] reviewed the improvements to the nonlinear techniques, introducing recent advances in understanding the micromechanical contributions from dislocations and evaluating the experimental constrains. Matlack [119] presented a review of second harmonic generation (SHG) measurement techniques in metals, which focused on longitudinal and Rayleigh wave methods. The article is a critical review of the literature using SHG methods for non-destructive evaluation of fatigue, creep, radiation damage and more. Chillara [34] summarised the theoretical background of nonlinear guided wave propagation and reviewed results from higher harmonic generation guided wave experiments. Each of these review articles focuses on different aspects of nonlinear ultrasonic techniques, and provides analysis of the current limitations and restrictions of non-contact ultrasonic techniques. Some of these obstacles can be challenged by non-contact methods. Each nonlinear measurement technique: through thickness harmonic generation, Rayleigh-Lamb wave higher harmonics generations, shear horizontal higher harmonic generation, NRUS and nonlinear wave mixing, will be discussed in detail regarding the experimental methods, previously available results and potential EMAT configurations.

4.1 Higher harmonic generation

Higher harmonic generation ultrasonic techniques exploit the material nonlinearity in order to measure the acoustic nonlinearity parameter β. During the propagation of a monochromatic incident elastic wave, higher harmonics are generated due to the lattice anharmonicity and contributions of microstructural defects, as presented in Chapter 2. Measurements of the amplitude of the higher harmonics can be related to the fatigue state of the material [22; 25; 50; 51; 140; 216]. The relative nonlinear acoustic parameter β is normalised with respect to the amplitude of the fundamental acoustic signal and to the distance travelled through the material. For bulk waves the definitions of the nonlinear parameter β for second and third order harmonics are:

$$\beta_2 = \frac{8}{xk^2}\frac{A_2}{A_1^2} \qquad \beta_3 = \frac{8}{xk^3}\frac{A_3}{A_1^3} \tag{4.1}$$

Where A_1, A_2, A_3, x, k are the amplitude of the fundamental, second harmonic, third harmonic, the distance travelled and the acoustic wavenumber. In most studies, only the relative change of the nonlinear parameter is reported, as absolute measurements of the ultrasonic amplitudes are difficult to perform.

Higher harmonic nonlinear ultrasonic techniques typically provide measurements of the harmonic component amplitudes as a function of the fundamental acoustic wave amplitude and propagation distance, see Fig. 4.1. It is important to note that the measured nonlinearity has contributions from both material generated nonlinearity and experimental apparatus induced nonlinearity. Minimising the nonlinearity components generated by the measuring system is the biggest challenge of NLU techniques.

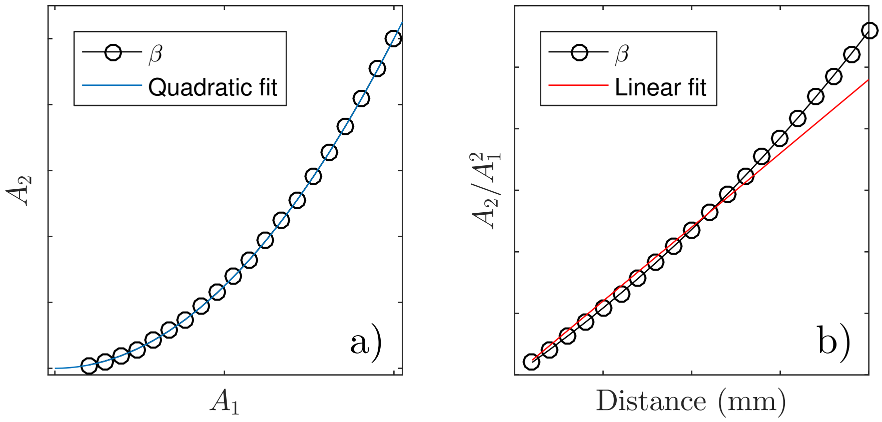

Figure 4.1: Schematic of the expected results from measurements of the nonlinear acoustic phenomena. These trends are used to confirm the experimental results. The quadratic relation of the second harmonic amplitude as a function of the amplitude of the generated fundamental signal (a) and the increase of β with distance (b). After travelling a certain distance, the amplitude of the second harmonic falls below the noise level and the measurement no longer represents the nonlinear parameter.

The nonlinear parameter changes with progression of the fatigue lifetime of the material component [6; 50; 98; 139]. As the number of microstructural defects increases, the generation of higher harmonics increases and a significant increase of the nonlinear parameter can be measured before fatal failure occurs, as shown in Fig. 4.2. Nonlinear higher harmonic measurements have been conducted on a variety of materials with a variety of wave modes: aluminium alloys [23; 25; 131; 162; 216], steels [79; 145; 201], titanium alloys [7; 14; 51] and nickel-based superalloys [24; 61; 98].

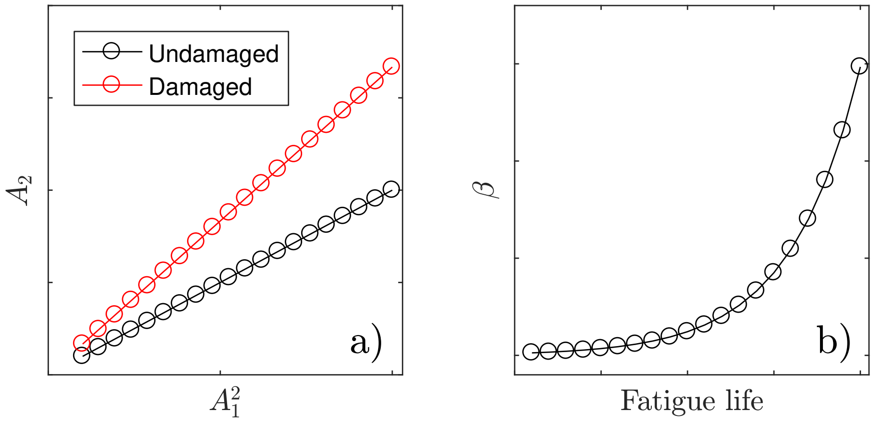

Figure 4.2: The nonlinear parameter β changes during the fatigue lifetime of the sample after Nagy [140].

Experimental measurements of the nonlinear parameter have to incorporate multiple correction factors, so that an absolute measurement of $\tilde{\beta}$ can be obtained. The influence of properties on ultrasonic wave propagation such as diffraction [196], attenuation [115; 196] and reflection [10; 11; 225; 226] must be considered. Extensive investigation of the effects of different experimental parameters have been conducted to reduce the system nonlinearity: for an example investigations into the amplifier [178], piezoelectric transfer function [84; 138], transducer loading conditions [172], transducers misalignment[178], couplant transfer-function [8; 172; 180], toneburst length [115], window functions[172], window length [172] and excitation frequency [178].

4.1.1 Bulk waves

Higher harmonics nonlinear measurements have been conducted in both pitch-catch through thickness and pulse-echo configurations. The experimental configurations for the longitudinal and shear bulk waves are similar, although in the case of shear wave generation, elastic theory prohibits second harmonic generation. The amplitude of the bulk ultrasonic waves can only be measured at the sample surface. This reduces the number of measurement points along the wave propagation path, therefore explanation of the propagation of bulk waves requires complex analytical models.

Longitudinal waves

Longitudinal nonlinear techniques typically use transmitting and/or receiving transducers, which are fixed and aligned on opposite sides of the sample. In pitch catch configurations high amplitude ultrasonic waves of the fundamental frequency f_1 are generated and propagate through the sample thickness. The receiving transducer is selected with a centre frequency equal to either the second or the third harmonic frequencies - $2f_1, 3f_1$, as shown on Fig. 4.3. Fundamental, second and third harmonic amplitudes are extracted from the received signal and are used to calculate the relative nonlinear parameters β. Pulse-echo techniques have been investigated for single-sided nonlinear ultrasonic measurements [10; 11; 77], as these are more viable for in-service measurements.

When piezoelectric transducers are used for higher harmonic NLU, certain precautions must be taken to reduce the system nonlinearity. A thin layer of coupling is required for the efficient mechanical transfer of ultrasonic vibration from the piezoelectric transducer to the material. Inconsistency in the coupling can lead to a large variation in the measured nonlinearity. Light oil and a low level of coupling force have been used to improve the consistency of the measurements [178].

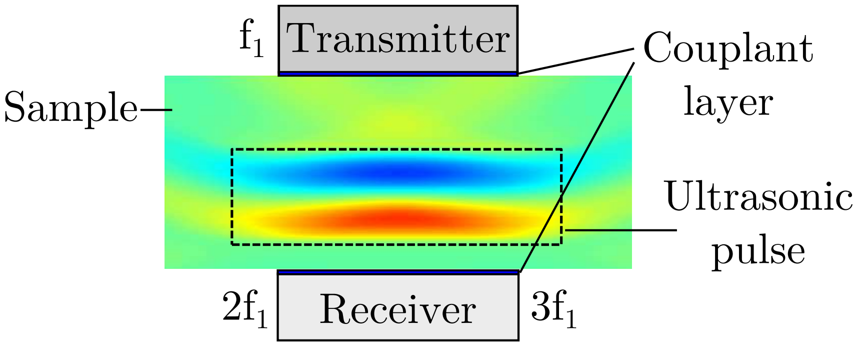

Figure 4.3: Through thickness nonlinear measurement using piezoelectric transducers. A transmitting transducer generates acoustic waves at the fundamental frequency f_1 and a receiving transducer detects waves with a central frequency at the harmonics mode - $2f_1, 3f_1$. The transducers are fixed to the sample by a small force and couplant is applied between the transducers and the sample.

Piezoelectric contact methods exert a mechanical load on the sample surface, which interferes with the reflection of acoustic signals. Additional ultrasonic losses occurs at reflections due to transmission of ultrasonic waves into the coupling medium. A two step calibration procedure, reducing the effects of the contact frequency-dependent conditions, is described by Bernard [8].

Shear waves

Higher harmonic generation using shear waves has been reported in single crystal [53; 85; 179; 208] and polycrystalline metals [53]. Two distinct sources of shear wave nonlinearity have been defined: lattice anharmonicity and microstructural defects. In isotropic materials, the generation of shear wave second harmonics (SWSH) due to the lattice anharmonicity is prohibited due to symmetry in the second-order elastic constants. Only a small number of crystal groups exhibit strong anisotropy, allowing for shear waves to generate SWSH [85]. As presented previously in section 2.2.4, shear wave interaction with the geometrical nonlinearity of the lattice generates longitudinal wave second harmonic and shear wave third harmonic components. The effect of dislocation density on the generation of SWSH has not been studied in detail, although studies have reported a relationship between the generation of SWSH and the material microstructural damage state [67; 145; 152].

Pulse echo considerations

Corrections must be applied for the second harmonic component, if the ultrasonic wave is measured after multiple reflections. Theoretically, if attenuation and diffraction are neglected, the second harmonic component generated during the forward propagation is cancelled out by the harmonic component from the return path [10]. A more detailed study [11] theoretically and experimentally determined that a significant part of the second harmonic component is retained, even after multiple reflections, due to disturbances from diffraction and attenuation. Third harmonics components are unaffected by reflection phase shifts.

4.1.2 Guided wave techniques

Guided wave nonlinear techniques have been used to measure acoustic nonlinearity in a variety of different transducer configurations: wedge-contact [61; 98; 113; 173; 201], air coupled [182], laser interferometer [14] and EMAT [35; 136; 145], see figure 4.4. Nonlinear guided wave research can be split into two categories: Lamb-Rayleigh wave and shear horizontal wave. Chillara [34] has summarised the theoretical framework of nonlinear guided wave interactions. Due to the dispersive nature of the guided waves, only a limited number of guided wave mode combinations can generate cumulative higher harmonics. Corrections for diffraction, attenuation and source must be considered for experimental measurements [196], but this has not always been clearly described in the published literature [111; 136; 201].

Lamb-Rayleigh waves

Experimental measurements of nonlinear Lamb-Rayleigh waves must meet multiple conditions: non-zero power flux, phase velocity matching, group velocity matching and fundamental wave excitability. Complex analysis of the influence of dispersion on the possible nonlinear guided wave interactions is presented in Mueller [132]. Five families of guided mode pairs are identified as potential candidates for nonlinear Lamb wave measurements: cut-off modes, symmetrical modes at longitudinal velocity, Lamé modes, mode intersections and quasi-Rayleigh modes. Pair modes have different experimental limitations, with symmetrical modes at longitudinal velocity and quasi-Rayleigh modes showing practical advantages: exactly matched phase and group velocity and a good rate of second harmonic generation.

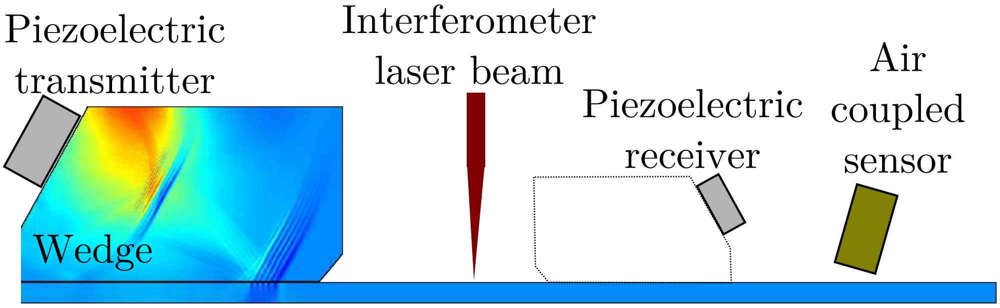

Figure 4.4: Nonlinear Rayleigh wave measurements: A piezoelectric transmitting transducer is mounted on a wedge. Acoustic coupling is applied to both transducer-wedge and wedge-sample interfaces. Different detection transducers can be used to measure Rayleigh waves: laser interferometer, air coupled, EMAT and wedge-contact.

Experimental measurements of Lamb-Rayleigh nonlinear guided waves require large number, toneburst, narrow bandwidth, high amplitude excitation. Measurements at different distances and different excitation amplitudes enable assessment of cumulative harmonic generation. Transmitter and receiver coupling is important as ultrasonics gel couplants exhibit significant nonlinearity, which can mask the small contribution from the material nonlinearity. For Rayleigh waves the nonlinear acoustic parameter, $\tilde{\beta}_R$, has been defined by Herrmann [61] as:

$$\tilde{\beta}_R = \frac{8iA_2^z}{k_l^2 x (A_1^z)^2} \frac{p}{k_R} \left(1 - \frac{2k_R^2}{k_R^2 + s^2} \right) \tag{4.2}$$

where $p^2 = k_R^2 - k_l^2; s^2 = k_R^2 - k_s^2$; and $k_R\, k_l$, and k_s are the wavenumbers for Rayleigh,longitudinal and shear waves, while A_1^z and A_2^z are out-of-plane displacements amplitudes of the fundamental and second harmonic waves. To actuate preferential wave modes within the sample, angled wedge, comb or magnetostrictive transducers must be used. The beam angle is selected by Snell's law, while the comb and magnetostrictive transducer have a predefined wavelength. Multiple types of ultrasonic detectors can be used to measure the Rayleigh waves: piezoelectric angled wedge [113], laser interferometer [62], air coupled [182] sensors or EMATs [35].

Shear horizontal waves

Third harmonic generation by shear horizontal waves has been proven to be sensitive to microstructural damage [111]. A contact magnetostrictive patch transducer with predefined pitch was used to generate SH0 modes in a sample of 1 mm thick aluminium AL2024. The receiver magnetostrictive transducer had a meander coil with a pitch equal to 1/3 that of the transmitter, therefore maximising the receiver response with respect to the third harmonic component.

Phase and group velocity matching of third harmonic shear horizontal waves is valid for all modes and frequencies. The dispersion curves for shear horizontal waves on flat plates are defined by the following equations [171]:

$$c_{ph}(fd) = \frac{2c_T fd}{\sqrt{4(fd)^2 - n^2 c_T^2}} = \frac{2c_T 3fd}{\sqrt{4(3fd)^2 - 3n^2 c_T^2}} = c_{ph}(3fd) \tag{4.3}$$

$$c_g(fd) = c_T\sqrt{1 - \frac{(n/2)^2}{[(fd/\pi c_T)]^2}} = c_T\sqrt{1 - \frac{(3n/2)^2}{[(3fd/\pi c_T)]^2}} = c_g(3fd) \tag{4.4}$$

where c_{ph} is the SH phase velocity, c_g is the SH group velocity, f is the wave frequency, c_T is the shear wave velocity of the material, d is the sample's thickness and n is the SH mode number.

4.1.3 Limitations of harmonic generation methods

A typical nonlinear experimental system comprises: synthesizer, amplifier, cables, transmit transducer, coupling media, test material, more coupling media, receiver transducer, cabling, preamplifier, receiving amplifier and oscilloscope. Filters are used to improve system performance by reducing the input nonlinearity and increasing the relative ratio of higher harmonics to the fundamental signal at the receiver side. It is important that the signal contribution from the material nonlinearity dominates the system nonlinearity associated with other elements of the measurement system.

Filtering

The amplitude of the second harmonic wave is typically three orders of magnitude smaller than the fundamental wave. The high amplitude fundamental wave can generate further nonlinearities in the receiver apparatus, therefore it is recommended that high pass filters are placed immediately after the receiving transducer. Low pass filters can be used to reduce the driving amplifier harmonic components and therefore reduce the harmonic content of the generated ultrasonic waves. Caution should be exercised when adding supplementary electronics to the nonlinear measurement configuration. Each electronic component may become a source of harmonic distortion and increase the system baseline nonlinear content.

Pulse inversion

Extraction of the second harmonic amplitude from the ultrasonic signal can be improved by using the pulse inversion technique [98]. Measurements of the ultrasonic waves are taken for two different generation pulses. The phase between the two generating signals is 180°. Then, the two received signals are then superimposed in post-processing. Due to the phase difference between the fundamental and the second harmonic, the fundamental frequency component is greatly reduced, while the second harmonic signal is doubled. This technique can only improve the resolution of even numbered harmonics.

Signal processing

A fast Fourier transform (FFT) is used to extract amplitude and frequency content information from the measured acoustic signal. The use of windowing functions reduces the spectral leakage and improves the consistency of the signal processing [134]. For long signals, Blackman windows have the highest side lobe suppression and the Hanning window has optimal performance for shorter length signals. Use of Short Time Fourier Transforms (STFT) has been demonstrated to be capable of measuring slowly varying harmonic amplitudes [134]. Window length must be carefully selected, as it affects the side lobe attenuation and time-space resolution.

Electronics nonlinearity

Multiple factors can affect a high power amplifier's nonlinearity [172]: for example environmental temperature, gain or output impedance mismatch. To reduce the system nonlinearity, a warm-up procedure and electrical matching networks must be used.

4.2 Nonlinear wave mixing

Wave mixing is prohibited under the linear elasticity framework. Due to higher order elastic constants, phonon-phonon interactions allow for wave interactions within a nonlinear medium [168]. Nonlinear wave mixing and nonlinear wave modulations (NWMS) [2; 122] share similar experimental configurations. An exhaustive list of possible three phonon interactions, resulting in nonlinear waves, is presented in Korneev [104]. Non-collinear nonlinear shear-shear wave mixing showed correlation between the nonlinear parameter and plastic strain [36]. Two angled wedge shear wave transmitters were used to generate an intercepting wave pattern within the volume of a plastically strained sample. The resultant nonlinear longitudinal wave was measured by a receiver positioned above the interaction volume. The receiver frequency must be equal to the sum or difference of the generation signals. Three sets of measurements are produced: one for each transducer excited separately and one for the simultaneous excitation. This method benefits from the ability to reduce the system nonlinearity, as the nonlinear interaction only occurs when the two shear waves are combined, while the singular excitations can serve as a baseline nonlinearity measurement. Imaging performance is greatly improved as the nonlinear measurement is strictly localised, due to the small interaction volume. Using two different excitation frequencies can further improve the system nonlinearity rejection ratio, as the frequency of the resultant nonlinear wave differs from the harmonics of the input signals [37; 223]. Collinear wave mixing has been studied for both bulk [31; 86; 114] and guided wave modes [129; 130].

4.3 Nonclassical nonlinear techniques

Nonclassical nonlinear techniques have been studied to measure the hysteretic behaviour of fatigued materials [58; 122; 133; 142; 157; 197]. Nonlinear ultrasonic resonance spectroscopy (NRUS) uses high amplitude resonance mode excitation to measure changes in the frequency of oscillation, see Fig 4.5a.

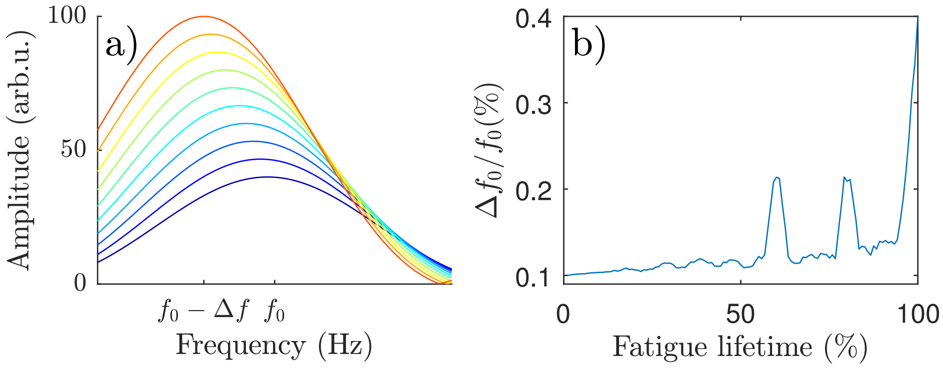

Figure 4.5: NRUS frequency shift during stainless steel lifetime. (Adapted from Ohtani [151]). The frequency of the resonance mode changes with the amplitude of the ultrasonic waves (a). The change in the frequency shift shows two distinct peaks during the fatigue lifetime of the sample (b).

The ultrasonic wave frequency is selected to match the geometrical resonance conditions, so that high displacement amplitudes can be achieved as shown in Fig. 4.6.

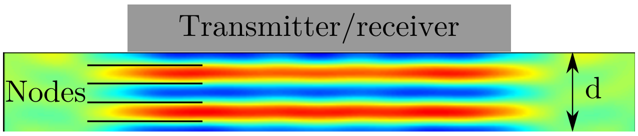

Figure 4.6: Nonlinear resonance methods: NRUS and harmonic generation. A single transmitting and receiving transducer generates acoustic waves at a geometrical resonance mode: multiple integer values of the ultrasonic wavelength $n\lambda$ must equal twice the sample thickness d. The sketch presents the wave oscillation pattern for the fourth resonance mode, where the colour scale represents the in-plane displacement.

Materials with highly nonlinear mesoscopic elasticity such as rocks [163], concrete [157] and bone [133] have shown a strong relation between the micro-damage state and the nonlinear hysteretic frequency response. Common experimental conditions limit the relative measurements of the frequency shift to $\frac{\Delta f}{f_0} = 10^{-4}$. The experimental protocol used by Haupert [58] improves the sensitivity of the NRUS method by incorporating a two-step temperature compensation measurement procedure. A strong correlation between temperature variation and frequency shift has been shown. Failing to report temperature variation during the NRUS experiments may reduce the reliability of the nonlinear measurements.

Chapter 5

EMAT and nonlinear ultrasonics

5.1 Review of EMAT nonlinear techniques

Research on EMAT nonlinear applications is very limited and has been approached only partially. Studies of EMAT measurements for both classical and nonclassical nonlinear techniques have been conducted. A review of these studies and analysis of the use of EMATs for nonlinear ultrasonics will be presented.

5.1.1 EMAT harmonic generation review

Higher harmonics nonlinear studies using EMAT transducers have been conducted that measured second harmonic Rayleigh wave [35], Lamb and SH0 waves [135; 136], circumferential shear horizontal waves [67; 145; 152] and wave-mixing [148; 150].

Ogi and Hirao [67; 145] and Ohtani [152] have used EMATs to measure the fatigue state of steels. Magnetostrictive meanderline EMATs were used to generate surface shear waves with axial polarisation, travelling circumferentially around cylindrical steel samples, see Fig. 5.1. The generating frequency is selected such that the second harmonic component is matching the geometrical resonance conditions. This allows for coherent accumulation of second harmonic waves. Additionally, the fundamental amplitude is reduced due to the destructive interference conditions. The study, by Ohtani [152], focussed on measuring the contact acoustic nonlinearity of microcracks generated during fatigue. Four point bending was used with interruptions for attenuation, velocity and nonlinear measurements. In Ohtani's study [152], the nonlinear ultrasonic parameter was defined as A_2/A_1 (ratio of second to fundamental harmonics), compared to the NLU theory parameter A_2/A_1^2. The use of the alterna-

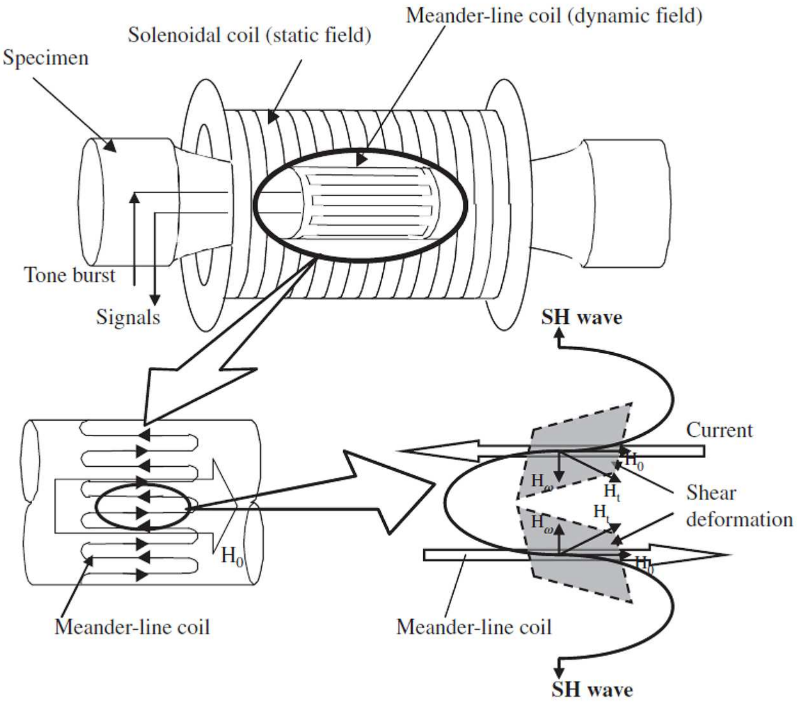

Figure 5.1: Axial-shear-wave EMAT: Solenoid coil is providing the static magnetic field. Meander-line coil surrounding the cylindrical surface generates a dynamic magnetic field. The magnetostrictive force generates axial surface SH waves (adapted from [152]).

tive definition of the nonlinear parameter was argued by the inability to measure the amplitude of the short-lived fundamental wave accurately. The observed changes in the nonlinear parameter were correlated with the changes in the microstructure of the material surface [152]. The distinct peaks in the nonlinearity parameter are related to the microstructural evolution during creep or fatigue damage, as shown in Fig. 5.2.

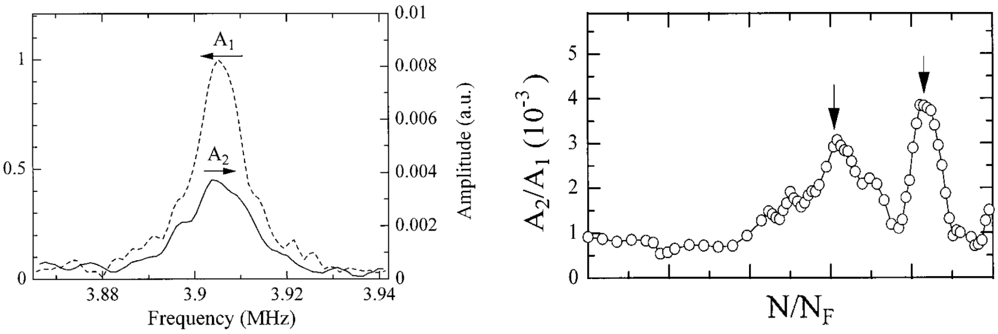

Figure 5.2: Frequency spectra of off-resonance fundamental generation and nonlinearity index change with fatigue, where N is the number of undergone cycles and N_F is the number of cycles to failure (adapted from [67]).

In the article [152], the changes to the nonlinear parameter were attributed to the lattice anharmonicity, dislocation movement and microcracks contact nonlinearity. Second harmonics cannot be generated by shear waves due to lattice anharmonicity (see section 2.2.4). Therefore, contributions to the second harmonic surface shear wave can only be dislocation defects and contact nonlinearity from microcrack interfaces. The study does not report measurements for different driving signal amplitudes or different propagation lengths.

Murayama [135; 136] evaluated the use of EMATs for fatigue measurements using nonlinear S0-Lamb and SH0 shear horizontal waves. Magnetostrictive meanderline coils EMAT transducers were used for transmission and reception of ultrasonic waves in 0.5 mm thick, low carbon steel samples. The ultrasonic oscillation and travelling directions of the used transducer are shown in Fig. 5.3.

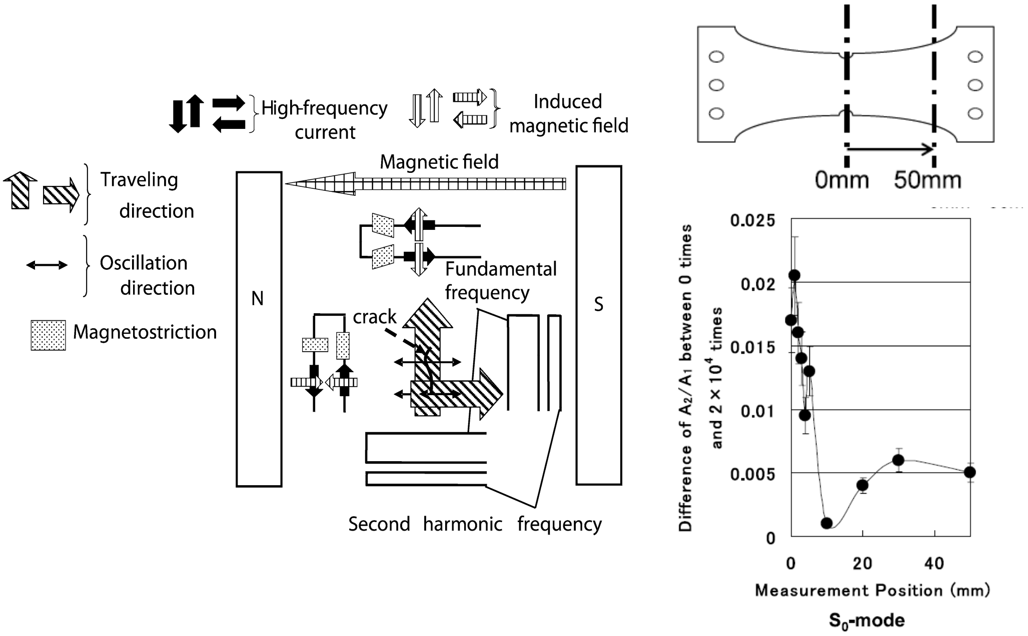

Figure 5.3: Magnetostrictive EMAT sensors capable of generating Lamb or shear horizontal waves (left), nonlinear variation with specimen position (adapted from [135]).

The Murayama's study [135] focuses on the contact acoustic nonlinearity measurement of cracks with nanoscale openings. The static magnetic field was optimised to maximise the amplitude of ultrasonic oscillation - 1 nm was reported. Four specimens, with variable gauge width, were fatigued using interrupted tensile tests - $0\%, 25\%, 50\%, 100\%$ of remaining lifetime. The test samples were designed so that higher amount of stress is concentrated on the centre section. The nonlinear index A_2/A_1 (ratio of second to fundamental harmonics) was measured as a function of position and different fatigue loads. The experimental results showed that the nonlinear ultrasonic index, for S0 Lamb waves, increased only from the undamaged state 0% to the first damaged state 25% and did not change with further fatigue, while the SH0 wave index showed a reverse trend. The nonlinear index decreased with distance further away from the centre of the test samples. This suggests higher contributions from microcracks generated in the high-stress central area, see Fig. 5.3. Murayama's study [135] does not report the variation of the harmonic generation with propagation distance and/or fundamental wave amplitude, and mainly focused on second harmonic generation from microcracks contact nonlinearity.

Cobb [35] investigated nonlinear Rayleigh wave EMATs as a possible field deployable measurement technique. Meanderline Rayleigh wave EMAT transducers were used for transmission and reception. The generation meanderline coils were designed for Lorentz force excitation of waves with frequencies of 1 MHz, 1.5 MHz and 2.25 MHz. Each coil was electrically matched to the impedance of the power amplifier (RITEC SNAP). The reception meanderline coils had a spacing half that of the generating coils, to improve their sensitivity to the second harmonic component. Four 9.5 mm thick stainless steel specimens were fatigued up to 2 million cycles. The fatigue process was interrupted, and ultrasonic measurements were taken. Cobb's study [35] reports measurements at different generation signal amplitudes for the 2.25 MHz - 4.5 MHz transducer pair. A linear relationship is measured between the second harmonic amplitude A_2 and the square of the amplitude of the fundamental A_1^2, as the result of the material nonlinearity. The article ignores any possible contribution to the second harmonic from the dynamic magnetic field generation (see sec. 3.2.4) or amplifier nonlinearity. A plastic fixture was used to allow repeatable measurements of two different prefixed distances. A limited number of measurements for the fundamental and second harmonic at different propagation distances are reported and hence provides insufficient evidence for second harmonic generation due to material nonlinearity.

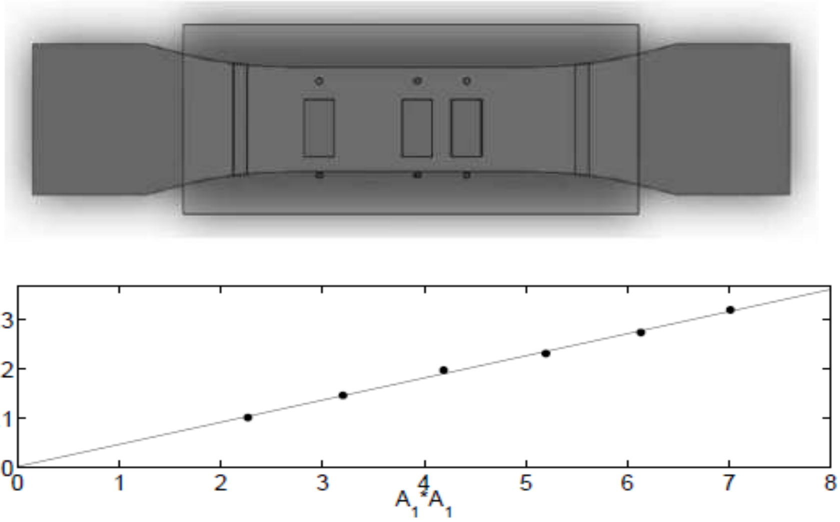

Figure 5.4: Plastic fixture and test specimen (top). Relation between second harmonic and fundamental amplitude for Rayleigh wave, Lorentz force EMAT transducers (bottom) (adapted from [35]).

Results for four different specimens were presented with no strong correlation between the fatigue state and the nonlinear parameter. A list of potential causes for the measurement variance has been given: ultrasonic wave interaction with edges of the gauge width, transducer misalignment, capacitor variation and residual magnetisation.

Lissenden [111] has used contact (thin-film) magnetostrictive transducers to measure higher harmonic guided waves in plastically strained aluminium. Shear horizontal waves were generated by a magnetostrictive transducer with pitch spacing p of 1.8 mm (wavelength 3.6 mm). A receiver with pitch of $p/3 = 0.6$ mm (wavelength of 1.2 mm) was used to increase the transmitter sensitivity to the third harmonic component. Two Iron Cobalt foils (25 mm x 35 mm) were bonded at fixed distance of 400 mm from each other. Five 1 mm thick aluminium (AL2024) samples, with equal sample length 610 mm and various gauge lengths were plastically strained. Different notch sizes were used to control the plastic zone. Scribed scratch marks were used to measure plastic deformation. Measurements of the harmonic to fundamental amplitudes ratio are provided as a function of the amplifier output level, and as a function of plastic zone-to-propagation length ratio, as shown on figure 5.5. Generation signal amplitude is shown to have negligible influence on the nonlinear parameter for multiple amplifier output levels. Results also show nonlinear acoustic parameter increasing with plastic strain for the same propagation length.

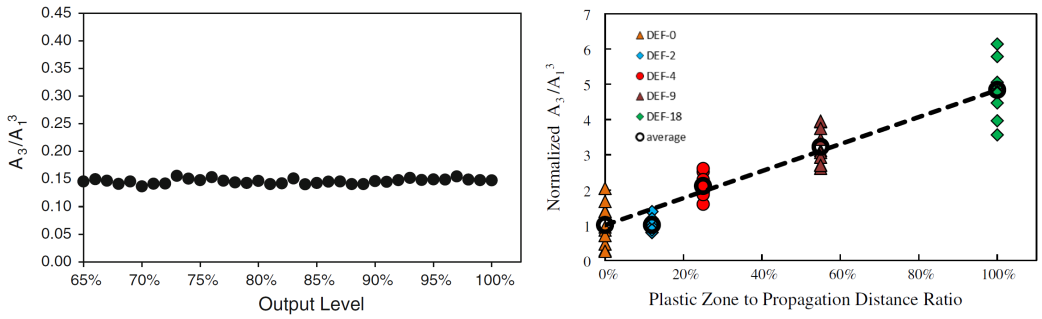

Figure 5.5: The relationship between the third harmonic and the fundamental amplitude for different excitation levels (left) and different plastic-zone/propagation distance ratios, normalised to unfatigued sample value (right) (adapted from [111]).

Ohtani [148; 150] has evaluated the change of the nonlinear acoustic parameter with creep damage for high Cr ferritic steel. Two polarised shear wave magnetostrictive EMAT transducers were used to generate ultrasonic waves of different frequencies. The transducers were positioned on opposite sides of a 3.5 mm thick plate specimen, as shown in Fig. 5.6. The samples were cut from thick welded joint plate of GR. 122 steel.

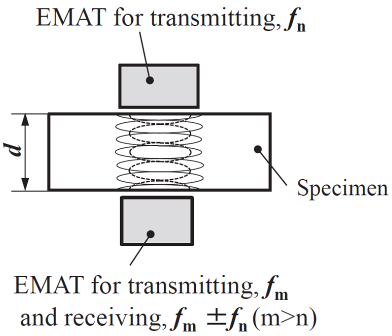

Figure 5.6: Dual EMAT configuration: Two shear wave transducers positioned on opposite sides of the sample, generated acoustic signals of different frequencies f_5 f_8. The nonlinear interaction within the specimen volume generates side-band signals for the difference or the sum of the initial frequencies $f_{8\pm5}$, adapted from [148].

Polarised shear waves were generated at the 5^{th} and 8^{th} through-thickness resonance modes. The nonlinear parameter in [148] is defined as:

$$\beta_{mix} = \frac{A_3}{A_5 A_8} \tag{5.1}$$

Where A_3, A_5, A_8 are the amplitudes of the third, fifth and eight resonance modes. The nonlinear parameter shows a dramatic increase towards the end of the fatigue lifetime. Measurements of the variation of β_{mix} with different excitation levels of A_5 and/or A_8 or with propagation time are not reported.

5.1.2 EMAT and nonclassical nonlinearity

NRUS EMAT experimental techniques have been used to measure fatigue induced microstructural changes in pure copper [72; 149], stainless steel [107; 151] and ferritic steels [150]. Only two of these studies [150; 151] provided additional measurements of the changes in the material microstructure and information is not provided regarding the temperature variation during the measurement process. In all reported experiments, shear wave EMATs were used to generate and measure bulk ultrasonic waves matching the geometrical resonance conditions:

$$2d = n\lambda = \frac{nc}{f} \tag{5.2}$$

Where d, n, λ, c, f are respectively the sample thickness, resonance mode number, wavelength, velocity and frequency of the ultrasonic wave. Due to the low EMAT transmission efficiency, such conditions can ensure the generation of high amplitude signals. Measurements for different excitation amplitudes are provided in [151], showing a negative shift of the resonance frequency with increased amplitude of the input signal. Changes to the nonlinear frequency shift as a function of fatigue are presented. Two experiments using the NRUS technique in pure copper are reported [72; 149]. Measurements of the frequency shift contradict each other, as the results presented differ by a order of magnitude and data trends change. The studies used sixth-order shear wave resonance mode which has a frequency close to the third-order longitudinal resonance mode and can cause significant interference with the results, as the EMAT design used can generate and receive both wave types.

5.2 Analysis of EMAT for NLU

Multiple ultrasonic techniques have been investigated to overcome the practical challenges associated with nonlinear ultrasonics. Measurement uncertainties related to the ultrasonic transduction are reported as the biggest obstacle to field deployable nonlinear ultrasonic techniques. The use of non-contact method can improve measurement repeatability, due to reduced variation and nonlinearity in the coupling medium, and allow for optimised procedures for measurements at multiple positions or propagation distances. Various noncontact ultrasonic techniques have been studied [55]: air-coupled transducers, laser generation and interferometric detection, EMAT and capacitive transducers. The focus of this thesis is electromagnetic generation and detection of nonlinear ultrasonic waves. EMAT transduction phenomena has not been investigated in depth with regard to nonlinear ultrasonic applications. Possible EMAT nonlinear techniques can include higher harmonic generation: longitudinal or shear bulk waves, Lamb-Rayleigh or shear horizontal guided waves. Other methods can include nonclassical nonlinearity: resonance frequency shift and three wave interactions, and contact acoustic nonlinearity: Rayleigh or surface shear waves.

5.2.1 EMAT generation

Magnetostrictive EMAT transducers

The transduction efficiency of noncontact magnetostrictive EMATs greatly depends on the material properties and the applied external magnetic field. Extended research is required for the detailed understanding of the ultrasonic transduction nonlinearity:

effects of the magnetisation hysteresis nonlinearity, remanent magnetization, microstructural changes to magnetostriction with fatigue damage and magnetostriction properties of different materials. Magnetostrictive EMAT applications have not been considered in this research.

Bulk waves

Bulk wave EMAT transducers have wider bandwidth allowing for the detection and generation of ultrasonic signals at multiple frequencies. A wider bandwidth permits a single transducer to be used for multiple measurements of the nonlinear parameter, without changing the experimental conditions, as well as reception of higher harmonics. Collinear wave-mixing techniques can also be easily implemented as multiple combinations of wave frequencies can be generated and detected. The transducer bandwidth can be optimised for a specific frequency range by the use of impedance matching networks.

Lorentz force longitudinal EMAT have reduced transduction efficiency compared to piezoelectric ultrasonic sensors. Due to the dynamic magnetic field induced by the coil, second harmonic longitudinal waves are generated simultaneously with the generation of the fundamental ultrasonic excitation [81]. The amplitude of the second harmonic component generated by the self-field varies quadratically with the fundamental wave amplitude. This relationship matches the nonlinear parameter relationship A_2/A_1^2 from the material nonlinearity. Distinguishing between the contribution from the two phenomena requires a refined experimental procedure. Measurements are taken with and without the externally applied static field. The 'no-magnet', self-field only, signal is subtracted from the 'magnet' signal to diminish the contributions from the dynamic field forces. Alternatively, the ultrasonic waves generated by the self-field force can be used as source of fundamental wave for driving currents of 150 A or higher. Due to the inefficient transduction, the generation of longitudinal third harmonic ultrasonic waves is considered unachievable. Measurement of the frequency shift due to generation amplitude has the potential to have practical applications.

Shear wave generation EMATs have better transduction efficiency with lift-off, compared to the longitudinal EMATs. Higher out-of-plane magnetic field amplitude can be generated, compared to the in-plane magnetic field component. Shear waves do not generate shear wave second harmonics due to lattice anharmonicity. However, shear wave second harmonics can be generated by dislocation interaction with externally applied stress [208] and by surface contact acoustic nonlinearity [152]. The self-field force, associated with shear EMATs transmission, generates longitudinal waves, which are also generated from the self-interaction of shear waves in nonlinear materials. Sophisticated analysis is required to distinguish between contributions from these two source of longitudinal wave second harmonics.

The theory of elasticity predicts that odd harmonics can be generated by incident shear waves. The third harmonic component has been proposed to have higher sensitivity to microstructural damage than to lattice anharmonicity [20; 164; 194]. Measurements of the third or higher harmonics are challenging, due their small amplitudes, compared to the amplitude of the fundamental waves.

Shear wave EMATs have been used to measure nonclassical nonlinearity in copper and steel [149; 151]. NRUS measurements of other polycrystalline metals are required to assess the limitations and applications of the experimental technique.

5.2.2 Guided waves

The results from meanderline Lamb-Rayleigh EMAT experiments measuring ultrasonic nonlinearity have been inconclusive [135; 136]. EMAT ultrasonic generation processes have not been studied with regards to nonlinear ultrasonics: self-field generation, diffraction and ultrasonic amplitude. Compared to liquid coupled contact methods, meanderline EMATs benefit from improved repeatability of the transducer coupling. The self-field generation of the Rayleigh wave EMATs and the parameters that influence it, have been studied [203; 205]. The pattern of the self-field generated force matches that of the meanderline spacing ($p = \lambda/2$), while the frequency of the force is double the driving signal frequency f. The ultrasonic wave generated by the meanderline coil (without externally applied magnetic field), matches the wavelength and frequency of the second harmonic nonlinear ultrasonic wave. Also the amplitude of the dynamic magnetic field force increases quadratically with the amplitude of the driving signal, which also resembles the nonlinear harmonic generation relationship A_2/A_1^2.

Shear horizontal wave periodic permanent magnet (PPM) EMATs can be used to generate third harmonics due to material elasticity and dislocations, or second harmonics due to surface contact nonlinearity [111]. The structure of the PPM EMAT defines the ultrasonic wavelength by the length of the magnets' pitch. The combination of transmitter and receiver transducers with a ratio of magnet pitches 3:1 can be used to measure the third harmonic ultrasonic wave (see equations 4.3 and 4.4, and Fig. 5.7). As the group and phase velocity for the fundamental wave and the third harmonic match for all frequencies of generation, this combination of transducers can be used for samples of different thickness and multiple shear wave modes - SH0-SH0, SH1-SH3, etc. The ratio between the magnetic sizes and the spacing between them can be used to reduce the generation of the third harmonic from the EMAT transmission.

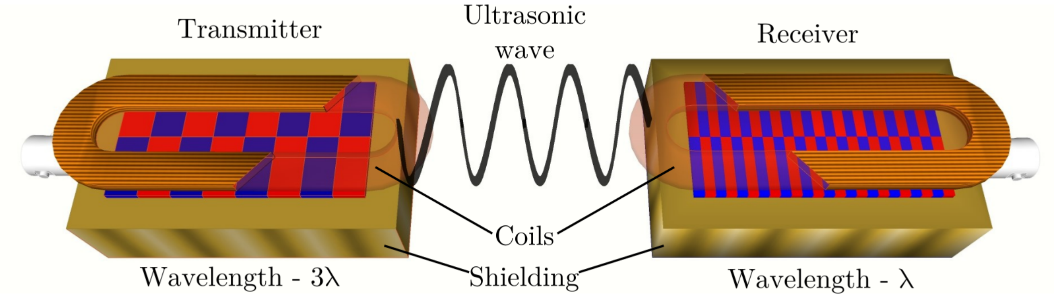

Figure 5.7: Combination of transmitter and receiver SH PPM transducers with a ratio of magnet pitches - 3:1.

The self-field force distribution from the racetrack coil PPM EMAT is even across the surface of the sample and therefore does not contribute to the nonlinear harmonic generation. Additionally, the shear horizontal waves have been shown to travel around smooth corners, which will allow for nonlinear ultrasonic inspection of curved and irregular shape samples [159].

5.2.3 EMAT reception

Bulk wave EMAT receivers have a wide bandwidth, which allows for multiple harmonics to be measured using the same transducer, while guided wave EMAT transducers are wavelength selective and can be optimised for a specific wave mode and frequency. The reception mechanism used by EMAT transducers is inherently linear, due to the non-contact electromechanical coupling. Therefore, there is no contribution to the system nonlinearity. EMATs electromechanical coupling is quite weak, and so the ultrasonic absorption by the transducer is negligible and no mechanical loads are applied to the sample surface. Transduction efficiency is significantly reduced by lift-off, which must be carefully considered. To increase the signal-to-noise ratio, electrical shielding must be used around the EMAT coil and the measured sample must be electrically grounded.

5.3 Summary: Introduction

Nonlinear ultrasound theory is well developed and has a good description of the nonlinear ultrasonic generation process from microstructural defects. Theoretical predictions of the contributions from single microstructural elements have been made, but require further experimental validation.

Multiple contact ultrasonic methods have been used to measure the nonlinear ultrasound parameter, β, and to observe its change during material fatigue. The changes in β have been linked to the changes in the dislocation density. In laboratory conditions, the use of contact ultrasound methods permits non-destructive measurements of the nonlinear ultrasonic parameter. However, the contact transduction process is inherently nonlinear, which limits the practical applications. Alternative methods for measuring the dislocation density, such as X-Ray back scatter diffraction, TEM and chemical etching, are either destructive or are impractical for field measurements.

The use of EMATs for non-contact ultrasonic measurements of the nonlinear ultrasonic parameter has been studied scarcely. Previous attempts to determine the potential use of EMATs for nonlinear measurements have been incomplete or inconclusive, with insufficient or partial understanding of the EMAT transduction process. Recently, improvements have been made to the EMAT transducer design, the supporting electronics and the computer simulation capabilities. Therefore, this thesis focuses on the EMAT transduction process and the applications of EMATs for nonlinear ultrasound measurements: through-thickness resonance higher harmonics measurement, NRUS, second harmonic Rayleigh wave measurements and third harmonic shear horizontal ultrasonic wave measurements.

Chapter 6

Experimental development: Bulk waves

6.1 Computer control

Computer control was used to automate the process of experimental measurements. Experimental procedures written in C++ are used to communicate with the experimental apparatus: high power amplifier (Ritec RPR4000), digital oscilloscope (Tektronix DPO2014), arbitrary function generator (Tektronix AFG3102C), USB multimeter (Keithley 2100), custom built XY gantry positioning system (Zaber). The computer control allows a large amount of measurements to be taken and analysed, which are required for nonlinear ultrasonic techniques.

6.2 Signal processing

The acquired ultrasonic signals are analysed using discrete fast Fourier transforms. Amplitudes and frequencies of the harmonics are extracted from the frequency spectrum. Zero-padding is used to improve the spectral resolution. A quadratic fit of the peaks is used to further improve the frequency and amplitude harmonic component resolution. A Hanning window is applied to all measured signals to reduce spectral leakage from transient behaviour at the beginning and the end of the window [134]. For resonance mode techniques, short time Fourier transforms (STFT) are used to measure the variation of harmonic amplitudes and their frequencies with time. A Hanning window with length of 20 μs provides a compromise between spectral leakage amplitude and time resolution in the time-frequency space. The spectral leakage into second and third harmonic from the fundamental for frequencies higher than 1 MHz is less than $-100\,dB$ and $-120\,dB$ respectively, as shown in Fig. 6.1.

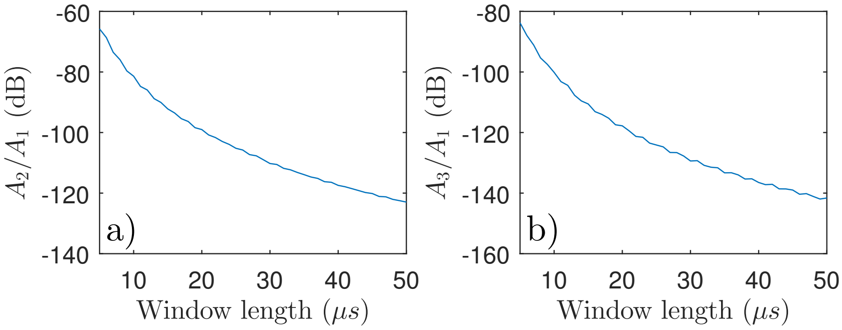

Figure 6.1: Spectral leakage into the second (a) and third (b) harmonic of Hanning window lengths for fundamental signal of 1.683 MHz.

6.3 Electronic components nonlinearity

6.3.1 Receiving electronics

The combined nonlinearity of the receiving apparatus was tested as a function of the signal amplitude. An arbitrary function generator (Tektronix AFG3102) was used to provide a continuous wave signal with a frequency of 1.5 MHz and variable excitation amplitude. The signal was measured by a digital oscilloscope (Tektronix DPO2014). Harmonic components of the signal were recorded and fall within the product specification of -60 dB of maximum total harmonic distortion (THD). A peak of the third harmonic component was observed at low signal amplitude 0.3 V, see figure 6.2. Measurements were repeated with multiple signal sources to confirm that the oscilloscope is the nonlinearity source. Such variation can cause artificial sources of third harmonics when the measured signal has a time-varying amplitude: toneburst wave packets or decaying amplitude resonance signals. The ratio between the fundamental wave ultrasonic amplitude and the amplitude of the second harmonics waves, generated by the material nonlinearity, is typically in the range of $40\,dB - 60\,dB$. Therefore the ultrasonic signals must pass through frequency filters to reduce the fundamental component amplitude, or the receiving transducer must have frequency selective sensitivity. Similar analysis was performed for the receiver amplifier (RITEC RPR4000). Attenuated signals with different amplitudes are fed into the internal amplifier with the signal gain set at $60dB$. The resultant nonlinearity is a convolution of the receiving amplifier and the oscilloscope nonlinear contributions.

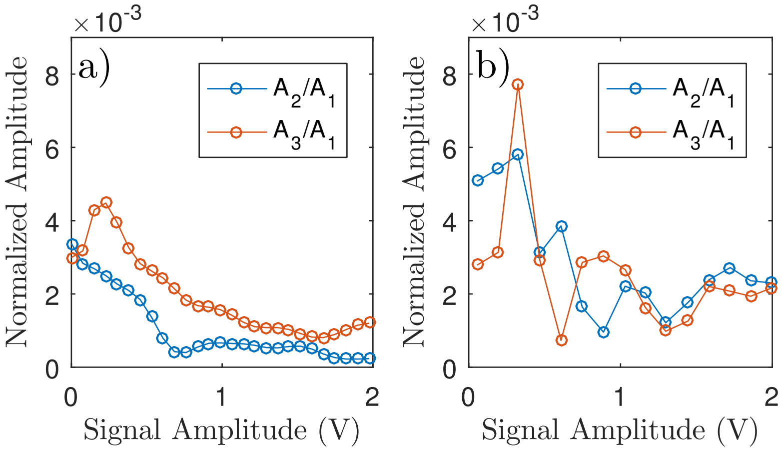

Figure 6.2: Ratio of harmonic component as function of signal amplitude: oscilloscope (a), and combined oscilloscope and receiver amplifier (b).

6.3.2 Generating electronics

Power amplifier

A high power amplifier system (RITEC RPR4000) is used to drive the EMAT transducers. The nonlinearity specifications of the RITEC SNAP system for the second harmonic and the third harmonic components are in the range of $-40dB$ and $-20dB$ for frequencies around 1.5 MHz (see fig. 3.15). The high harmonic distortion of the driving signal can be reduced by the use of high power low pass filters for pitch-catch measurements or high power diplexers for pulse echo techniques. The introduction of additional components to the measurement system increases the complexity of the experimental setup.

An alternative option is to overwrite the amplifier's output harmonic component by introducing a compensating harmonic signal to the amplifier's input. An arbitrary function generator supplies a continuous sine wave signal composed of a high amplitude fundamental component and phase shifted harmonic components with lower amplitude. Then the high power output from the amplifier is driven into a transmitting transducer and is monitored by a high voltage probe (Tektronix P6009). Combinations of harmonic compensation amplitude and phase were varied so that the lowest harmonic distortion can be obtained. Ultrasonic measurements were taken to investigate the effect of the amplifier's harmonic compensation (see section 7.1.2).

6.3.3 Transducer impedance matching

The impedance mismatch between the driving electronics and the acoustic transducer greatly reduces the transmission efficiency. The impedance of a racetrack coil EMAT transducer was measured by an impedance analyser (Agilent 4294A). The operational frequency of 1.683 MHz was selected for which the EMAT transducer has an impedance of $Z = 2.6 + j29.886\Omega$. Two types of matching networks, composed of capacitive elements, (fig. 6.3) were built to investigate the effect on the fundamental amplitude and the higher harmonic rejection ratio. The magnitude and phase of the impedance of the two matching network configurations can be seen in figure 6.4.

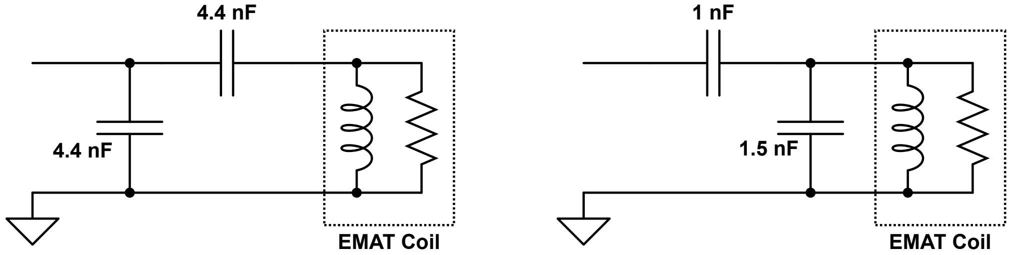

Figure 6.3: Matching network schematics for racetrack EMAT transducer. Network A (left) and Network B (right).

The networks match the EMAT impedance to the RITEC $50\,\Omega$ output. The voltage signal measured across a high power $0.1\,\Omega$ resistor, in series with the transmitting transducer, was used to measure the dynamic current and its harmonic content. The combined measurement of the voltage and current signals provides a measurement of the transducer's dynamic impedance.

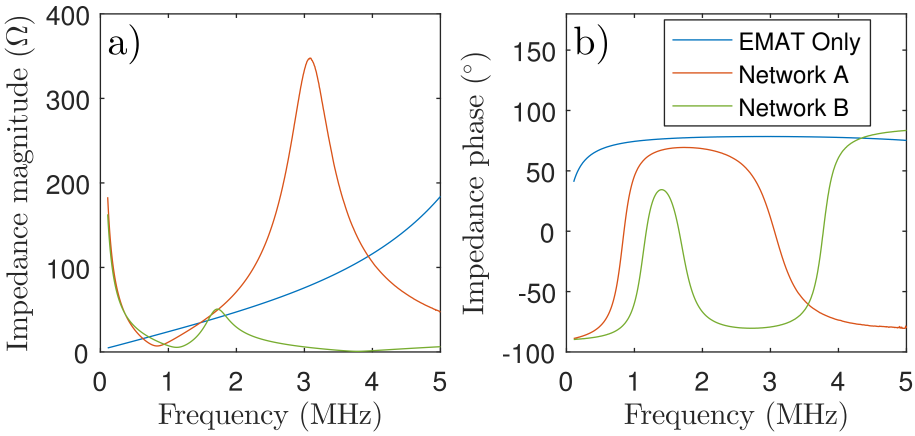

Figure 6.4: Impedance spectrum of different EMAT configurations measured by impedance analyser.

Ultrasonic measurements were conducted in a pitch-catch configuration to investigate the effect on EMAT generation efficiency (see section 6.5.2).

6.4 Fatigue tensile machine

A tensile fatigue machine (Instron 8800) with a maximum load of 25 kN was used to induce microstructural damage to samples of aluminium Al6061. The resonance and guided wave ultrasonic techniques investigated in this research require samples with parallel surfaces. Flat dogbone shape samples were cut out of 4.76 mm thick aluminium plate. The maximum load of the fatigue machine limits the cross-sectional area of the dogbone sample and/or the minimum number of cycles required for fatal failure. A high cycle fatigue regime was chosen to reduce the plastic deformation of the sample. The maximal cross-sectional area for the high-frequency fatigue regime (10 Hz) is limited up to 80 mm^2. Dogbone specimens were cut with the rolling direction perpendicular to the gauge length. The dogbone sample shape is shown in Fig. 6.5. Sample surfaces were first hand-polished and then machine polished using metal polishing soap until the surface had a mirror-like reflection.

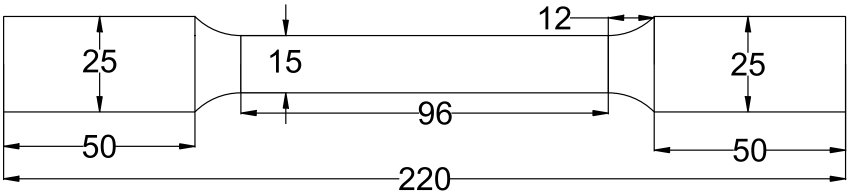

Figure 6.5: Dogbone specimen design for 4.76 mm thick Aluminium Al6061. All dimensions are in millimetres (mm).

A high cycle fatigue regime was selected at 100,000 cycles to failure, with a stress ratio of $R = 0.1$. A fully reversed stress of amplitude of 142 MPa is required for this configuration, see the SN curve in Fig. 6.6. The mean stress applied was 139 MPa with a stress amplitude of 114 MPa, which is equal to a fully reversed stress of 142 MPa [54]. The maximum strain measured was 0.15%, which is below the plastic deformation limit of the samples. Five samples were fatigued without interruption to confirm the failure prediction. The number of cycles to failure was recorded: 89k, 97k, 106k, 112k and 122k and are in good agreement with the results reported by Yahr [215]. Three samples were fatigued with interruptions to measure the nonlinear ultrasonic properties (see sections 7.2 and 7.3).

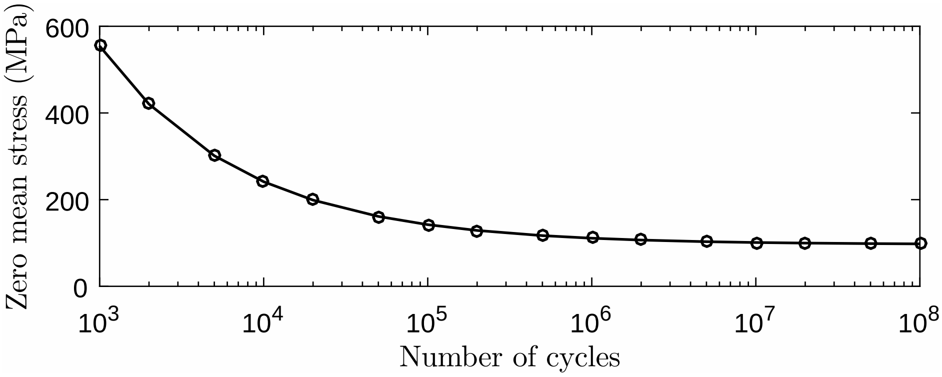

Figure 6.6: SN curve for fully reversed tensile test based on 6061 fatigue data from [215].

6.5 Shear wave EMAT experiments

A racetrack coil was chosen from the three bulk shear wave EMAT designs [204], instead of the pancake coil, as it generates polarised shear waves, and is preferred to the double coil (butterfly) design as it has a higher ratio of active to non-active coil area. The use of polarised shear waves is important as the acoustic birefringence effect can interfere with the ultrasonic signal [39]. The effect of birefringence can be seen in figure 6.7. The frequencies of the resonance modes in two orthogonal directions, one of which parallel to the rolling direction, for the same measurement location, have a small, but significant, difference.

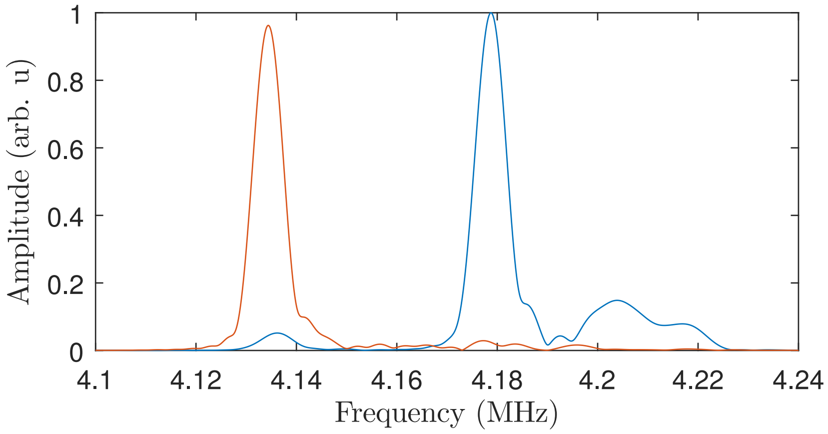

Figure 6.7: Birefringence frequency spectra of two orthogonal principal directions in rolled 380 μm thick aluminium plate.

A racetrack EMAT with coil dimensions of 15 mm × 25 mm was wound using copper wire with a diameter of 0.15 mm. The schematic of the design is shown in Fig. 6.8. The number of turns was 40, and the inner spacing of the coil was selected to be 3 mm to reduce any longitudinal wave generation (see fig 6.16). A PCB board of 1 mm thickness was placed between the magnet and the coil to increase the magnet-coil spacing. The copper side of the PCB was grounded and faced the magnet. The board was used to provide electrical shielding and to reduce any acoustic generation in the $NdFeB$ magnets. Two semi-cylinder high-grade $NdFeB$ magnets were aligned with opposite sides and placed on top of the PCB board and EMAT coil.

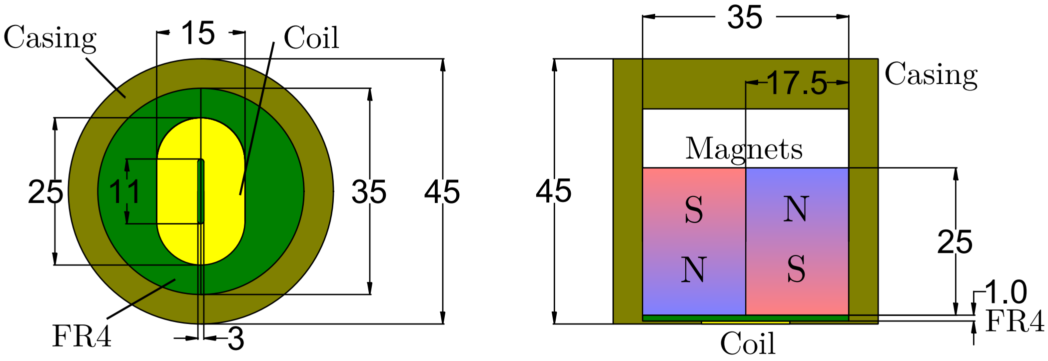

Figure 6.8: Bulk shear wave racetrack coil EMAT design using twin magnets and PCB electric shield. The coil has 40 turns and is wound with 0.15 mm diameter copper wire. All dimensions are in mm.

6.5.1 FEM simulations

The magnetic field of the transducer and the force generated by the coil were simulated in FEM software (COMSOL). Static simulation was used to obtain the magnetic field density (see Figure 6.9). The model used two opposing magnets with a remanent flux density of 1.3 T. Dynamic simulations of the surface current density were run for the racetrack EMAT design. The average of the current density at a thickness of half of the electrical skin depth was simulated and then combined with the static magnetic field. The distribution of the Lorentz force generated at the sample surface (see Figure 6.10) was then used as input for ultrasonic wave simulations in PZFlex. It is important to note that the out-of-plane Lorentz force generated has similar amplitude to the in-plane Lorentz force. However, the out-of-plane Lorentz force spatial distribution is asymmetric about the split-magnet axis. The Lorentz force distribution follows the magnetic field patterns closely. The amplitude of the out-of-plane Lorentz force reduces exponentially with the distance from the transducer centre. The forces from the radial part of the coil generate: perpendicularly polarised out-of-phase shear waves and in-phase parallel polarisation shear waves. The contributions from the self-field magnetic field generation are disregarded.

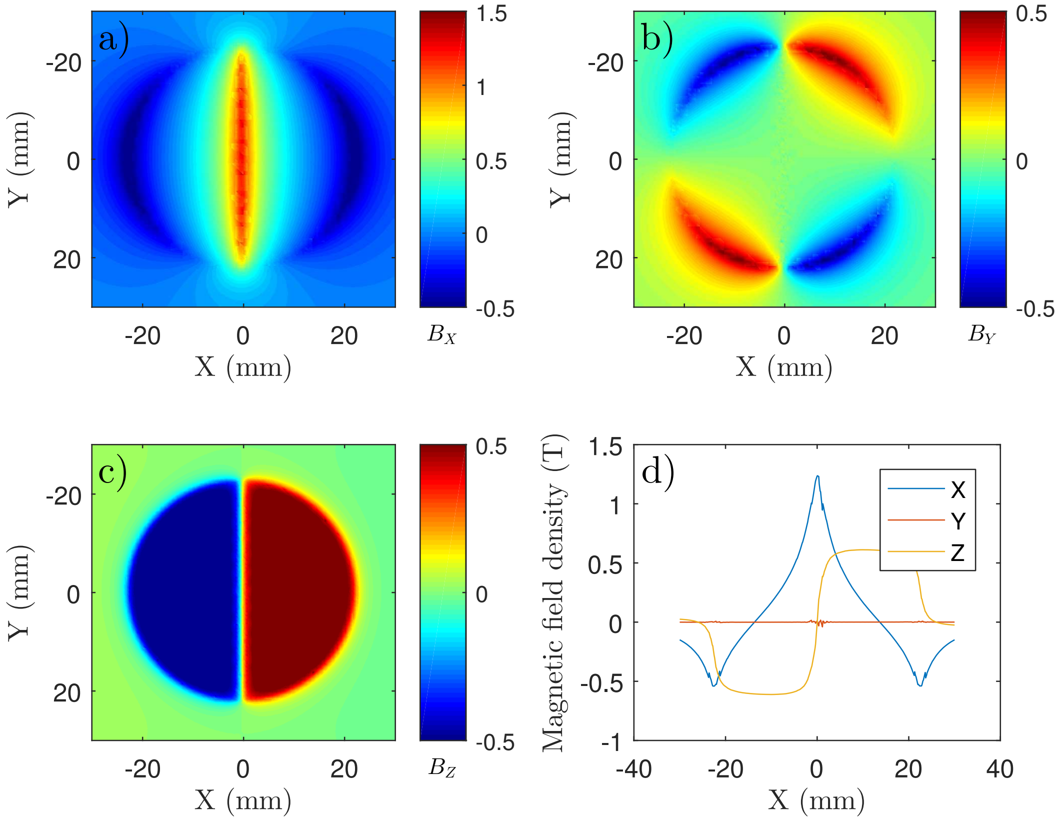

Figure 6.9: Simulated distribution of the magnetic field of a racetrack bulk shear wave EMAT. Magnetic fields applied in the out-of-plane direction (Z-axis). The magnetic field parallel to the shear wave polarisation (X-axis), (a), generates strong in-plane component between the twin-magnet configuration. The magnetic field perpendicular to the shear wave polarisation (Y-Axis), (b), is concentrated at the magnet edges and has negligible amplitude. The out-of-plane magnetic field density, (c), shows minimum variation across the magnet size. A comparison of the different components of the magnetic field for Y = 0 mm is presented, (d).

The distribution of the Lorentz force force components at the sample surface was used as an input for 2D ultrasonic wave simulation in PZFlex FEM software. The surface was loaded element-wise to closely match the simulated forces from the EMAT generation. Contributions from the self-field force generated by the dynamic magnetic field were disregarded. The simulation was used to acquire the shear and longitudinal wave diffraction patterns, see figure 6.11.

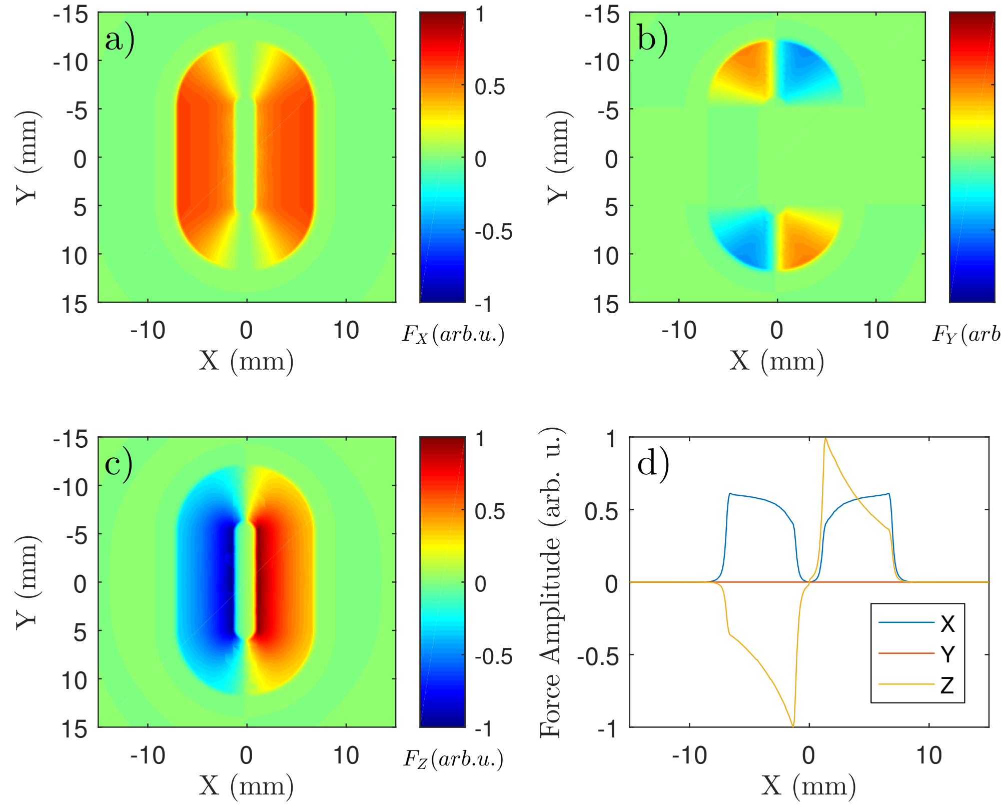

Figure 6.10: Simulation of the Lorentz forces distribution for a racetrack bulk shear wave EMAT. The Lorentz force parallel to the polarised shear wave, (a), perpendicular to the shear wav,e (b), longitudinal wave generation Lorentz forces, (c), and the force amplitude for different Lorentz force components at Y = 0 mm, (d). All forces are normalised to the maximum amplitude of the longitudinal Lorentz force and share a common colour scale.

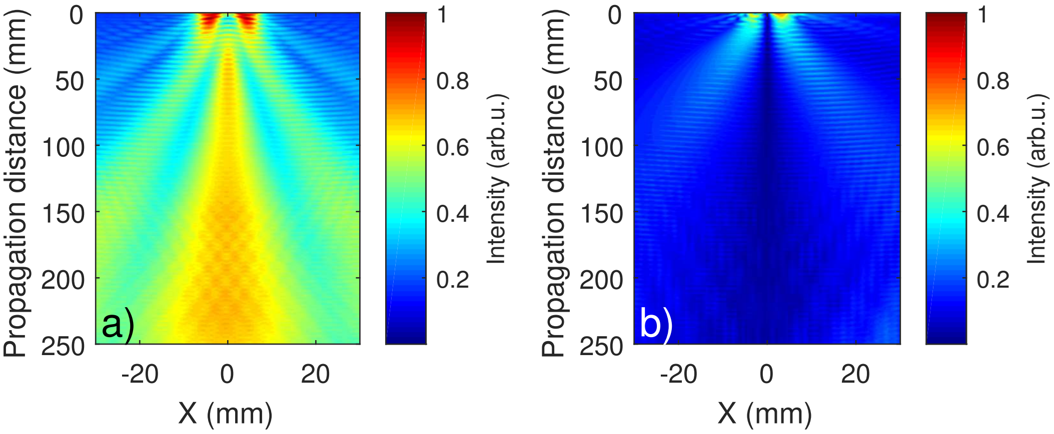

Figure 6.11: Diffraction pattern for shear, (a), and longitudinal, (b), wave generated by a racetrack EMAT.

The side lobes of the diffraction pattern for shear waves travel at large angles to the normal, while the main lobe generates a low divergence ultrasonic beam. The diffraction pattern for the longitudinal waves has two main-lobes travelling at a small angle to the surface normal direction. The asymmetry of the longitudinal components reduces the generation of longitudinal waves along the central line of propagation.

6.5.2 EMAT to shear piezoelectric transducer

Experimental measurements of the spatial distribution of the Lorentz force generation were taken to confirm the simulated force distribution. A polarised shear piezoelectric transducer, with a centre frequency of 2 MHz and dimensions 8 mm × 8 mm, was coupled using high viscous honey to an aluminium block of dimensions: 250 mm × 100 mm and thickness of 25 mm. Hot-melt adhesive was used to fix the sensor, ensuring constant contact conditions. The piezoelectric sensor polarisation was aligned to the longest block dimension and positioned in the samples centre to reduce ultrasonic contributions from side wall reflections. The transmitting EMAT transducer was placed and aligned on the opposite side of the aluminium block. The EMAT coil was excited by a short toneburst of 10 cycles at 1.683 MHz. Ultrasonic measurements were taken for multiple EMAT orientations, lift-off distances and excitation levels (see section 7.1).

The experimental configuration was also used to measure the variation of the second and third harmonic components as a function of the frequency spectrum of the input signal to the RITEC amplifier as explained in section 6.3.2. An arbitrary function generator (Tektronix AFG3102C) was used to provide signal to the RITEC amplifier input. A high power current and voltage monitor were connected to the system to measure the RITEC generation amplifier output. Additional higher harmonic components with different phases and amplitudes were added to the RITEC amplifier input, to compensate for the nonlinear generation from the last stages of the RITEC amplifier (see sec 7.1.2).

The effect of impedance matching was investigated in a pitch-catch configuration. The ultrasonic amplitudes generated using two different matching networks were compared to the performance of the non-matched EMAT transducer, see Fig. 6.12. The harmonic content of the received signals was analysed with regards to the fundamental signal amplitude and the harmonic to the fundamental ratio. Both matching networks improve the ultrasonic wave generation and reduce the second harmonic content. However, the third harmonic component shows an increased percentage content when matching electronics is used.

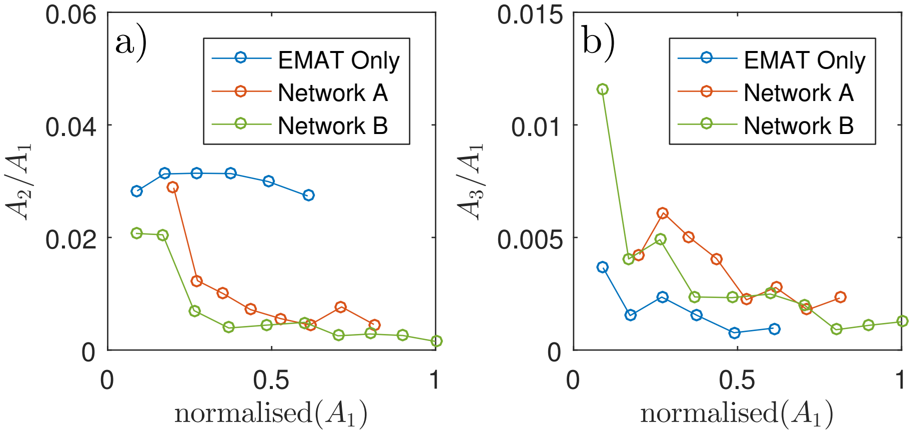

Figure 6.12: Harmonic content minimization for EMAT generation using impedance matching networks. The generation second harmonic is reduced significantly (a), while third harmonic generation is less affected (b).

6.5.3 Shear wave resonance

A shear EMAT transducer was used in a pulse-echo mode, to generate ultrasonic waves matching the through-thickness resonance modes of 4.76 mm thick aluminium specimens (Al6061). The material's Poisson's ratio is 0.33, therefore the longitudinal wave velocity is double the shear wave velocity, as shown in figure 6.13. Even number shear resonance modes will match the conditions for longitudinal wave resonance. Therefore, to reduce any wave interference, only odd numbered modes were used for the resonance mode techniques (see figure 6.16).

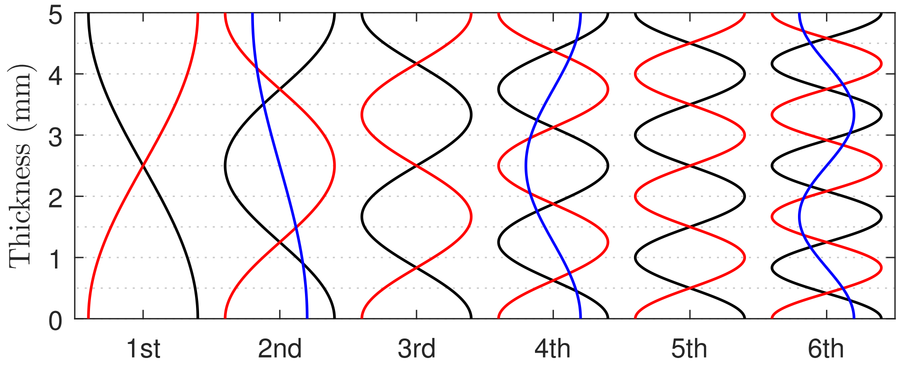

Figure 6.13: Ultrasonic wave amplitude profile for multiple through-thickness resonance modes in aluminium. Black and red lines represent initial and reflected signal for shear waves. Blue lines show resonance modes for longitudinal waves.

Frequency selection

Experimental measurements were performed to measure the transduction performance of shear wave EMATs over multiple modes of resonance. An aluminium sample plate (Al2024-T351) with thickness of 10.11 mm was used to measure the amplitude of the ultrasonic wave generated and detected in a pulse-echo configuration over a wide range of frequencies. A wide bandwidth, short temporal pulse was used to excite the EMAT coil. The frequency spectrum of the resonating signal was analysed using FFT. The frequency spectra for the pulsed generation can be seen in Fig. 6.14a. The frequency separation between the resonance modes is consistent with the theoretical calculations. The maximum amplitude of generation was in the $2.5 - 3.5$ MHz range.

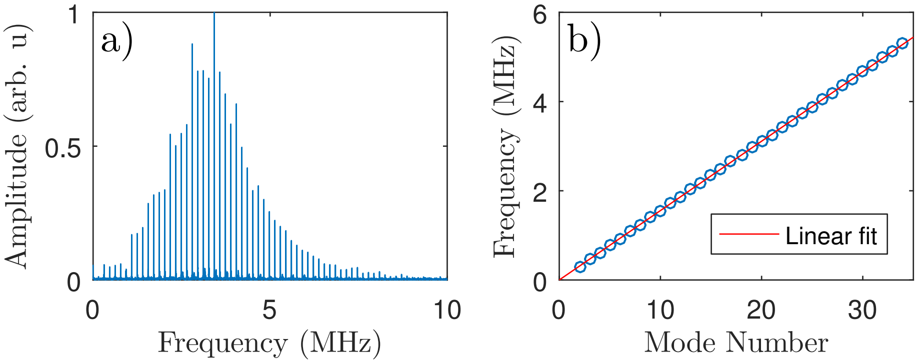

Figure 6.14: Frequency spectrum for through thickness resonance modes (a), generated by wideband pulse excitation, in 10.11 mm thick aluminium sample (AL-2024). The frequency separation between different resonance modes (b), is consistent with theoretical calculations $f_N = N \times 1.55 \times 10^5 + 904.5$ Hz.

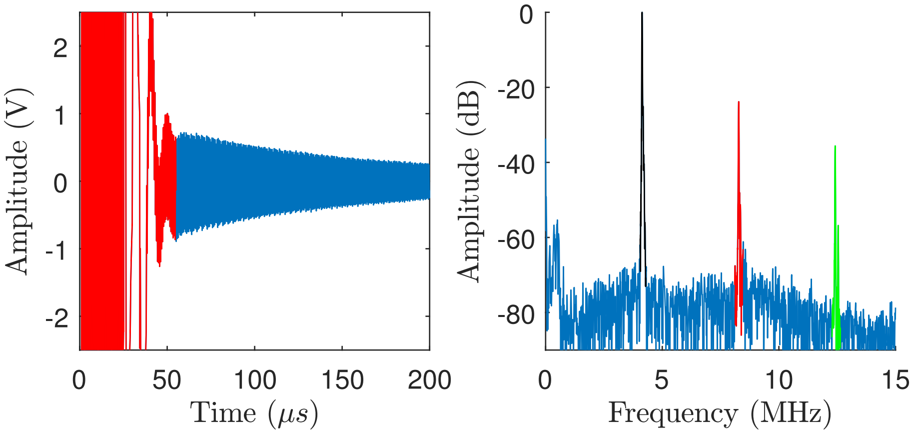

Figure 6.15: Signal, (a) and frequency spectrum, (b), of the fundamental resonance mode in 0.30 mm thick aluminium sample Al6061.The signal received during dead-time of the receiver amplifier is ignored coloured in red. Fundamental resonance mode at 4.1 MHz (black) and higher harmonics of significant amplitude are observed: second (red) and third (green).

Narrow band toneburst signals of 60 cycles were used to measure single resonance mode excitations. The signal is generated using the RITEC amplifier and measured through the RITEC built-in diplexer and receiver amplifier. FFT analysis of the received signal shows the presence of higher harmonic components in the ultrasonic signals, see figure 6.15.

Racetrack shear wave EMATs with two different coils, inner radius of 1 mm and 3 mm, were tested to measure the interference from the longitudinal wave generation. To increase the separation between the resonance frequencies an aluminium plate of thickness 4.76 mm was used. The frequency of the 20 cycle toneburst generation signal was swept with 10 kHz steps. It can be seen in Fig. 6.16 that the amplitudes of the even numbered shear resonance modes are reduced for the 1 mm separation EMAT coil.

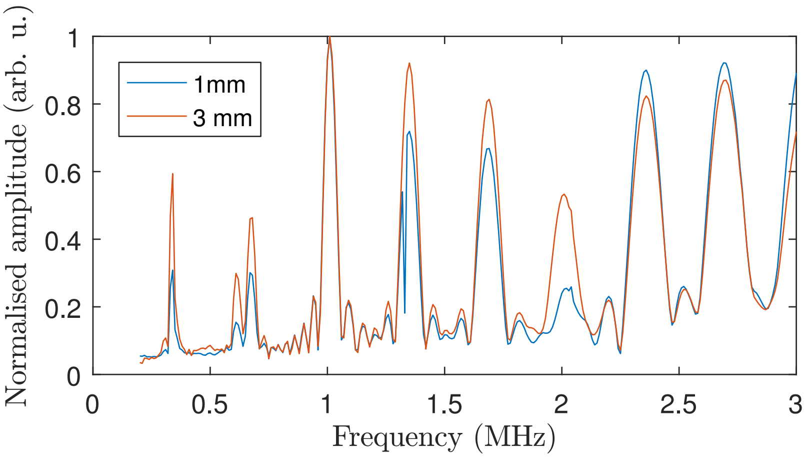

Figure 6.16: Resonance mode amplitude variation for EMATs with coils of different inner radius: 1 mm (blue) and 3mm (red).

6.5.4 Frequency shift

Measurements using the nonlinear resonance ultrasonic spectroscopy (NRUS) technique were performed on an aluminium dogbone sample, to evaluate the change of the nonclassical nonlinear parameter with fatigue. The specimen was fatigued with interruptions at $0, 20k, 30k, 43k$ and $65k$ cycles and failure occurred at $72k$ cycles. Measurements of the frequency shift were taken using the procedure presented in Haupert [58]. For each high amplitude measurement, a second measurement was taken at a significantly lower amplitude. The frequencies of the two measurements are subtracted to minimise the effect of temperature variation during the measurement process.

The third shear wave resonance mode was chosen for the experimental measurements, as the combined amplitude of the generation and detection was the greatest (see figure 6.16). The frequency value is extracted by FFT of the first 100 μs of the received signal. The number of averages taken per measurement was 128. Zero padding and Gaussian fit were used to acquire precise values for the amplitude and frequency of the FFT peak. The full-width half-maximum (FWHM) for the resonance mode was measured to be 0.8% for 100 cycles toneburst signal.

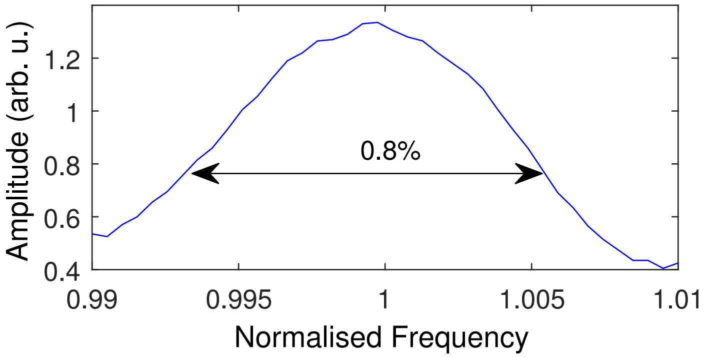

Figure 6.17: Frequency sweep for third resonance mode in 4.76 mm thick aluminium sample. Full-width half-maximum at 1.011 MHz frequency is 8 kHz for a driving toneburst signal of 100 Cycles.

The variation of the frequency and fundamental amplitude was measured across the aluminium plate used to cut out the fatigued dogbone samples. The frequency variation is due to thickness and material properties variations. Figure 6.18 shows the frequency range across the plate, which is less than 1000 Hz, and the variation of the amplitude, which is less than 10%. Therefore, it is important to account for these frequency variations.

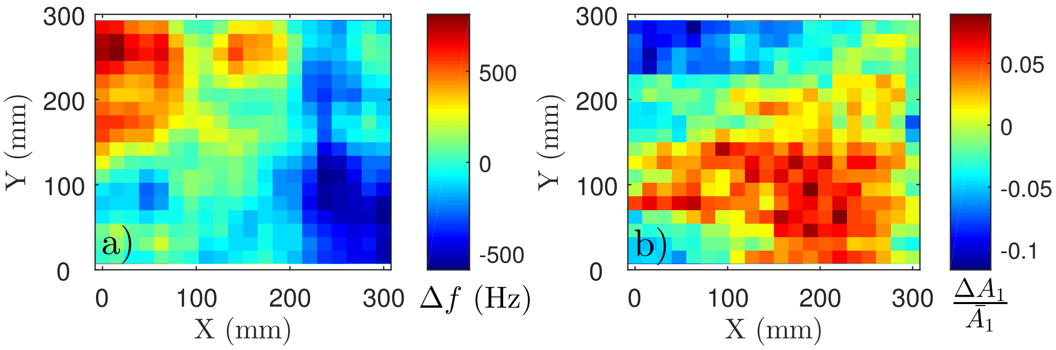

Figure 6.18: The frequency and amplitude variation of the third shear wave resonance mode on a 300 mm × 300 mm aluminium plate.

A linear frequency sweep around the resonance mode frequency was used to minimise the effect of thickness variations. The linear frequency sweep had a range of 4000 Hz (0.4%) around the average resonance frequency of the aluminium plate. The length of the toneburst signal was 200 μs to ensure high amplitude, narrow band signals at the resonance frequency.

For the fatigued dogbone samples, scans were performed using a gantry XY positioning system and a custom made plastic sample holder. Constant EMAT lift-off throughout the experiments was maintained for each fatigue sample. Measurements of the frequency shifts were performed as B-scans and at multiple excitation amplitudes (see section 7.2). Twenty measurement positions were equally spaced over the gauge length of the sample. The sample was firmly attached to the baseplate of the XY table and plastic sample holders were used to ensure proper alignment and positioning. The racetrack EMAT transducer was attached to the arm of the XY table and lift-off was reduced to a minimum while maintaining no contact with the sample surface. The variation of the lift-off across the length of the sample was kept to a minimum, by using feeler gauges. The linear part of the racetrack coil was centred in the middle of the sample width. The shear wave polarisation is parallel to the gauge length, to reduce the edge effects from the finite width of the sample.

Temperature variations of the samples were monitored using a digital multimeter (Keithley 2100). A four wire PT100 sensor was attached, to the middle section of the aluminium samples, using silicone thermal grease. A hot plate (Corning PC-400D) was used to vary the temperature during the measurement of the resonant mode frequency shift (see figure 7.22).

6.5.5 Higher harmonic

Nonlinear ultrasonic measurements of the higher harmonic components were conducted in the through-thickness resonance configuration. Due to the elastic constant symmetry (section 2.2.4), shear waves are prohibited from generating second harmonics due to the lattice anharmonicity. However, dislocations and microscopic voids/cracks may still contribute to the second harmonic component. Therefore, the third harmonic nonlinear parameter was measured as a function of the fatigue state. Similar to the second harmonic interaction at a stress-free boundary, the third harmonic component of the reflected ultrasonic wave is partially cancelled by the third harmonic component in the incident wave [9; 11]. Additionally, the self-field Lorentz force contributes only to the second harmonic amplitude, therefore the measured third harmonic component is due to the material or system nonlinearities.

An aluminium dogbone sample was fatigued to failure (129,000 cycles) with interruptions for ultrasonic measurements at: 0k, 40k, 60k, 80k, 100k, 120k. As fatigued damage causes localised changes to the microstructure, measurements across the length of the sample were taken at 18 equally spaced locations along the gauge length. To ensure consistency of the measurement locations, a custom plastic sample holder was fixed to the baseplate of the motorised XY stage. The shear wave EMAT was attached to the movable arm and levelled to the sample surface using a feeler gauge. Lift-off distance was maintained at 0.2 mm, while keeping the variation to a minimum.

The fifth shear wave resonance mode, at a frequency of 1.683 MHz, was used to excite high amplitude ultrasonic waves. The driving signal was compensated for the higher harmonic content generated by the system nonlinearity (see section 7.1.2). The excitation toneburst had a length of 40 μs with a frequency sweep of 2000 Hz, to compensate for thickness variation in the sample.

A diplexer (RITEC RPR4000) was used to separate the driving and received signal from the EMAT transducer. The acoustic signal was recorded after the dead-time recovery and analysed using a STFT with Hanning window function of 20 μs. Amplitudes of the higher harmonic components were measured as a function of the amplitude of the input electrical signal. The results, seen in Fig. 6.19, show a peak in the third harmonic amplitude at signal levels around 0.4 V.

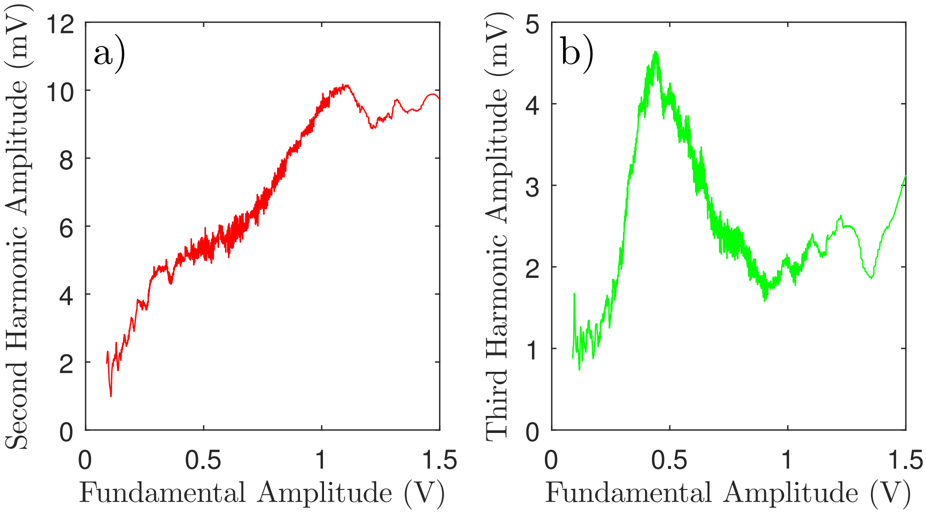

Figure 6.19: Higher harmonic content in the received signal as a function of the electrical signal amplitude: second harmonic, (a), and third harmonic, (b). The third harmonic component shows a distinct peak at 0.42 V, which can cause false-positive results.

The received signal, from the diplexer output, was filtered to reduce the amplitude of the fundamental frequency signal. A five stage notch filter, $-90dB$, was built using passive electrical components. Two sets of measurements were taken for each fatigue state: unfiltered, to measure the amplitude of the fundamental mode, and filtered, to acquire the amplitude of the higher harmonics. To reduce the signal to noise ratio, 128 averages were taken for each measurement. The relationship between the amplitudes of the fundamental and third harmonic components was measured as a function of driving signal amplitude. Additionally, the evolution of the third harmonic component was measured as a function of propagation time. The nonlinear parameter β_3 was analysed with respect to the fatigue state of the sample.

6.6 Summary

To improve the measurement reliability of the experimental configuration, investigations of the possible sources of system nonlinearities were preformed. The contributions to the system nonlinearity from the receiving and generating EMAT electronics were evaluated. The receiver electronics showed a variation in the amplitude of the third harmonic components with the received signal amplitude. To reduce this effect, electrical filtering of the fundamental component is required. The high-power generating electronics also generate significant harmonic distortion. A new method was proposed to reduce the harmonic content produced by the high power amplifier system (RITEC RPR4000).

A suitable signal processing technique was identified to study the harmonic amplitude evolution with propagation distance - short time Fourier transforms using a Hanning window with length of 20 μs.

Aluminium dogbone specimens were selected to undergo high cycle tensile fatigue with an equivalent fully reversed stress amplitude of 142 MPa. Three samples were fatigued in stages to measure the changes in their nonlinear ultrasonic properties.

The surface force distribution of a polarised shear wave EMAT was simulated in COMSOL. The results were used for ultrasonic wave simulations in PZFlex to determine the diffraction pattern of the EMAT design.

Experimental measurements using a shear wave piezoelectric transducer were conducted to optimise the EMAT transduction parameters: frequency, matching network, inner coil radius and frequency sweep range. The experimental configurations for the NRUS and higher harmonic measurements are also detailed.

Chapter 7

Nonlinear ultrasonics using bulk waves

7.1 EMAT racetrack coil

The performance of the racetrack coil shear wave EMAT is investigated with regard to nonlinear ultrasonic wave generation. The EMAT ultrasonic transduction process is studied in detail: spatial profile of the ultrasonic displacements, harmonic compensation and lift-off performance.

7.1.1 Ultrasonic displacement profiles

Measurements of the displacement profile of the ultrasonic waves generated by a racetrack coil were taken. A piezoelectric transducer was securely fixed, using hot-melt adhesive, and coupled, using high viscous honey, to the bottom side of an aluminium plate. For the shear wave measurements, a shear polarised 2 MHz sensor was used, while for the longitudinal measurements, a longitudinal 2.25 MHz piezoelectric transducer was used. The EMAT is attached to the arm of a gantry positioning system and was moving in the XY plane as shown in the schematic diagram in Fig. 7.1. The lift-off is maintained constant across the scan area. Three different EMAT configurations were tested: two with the EMAT polarisation parallel and perpendicular to the piezoelectric sensor polarisation, and one for an EMAT without a permanent magnet. C-Scan measurements were taken in the scan area with a typical size of 25×25 mm. The coordinates of the centre of the EMAT coil were used for the XY coordinate of all the measurements, while the origin of the coordinate system was the centre of the piezoelectric sensor. To reduce any edge wall reflections, an aluminium block of size was 250 mm $\times$ 100 mm $\times$ 25 mm used.

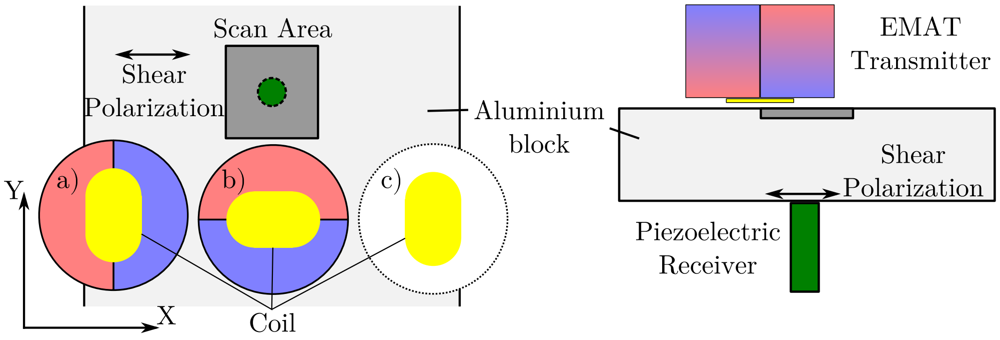

Figure 7.1: Experimental schematic for measuring displacement profiles. The piezoelectric transducer is fixed to the bottom side of an aluminium plate, while the EMAT is moving in the XY plane above an aluminium block. C-Scan measurements are taken in the scan area: typical size 25×25 mm^2. Three configurations of the EMAT transducer are tested: a) parallel polarisation, b) perpendicular polarisation, c) coil only generation.

The longitudinal displacement profiles are measured using a longitudinal piezoelectric transducer with a centre frequency of 2.25 MHz, instead of the shear piezoelectric sensor. The measurements are performed using the same experimental configuration as drawn in figure Fig. 7.1 and described in section 6.5.2.

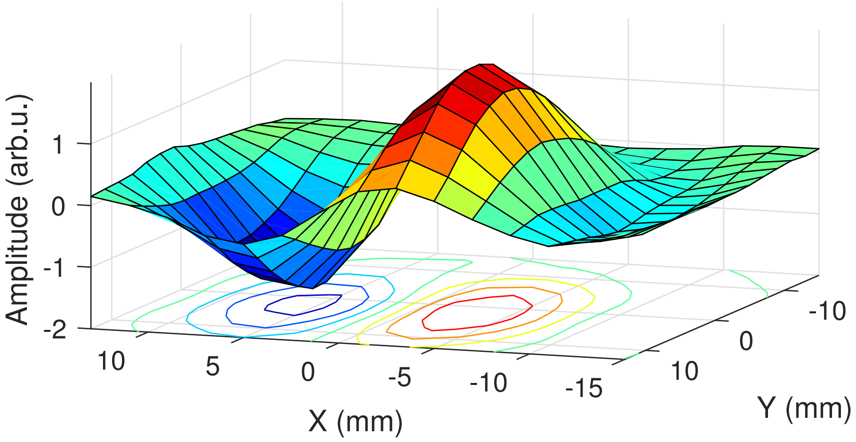

Figure 7.2: Experimentally measured longitudinal wave displacement profile of a racetrack coil EMAT with a permanent magnet. The displacement profile has a symmetry line at X = 0 mm, in agreement with the simulated Lorentz force distribution in Fig. 6.10c.

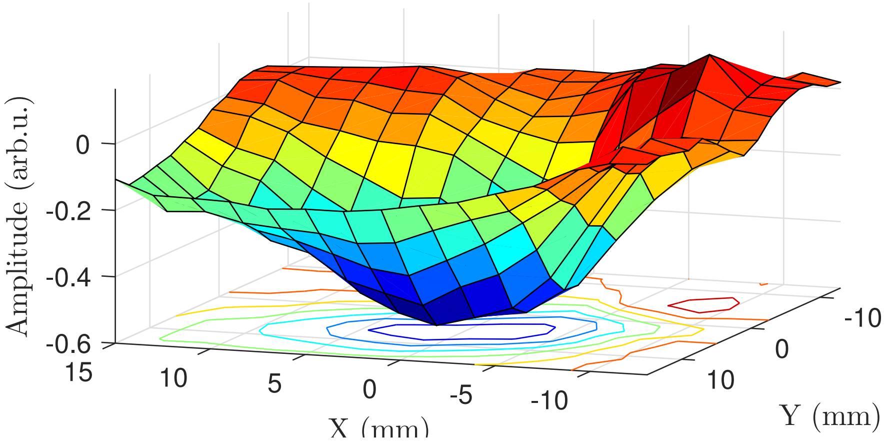

Figure 7.3: Experimentally measured longitudinal wave displacement profile of a racetrack coil EMAT without a permanent magnet. The displacement profile is similar to that of a piston-like transducer.

The displacement profile for the longitudinal waves is in good agreement with the simulated force profile for a permanent magnet EMAT (see Fig. 6.10c). The displacement is asymmetric about the split-magnet line (X = 0), as shown in figure Fig. 7.2. The measured displacement profile for the ultrasonic wave generated by the EMAT without a permanent magnet shows the contribution from the self-field Lorentz force (see Fig. 7.3). The displacement profile under the coil is symmetric with respect to the central line, as described by EMAT theory. The ratio between the longitudinal wave amplitude of the self-field Lorentz force F_L^{dyn} and the static magnetic field Lorentz force F_L^{stat} is: $F_L^{dyn}/F_L^{stat} = 0.05 \approx -26dB$. Therefore, the longitudinal ultrasonic waves generated by the self-field Lorentz force, have a significant contribution to the measured second harmonic component.

The displacement profile for the shear wave, whose polarisation is perpendicular to the linear segment of the racetrack coil, also has a symmetrical distribution, in agreement with the simulated force distribution (see Fig. 6.10a). The measured ultrasonic beam spread shown in Fig. 7.4, also matches the simulated ultrasonic beam divergence, see Fig. 6.11. The amplitude of the shear wave component generated by only an EMAT coil was also measured (see Fig. 7.5). The ratio between the self-field Lorentz force F_S^{dyn} and the static magnetic field Lorentz force F_S^{stat} is: $F_S^{dyn}/F_S^{stat} = 0.0015 \approx -56dB$. The second shear wave harmonic component generated from the EMAT coil has a negligible amplitude and can be attributed to the sensitivity of the shear piezoelectric sensor to longitudinal waves.

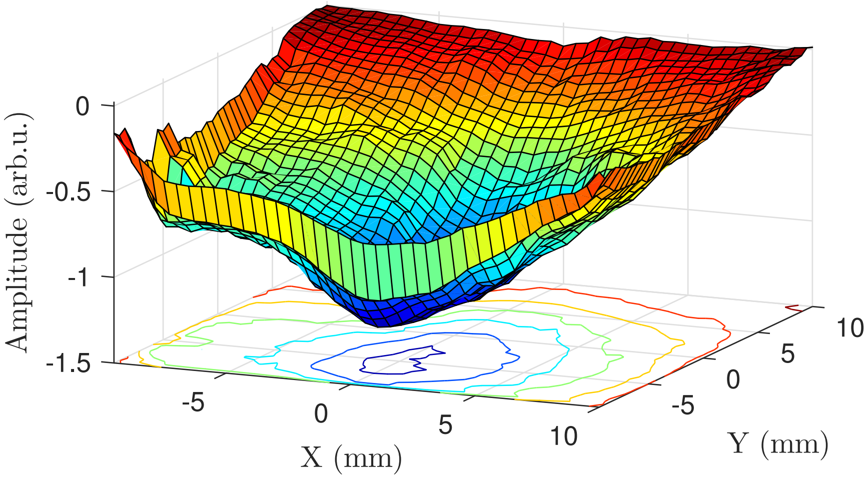

Figure 7.4: Experimentally measured shear wave displacement profile of a racetrack coil EMAT with a permanent magnet with polarisation perpendicular to the linear segment of the racetrack coil.

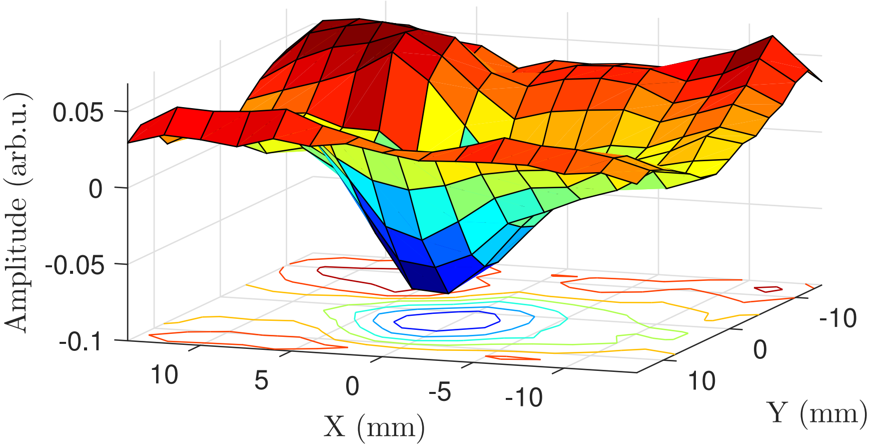

Figure 7.5: Experimentally measured shear wave displacement profile of a racetrack coil EMAT without a permanent magnet.

The displacement profile for the shear waves (Fig. 7.6), generated by the radial part of the racetrack coil, matches the simulated Lorentz force surface distribution (see Fig. 6.10b). The B measurement configuration from Fig. 7.1 was used for this measurement, for which the polarisation of the EMAT was perpendicular to the polarisation of the piezoelectric transducer. Therefore, the measured shear waves were only generated from the radial part of the racetrack coil, as shown in Fig. 6.10b. The amplitude of the shear ultrasonic waves, generated from the radial portion of the coil, was approximately 15% of the amplitude of the polarised shear waves. The displacement profile of the non-polarised shear waves has two lines of symmetry about the centre of the transducer coil. This agrees with the simulated Lorentz force pattern for the radial shear waves, see Fig. 6.10b.

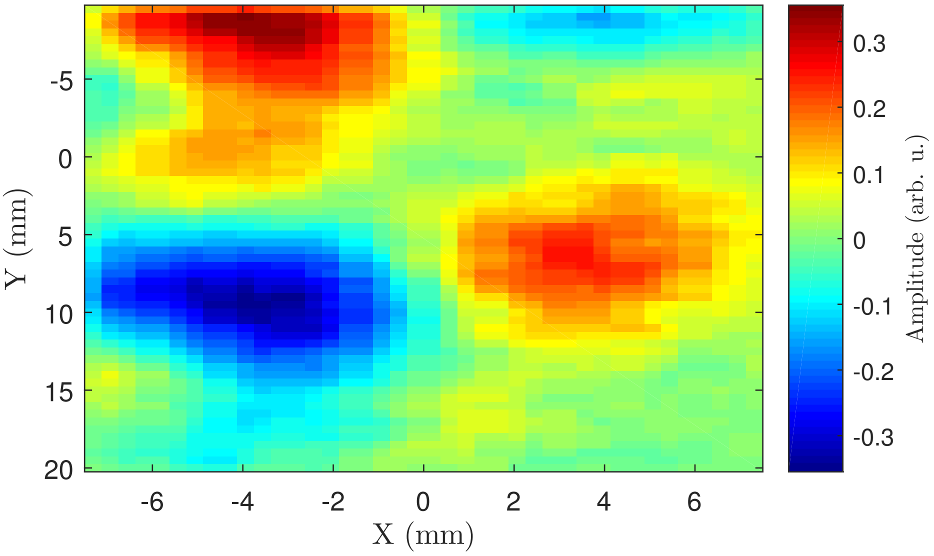

Figure 7.6: Experimentally measured shear wave displacement profile of a racetrack EMAT with a permanent magnet with the polarisation of the EMAT generated shear waves perpendicular to the polarisation of the piezoelectric shear wave receiver.

The diffraction pattern at the centre line of the transducer was measured for the polarised shear wave component, see Fig. 7.7. B-Scan of the ultrasonic field at the $Y = 0$ mm axis of the EMAT coil is performed using EMAT configuration A from figure Fig. 7.1. The acoustic beam spread of the experimental measurements have a similar width to the simulated diffraction pattern, see Fig. 6.11a. However, the generated ultrasonic beam profile is asymmetrical with respect to the propagation centreline. This can be explained by a small difference between the generated magnetic field from the two semi-cylindrical magnets and an uneven distribution of the copper wires in the hand-wound coil. For propagation distances shorter than 250 mm, a significant part of the ultrasonic beam amplitude is concentrated underneath the EMAT coil footprint.

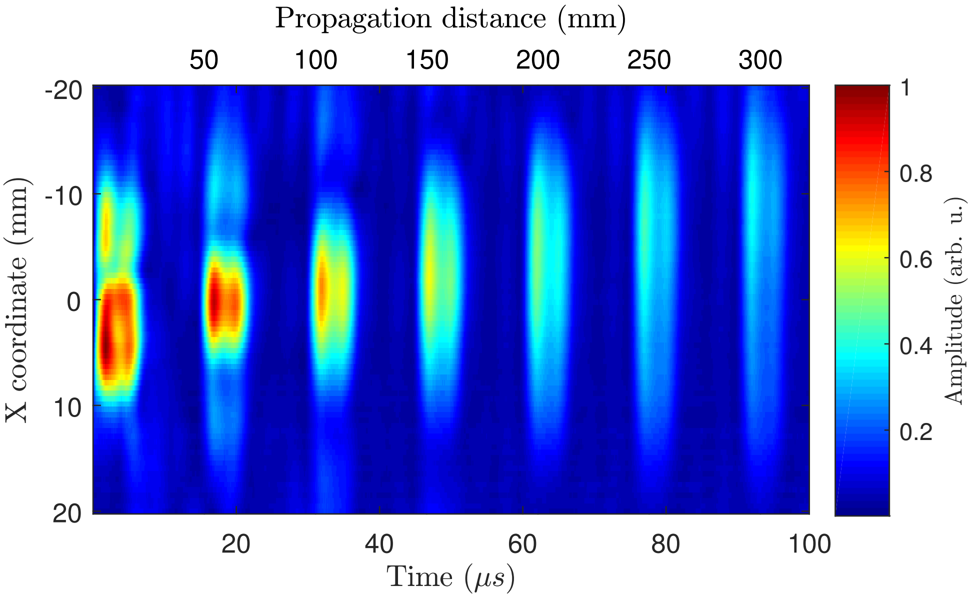

Figure 7.7: Experimentally measured shear wave ultrasonic beam profile of a racetrack coil EMAT with a permanent magnet with polarisation of the ultrasonic waves parallel to the shear piezoelectric detector polarisation. The beam spread with propagation distance is in good agreement with the simulated diffraction pattern, although the ultrasonic beam profile is asymmetrical with respect to the centre line (X = 0 mm). This is caused by an asymmetry in the magnetic field of the EMAT.

The experimentally measured displacement profiles and ultrasonic beam propagation are in good agreement with the simulated Lorentz force spatial profiles and the ultrasonic diffraction pattern.

7.1.2 AFG harmonic compensation

An investigation into the harmonic content of the EMAT excitation signal was conducted, to reduce the contribution of the system nonlinearity to the measured ultrasonic nonlinear parameter. The signal from an arbitrary function generator (AFG) was used as an input for the generation amplifier of the RITEC (RPR 4000). Artificial harmonics were added to the supplied signal from the AFG at various amplitudes and phases, to measure the variation of the harmonic distortion in the generation amplifier output, see Fig. 7.8. Furthermore, measurements of the harmonic content of the generated ultrasonic waves were used to evaluate the improvement of the signal harmonic distortion. The measurements were performed in a pulse-echo configuration, using a shear wave EMAT. An excitation current of 40 amperes was used. Toneburst of 40 cycles at a frequency of 1.683 MHz was generated by the AFG, which matches the resonance conditions for the fifth shear resonance mode in 4.76 mm thick aluminium plate.

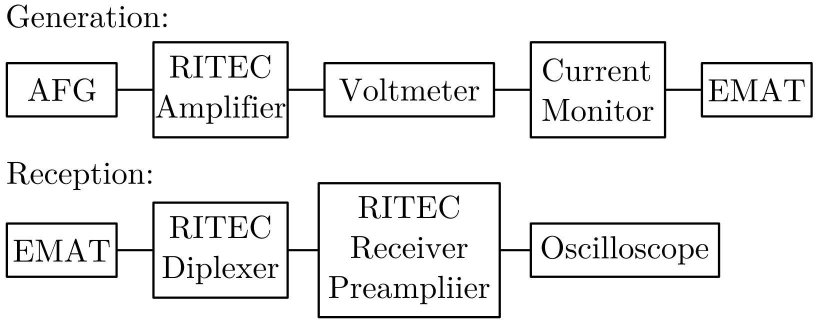

Figure 7.8: Schematic diagram of the apparatus used to measure the harmonic distortion of the RITEC generation amplifier.

Two parameters are varied to find the operation point of minimum harmonic distortion: the amplitude and the angle of the harmonic compensation. The amplitude of the harmonic compensation is defined as the ratio between the amplitudes of the fundamental and the higher harmonic component of the signal generated by the AFG. The angle of the harmonic compensation is defined as the phase between the fundamental and the higher harmonic components of the signal generated by the AFG. The harmonic distortion in the RITEC output is measured as the ratio between the amplitudes of the higher harmonics and the fundamental component in the amplifier output signal.

A minimum of the second harmonic distortion is achieved for a compensation angle of 300 degrees and compensation amplitude of 0.018%, while for the third harmonic distortion the minimum is achieved for a compensation angle of 270 degrees and a compensation amplitude of 0.012%, as shown in figure Fig. 7.9. The amplitude of the second harmonic distortion is reduced from 4.2% to 1.4% (see Fig. 7.10a), and the third harmonic distortion is reduced from 1.4% to 0.2% (see Fig. 7.11a), as a percentage of the fundamental component amplitude of the generation signal. The ultrasonic waves generated using the optimum angles were measured to evaluate the reduction of the generated higher harmonic ultrasonic waves. Significant improvement was achieved in the reduction of the generated second harmonic ultrasonic wave. The generated ultrasonic harmonic content was reduced by a factor of 3.5 for the second harmonic (see Fig. 7.10b), while the third harmonic ultrasonic component is reduced by a factor of 1.4 (see Fig. 7.11b).

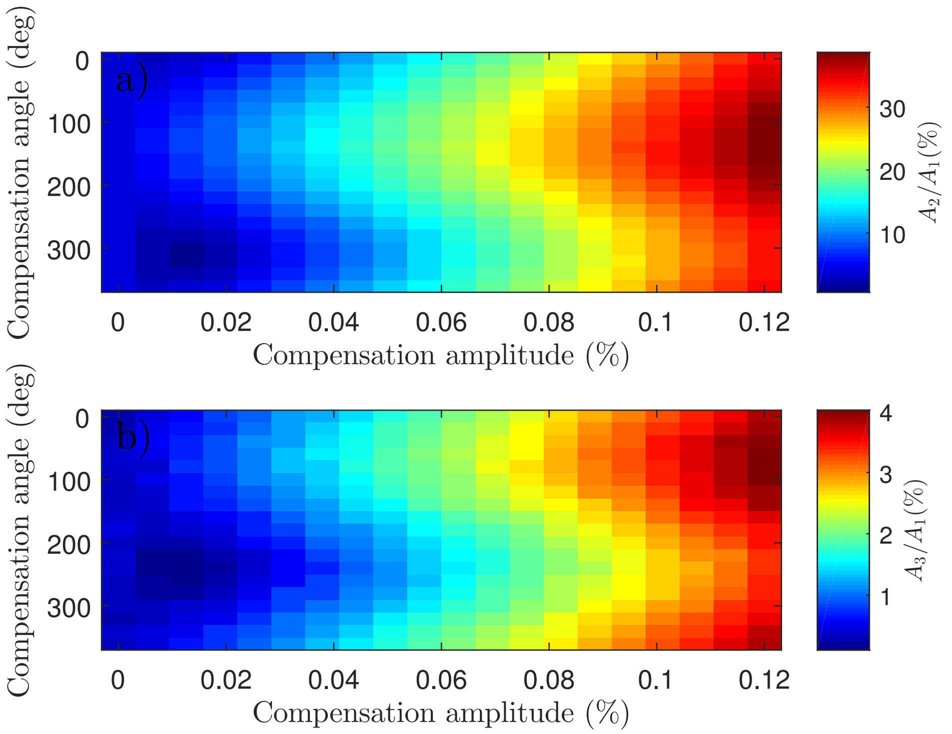

Figure 7.9: Map of the harmonic distortion of the RITEC output signal as a function of the compensation amplitude and compensation phase angle: second harmonic, (a), and third harmonic, (b). A distinct minimum is observed for both cases, with harmonic disturbance values lower than the non-compensated RITEC output.

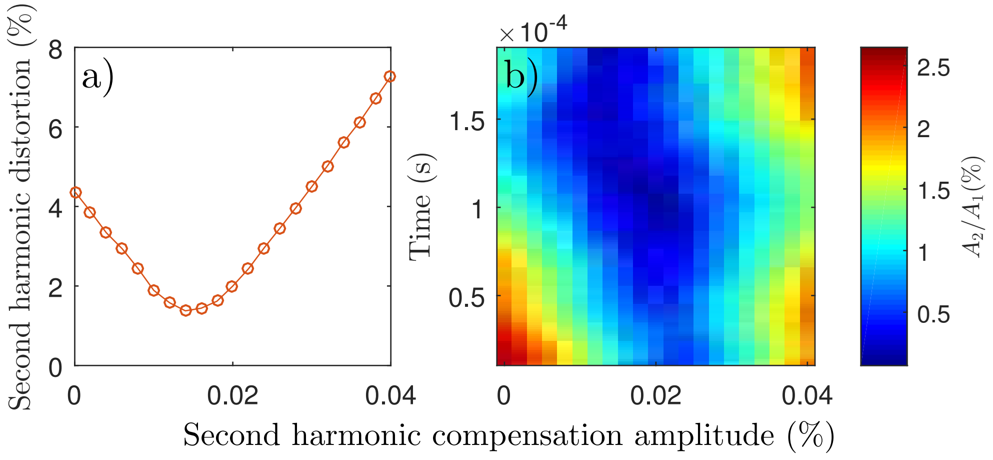

Figure 7.10: Second harmonic distortion compensation as a function of compensation amplitude, (a). The minimum harmonic distortion is achieved at a compensation amplitude of 0.18%. The ultrasonic harmonic content is significantly reduced for the optimum compensation amplitude and angle, (b).

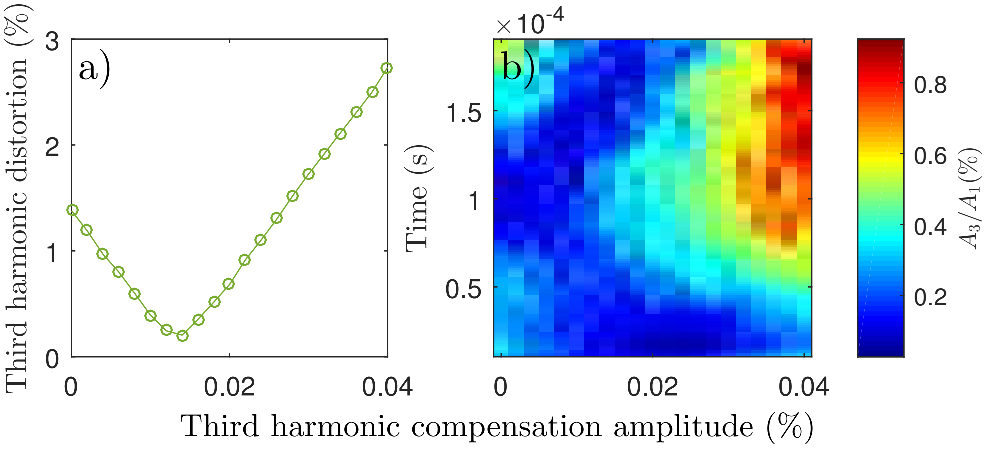

Figure 7.11: Third harmonic distortion compensation as function of compensation amplitude, (a). The minimum harmonic distortion is achieved at a compensation amplitude of 0.12%. The ultrasonic harmonic content is reduced for the optimum compensation amplitude and angle, (b).

The performance of the optimised RITEC generation was tested for a range of excitation levels of the generation signal (see Fig. 7.12). The amplitude of the second harmonic distortion is consistently lower for the compensated generation, while the third harmonic distortion does not show a significant reduction. The optimisation of the compensation parameters was conducted at a driving current of 40 A, which explains the local minimum for the third harmonic distortion. Although the compensated generation signal reduces the absolute value of the third harmonic distortion, the measurements show an upward trend similar to the uncompensated case for currents higher than 40 A.

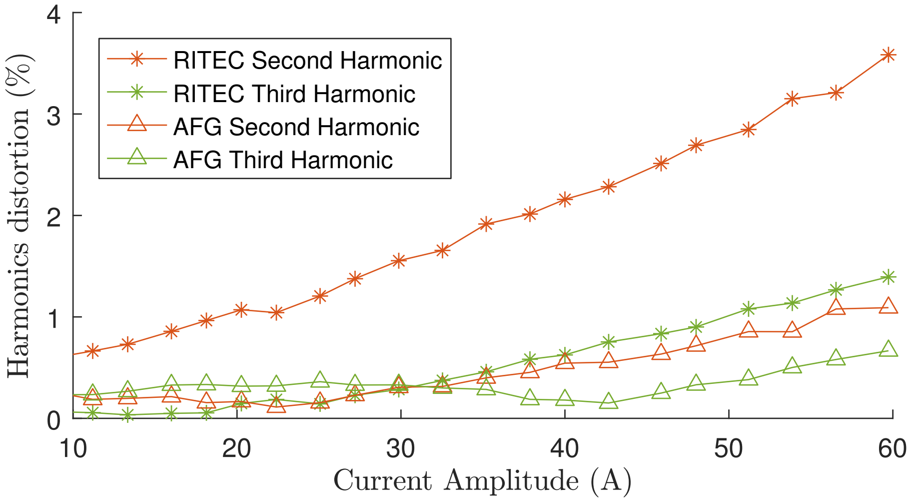

Figure 7.12: Harmonic distortion dependence on RITEC Control level. The harmonic content in the measured ultrasonic waves is reduced for the harmonic compensation method (triangles) for both the second (orange) and third (green) harmonics, compared to the RITEC standard toneburst generation (stars).

The harmonic compensation methodology proposed in this thesis has been proven effective in reducing the generated higher harmonic ultrasonic content and can be used to investigate and improve the system nonlinearities. The reduction of the higher harmonic content from the high amplitude current output can allow measurements of even smaller values of the material nonlinearity parameters. This technique can improve pulse-echo single-side nonlinear measurements and can be used in addition to high power filters for pitch-catch measurement configurations. In the pulse-echo mode, a single transducer must both excite high amplitude fundamental frequency ultrasonic waves and be able to measure small amplitude higher harmonic waves. Additionally, the frequency bandwidth of transmission and reception of ultrasonic transducers are strongly linked. Therefore, the passive filters used to reduce the generation of higher harmonics will also limit the higher harmonic reception. Further investigation is required to improve the optimisation method algorithm, such as direct measurement of the compensation amplitude and angle. Alternatively, the technique can be used to control the amount of system nonlinearity from the current source, and thus assess its contribution to the total system nonlinearity.

7.1.3 Dynamic Lorentz force

The dynamic Lorentz force generates repelling surface forces with a frequency twice that of the driving electrical signal. Measurements of the amplitude of longitudinal ultrasonic waves were carried out at different small lift-off distances to quantify the self-field force generation. A pitch-catch configuration with a longitudinal piezoelectric sensor was used in combination with a precision positioning XY gantry system. A schematic diagram of the configuration is shown in Fig. 7.13. Lift-off was varied between 0 mm and 0.5 mm with a step of 0.05 mm. For clarity, only three of those measurements will be presented. The omitted data is in good agreement with the presented results. Lift-off distances larger than 0.5 mm are affected by the induced current in the shielding layer of the PCB copper, placed above the coil.

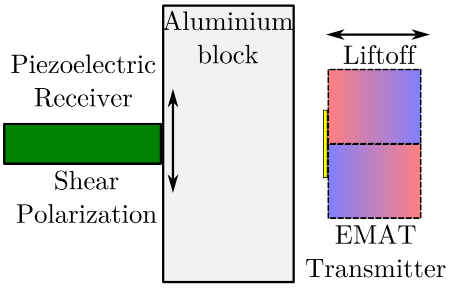

Figure 7.13: Schematic diagram of the ultrasonic transducers for EMAT lift-off measurements. The piezoelectric transducer is fixed to the sample surface, while the EMAT is attached to the moving arm of a motorised XY gantry system.

Two racetrack coil EMAT configurations were used: one with and one without a permanent magnet. To reduce the impedance variation from the coil-magnet eddy current coupling, an electrically grounded thin copper layer was placed between the coil and the magnet. A dummy plastic cylinder block was placed to substitute the permanent magnet in the EMAT structure. The magnet configuration was used to measure the variation of the coil impedance and amplitude of the fundamental ultrasonic wave, with respect to the driving current and lift-off.

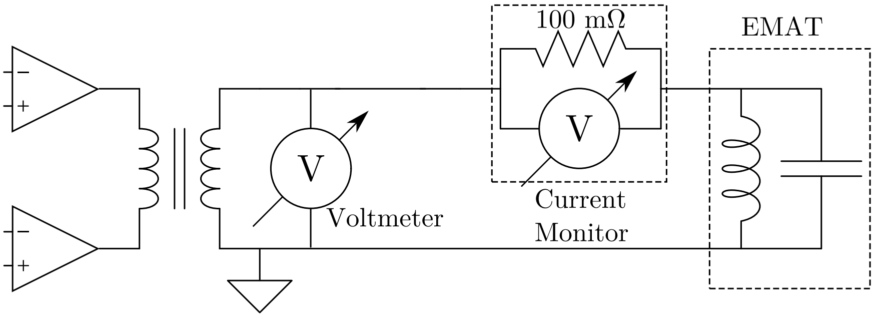

Figure 7.14: Schematic diagram of the electrical components used to measure the dynamic impedance.

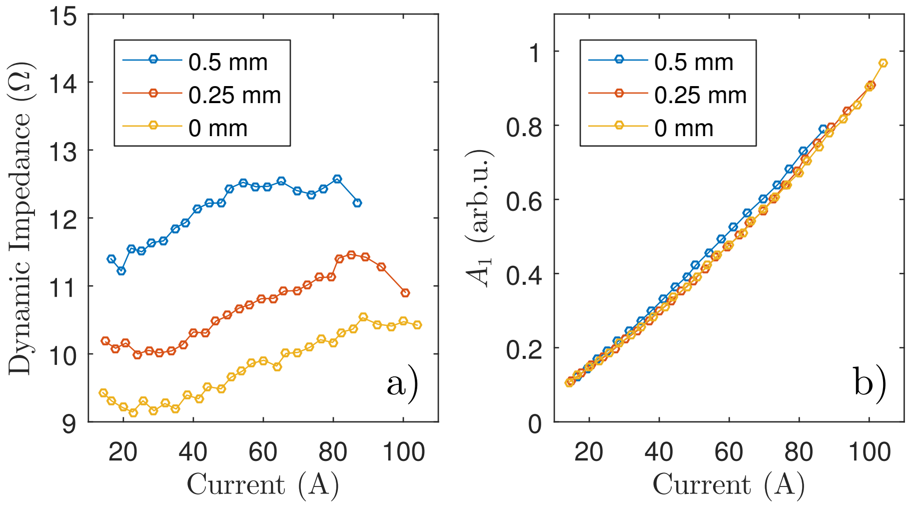

Figure 7.15: Dynamic impedance, (a), and fundamental ultrasonic wave amplitude, (b), variation with lift-off distance and driving current. The ultrasonic waves are generated by the permanent magnet Lorentz force. The fundamental wave amplitude shows a linear dependence on the driving current amplitude, while the lift-off affects the coil impedance. The impedance increases with increasing the lift-off: in contact with the sample (yellow), 0.25 mm (red) and 0.5 mm distance (blue).

The dynamic impedance was measured as the ratio between the amplitudes of the measured driving signal voltage and current. Therefore, it represents the magnitude of the electrical impedance. The schematic diagram of the measurement configuration is shown in Fig. 7.14. The generation output of the RITEC amplifier is limited by the maximum peak-to-peak voltage of the RITEC output. Therefore, the maximum excitation current amplitude will decrease with lift-off distance. The measured dynamic impedance increases with the amplitude of the excitation current Fig. 7.15a. This is important to consider if matching networks are used.

The relationship between the ultrasonic wave amplitude of the fundamental wave and the excitation current amplitude is linear, as shown in Fig. 7.15. For small lift-off distances, 0 - 0.5 mm, the amplitude of the generated signal depends only on the amplitude of the excitation current.

The equivalent measurements were performed for the self-field Lorentz force generation, see Fig. 7.16. Longitudinal waves with the second harmonic frequency are generated. The amplitudes of the waves have a quadratic relationship with respect to the current excitation level. For small lift-off distances, 0 - 0.5 mm, the amplitude of the generated signal depends only on the amplitude of the excitation current.

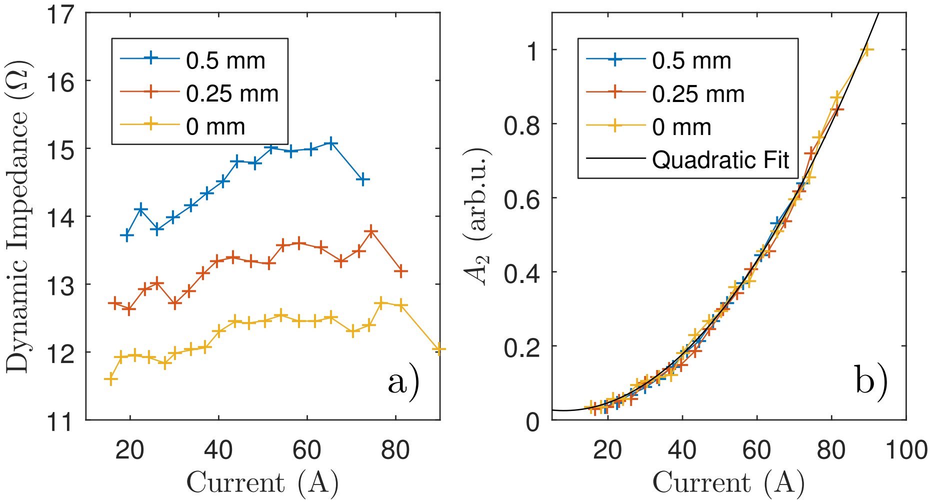

Figure 7.16: Dynamic impedance (left) and second harmonic ultrasonic wave amplitude (right) variation with lift-off and driving current. The ultrasonic waves are generated by self-field Lorentz force. The second harmonic wave amplitude shows a quadratic dependence on the driving current amplitude, while the lift-off affects the coil impedance. The impedance increases with increasing the lift-off: in contact with the sample (yellow), 0.25 mm (red) and 0.5 mm distance (blue).

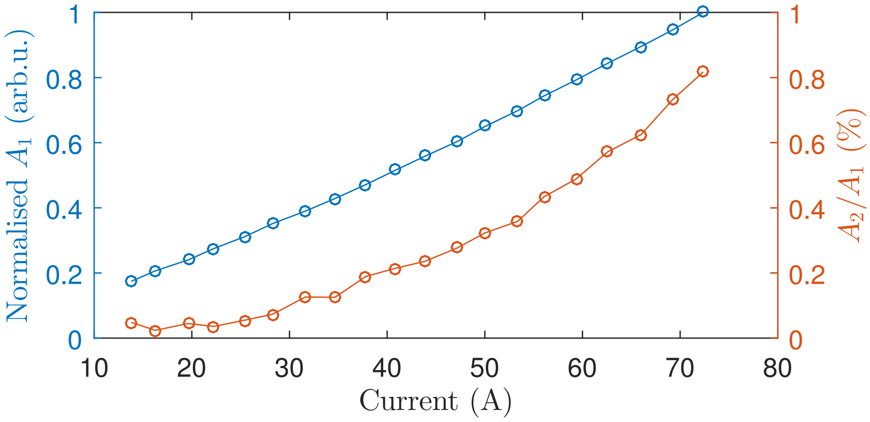

Figure 7.17: Amplitude of fundamental mode ultrasonic wave, generated by static field Lorentz force (magnet) and the amplitude of second harmonic generated by dynamic Lorentz force (no magnet). The ratio between the fundamental and second harmonic ranges from -50 to $-40dB$.

Therefore, for small lift-off distances, comparable with the magnet-coil spacing, the amplitudes of the Lorentz forces generated from the self-field and from the permanent magnet depend only on the current amplitude and show no change with lift-off. The ratio between the generated second harmonic amplitude from the no-magnet case and the fundamental wave amplitude from the permanent magnet case has a minimum value of $-50dB$ and a maximum value of $-40dB$, see Fig. 7.17. The square dependence of the amplitude of the self-field ultrasonic waves with respect to the amplitude of the fundamental ultrasonic wave generated by the permanent magnet mimics the material nonlinearity phenomena. These two phenomena make the longitudinal waves EMAT generation impractical for nonlinearity measurements.

7.2 NRUS frequency shift

Measurements of the frequency shift caused by high amplitude ultrasonic waves were taken to evaluate the NRUS technique for aluminium. The measurement procedure from Haupert [58] was adapted. Measurements for the third shear wave through thickness resonance mode were taken for excitation levels of 100 % and 5% of the maximum output power of the RITEC amplifier. From all the shear resonance modes, the third mode has the highest amplitude of the received signals and has the lowest level of attenuation. Therefore, the third resonance mode was chosen for the frequency shift measurements.

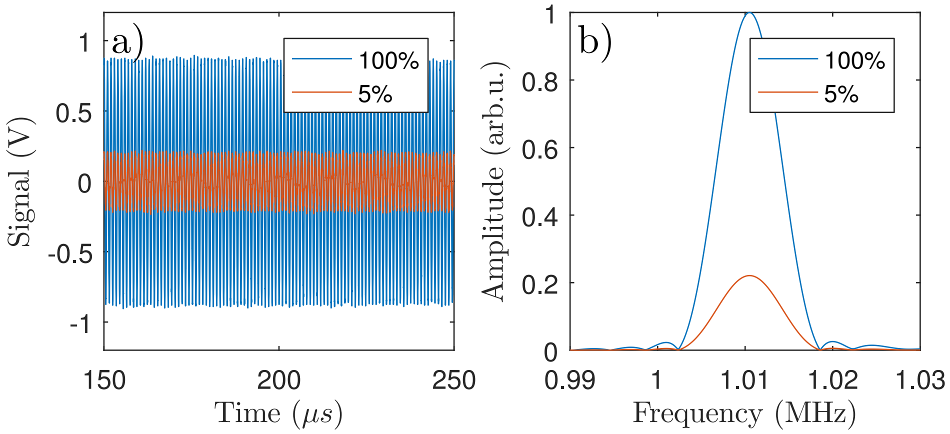

Figure 7.18: Typical NRUS signal, (a), and the corresponding frequency spectra, (b), used for measuring the frequency shift of the fundamental harmonic component for two different excitation levels.

Measurements of the sample temperature and the frequency shift were taken for multiple upward and downward sweeps of the excitation amplitude, see Fig. 7.19. The frequency shift of the measured signals shows a hysteretic behaviour, and there is a shift of the lowest excitation level resonance frequency. The measured sample temperature is linear with regards to the frequency shift. The Joule heating, from the surface eddy currents generated by the EMAT, heats up the aluminium sample. Therefore, the increase in excitation current amplitude leads to an increase in the sample's temperature underneath the EMAT. As a result, temperature measurements or compensation techniques must be employed for EMAT NRUS measurements, to ensure that the data is representing material nonlinear properties. The frequency shift has a linear gradient of around -350 $Hz/°C$, for the third through thickness resonance mode.

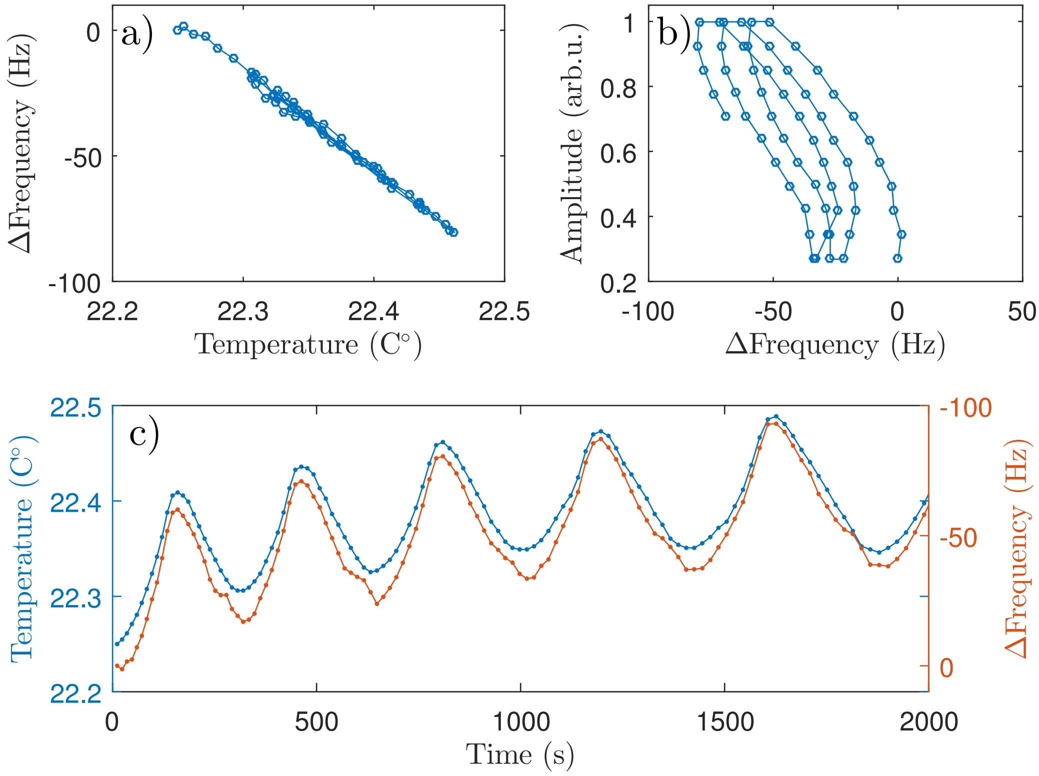

Figure 7.19: EMAT Joule heating of the aluminium plate causing frequency shifts, (a). The continuous up-down-up sweeps of the excitation amplitude of the NRUS EMAT, (b), lead to variation in the sample's temperature and cause variation in the frequency shift, (c). A strong correlation between the sample's temperate and the frequency shift of the ultrasonic signal is observed.

Using the temperature compensation method outlined in Haupert [58], frequency shift measurements were acquired for an unfatigued dogbone sample at 20 equally spaced locations along the sample gauge length, see Fig. 7.20. The frequency difference between the lowest and the highest excitation levels, after temperature compensation, have values of less than 5 Hz. For 1 MHz excitation frequency, the frequency shift is less than 0.001%, which is significantly lower than the reported values for pure copper [72].

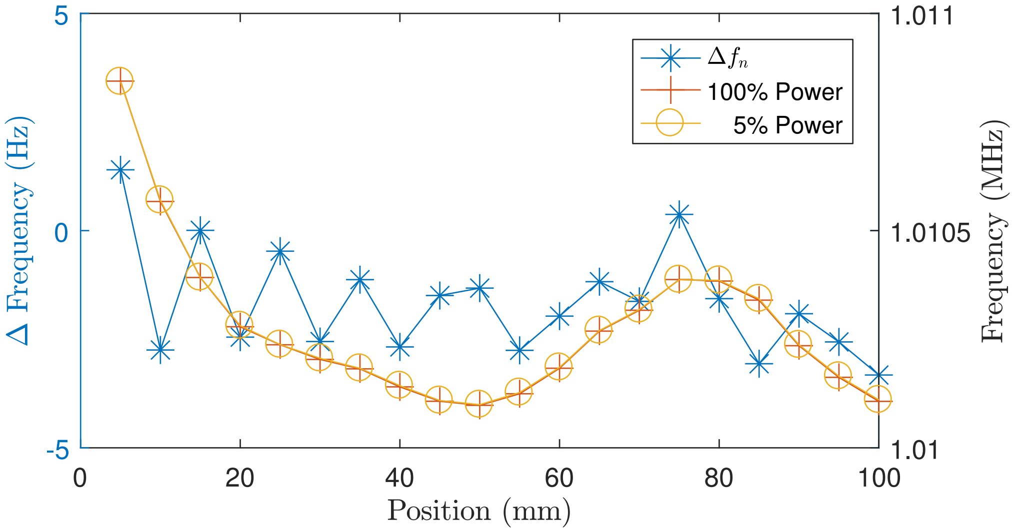

Figure 7.20: Temperature compensated frequency shift along the gauge length of an unfatigued sample.

The change in the frequency shift does not show any clear trends for any of the sample locations. The maximum deviation of 10 Hz, corresponds to a temperature fluctuation of 0.02 °C and is equal to a frequency shift of:

$$\frac{\Delta f_n}{f_0^n} = \frac{f^n - f_0^n}{f_0^n} = 0.001\% \tag{7.1}$$

NRUS measurements were taken of the same sample at different stages of the fatigue lifetime. The fatal failure of the sample occurred at the 60 mm position. The trend of the frequency shift at that location does not show any notable differences from the rest of the gauge length measurements, see Fig. 7.21. Therefore, the EMAT NRUS technique cannot be used to measure the fatigue states and provide information regarding the microstructural evolution for materials with low value of the nonclassical nonlinear parameter, such as aluminium alloys. However, the technique may still be applied to materials with high value of the nonclassical nonlinear parameter such as: stainless steel [58; 151], brass [58] and pure copper [72]. Further investigation is required to assess the viability of the technique for other types of metals: titanium alloys, mild steels and cast iron. Presenting temperature measurements in combination with the frequency shift results of the NRUS technique is essential for the credibility of the reported results.

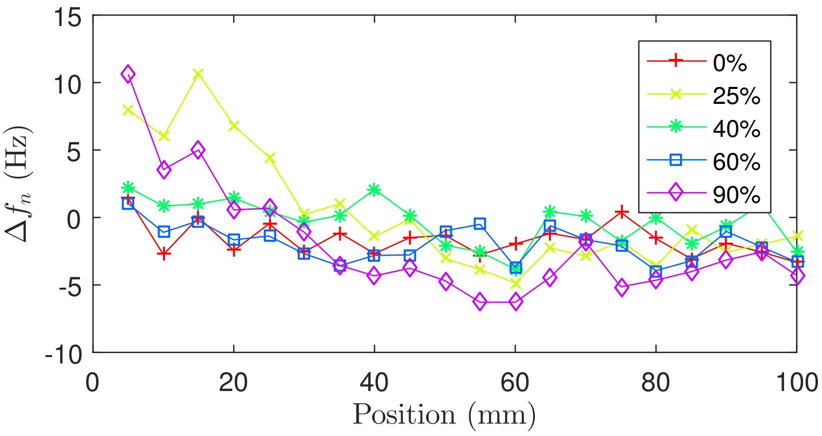

Figure 7.21: NRUS frequency shift, with temperature compensation, measured along the gauge length of a dogbone sample. The different traces correspond to different percentages of the fatigue life-cycle, from 0 % to 90 %. The failure crack occurred at 60 mm. No significant change is observed over the fatigue evolution.

Measurements of the temperature dependence of the resonance ultrasonic spectroscopy (RUS) frequency as a function of fatigue were performed. The results are analysed to investigate the sensitivity of EMAT RUS technique to changes in the second and third order elastic constants, which affect both the temperature dependence of the ultrasonic wave velocity and the coefficient of thermal expansion. The sample was heated to temperatures of 45 °C by a hotplate. Measurements were taken during the cooling of the sample. The temperature of the sample was monitored using the PT100 temperature sensor. The sensor was positioned below the ultrasonic measurement location.

The change in temperature affects both the sample thermal expansion and the higher order elastic constants [110; 124]. Previous studies have shown that the rate of change of the temperature dependence of the ultrasonic velocity, dc/dT, depends on the applied external, and/or residual, stress [32; 174; 175]. The RUS method measures the change in the resonance frequency, which has a linear relationship to the ultrasonic velocity and inverse relationship with the sample thickness. Therefore, contributions from both parameters would effect the frequency change.

$$\frac{\partial f}{\partial T} = \frac{nc}{2}\frac{\partial(d^{-1})}{\partial T} + \frac{n}{2d}\frac{\partial c}{\partial T} \tag{7.2}$$

Where f, T, n, c and d are the resonance mode frequency, the temperature, the resonance mode number, the ultrasound velocity and the sample thickness respectively. The thermal expansion coefficient (CTE) affects the frequency shift of the RUS measurements, as the sample thickness is changing. Optical methods have measured the change of CTE with localised damage [161], and multiple methods have been used to measure CTE, including non-contact techniques. To the author's knowledge, no investigation, using ultrasonic techniques, has been carried out to measure the CTE or the temperature dependence of ultrasonic velocities as a function of fatigue or creep damage. The EMAT RUS technique allows for high temperature non-contact measurements of the combined effect of thermal expansion and ultrasonic velocity temperature dependence. The measured results show significant change between the initial (unfatigued) state of the sample and the later stages of the fatigue cycle, see Fig. 7.22b. This can be explained with the increase of the residual stress and the formation of persistent slip bands. Further studies are required to evaluate the proposed technique.

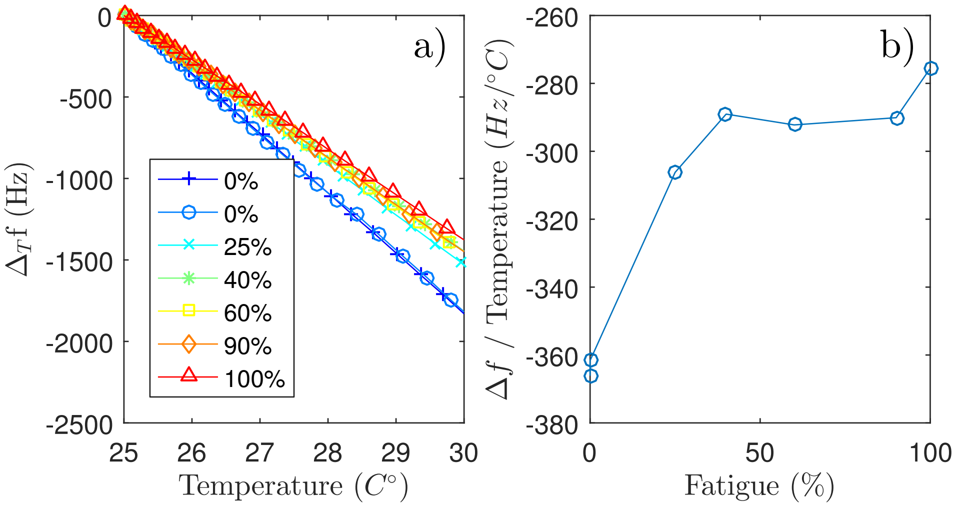

Figure 7.22: Frequency shift as a function of sample temperature for different fatigue levels, (a). Rate of frequency shift as a function of fatigue state, (b).

7.3 NRUS third harmonic NLU

Measurements of the higher harmonic ultrasonic components were taken during the fatigue process for a different AL6061 dogbone sample. The configuration used for NRUS frequency shift measurements was also used for the higher harmonic measurements. For all the presented data, the fundamental resonance mode amplitude is measured from the amplified signal from the RITEC diplexer output. While, the amplitudes of the higher harmonics were measured with a notch filter connected between the diplexer output and the receiver amplifier input. A higher amplifier gain (+20 dB) was selected for the filtered case to provide better vertical resolution for the small amplitude higher harmonic electrical signals. The ratio between the amplitudes of the third and fundamental harmonics for the unfiltered measurements was 0.002, while for the filtered case the ratio is 0.03. Therefore, the contribution from the receiver amplifier and the oscilloscope to the total nonlinearity is reduced (see Fig. 6.19). The signal is analysed from 65 μs onwards, to reduce the transient effects on the electrical signal from the recovery time of the RITEC diplexer.

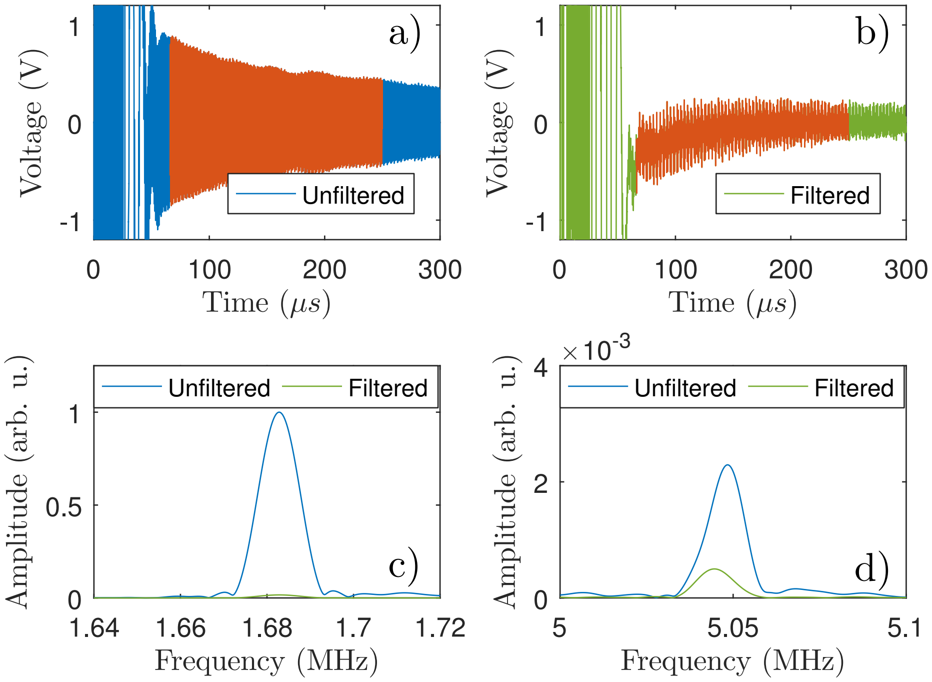

Figure 7.23: Typical NRUS signal for the fifth order shear resonance mode in 4.76 mm thick aluminium. The unfiltered signal, (a) is used to extract the amplitude of the fundamental harmonic, while the higher harmonics are extracted from the filtered signal, (b). The frequency spectra for the fundamental harmonic, (c), and the third harmonic amplitude, (d), show the effect of the electrical filter. All frequency spectra are normalised to the amplitude of the fundamental harmonic of the unfiltered case.

The RITEC control levels were swept to confirm the power law relationship between amplitudes of the fundamental harmonic and higher harmonic waves. The harmonic distortion compensation method was employed as described in section 7.1.2.

The third harmonic distortion shows a minimum at 40 A excitation current, while the third harmonic acoustic amplitude shows uninterrupted cubic trend with respect to the current amplitude. Therefore, the measured nonlinearity originates from the material properties, and not from the generator's nonlinearity. For the range of excitation currents available, the third harmonic amplitude shows the expected cubic trend, while the second harmonic increase does not follow the quadratic power law, defined by the NLU theory. Measurements of the fundamental, second and third harmonic are taken at a propagation time of 30 μs (approximately 100 mm propagation distance) after the end of the excitation signal, to reduce the transient effects and allow cumulative generation of nonlinear ultrasonic waves.

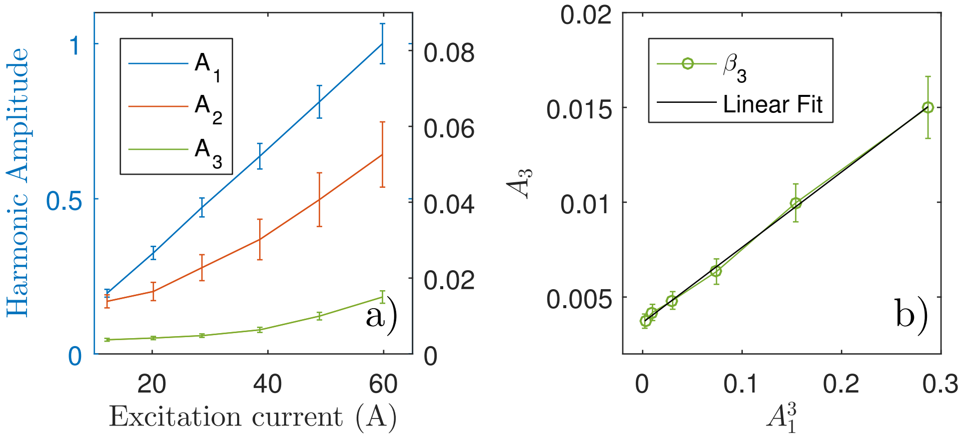

Figure 7.24: Variation of the second and third harmonic amplitudes, generated by a shear ultrasonic wave, as a function of excitation current, (a), and the third harmonic amplitude relationship to the fundamental amplitude, (b). The errors show the variation of the measured harmonic content across 10 locations along the gauge section of the dogbone sample. All data is normalised to the maximum amplitude of the fundamental harmonic.

The presented harmonic amplitudes in Fig. 7.24 are the average of the measured signals from 10 locations along the gauge length of the unfatigued dogbone sample. The variation in the fundamental amplitude is caused by different electromagnetic coupling conditions. Current and voltage variation are measured to asses to variation of lift-off distance. The current amplitude variation was less than 2%.

The evolution of the harmonic amplitudes with propagation distance is analysed using a STFT with Hanning window of 20 μs length. The acquired amplitudes are used to calculate the relative nonlinear ultrasonic parameters β_2 and β_3. The second harmonic nonlinear parameter starts to decline with propagation distance and then increases again. Therefore, the measured second harmonic amplitude is not generated from the material nonlinearity, but is a result of combined system nonlinearities. Conversely, the third harmonic nonlinear parameter shows a linear increase with propagation distance, as predicted by NLU theory. The propagation distance is calculated from the elapsed time since the end of the excitation toneburst and the measured shear wave velocity - 3210 m/s. The linear relationship of the third harmonic nonlinear parameter is disturbed by side and edge walls reflected shear waves travelling inside the sample. Therefore, the values for β_3 were extracted from the initial 200 mm of wave propagation, using a linear fitting algorithm.

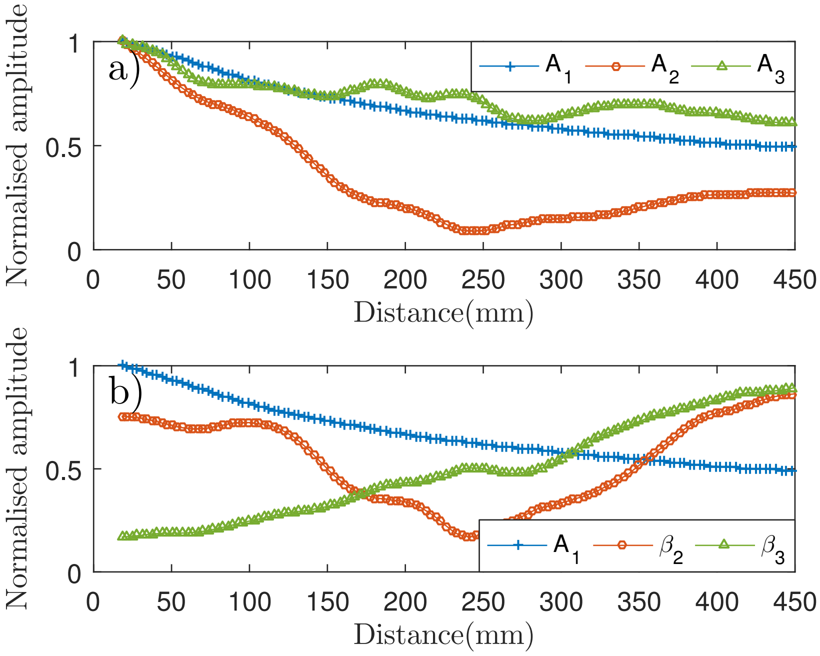

Figure 7.25: Fundamental A_1, second A_2 and third harmonic A_3 amplitudes as a function of propagation distance (a). Nonlinear ultrasonic parameters for the second β_2 and third harmonic β_3 as a function of propagation distance (b). The values are extracted from the NRUS signal using STFT (20 μs Hanning window). All time-series are normalised to their maximum values.

The third harmonic nonlinear parameter values were acquired for 20 different locations at all fatigue stages of the sample. For each position the β_3 values were normalised to the initial value for that location - β_3^n. Then, the β_3^f for each fatigue stage was calculated as the average from all the β_3^n values along the specimen's gauge length. The standard error of the β_3^f values - σ_β is calculated to show the parameter variation from the materials properties at different measurement locations.

The cumulative fatigue nonlinear parameter, β_3^f, shows no significant change until the failure damage occurs - 100%. The final stage of the tensile fatigue cycling is interrupted at 2% elongation, before significant plastic deformation has occurred. A visible crack with opening of 150 μm and length of 3 mm is located 35 mm away from the centre of the gauge length. Measurements at this location are comparable with the average values of the β_3^f.

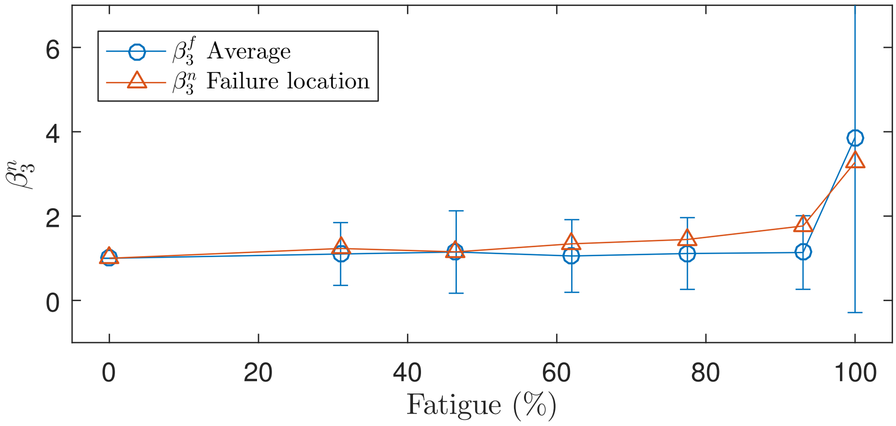

Figure 7.26: The third harmonic shear nonlinear parameter as a function of the fatigue life.

The values of β_3^n at the failure location do have an upward trend towards the final stages of the fatigue life. However, the failure location values are within the error range of the average β_3^n. Therefore, the results from the third harmonic NRUS can not be used to conclusively measure or predict the damage state of the sample as the β_3^f values show large variation. Further reductions in the system nonlinearity will allow for more precise measurements of the nonlinear parameter. This will allow for the evaluation of the local material properties variation contribution to the nonlinear parameter. Additionally a supplementary microstructural damage state evaluation using a different measurement technique can be used to measure the variation of TOEC within the specimen. Thus, providing more detailed insight in the relation between the third harmonic parameter and the microstructural defects. This will allow one to verify whether higher harmonic nonlinear measurements have the potential to measure changes in the third order elastic constants and the material microstructural damage state.

7.4 Conclusions

The simulated displacement profiles of a shear wave polarised racetrack EMAT are in good agreement with the experimentally measured results. Experimentally measured nonlinear parameters using a shear wave EMAT have shown no significant change in the nonlinear parameter during the fatigue life-cycle of an aluminium sample alloy (Al6061). Third harmonic shear wave nonlinear parameters have been measured using a through thickness resonance method. No significant change in the third harmonic nonlinear parameter is observed during the fatigue lifetime of an aluminium alloy sample.

Measurements of the nonclassical nonlinear parameter of aluminium show strong temperature dependence and no significant change with fatigue damage. Experiments employing the NRUS technique and EMAT generation must include measurements of the sample temperature or use temperature compensation methods, as Joule heating from the generated eddy currents occurs in the specimen.

The temperature dependence of the resonance mode frequency was investigated. The coefficient of thermal expansion (CTE) were found to change with fatigue. Measurements of the temperature variation of ultrasonic velocity throughout the fatigue lifecycle can reveal changes to the third order elastic constants [174; 175]. Due to the non-contact electromechanical coupling, EMATs can be used to make practical measurements of the variation of the ultrasonic parameters with temperature.

Chapter 8

Experimental development: Guided waves

8.1 Rayleigh waves

Rayleigh wave experiments were carried out to evaluate EMATs as generators and detectors of nonlinear ultrasonic waves. Surface wave nonlinear techniques use measurements of the second harmonic component to evaluate the nonlinear parameter. A quasi-Rayleigh wave regime was chosen to reduce the dispersion effects [132]. Meanderline coils for multiple wavelengths were wound using 0.15 mm copper wire. Additionally, printed circuit board (PCB) coils were manufactured for the high frequency 4.5 MHz EMAT receivers.

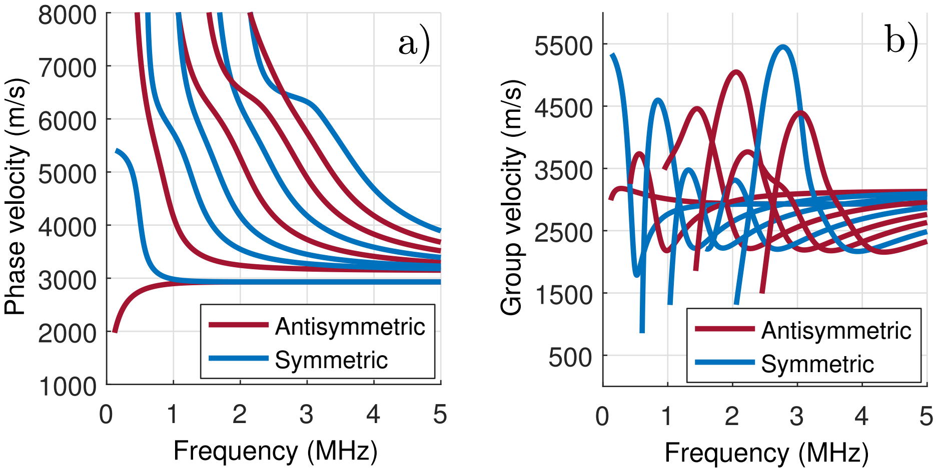

Figure 8.1: Dispersion curves for Lamb-Rayleigh wave in a 4.76 mm thick aluminium plate (Al6061) - symmetric Lamb wave modes (blue) and antisymmetric Lamb wave modes (red).

Ultrasonic measurements were performed on aluminium plate with dimensions 300 mm × 300 mm and thickness 4.76 mm. For this thickness, the Rayleigh wave regime is established for frequencies higher than 2 MHz and has wave velocity of 2920 m/s. EMAT transducers were designed at the selected fundamental frequency of 2.25 MHz and second harmonic frequency of 4.5 MHz.

8.1.1 EMAT self-field generation

Measurements of the ultrasonic waves generated by the self-field force of a meanderline EMAT were performed. The results are used to evaluate the second harmonic component generated from the transduction process of the Rayleigh wave EMAT. Meanderline coils were wound for generation at 500 kHz and detection at 1 MHz. A thick aluminium block (80 mm) was used to ensure generation of only surface waves. The transmitting and receiving EMATs had dimensions 20 mm × 40 mm and were positioned 50 cm apart, measured from the coil's centres. Permanent $NdFeB$ magnets were used to generate an out of plane magnetic field. A 20 cycle high amplitude toneburst signal at 500 kHz was used to generate ultrasonic waves.

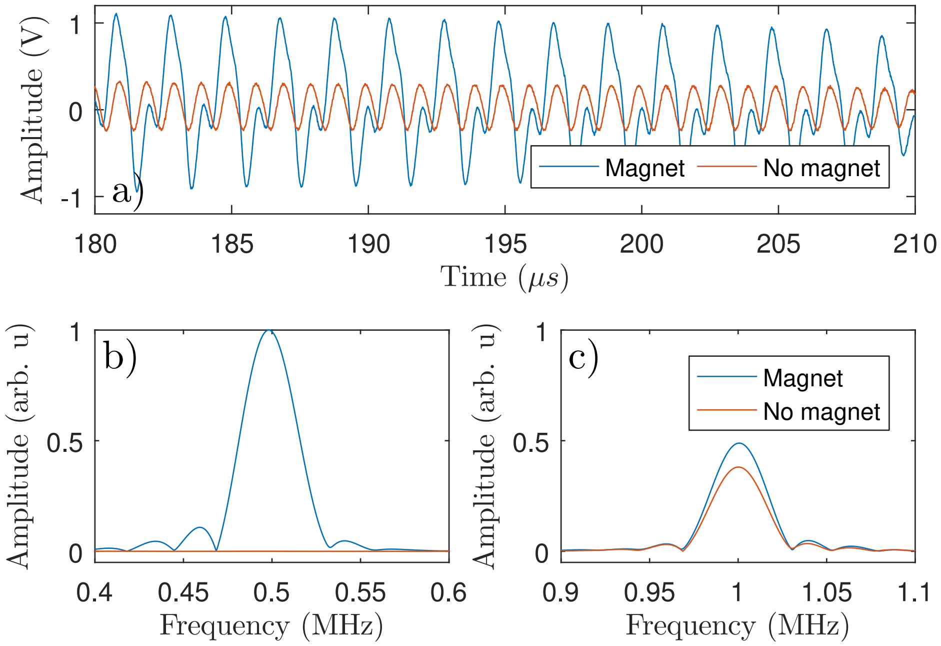

Figure 8.2: Rayleigh wave measurements of wave generated by EMAT with and without permanent magnet, (a). The no-magnet configuration generates no ultrasonic wave at the fundamental frequency - 0.5 MHz, (b). However, the second harmonic component, (c), generated by the self-field force has a large contribution to the total nonlinearity generation.

Measurements were taken for two configurations of the transmitting meanderline coil: with and without a magnet. The ultrasonic wave, generated by the latter, are only due to the dynamic magnetic field Lorentz force. The receiving coil is designed for optimal reception of second harmonics, therefore the measured fundamental wave amplitude is severely reduced. The second harmonic component generated by the dynamic field Lorentz force contributes significantly to the total measured nonlinear signal. The removal of the magnet causes variations in the impedance of the generating meander line coil which affects the measured amplitudes. The ultrasonic transmission mechanism of meanderline EMATs generates second harmonic ultrasonic waves with significant amplitude. Therefore, measurements of nonlinear surface waves conducted using EMAT generation must compensate for the transmission nonlinearity. Additionally the amplitude of the ultrasonic wave generated by EMATs is two orders of magnitude smaller than the one generated by piezoelectric sensors (see Fig. 8.5).

8.1.2 Piezoelectric wedge generation

An angled wedge transducer was used to generate high amplitude Rayleigh waves. A custom design wedge was made out of polyether ether ketone (PEEK). Ultrasonic measurements of the longitudinal velocity were taken, giving $V_L = 2550$ m/s. The wedge angle of 61° was calculated, for generation of Rayleigh waves in aluminium, using Snell's law. A piezoelectric transducer with diameter of 10 mm and centre frequency of 2.25 MHz is coupled and fixed to the wedge. The transducer's position on the angled face was selected such that the projected ultrasonic wave path is aligned with the wedge corner as seen in Fig. 8.3. A high power $50\,\Omega$ resistive load was connected in series to the gated amplifier output to reduce the distortion of the driving signal from the high impedance load of the piezoelectric transducer.

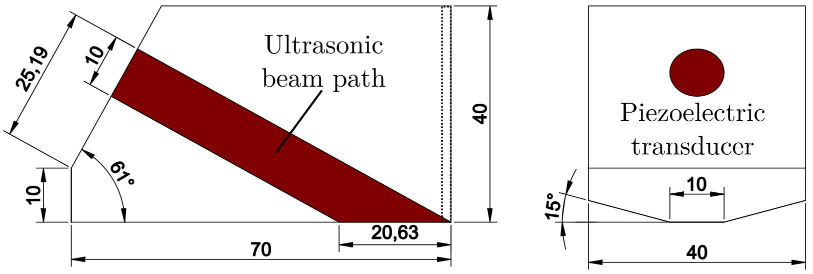

Figure 8.3: Angled wedge for Rayleigh wave generation in aluminium - side and back view. All sizes in millimetres (mm).

A double coil EMAT transducer was built for the reception of Rayleigh waves at 2.25 MHz and 4.5 MHz. The schematic diagram for the transducer can be seen in Fig. 8.4. A meanderline coil with spacing of 0.65 mm was wound by hand with six fingers and three turns using copper wire with diameter 0.15 mm. The coil is used for both generation and detection of fundamental ultrasonic waves at 2.25 MHz. A PCB meanderline coil with spacing of 0.32 mm was manufactured, with conducting copper tracks of width 0.16 mm and thickness $0.35\,\mu m$. The coil has 30 fingers and only a single turn of conducting track and designed centre frequency of 4.56 MHz. The PCB coil design is manufactured at the limit of the conventional technology, and any higher frequency EMATs require custom PCB production. The 4.5 MHz high frequency coil was used as a receiver of the second harmonic component of the nonlinear Rayleigh waves. Two EMAT transducers were built, one with dual coil configuration and one with high frequency coil only. Both transducers use $NdFeB$ permanent magnets with dimensions 25 mm × 25 mm × 12 mm to provide static out of plane magnetic field. The coils are positioned at the front of the transducers, to enhance the signal amplitude due to the magnetic field edge effects [108].

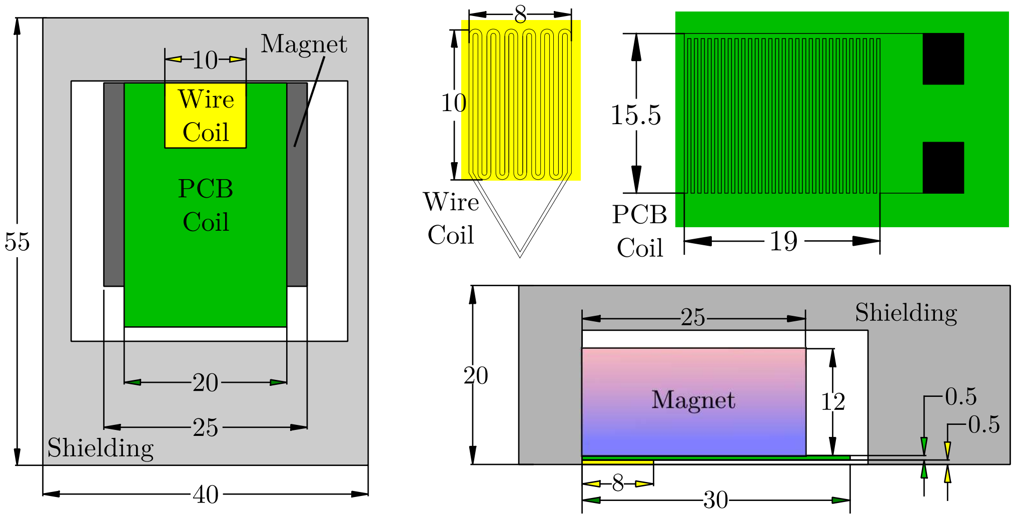

Figure 8.4: EMAT transducer design for Rayleigh wave generation and detection. Two meanderline coils, with spacing corresponding to Rayleigh waves with frequencies 2.25 MHz and 4.5 MHz for aluminium, are placed below a $NdFeB$ magnet. All sizes in millimetres (mm).

To compare the amplitudes of out of plane displacement generated by meanderline coil EMAT and the piezoelectric wedge transducer, a laser interferometer was used (Polytec OFV-5000 with sensor head sensor OFV534). The two ultrasonic transmitters were positioned 100 mm away from the measurement point of the laser interferometer. The absolute amplitude of the ultrasonic displacement was measured for multiple excitation levels for both transducers. The results from the measurements are presented in Fig. 8.5. The piezoelectric sensor showed nonlinear behaviour of the fundamental amplitude for driving voltages above $200V$. The magnitude of the Rayleigh wave generated by the EMAT transducer is only 2 % of the magnitude generated by the piezoelectric transducer. The generated second harmonic from such a small amplitude would be insignificant compared with the electrical noise and the system nonlinearity. The generation of higher amplitude ultrasonic waves, using meanderline EMATs, is limited by their transduction efficiency. Significant improvement in the generated ultrasonic wave amplitude is required, if EMATs are to be used as ultrasonic transmitters for nonlinear Rayleigh wave measurements.

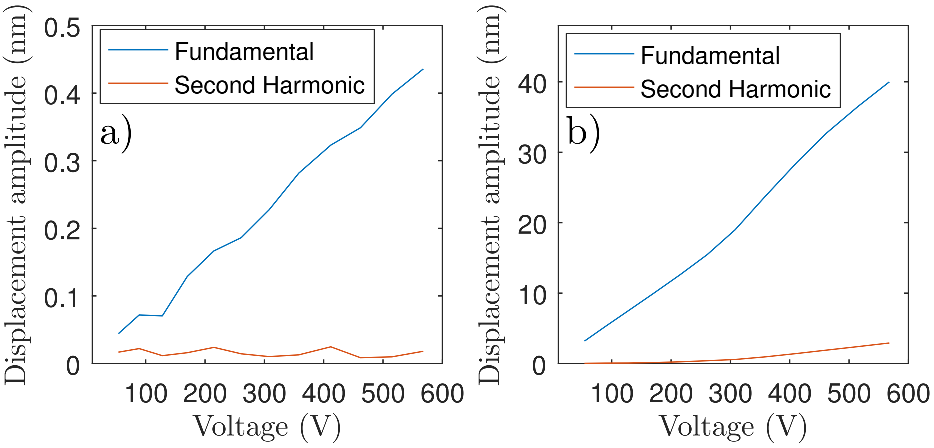

Figure 8.5: Amplitude of the out of plane displacement for ultrasonic waves generated by EMAT, (a), and piezoelectric transducer, (b).

All of the following experimental measurements use the piezoelectric transducer as the source of high amplitude ultrasonic waves. Vibrometer measurements were used to measure the variation of the ultrasonic signal amplitude with regards to the excitation frequency and the number of cycles in the generation toneburst, see Fig. 8.6 for results. The maximum of the signal amplitude increases with the number of cycles up to 15 cycles per toneburst and plateaus after that. The piezoelectric transducer has centre frequency of 2.25 MHz and FWHM of 0.7 MHz for 20 cycles toneburst excitation.

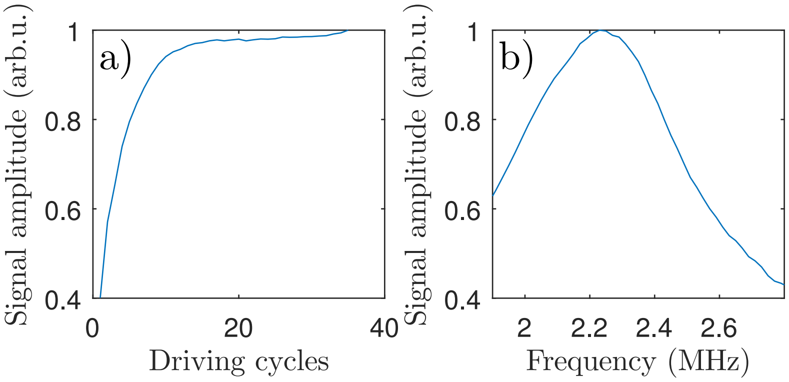

Figure 8.6: Signal amplitude variation with number of cycles in the generation toneburst signal, (a), and the generation frequency, (b), for a piezoelectric wedge transducer.

The high frequency EMAT coil has been used as a receiver for the second harmonic component of the nonlinear Rayleigh waves. The coil was matched to the impedance of the receiver using a capacitor network for the frequency of the second harmonic signal at 4.5 MHz. Nevertheless, the received signal is still dominated by the fundamental wave, as the amplitude of the fundamental ultrasonic wave is at least two orders of magnitude larger than that of the second harmonic. In addition, the first finger of the meanderline coil acts as a line receiver with wide bandwidth.

The geometry of the receiving coil affects the measured acoustic amplitude. To evaluate the effect, a simulation of the ultrasonic field generated by a 10 mm wide ideal line source was carried out for two different driving frequencies: 2.25 MHz and 4.5 MHz. Huygens' principle was used to model the acoustic field pattern. The spatial impulse response for three types of receivers was analysed and results are shown in Fig. 8.7: point (laser interferometer), line (linear EMAT coil) and rectangle reception (meanderline EMAT). The divergence of the ultrasonic beam causes phase differences between different receiver segments, therefore, reducing the received signal amplitudes. Additionally the diffraction pattern can strongly affect the amplitude of the ultrasonic waves as they propagate longer distances. A clear model of the expected diffraction pattern of the ultrasonic source is required to distinguish between the second harmonic ultrasonic waves generated by the transmitting transducer and the material generated nonlinearity.

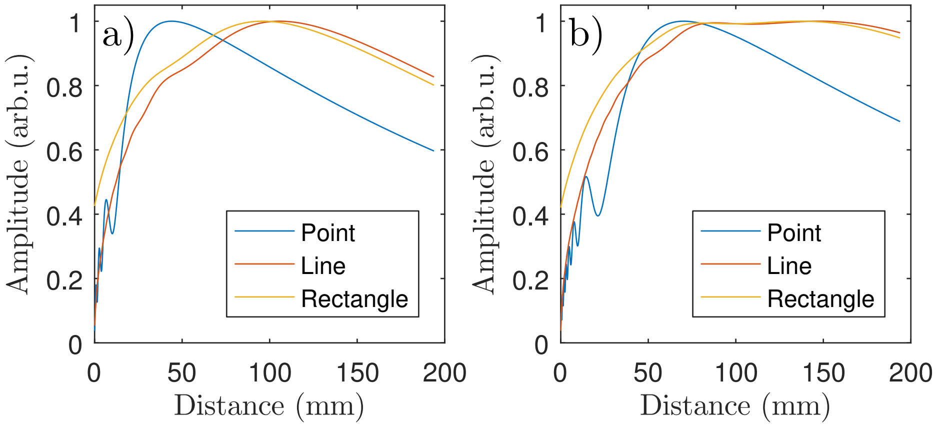

Figure 8.7: Spatial impulse response of different receiver geometries for fundamental (a) and second harmonic (b), generated by an ideal line source. Line receiver has width of 15 mm and the rectangular receiver has width 15 mm and length 20 mm.

Measurements of the nonlinear Rayleigh parameter were conducted on a large aluminium plate 300 mm × 300 mm × 4.76 mm. Due to the limit of the fatigue machine the fatigued dogbone sample's cross section was limited to 80 mm^2. For the selected transducer combination a minimum thickness of $3 \times \lambda = 3.9$ mm is recommended to ensure that one is in the Rayleigh wave regime. This limits the gauge width of the fatigued samples to 20 mm. For a wave propagating along the gauge length, ultrasonic interference is expected from the edge reflections. Therefore, measurements for the nonlinear Rayleigh parameter were only conducted on a large aluminium plate. The piezoelectric wedge transducer was coupled to the sample using light oil (WD-40) and a constant load force was applied (5 N) to ensure good contact at both piezoelectric transducer-wedge and wedge-sample interfaces. The dual EMAT coil was attached to a XY gantry positioning arm. The coil lift-off was minimised, while still maintaining no contact with the surface, and maintained constant across the measurement space. The excitation signal was a toneburst of 20 cycles at 2.25 MHz. Measurement of the fundamental and second harmonic ultrasonic waves were taken at different excitation amplitudes and distances (see section 9.1). Pulse-inversion technique was used to confirm the source of the nonlinear signal.

8.2 Shear horizontal waves

Nonlinear ultrasonic experiments using shear horizontal waves were conducted by Lissenden [111] using contact magnetostriction patch transducers. To the authors knowledge, no other experimental results have been reported for third harmonic generation using shear waves. The performance of PPM SH EMATs for nonlinear ultrasonic measurements have not been studied in depth [136].

The effects of the magnetic field spatial distribution on the transduction frequency spectrum were simulated using a FEM software (COMSOL). Multiple transducer parameters were studied: magnet height, magnet width, magnet filling ratio (MFR), magnet lift-off and number of magnet columns, see Fig 8.8 for diagram. The aim was to minimise the generation of third harmonic components. The lift-off and MFR are expected to have the greatest impact on the harmonic distortion. The results from [16; 205; 218] suggest that the spatial impulse response can be used to filter the transduction of higher harmonics.

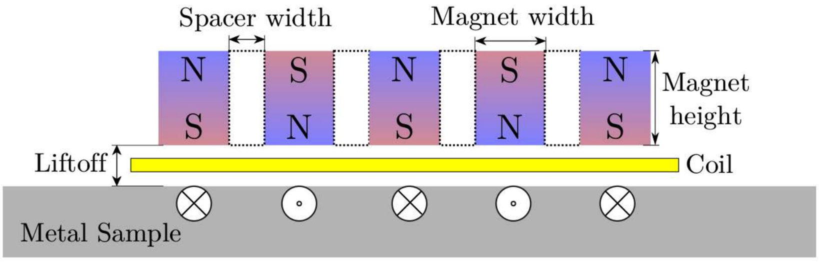

Figure 8.8: SH PPM EMAT structure.

PPM EMAT transducers were built using the optimised parameters from the simulations. The transmission EMAT was designed to reduce the generation of third harmonic components, while the receiving PPM EMAT was optimised for third harmonic reception.

The shear horizontal wave wavelength is limited by the magnet size of the reception EMAT a magnet width of 3 mm. Therefore, a receiver EMAT of wavelength 6 mm and a transmitter with wavelength pitch of 18 mm were built. The generation EMAT was constructed using plastic spacers with width of 3 mm, while the reception EMAT used no spacers. The design of the PPM EMATs can be seen in Fig 8.9. Two racetrack coils are wound with copper wire diameters of 0.3 mm and 0.15 mm for transmission and reception respectively. The width of the coils was chosen to reduce the angular divergence of the ultrasonic beam [117], while having the lowest impedance value.

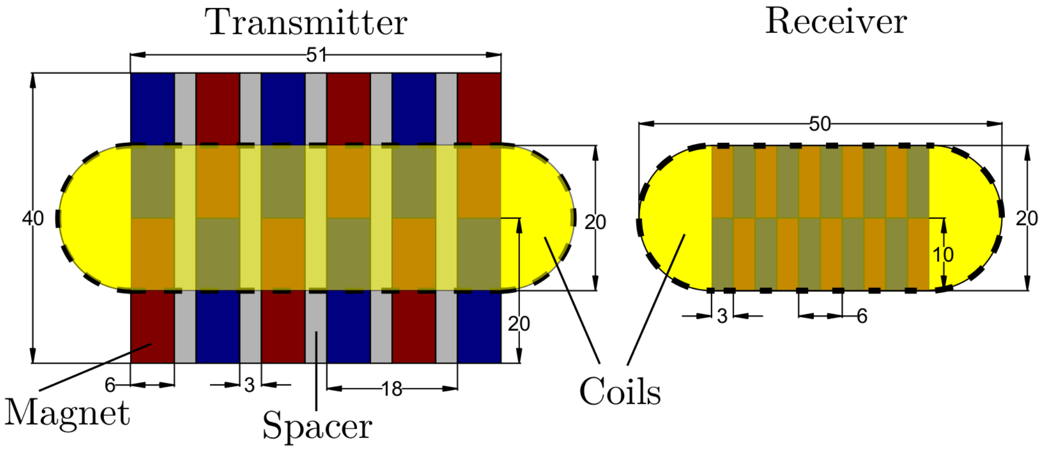

Figure 8.9: Designs of the transmitting and receiving SH PPM EMATs for third harmonic measurements. The ratio between the wavelengths of the transducers is 3:1. Transmitter height is 6 mm and the receiver height is 10 mm.

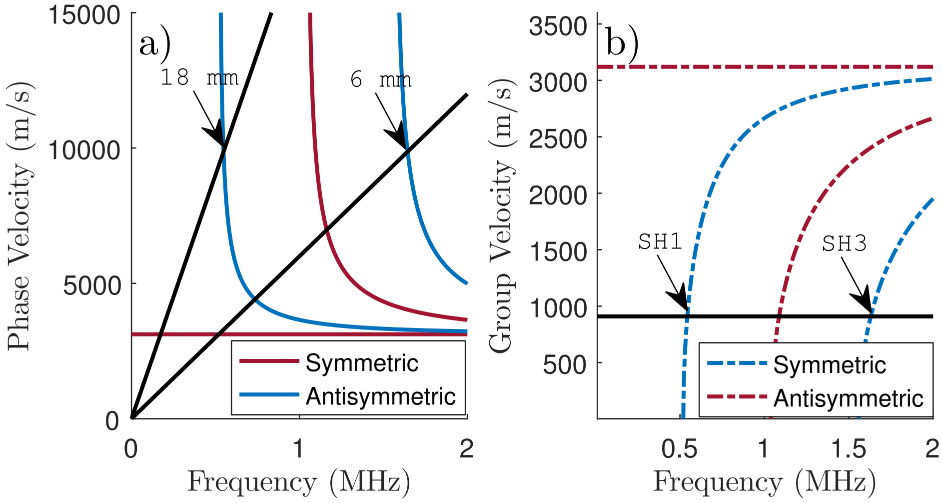

Figure 8.10: Shear horizontal wave dispersion curves for 3 mm aluminium. The lines correspond to wavelengths of 18 mm and 6 mm.

Dispersion curves for the shear horizontal waves in 3 mm aluminium were calculated [171] and are shown in Fig. 8.10. For an 18 mm wavelength transducer, the frequency of the SH1 mode and SH3 mode are respectively 541 kHz and 1.63 MHz. Toneburst signal of 25 cycles at a frequency of 0.54 MHz was used to generate SH1 fundamental waves. A high-pass filter, with cut off frequency of 1.2 MHz, was used to suppress the amplitude of the fundamental wave in the received signal. A Hanning window with length of 50 μs was used to extract the harmonic amplitude and frequency of the received signals. The number of averages used was 64, to improve the signal to noise ratio.

Measurements of the third harmonic component were taken as a function of excitation level and distance from the transmitter. The generation EMAT was fixed to the sample, while the receiving EMAT was attached to the movable arm of a gantry XY table. The transducers were aligned and the receiver lift-off was maintained using a feeler gauge.

8.3 Summary

Experimental configurations for nonlinear guided wave EMAT measurements were designed and characterized for second harmonic Rayleigh waves and third harmonic shear horizontal waves.

A strong generation of artificial second harmonic component was observed for the meanderline Rayleigh wave EMAT transmitter. Due to the self-field force wave generation and the periodicity of the meanderline EMAT, the supplementary generated waves mimics the second harmonic waves generated from the material nonlinearity. To reduce the complexity of the measurement, a piezoelectric wedge transducer was used to generate high amplitude Rayleigh waves, while a dual-coil meanderline EMAT receiver was used to measure the amplitudes of the fundamental and second harmonic components. The diffraction pattern for different EMAT configurations was simulated to distinguish between contributions from the source nonlinearity and the material nonlinearity.

A pair of PPM shear horizontal wave EMAT transducers were prepared with respect to the limitations and availability of small sized magnets. The transmitter-receiver pair were designed for optimal measurements of the third harmonic component of a shear horizontal wave. COMSOL models were generated to study the effect of different transducer parameter on the source nonlinearity.

Chapter 9

Nonlinear ultrasonics using guided waves

9.1 Rayleigh wave

The amplitude of the generated second harmonic Rayleigh waves was measured using a pulse-inversion method [98]. The technique is very efficient in the reduction of the fundamental wave dominance and the extraction of the second-harmonic amplitude, see Fig. 9.1. Two consecutive out-of-phase signals, generated by an AFG, were fed to the generating amplifier.

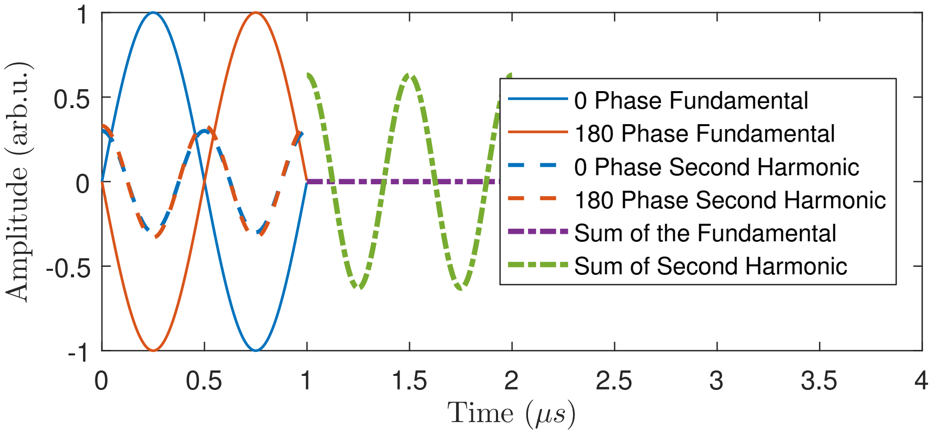

Figure 9.1: Pulse-inversion method signal sketch. The two out-of-phase fundamental waves cancel each other, while the second harmonic contributions are summed. This is a result of the phase offset of $\pi/2$ between the fundamental wave and the generated second harmonic waves from the material nonlinearity.

Consecutive measurements were taken without changing the experimental conditions and were combined in the time domain, without introducing any signal adjustments. The frequency spectra of the combined signals were used to extract the small amplitude second harmonic component. This technique does not reduce the second harmonic generation from the self-field force in meanderline EMAT coils. The phase offset, between the fundamental wave and the second harmonics, from the material nonlinearity, equals that from the electromagnetic coupling. Therefore, for EMAT Rayleigh wave generation the contributions from the two effects cannot be distinguished.

Experimental measurements of the nonlinear Rayleigh wave were taken using a single meanderline EMAT with a centre frequency of 4.5 MHz, while the ultrasonic waves are generated by an angled-wedge piezoelectric transducer, as presented in Fig. 9.2. The centre frequency of a meanderline EMAT is defined by the meanderline spacing and the Rayleigh wave ultrasonic velocity. The meanderline spacing defines the ultrasonic wavelength. The frequency of the generated ultrasonic wavelength is calculated from $f = c/\lambda$. Throughout this thesis, the meanderline coil spacing will be defined through their frequency of generation for aluminium Al(6061). For this material a Rayleigh wave velocity of 2920 m/s is measured, which agrees with the published literature.

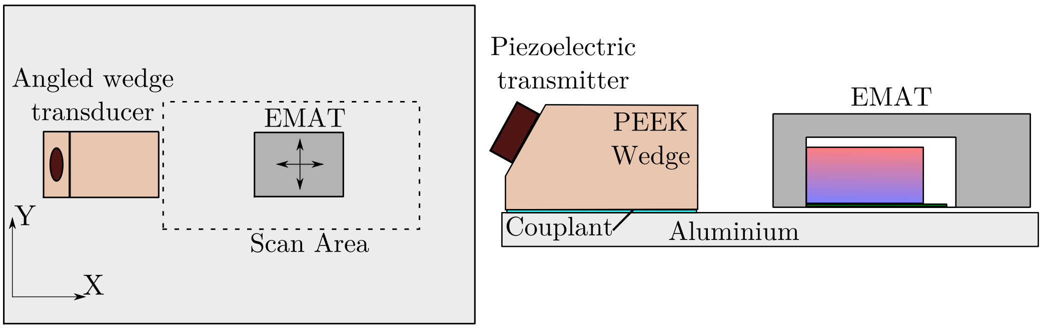

Figure 9.2: Schematic diagram of the Rayleigh wave nonlinear measurements. Piezoelectric angled wedge transducer is used to generate the ultrasonic waves, while a 4.5 MHz single coil EMAT is used as a receiver. The EMAT is attached to the moving arm of a gantry XY positioning system.

The excitation signal used for all the measurements is a 20 cycles toneburst at 2.25 MHz, with a total length of 8.8 μs . The receiver EMAT coil receives both fundamental and the second harmonic components, see Fig. 9.3. The fundamental signal is picked-up by the first and last copper tracks of the PCB meanderline coil, which act like individual line coils. The signal at the first PCB copper track is enhanced by the in-plane component of the magnetic field [108], as can be seen in Fig. 9.3. The fundamental wave signal response has a rectangular shape, with the measured signal from the first copper track starting at 35 μs and ending at approximately 44 μs and the signal from the last copper track starting at approximately 42 μs and ending at 50 μs. This matches the expected propagation time for the length of the PCB Rayleigh track ≈ 7 μs. The overlapping portion of the signal will have a reduced amplitude of the fundamental component due to the phase mismatch of the two signals. The second harmonic component amplitude has a bell curve shape. The peak of the bell curve is located at the time of arrival of the ultrasonic wave under the middle point of the meanderline coil. This bell curve shape is expected for a meanderline EMAT reception, as different portions of ultrasonic wave package propagate under the meanderline coil.

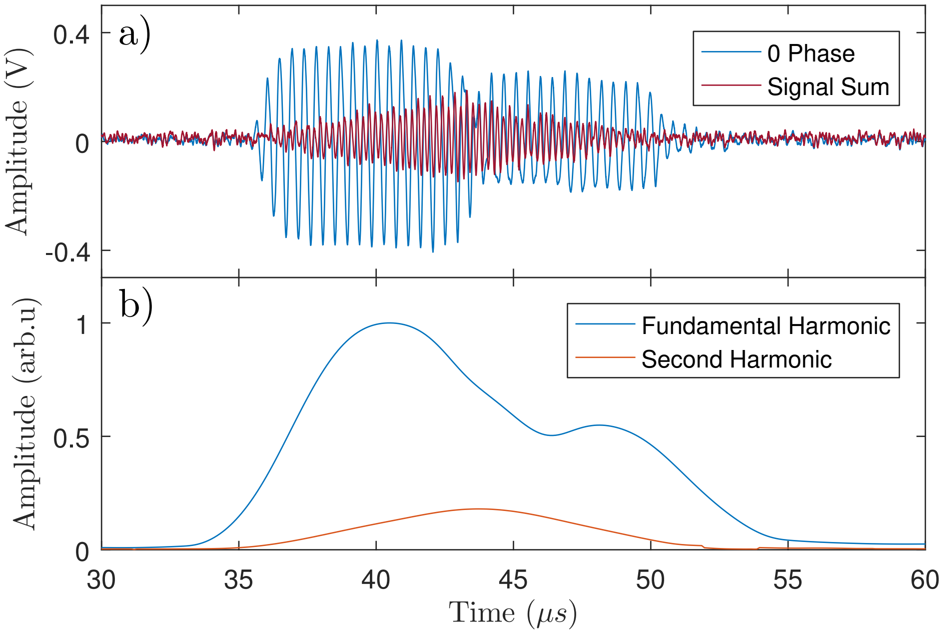

Figure 9.3: Typical nonlinear Rayleigh wave signal of aluminium plate (Al6061) measured using a single EMAT coil. Signals are shown, (a), for the 0° phase (blue) and the sum of the received signals for the opposite phases (red). The 180° phase signal is omitted for clarity. Time evolution of the harmonic amplitudes, extracted by STFT with 8 μs window length, (b) - fundamental harmonic amplitude, (blue), from the 0° phase signal, and the second harmonic amplitude, (red), from the summed signals.

The fundamental and second harmonic amplitudes, in figure Fig. 9.3, are extracted from the ultrasonic signal using STFT with a window length of 8 μs. For each measured ultrasonic signal, the values for each of the harmonic amplitudes are obtained from the maximum value of the STFT amplitude for that particular harmonic component.

The use of a dual-coil EMAT as a receiving transducer is tested. The combined EMAT have a worse lift-off performance for the second harmonic 4.5 MHz PCB coil, regardless of the coil order, while the fundamental wave coil 2.25 MHz has a strong signal response regardless of the lift-off. Therefore, the single coil EMAT configuration was used as it addresses the main challenge - measuring the small amplitude second harmonic component. The high number of meanderline fingers in the PCB coil narrows the bandwidth of the EMAT coil. The single coil EMAT can be used to measure the high amplitude fundamental component of the ultrasonic wave A_1 and the small amplitude of the second harmonics A_2. As the ratio between the components $A_2/A_1 \approx 0.2$ is relatively high, the pulse inversion technique is not required to acquire the values of both harmonic components.

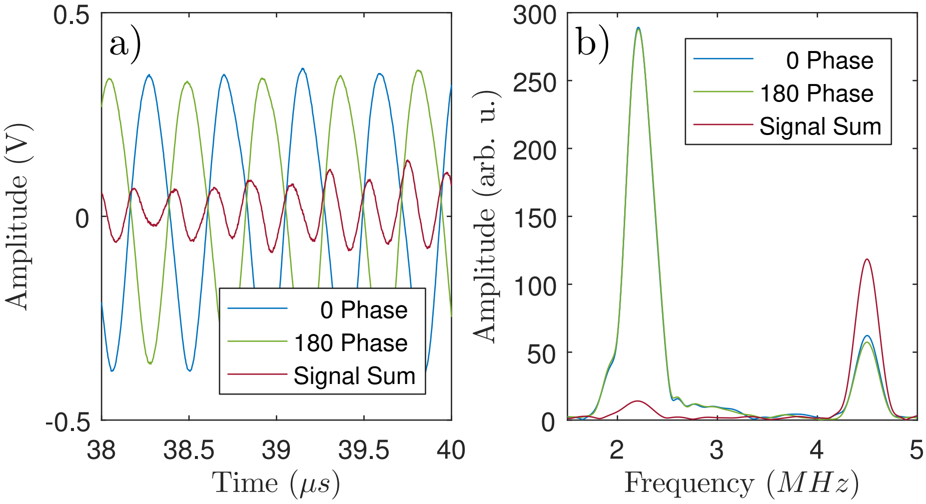

Figure 9.4: Pulse inversion measurements of nonlinear Rayleigh waves, generated by an angled-wedge piezoelectric transducer and measured with single high frequency meanderline EMAT coil. The measured signals, (a), and the frequency spectra, (b), the initial and combined signals.

The relationship between the nonlinear Rayleigh parameter and the excitation voltage amplitude was studied. A 50 Ω high power resistor was connected before the piezoelectric transducer to reduce any distortion in the excitation current signal. The highest excitation level was limited by the heat dissipation of the piezoelectric transducer, as well as the piezoelectric material nonlinearity for driving voltages higher than 200 V.

For the lower level of the driving voltage amplitudes, the generated ultrasonic amplitude of the second harmonic is close to the noise floor. For those excitation levels, large variations in the β_R parameter are expected as the contributions from the material nonlinearity are negligible, compared to the noise floor values. Therefore, the nonlinear Rayleigh wave parameter β_R is expected to converge to its real value as the driving voltage increases.

$$\tilde{\beta}_R = \frac{8iA_2^z}{k_l^2 x (A_1^z)^2} \frac{p}{k_R} \left(1 - \frac{2k_R^2}{k_R^2 + s^2}\right) \propto \frac{A_2}{xA_1^2} \tag{9.1}$$

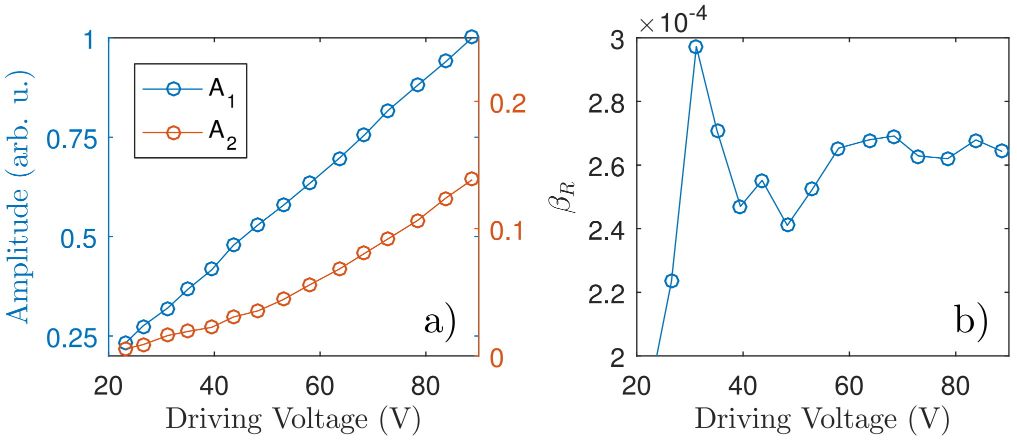

Figure 9.5: Nonlinear Rayleigh wave parameter β_R as a function of excitation amplitude level, (a). The β_R parameter converges to its real value for higher levels of excitation, (b).

The relationship between the fundamental and second harmonic amplitudes as a function of excitation level agrees with the NLU theory. The harmonic amplitude content was measured at a propagation distance of 65 mm to reduce the effect of the system nonlinearity. All distances were calculated from the centre point of the ultrasonic footprint of the angled wedge to the centre point of the PCB coil. It is important to note that the fundamental wave amplitudes were measured at the first line of the meanderline coil. Therefore, their propagation distance was 9.5 mm shorter than the propagation distance for the second harmonic waves. This is considered and corrected for in all of the experimental measurements.

The amplitudes of the fundamental and the second harmonic waves were measured in the XY plane in front of the wedge transducer to evaluate the ultrasonic beam divergence. The schematic of the experimental configuration is drawn in figure Fig. 9.2. The excitation toneburst signal of 20 cycles at a frequency of 2.25 MHz, generates the fundamental ultrasonic Rayleigh wave, while the second harmonic component is the cumulative results of the nonlinearity contributions from the source, the wedge material, the couplant and the aluminium sample.

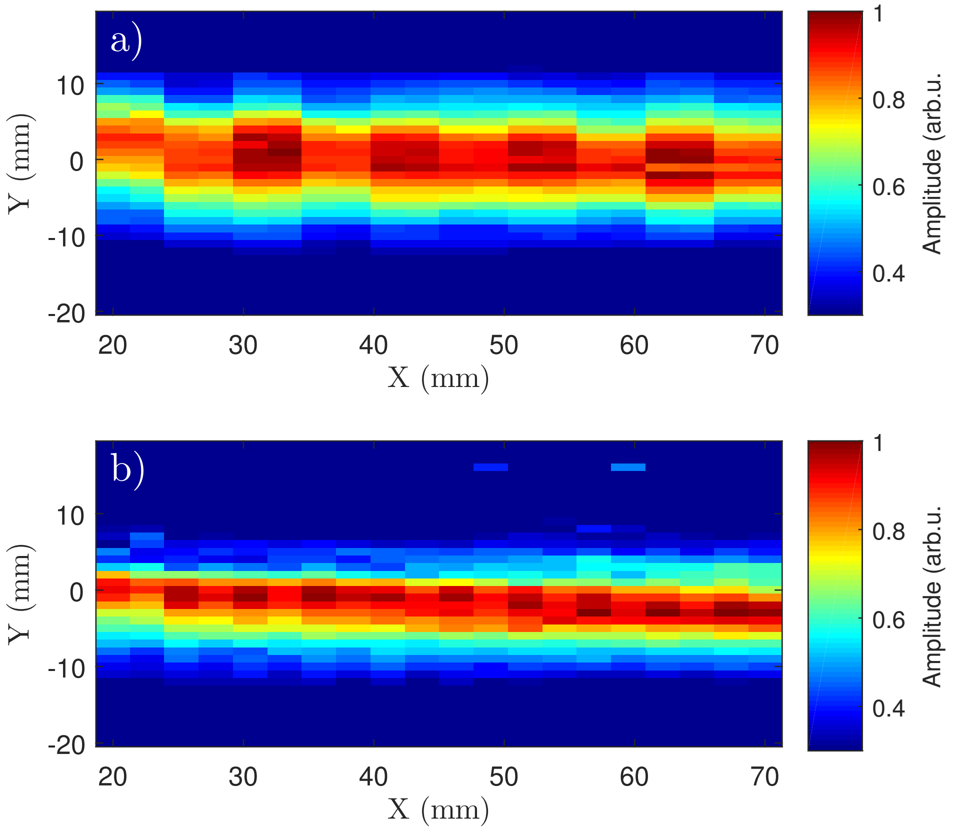

Figure 9.6: Fundamental, (a), and second harmonic wave, (b), beam divergence for angled wedge transmitter and meanderline EMAT receiver.

The high number of fingers and the overall area of the meanderline PCB coil increases the directivity of the EMAT receiver and reduces the effects of the source diffraction. However, the ultrasonic beam for the fundamental harmonic component is wider than that of the second harmonic wave, as the signal is received by only the first PCB track line of copper.

The diffraction corrections for the fundamental and second harmonic components for a wedge-transducer and a meanderline EMAT receiver can be approximated to a model similar to that in Zhang [222]. A simple model using Huygens' principle is used to assess the effect of the receiver's finite size on the diffraction pattern (see figure 8.7). The diffraction model for a line receiver is in good agreement with the measured fundamental wave amplitude. While, the diffraction model for a meanderline coil does not explain the increase of the second harmonic amplitude for the propagation distance range of 100 - 150 mm. The second harmonic generated by the system nonlinearities (from the piezoelectric transducer, the angled wedge and the contact transfer function) has a finite amplitude, which decays with propagation distance. However, the material nonlinearity contribution to the second harmonic generation is expected to increase with propagation distance. The measured SHG is a result from the cumulative contributions from the source and the material nonlinearities.

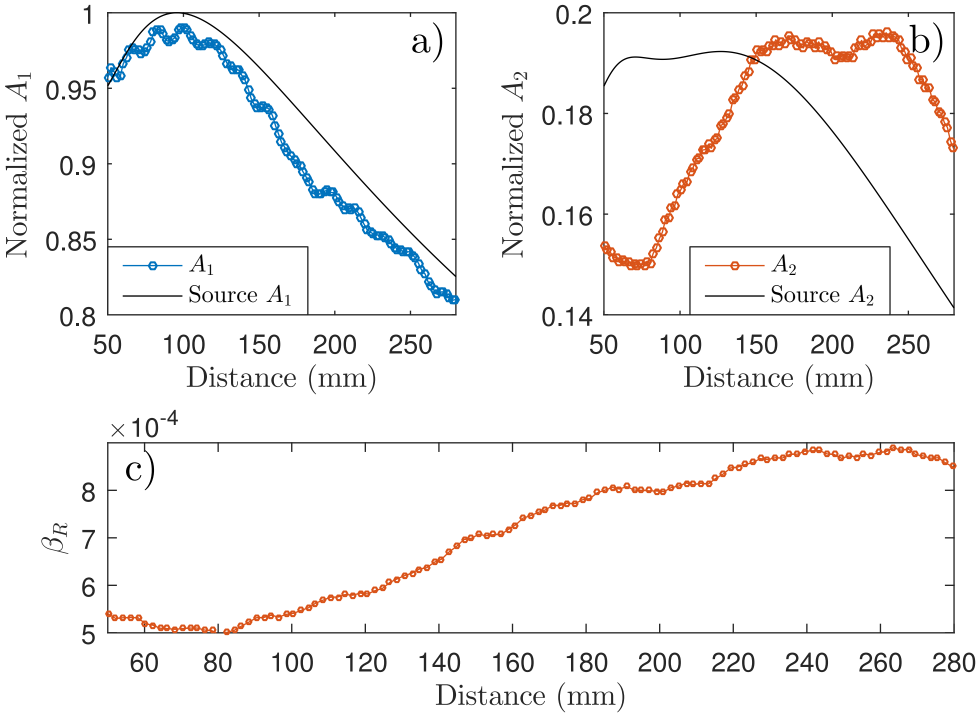

Figure 9.7: Nonlinear Rayleigh wave measurements of the fundamental, (a), second harmonic amplitudes, (b), and the calculated nonlinear Rayleigh wave parameter, (c), as a function of propagation distance. The measured fundamental amplitude blue, (a), match closely the simulated, linear Huygens principle, diffraction model results (black), while the second harmonic (red), (b), shows significant difference from the simulated linear model results (black).

The increase in the second harmonic amplitude from the material nonlinearity can be observed for propagation distances from 100 to 150 mm, where the source nonlinearity diffraction corrections have approximately constant values. With longer propagation distances, the source nonlinearity contributions start to decrease. This effect opposes the SHG from the material nonlinearity, resulting in a flat A_2 amplitude response from 150 to 250 mm. As the ultrasonic wave propagates further across the material ,from 250 mm upwards, the second harmonic generation is reduced by the effects of attenuation and the decrease in the fundamental wave amplitude. This leads to a decay in the total second harmonic amplitude.

The relative nonlinear Rayleigh wave parameter value should be independent of the propagation distance.

$$\beta_R \propto \frac{A_2}{A_1^2 x} \tag{9.2}$$

However, the corrections for the diffraction pattern of the source nonlinearity, can cause significant inaccuracies. The harmonic amplitudes from the range of increasing second harmonic component are used to calculate the nonlinear parameter. Furthermore, EMAT receivers cannot measure the absolute displacement amplitude of the ultrasonic waves. Therefore, the values of the β_R are relative and can only be used in comparison to other measurements using the same experimental configuration. The single meanderline coil EMAT design significantly reduces the experimentally measured fundamental wave amplitude, which causes a reduction in the nonlinear parameter (see equation 9.2). Additionally, calibration of the frequency response of the meanderline coil for the fundamental and second harmonic ultrasonic wave amplitudes can be used to scale the β_R parameter with regards to the actual fundamental wave amplitude. Consideration of the effect of lift-off on the receiver coil must be made, as the amplitude of the received signals decays exponentially with increased stand-off distance. During experimental measurements, constant lift-off, much smaller than the ultrasonic wavelength, must be maintained or compensation factors must be used in combination with high precision lift-off distance measurements.

9.2 Shear horizontal waves

Simulations were carried out in COMSOL to evaluate the influence of different PPM EMAT parameters on the spatial distribution of the magnetic field: magnet filling ratio (MFR), magnet lift-off, magnet height, magnet width and the number of magnet columns. The model assumes that the eddy currents generated from the linear segment of the racetrack coil, have a uniform distribution and the coil - sample stand-off is kept constant. Thus, the wavelength of the generated ultrasonic wave is defined only by the shape of the out-of-plane magnetic field. The simulations were constructed in 2D to reduce the complexity and the simulation time of the model. The generation of ultrasonic waves from the in-plane components of the magnetic field was neglected. Analysis of the directivity of PPM SH EMATs can be found in Ma [117]. Ma's study investigates the effects of inner and outer coil width, the magnet length (z-axis) and the number of magnets. Ma's study concludes that the directivity can be improved by building the EMAT with a larger outer coil width and smaller magnet width. Additionally, the amplitude of the generated signal can be improved by using a higher number of magnet columns.

The simulations are conducted in the following order: starting with MFR, then magnet lift-off, magnet height, magnet width and conclude with the number of magnet columns. The MFR and lift-off parameters are expected to have the largest effect on the harmonic content, while the magnet width and columns are expected to have a strong effect on the spatial bandwidth of the PPM EMAT. The outcome of the analysis of the simulated models is to optimise the PPM structure of the transmitting transducer for third harmonic, nonlinear wave measurements. The analysis will focus on: reducing the higher harmonic content of the generated ultrasonic wave, increasing the amplitude of the generated fundamental wave and narrowing the spatial bandwidth of the generated wavelengths. When building an SH PPM EMAT, these parameters are constrained by the practical limitations: minimum magnet width, maximum transducer size, etc. Therefore the optimal parameter values will be selected, in consideration of both the simulated results and the experimental constraints.

The initial parameters for the simulations are:

Fundamental wavelength	12 mm	Number of columns	8
Magnet filling ratio	2/3	Magnet height	5 mm
Magnet width	4 mm	Magnet lift-off	0.5 mm

The magnetic field is generated by a NdFeB permanent magnet with residual magnetization of 0.6 T. The out-of-plane component of the magnetic field at the aluminium specimen surface was recorded. The spatial distribution of the out-of-plane magnetic field was analysed using FFT. The amplitudes for the fundamental wavelength A_1 and the third harmonic wavelength A_3 were extracted from the wavenumber spectra (see figure 9.8). For the modelled ultrasonic wavelength, the wavenumbers of the fundamental wave and third harmonic are 0.083 mm^{-1} and 0.25 mm^{-1} respectively.

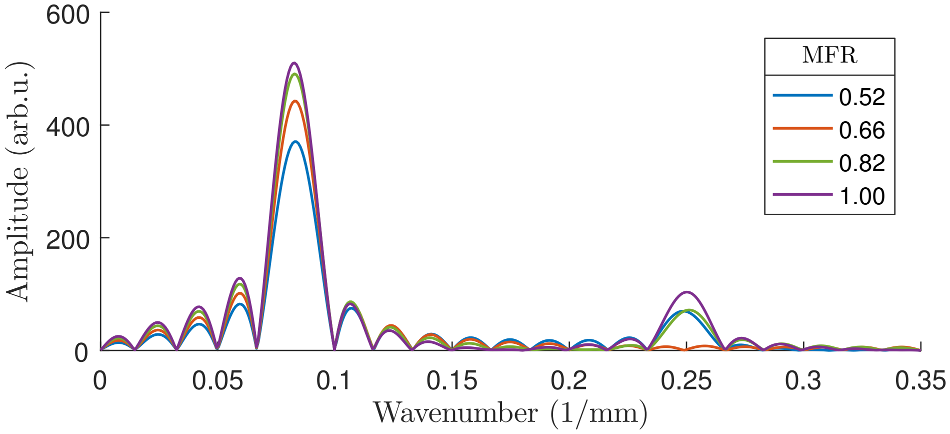

Figure 9.8: Wavenumber spectra for different MFR values.

The simulations are computed in consecutive order, setting the previously simulated parameters to their optimal value. MFR was the first parameter to be simulated as it is expected to have the largest impact on the third harmonic content.

The out-of-plane magnetic field curve significantly changes with MFR. The third harmonic to fundamental wavenumber ratio, A_3/A_1 is reduced from 0.2, for MFR of 100% PPM EMAT, to 6×10^{-4} for an MFR of 0.66 (see Fig. 9.9b). The magnet width, in this case, is 1/3 λ, while the spacer width is 1/6 λ. Hence, for the experimental measurements, the ratio between the magnet widths of the transmitter and receiver PPM EMATs is 2:1. The reduced magnet width is expected to reduce the amplitude of the fundamental wave. For MFR of 0.66, the fundamental wavenumber amplitude is reduced by 13%. MFR value of 0.66 is used for all the following simulation models.

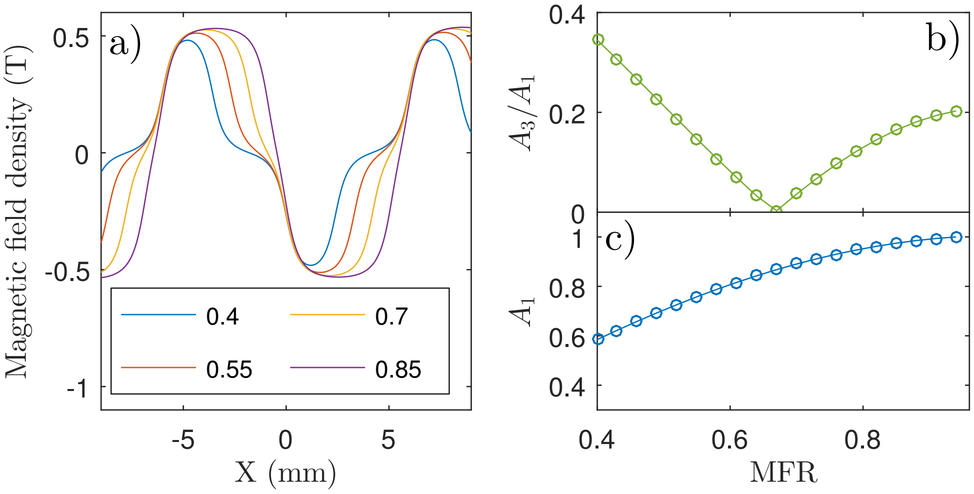

Figure 9.9: Out-of-plane magnetic field density, (a), at the surface of the specimen and ratio of the third harmonic content, (b), as a function of the MFR. The amplitude of the fundamental wavenumber content, (c), increase with increasing MFR. The minimum value for the A_3/A_1 is achieved at an MFR of 0.66.

The magnet lift-off has a strong effect on amplitude and directivity of the magnetic field (see Fig. 9.10b). The curve of the out-of-plane magnetic field component becomes less segmented as lift-off increases, which has a small effect on the wavenumber harmonic content. As lift-off distance increases, the amplitude of the fundamental wavenumber component decays exponentially. A lift-off value of 0.5 mm is chosen from practical considerations, as sufficient distance should be left for the racetrack coil and the air gap between the EMAT transducer and the sample surface.

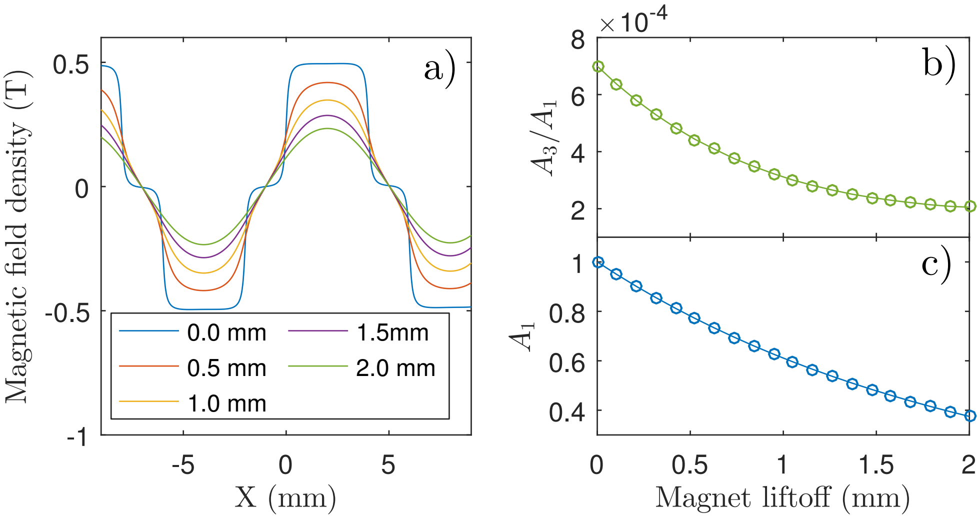

Figure 9.10: Out-of-plane magnetic field density, (a), at the surface of the specimen, the fundamental wavenumber content, (c), and the ratio of the third harmonic content, (b), as a function of the magnet lift-off. The values for the fundamental wavenumber amplitude, and the A_3/A_1 ratio, decay exponentially with lift-off distance.

The amplitude of the out-of-plane magnetic field density increases with the magnet height, see Fig. 9.11. The magnetic field maximum amplitude is expected to saturate as the magnet height becomes comparable to the magnet width, 4 mm. For bigger values of the magnet height, the magnetic field flux lines underneath the PPM magnet are predominantly closing through the bottom faces of the magnet array. Therefore, no significant improvement to the magnetic field amplitude is expected for larger values of the magnet height-to-width ratio, provided that the spacer width is kept constant. A magnet height of 5 mm is used for the rest of the simulations.

The shear horizontal ultrasonic wavelength is defined by the combined width of the spacer and the magnet. The total magnet area and the fundamental wavenumber amplitude increase with longer transducer wavelength, while keeping the other magnet parameters constant. A higher amount of harmonic content is generated for shorter magnet widths, see Fig. 9.12. The smaller spacer width reduces the penetration depth of the out-of-plane magnetic field, therefore changing the shape of the surface magnetic field. For the experimental measurements, magnet width of 4 mm is selected for the transmitting PPM EMAT, as the receiver magnet width is limited by the magnet availability. The smallest available combination of magnets with ratio 2:1 were of sizes: transmitter - 20 mm × 6 mm × 1.5 mm and receiver - 10 mm × 3 mm × 2 mm, with the magnet polling direction parallel to the smallest dimension.

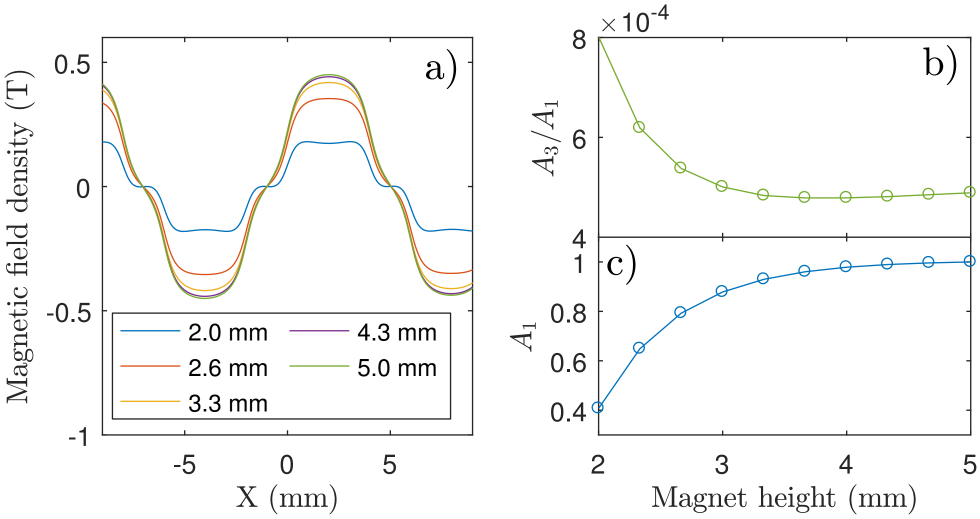

Figure 9.11: Out-of-plane magnetic field density, (a), on the surface of the specimen, the fundamental wavenumber content, (c), and the ratio of the third harmonic content, (b), as a function of the magnet height. The amplitude of the fundamental wavenumber increase for values up to 4 mm and then plateaus. The A_3/A_1 ratio is strongly affected by the increase in the fundamental amplitude.

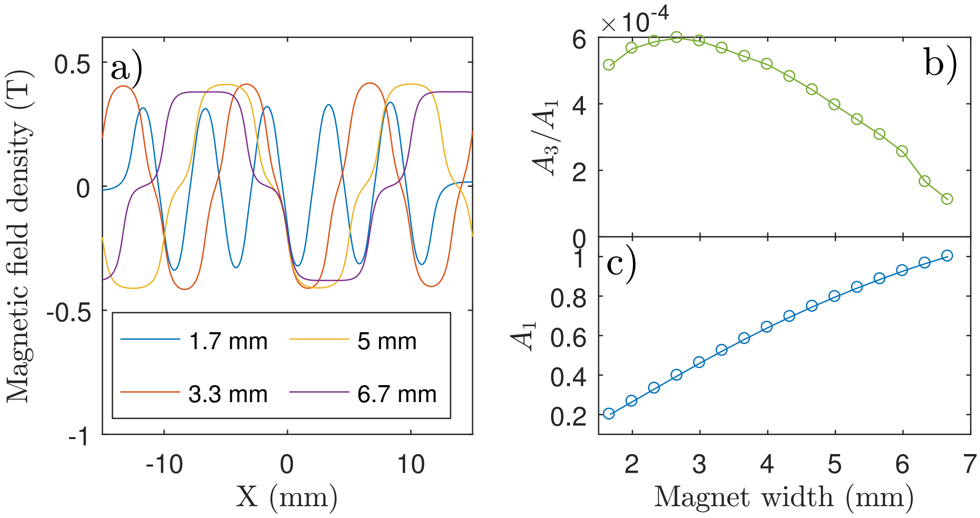

Figure 9.12: Out-of-plane magnetic field density, (a), at the surface of the specimen, the fundamental wavenumber content, (c), and the ratio of the third harmonic content, (b), as a function of the magnet width. The amplitude of the fundamental wavenumber increases with increased magnet width.

The number of magnet columns is expected to have the greatest effect on the transducer spatial frequency bandwidth. A large number of magnets increases the fundamental wavenumber amplitude and defines a narrower wavenumber content, see Fig. 9.13. The number of magnet columns has no significant effect on the third harmonic content, as each additional magnet increases the fundamental and third harmonic components proportionally. The transducer size is limited by practical considerations, therefore the number of columns is defined by the experimental constraints.

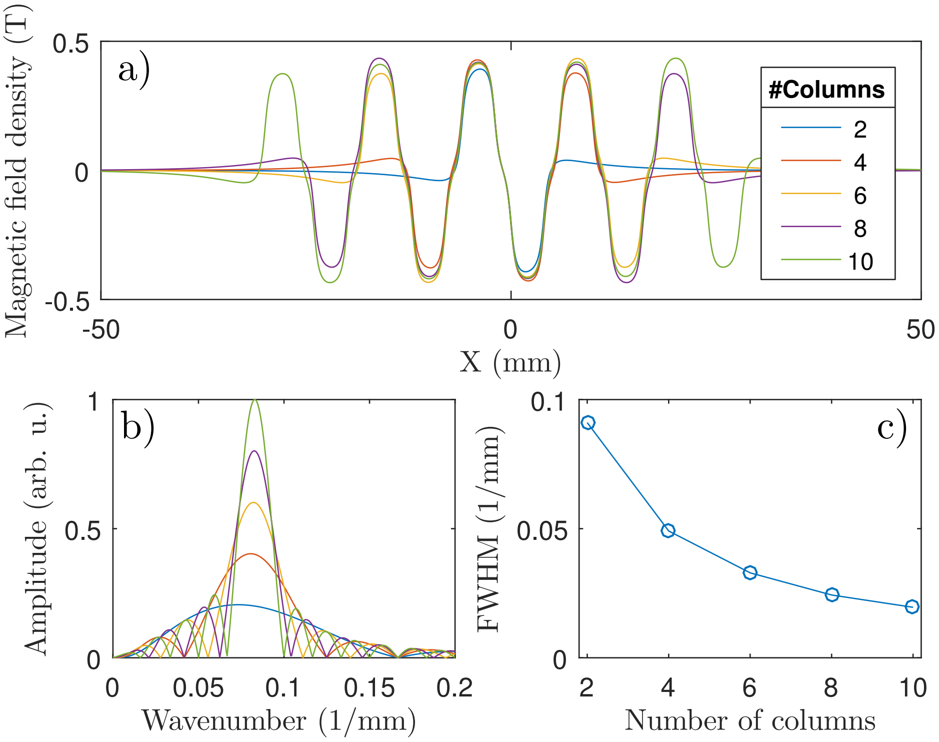

Figure 9.13: Out-of-plane magnetic field density, (a), at the surface of the specimen, wavenumber spectra of the fundamental harmonic component, (b), and FWHM, (c), as a function of the number of magnet columns.

The SH ultrasonic wave generation can only be achieved if the dispersion curve conditions are fulfilled. The multiplication of the wavenumber spectra (see Fig. 9.14) and the frequency spectra (see Fig. 9.16), produce a map of the excitation regions for the PPM EMAT, see Fig. 9.15. The analysis of the simulated models shows that the third harmonic ultrasonic content can be significantly reduced by the use of spatial filtering of the third harmonic wavenumber, see Fig. 9.14. The ultrasonic generation, of the improved SH PPM EMAT, is concentrated on the main wavenumber lobe. Therefore, any wave generation from the higher harmonic components of the excitation signal is significantly diminished. This allows for the generation of high amplitude, SH waves with narrow wavenumber spectra from an excitation source with high system nonlinearity.

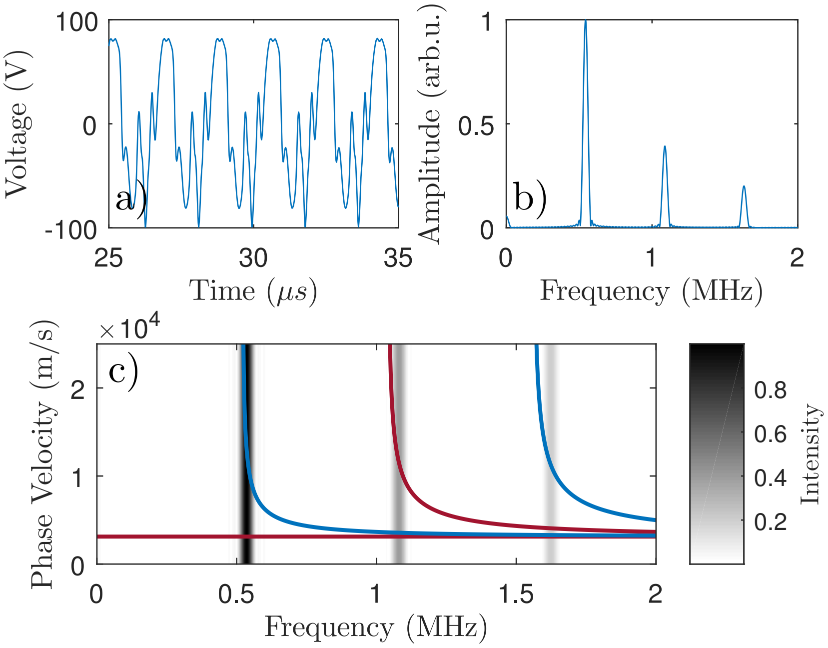

Figure 9.16: Bandwidth of the RITEC current pulse. The RITEC driving current signal, (a), for an excitation toneburst of frequency 540 kHz. The frequency spectra of the driving signal, (b), and the bandwidth of the RITEC current output, (c).

EMAT PPM transducers are built following the optimisation parameters derived from the simulations. A diagram of the transducers is presented in Fig. 9.17. The variation of the third harmonic SH parameter is measured as a function of distance and excitation level.

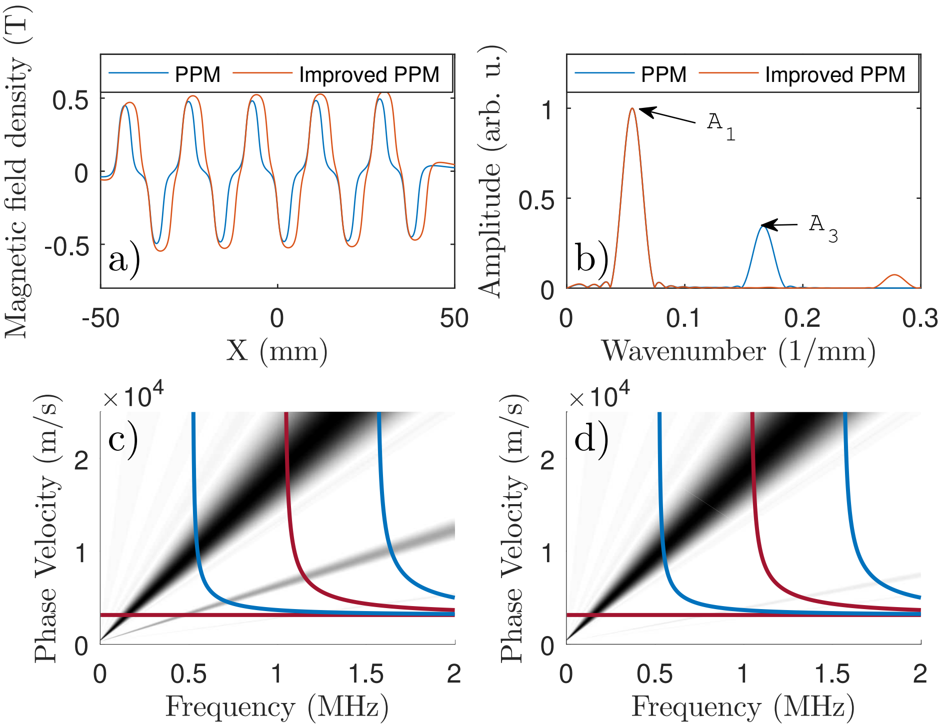

Figure 9.14: Simulated regions of ultrasonic wave generation for wavenumber spectra of the improved SH PPM design. Out-of-plane magnetic field for PPM EMATs standard (MFR = 1.00) and improved (MFR = 0.66), (a), and their wavenumber spectra, (b). Wavenumber selectivity of the standard, (c), and improved SH PPM EMAT, (d).

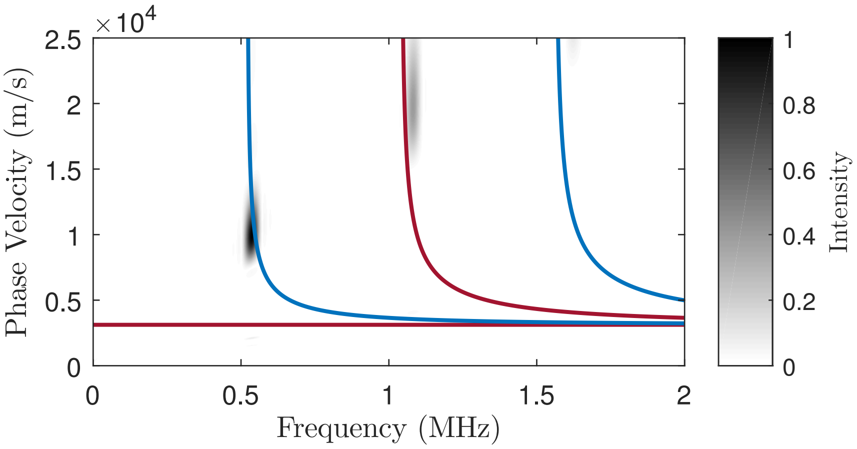

Figure 9.15: Simulated regions of ultrasonic wave generation excited by the improved PPM EMAT driven by 20 cycle toneburst at 540 kHz generated by RITEC amplifier. The colormap represents the intensity of the generated ultrasonic signals. A significant portion of the excitation region is confined within the SH1 mode around the frequency of 540 kHz.

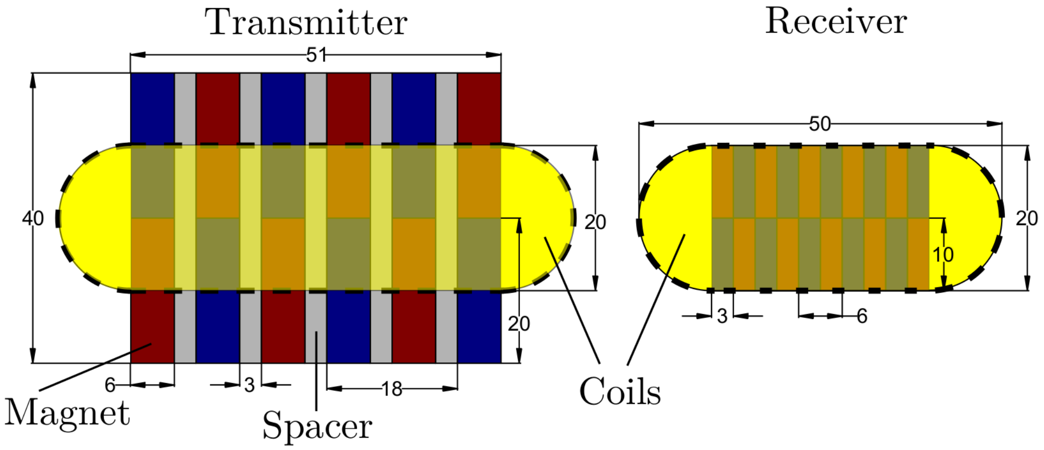

Figure 9.17: Designs of the transmitting and receiving SH PPM EMATs for third harmonic measurements. The ratio between the transducers wavelengths is 3:1. Transmitter height is 6 mm, and the receiver height is 10 mm.

The third harmonic receiver measures both the strong amplitude fundamental and the small amplitude third harmonic ultrasonic waves. From all the excitation regions of the PPM EMAT, the SH1 mode fundamental wave and the material generated SH3 third harmonic wave have the highest group velocity. They arrive earlier than the SH2 mode and SH3 modes generated by the intersection of the main wavenumber lobe with the higher harmonic components of the excitation signal. Those two modes have wavelengths equal to that of the fundamental SH1 mode, but have higher phase velocities and significantly lower group velocities than the ultrasonic waves of interest. Filtering the excitation signal can reduce the generation of these higher phase velocity modes and thus reduce their signal interference. Additionally, for a long toneburst signal of long wavelength SH waves, considerations must be taken for any edge wall reflections.

A toneburst excitation signal of 25 cycles is used to generate high amplitude SH1 waves in 3 mm thick aluminium with dimensions of 400 mm × 700 mm. The measured bulk shear wave velocity of the aluminium is 3210 m/s. The calculated frequency of excitation for the SH1 mode is 540 kHz for a PPM EMAT with a wavelength of 18 mm. The spatial length of the toneburst signal is 450 mm, while the sample dimension is 700 mm. Therefore, the reflected signals from the sample boundaries are expected to interfere with the later part of the received signals, as seen in figure 9.18.

The envelope of the signal shape is longer than the toneburst signal length (46 μs). The reason for this is that both the transmitter and receiver EMATs have finite sizes and different portions of the ultrasonic SH waves are propagating under their footprints. The shape of the received signal resembles that of a Tukey window, with a steady signal amplitude around the middle of the received ultrasonic wave package. The power law relationship between the third harmonic amplitude and the fundamental ultrasonic wave amplitude is measured as a function of excitation levels. Data points from multiple propagation distances and excitation levels are used to show the linear relation between the A_1^3 and A_3, as described by NLU theory. For longer propagation distances and lower excitation levels, the third harmonic amplitude is expected to be close to the noise floor level of the experimental measurements. Therefore, the data from the measured results, with low amplitude of the fundamental wave, can result in erroneous calculations. The amplitudes of the fundamental and third harmonic components presented on the excitation current variation plot in figure 9.19 are of the highest excitation level of the RITEC amplifier. The fundamental harmonic amplitude increases linearly with the excitation current amplitude, while the third harmonic amplitude has a cubic relation to the driving current. The cubic relation between the A_1 and A_3 can be confirmed for the higher amplitudes of the fundamental wave component, while the smaller values should be disregarded.

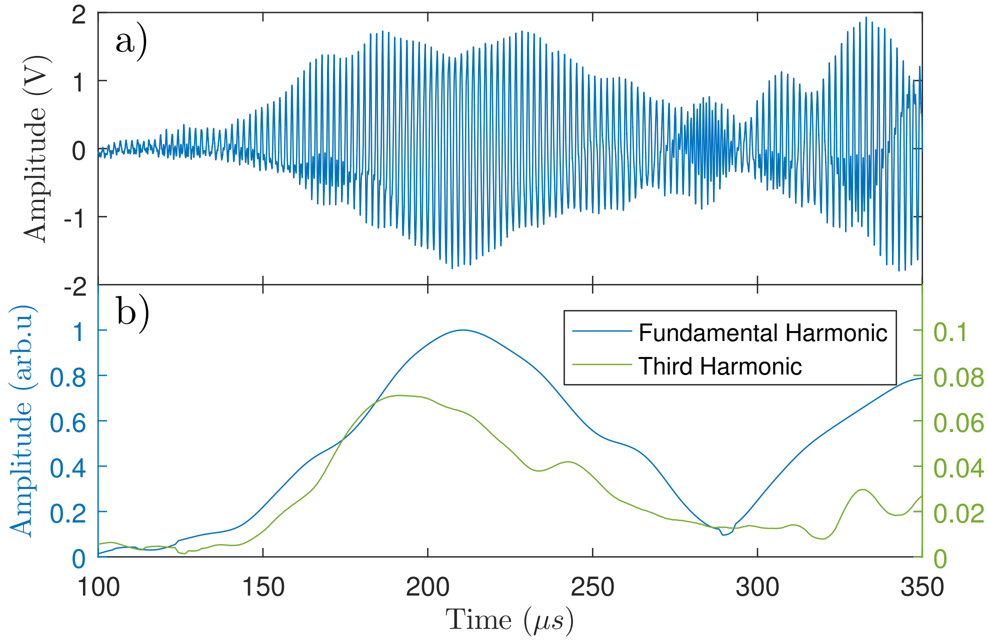

Figure 9.18: Nonlinear SH wave signal measured by an optimised pair of PPM EMATs, (a). Harmonic content as a function of time, (b). Values are extracted using an STFT (window length 20 μs).

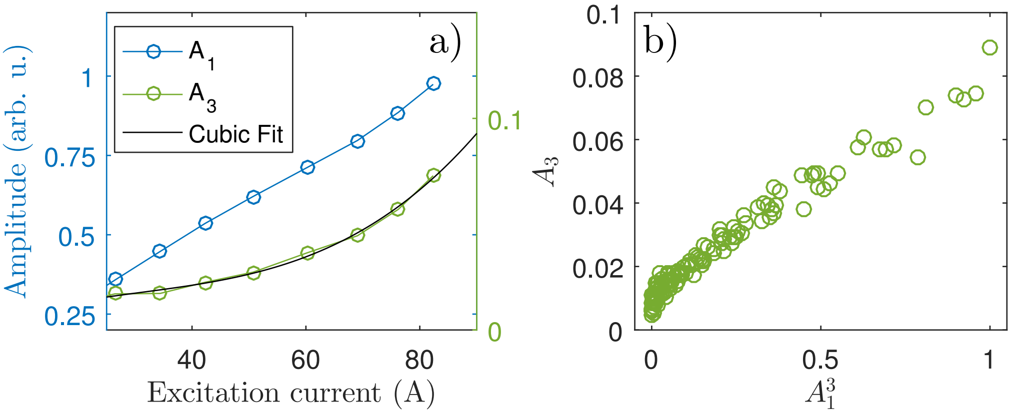

Figure 9.19: Variation of the shear horizontal nonlinear ultrasonic wave amplitudes as a function of the excitation current, (a). The relation between the fundamental and third harmonic amplitudes for multiple propagation distances and multiple excitation levels, (b).

To investigate the contribution of the system nonlinearity generation to the total measured third harmonic amplitude, calculation of the ultrasonic beam pattern was performed using Huygens' principle.

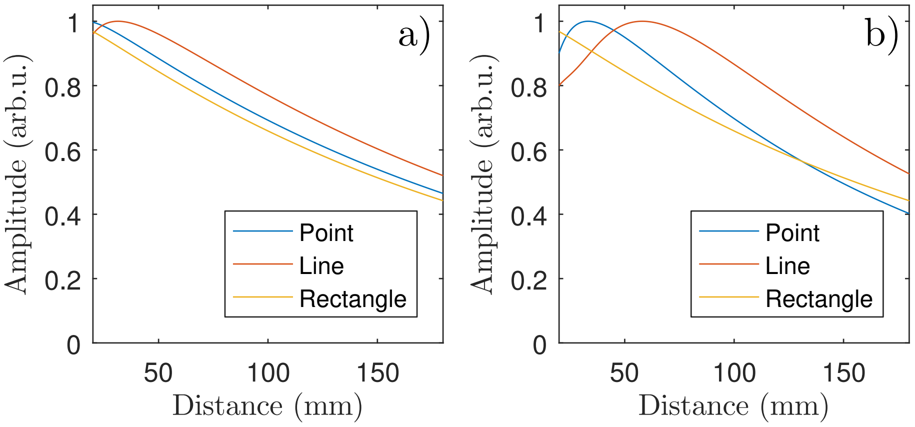

Figure 9.21: Spatial impulse response of different receiver geometries for fundamental, (a), and third harmonic, (b), generated by an finite size PPM EMAT transducer. The size of the transmitter is 51 mm × 20 mm. The line receiver has a width of 20 mm, and the rectangular receiver has a width of 20 mm and a length of 30 mm.

Measurements of the shear horizontal wave nonlinear parameter were taken at various distances to confirm the spatial variation of the parameter. The amplitudes of the harmonic components were extracted using an STFT with a window length of

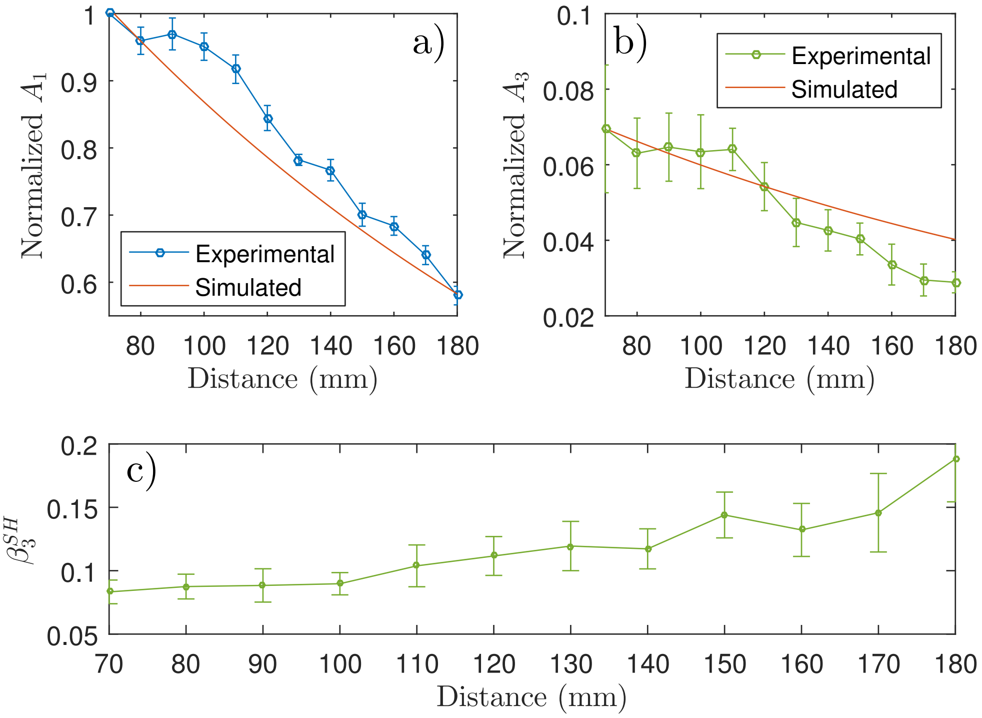

Figure 9.20: Variation of the shear horizontal nonlinear ultrasonic wave fundamental amplitude, (a), and third harmonic amplitude, (b), as a function of the propagation distance. The simulated diffraction pattern is in agreement with the fundamental wave decay. However, the simulated results do not match the decay of the measured third harmonic component. The shear horizontal wave nonlinear parameter increases with propagation distance, (c).

20 μs. The harmonic amplitudes of the ultrasonic signals generated from multiple current excitation levels were normalised to the fundamental amplitude of the shortest propagation distance for that particular current amplitude. The values of the fundamental and third harmonic amplitudes for the highest excitation levels were used to calculate an average value for the nonlinear parameter $\beta_3^{SH} = A_3/A_1^3$ for each propagation distance. The variation in the higher harmonic amplitude causes large variations in the calculated value for the nonlinear parameter. However, the value of β_3^{SH} increases with propagation distance.

Further studies are required to experimentally validate the method for measuring the shear horizontal third harmonic nonlinear parameter. Investigation of the changes in the measured SH third harmonic nonlinear parameter as a function of fatigue is necessary. A more advanced study and simulations of the diffraction pattern for SH PPM EMATs of various sizes must be conducted to analyse the diffraction corrections for the nonlinear parameter measurements.

Chapter 10

Conclusions

Nonlinear ultrasonic (NLU) techniques have been reported in the literature as having the potential to be the next step in improving the detection limit of ultrasonic NDE. NLU can detect microstructural damage at even earlier stages of the components life-cycle. However, recent studies have identified multiple practical challenges for the application of nonlinear measurements. Although promising results have been achieved in laboratory conditions, no field deployable method is currently available. The use of non-contact ultrasonic transducers addresses one of the main challenges of NLU techniques: variance in the nonlinearity related to the coupling conditions of the employed contact methods. The potential of EMATs to substitute the currently employed ultrasonic transducers has been analysed in detail in this thesis. Previous NLU EMAT studies have reported inconclusive results for the measured nonlinear parameters as a function of fatigue [35; 135; 136; 149; 151; 152]. They have failed to identify the limitations of the EMAT methods that prohibit the measurement of the material nonlinearity. In this thesis, different aspects of the EMAT transduction process are identified as the main limitation factors: self-field Lorentz force ultrasonic generation, insufficient amplitude of the generated ultrasonic waves and Joule heating of the material surface. Multiple experiments using EMAT NLU techniques have been conducted, to verify these arguments. Furthermore, the potential of these techniques as a practical solution for field deployable NLU measurements has been evaluated.

10.1 Electronics

A new method is proposed for reducing the contributions of the system nonlinearities to the measured nonlinear parameter. The electrical current, required for high amplitude ultrasonic excitation in NLU techniques, can contain significant harmonic content, which can obscure the results of the measured small amplitude harmonic generation from the material nonlinearity. The method employs artificial higher harmonic component added to the synthesised signal to compensate for the generated nonlinearity from the amplifier. The proposed method is tested and shows a significant reduction in the generated harmonic distortion of the higher harmonic components. An extension of the method can be used to determine the contributions from the system nonlinearity accurately. To achieve this, the amplitudes of the artificially added higher harmonic is controlled, and the amplitudes of the higher harmonic components of the ultrasonic signal are measured. Analysis of the variation of the higher harmonic ultrasonic components can be used to determine contributions of the system nonlinearity to the measured nonlinearity parameter.

10.2 Bulk waves

Measurements of nonlinear longitudinal bulk waves, employing EMAT generators, must consider the contribution from the self-field Lorentz force generation. The dynamic magnetic field ultrasonic generation closely mimics the generation of the second harmonic waves from the material nonlinearity. Thus, complex analysis of the measured amplitude is required to separate the contributions from the two phenomena to the total measured nonlinearity, which significantly reduces the practical applications of the method.

The simulated displacement profiles of a shear wave polarised racetrack EMAT are in good agreement with the experimentally measured results. Experimentally measured nonlinear parameters using a shear wave EMAT have shown no significant change in the nonlinear parameter during the fatigue life-cycle of an aluminium sample alloy (Al6061). The generation of second harmonic shear waves is forbidden by the symmetry in the higher order elastic constants, although studies have reported measuring contributions from the lattice nonlinearity [67; 152]. Third harmonic shear wave nonlinear parameters have been measured using a through thickness resonance method. No significant change in the third harmonic nonlinear parameter is observed during the fatigue lifetime of an aluminium alloy sample. Future research using third harmonic nonlinear techniques must include measurements of the third order elastic constants and the material microstructure, from another measurement source. This will allow verification that the contributions to the measured nonlinear parameter are from the material properties.

Measurements of the nonclassical nonlinear parameter of aluminium show strong temperature dependence and no significant change with fatigue damage. Other NRUS EMAT studies have reported observations of a greater change in the frequency shift for steel [151]. Significant inconsistencies are observed in the reported results for copper between [72] and [149]. Experiments employing the NRUS technique and EMAT generation must include measurements of the sample temperature or use temperature compensation methods, as Joule heating from the generated eddy currents occurs in the specimen. To extend the current NRUS method, measurements of the frequency shifts for multiple resonance modes can be taken.

Alternatively, the temperature dependence of the resonance mode frequency can be investigated. Changes in the coefficient of thermal expansion (CTE) with fatigue have been researched scarcely [161]. Measurements of the temperature variation of ultrasonic velocity throughout the fatigue lifecycle can reveal changes to the third order elastic constants [174; 175]. The non-contact electromechanical coupling of EMATs makes them well suited for measurements of the variation of the ultrasonic parameters with temperature.

10.3 Guided waves

The ultrasonic Rayleigh waves generated by a meanderline EMAT have significantly lower amplitudes compared to the waves generated by an angled wedge piezoelectric transducer. Additionally, the dynamic magnetic field Lorentz force generates Rayleigh waves matching the second harmonic generation from the material nonlinearity, which has been neglected in previous studies [35; 135]. Therefore, generation of high amplitude ultrasonic Rayleigh waves using EMAT transducers is impractical and would require complex analysis to separate the material nonlinearity contributions from the total measured nonlinearity.

However, the reception of nonlinear Rayleigh waves by EMAT transducers offers advantages compared to contact methods. The non-contact electromechanical transduction allows couplant free measurements of the small amplitude, higher harmonic content. Additionally, the EMAT transducers can permit measurements of multiple propagation distances to be taken in quick succession, reducing the experimental time and variability of the environmental conditions. Experimental results for the nonlinear Rayleigh parameter of aluminium alloy (Al6061), measured with a meanderline EMAT, are in good agreement with the NLU theory. Measurements of the relative nonlinear Rayleigh wave parameter for aluminium, using EMAT detectors, have the potential to become a field deployable technique.

Compared to laser interferometer measurements, EMATs require significantly less specimen preparation and are easier to use in field conditions. Nonlinear Rayleigh wave ultrasonic measurements using air-coupled ultrasonic detectors have been reported by Thiele [182]. Compared to EMAT transducers, the signal received by the air coupled receivers depends critically on the angular alignment of the transducer field deployable method [29]. Further investigation is required to measure the changes of the material properties with fatigue, using the angled wedge - EMAT receiver transducer combination.

An optimised design of PPM EMAT transducers for nonlinear shear horizontal waves has been simulated and analysed. The harmonic content of the generated ultrasonic waves is significantly reduced for a magnet filling ratio (MFR) of 0.66. The generation of third harmonic shear horizontal waves in aluminium has been measured experimentally. Further investigation is required to assess the potential of the nonlinear SH wave to measure microstructural material changes during the fatigue lifecycle.

10.4 Future work

The harmonic compensation method can be extended to measure the ultrasonic contribution from the total system nonlinearity. The measured ultrasonic signal amplitude profiles along the propagation distance, for different amplitudes of the artificial higher harmonic content, can be used to separate the source nonlinearity from the material nonlinearity. In this case, the amplitude of the source nonlinearity contribution varies, while the material generation harmonics will have a constant contribution to the total measured nonlinear signal.

EMAT application for the third harmonic longitudinal wave or the nonclassical longitudinal nonlinear parameter can be investigated to evaluate the potential of the method to measure the microstructural changes in the non-ferromagnetic materials. Collinear wave mixing using EMATs can be investigated for longitudinal wave generation or can be extended for the existing shear wave methods [148; 150]. The wide bandwidth of the EMAT transducers allows them to be used for multiple pairs of resonance driving modes. The combined results from the multiple nonlinear wave-mixing measurements might lead to an improved interpretation of the nonlinear ultrasonic parameters.

Experimental measurements, using the improved SH PPM EMAT design, are required to verify how the nonlinear SH parameter changes during the fatigue lifecycle of non-ferromagnetic materials. The design of the PPM EMAT may further be improved by the use of a Halbach array [202].

Bibliography

[1] D. Abajingin. Solution of Morse Potential for Face Centre Cube Using Embedded Atom Method. *Advances in Physics Theories and Applications*, 8:36–45, 2012.

[2] K. E.-A. V. D. Abeele, P. A. Johnson, and A. Sutin. Nonlinear Elastic Wave Spectroscopy (NEWS) Techniques to Discern Material Damage, Part I: Nonlinear Wave Modulation Spectroscopy (NWMS). *Research in Nondestructive Evaluation*, 12(1):17–30, 2000.

[3] J. D. Achenbach. *Wave Propagation in Elastic Solids.* Elsevier, Amsterdam, 1st edition, 1984.

[4] B. Auld. *Acoustic fields and waves in solids*, volume I. Wiley, New York, N.Y., 1973.

[5] A. Avinc and V. Dimitrov. Effective LennardJones potential for cubic metals in the frame of embedded atom model. *Computational Materials Science*, 13(4):211–217, jan 1999.

[6] K. Balasubramaniam, J. S. Valluri, and R. V. Prakash. Creep damage characterization using a low amplitude nonlinear ultrasonic technique. *Materials Characterization*, 62(3):275–286, mar 2011.

[7] D. J. Barnard. Monitoring Fatigue Damage Accumulation with Rayleigh Wave Harmonic Generation Measurements. In *AIP Conference Proceedings*, volume 657, pages 1393–1400. AIP, 2003.

[8] D. J. Barnard, G. E. Dace, and O. Buck. Acoustic Harmonic Generation Due to Thermal Embrittlement of Inconel 718. *Journal of Nondestructive Evaluation*, 16(2):67–75, 1997.

[9] F. A. Bender. *Analysis of Second Harmonic Generation At a Free Boundary for Oblique Incidence.* PhD thesis, Georgia Institute of Technology, 2010.

[10] F. A. Bender, J.-Y. Kim, L. J. Jacobs, and J. Qu. The generation of second harmonic waves in an isotropic solid with quadratic nonlinearity under the presence of a stress-free boundary. *Wave Motion*, 50(2):146–161, mar 2013.

[11] S. Best, A. Croxford, and S. Neild. Pulse-Echo Harmonic Generation Measurements for Non-destructive Evaluation. *Journal of Nondestructive Evaluation*, 33(2):205–215, jun 2014.

[12] R. T. Beyer. Parameter of Nonlinearity in Fluids. *The Journal of the Acoustical Society of America*, 32(6):719, 1960.

[13] R. T. Beyer. *Non linear Acoustics.* Naval Sea Systems Command, Washington, DC, 1974.

[14] J. L. Blackshire. Nonlinear Laser Ultrasonic Measurements of Localized Fatigue Damage. In *AIP Conference Proceedings*, volume 657, pages 1479–1488. AIP, 2003.

[15] S. Boonsang and R. Dewhurst. A sensitive electromagnetic acoustic transducer for picometer-scale ultrasonic displacement measurements. *Sensors and Actuators A: Physical*, 127(2):345–354, mar 2006.

[16] C. Borigo and J. L. Rose. A spacing compensation factor for the optimization of guided wave annular array transducers. *The Journal of the Acoustical Society of America*, 133(January 2013):127–135, 2013.

[17] D. E. Bray and D. Mcbride. *Nondestructive testing techniques.* John Wiley & Sons, 1992.

[18] M. A. Breazeale and D. O. Thompson. Finite-amplitude ultrasonic waves in aluminum. *Applied Physics Letters*, 3(5):77, 1963.

[19] G. Brekow. Non destructive testing. Radiography, ultrasonics, liquid penetrant, magnetic particle, eddy current. *Materials and Corrosion/Werkstoffe und Korrosion*, 47(10):579–579, oct 1996.

[20] O. Buck. Fatigue Damage and Its Nondestructive Evaluation: An Overview. In *Review of Progress in Quantitative Nondestructive Evaluation*, volume 17, pages 1–13. Springer US, Boston, MA, 1998.

[21] J. Cantrell. *Ultrasonic Nondestructive Evaluation.* CRC Press, dec 2003.

[22] J. H. Cantrell. Dependence of microelastic-plastic nonlinearity of martensitic stainless steel on fatigue damage accumulation. *Journal of Applied Physics*, 100(6):063508, 2006.

[23] J. H. Cantrell. Quantitative assessment of fatigue damage accumulation in wavy slip metals from acoustic harmonic generation. *Philosophical Magazine*, 86(11):1539–1554, apr 2006.

[24] J. H. Cantrell. Ultrasonic harmonic generation from fatigue-induced dislocation substructures in planar slip metals and assessment of remaining fatigue life. *Journal of Applied Physics*, 106(9):093516, 2009.

[25] J. H. Cantrell and W. T. Yost. Nonlinear ultrasonic characterization of fatigue microstructures. *International Journal of Fatigue*, 23:487–490, 2001.

[26] J. H. Cantrell and W. T. Yost. Acoustic nonlinearity and cumulative plastic shear strain in cyclically loaded metals. *Journal of Applied Physics*, 113(15):153506, 2013.

[27] W. D. Cash and W. Cai. Dislocation contribution to acoustic nonlinearity: The effect of orientation-dependent line energy. *Journal of Applied Physics*, 109(1):014915, 2011.

[28] W. D. Cash and W. Cai. Contribution of dislocation dipole structures to the acoustic nonlinearity. *Journal of Applied Physics*, 111(7):074906, 2012.

[29] M. Castaings, P. Cawley, R. Farlow, and G. Hayward. Air-Coupled Ultrasonic Transducers for the Detection of Defects in Plates. In *Review of Progress in Quantitative Nondestructive Evaluation*, volume 15, pages 1083–1090. Springer US, Boston, MA, 1996.

[30] R. W. Cheary, E. Dooryhee, P. Lynch, N. Armstrong, and S. Dligatch. X-ray diffraction line broadening from thermally deposited gold films. *Journal of Applied Crystallography*, 33(5):1271–1283, oct 2000.

[31] Z. Chen, G. Tang, Y. Zhao, L. J. Jacobs, and J. Qu. Mixing of collinear plane wave pulses in elastic solids with quadratic nonlinearity. *The Journal of the Acoustical Society of America*, 136(5):2389–2404, nov 2014.

[32] E. Chern, J. Heyman, and J. Cantrell. Determination of Material Stress from the Temperature Dependence of the Acoustic Natural Velocity. In *1981 Ultrasonics Symposium*, number 4, pages 960–963. IEEE, 1981.

[33] V. K. Chillara. *Higher harmonic guided waves in isotropic weakly non-linear elastic plates.* PhD thesis, The Pennsylvania State University, 2012.

[34] V. K. Chillara and C. J. Lissenden. Review of nonlinear ultrasonic guided wave nondestructive evaluation: theory, numerics, and experiments. *Optical Engineering*, 55(1):011002, aug 2015.

[35] A. Cobb, M. Capps, C. Duffer, J. Feiger, K. Robinson, and B. Hollingshaus. Nonlinear ultrasonic measurements with EMATs for detecting pre-cracking fatigue damage. In *AIP Conference*, volume 299, pages 299–306, 2012.

[36] A. J. Croxford, P. D. Wilcox, B. W. Drinkwater, and P. B. Nagy. The use of non-collinear mixing for nonlinear ultrasonic detection of plasticity and fatigue. *The Journal of the Acoustical Society of America*, 126(5):EL117, nov 2009.

[37] A. Demčenko, R. Akkerman, P. Nagy, and R. Loendersloot. Non-collinear wave mixing for non-linear ultrasonic detection of physical ageing in PVC. *NDT & E International*, 49:34–39, jul 2012.

[38] S. Dixon, C. Edwards, and S. Palmer. High accuracy non-contact ultrasonic thickness gauging of aluminium sheet using electromagnetic acoustic transducers. *Ultrasonics*, 39(6):445–453, oct 2001.

[39] S. Dixon, M. P. Fletcher, and G. Rowlands. The accuracy of acoustic birefringence shear wave measurements in sheet metal. *Journal of Applied Physics*, 104(11):114901, 2008.

[40] S. Dixon, S. Hill, Y. Fan, and G. Rowlands. The wave-field from an array of periodic emitters driven simultaneously by a broadband pulse. *The Journal of the Acoustical Society of America*, 133(6):3692, 2013.

[41] S. Dixon, B. Lanyon, and G. Rowlands. Coating thickness and elastic modulus measurement using ultrasonic bulk wave resonance. *Applied Physics Letters*, 88(14):141907, 2006.

[42] E. Dobbs and J. Llewellyn. Generation of ultrasonic waves without using a transducer. *Non-Destructive Testing*, 4(1):49–56, feb 1971.

[43] C. V. Dodd. Analytical Solutions to Eddy-Current Probe-Coil Problems. *Journal of Applied Physics*, 39(6):2829, 1968.

[44] B. Dutton, S. Boonsang, and R. Dewhurst. A new magnetic configuration for a small in-plane electromagnetic acoustic transducer applied to laser-ultrasound

measurements: Modelling and validation. *Sensors and Actuators A: Physical*, 125(2):249–259, jan 2006.

[45] B. Dutton, S. Boonsang, and R. Dewhurst. Modelling of magnetic fields to enhance the performance of an in-plane EMAT for laser-generated ultrasound. *Ultrasonics*, 44(SUPPL.):e657–e665, dec 2006.

[46] R. S. Edwards, Y. Fan, and S. Dixon. High Speed Detection and Characterization of Defects in the Railhead. In *AIP Conference Proceedings*, volume 894, pages 1406–1412. AIP, 2007.

[47] Y. Fan, S. Dixon, X. Jian, D. O. Thompson, and D. E. Chimenti. Lift-off performance of ferrite enhanced generation EMATs. In *AIP Conference Proceedings*, volume 975, pages 835–840. AIP, 2008.

[48] C. Fortunko and R. Thompson. Optimization of Electromagnetic Transducer Parameters for Maximum Dynamic Range. In *1976 Ultrasonics Symposium*, pages 12–16. IEEE, 1976.

[49] F. C. Frank and W. T. Read. Multiplication Processes for Slow Moving Dislocations. *Physical Review*, 79(4):722–723, aug 1950.

[50] J. Frouin, T. E. Matikas, J. K. Na, and S. Sathish. In-situ monitoring of acoustic linear and nonlinear behavior of titanium alloys during cycling loading. In G. Y. Baaklini, C. A. Nove, and E. S. Boltz, editors, *Nondestructive Evaluation of Aging Materials and Composites III*, volume 3585, pages 107–116, feb 1999.

[51] J. Frouin, S. Sathish, T. E. Matikas, and J. K. Na. Ultrasonic Linear and Nonlinear Behavior of Fatigued Ti6Al4V. *Journal of Materials Research*, 14(04):1295–1298, apr 1999.

[52] A. Gedroits and V. Krasilnikov. Finite-amplitude elastic waves in solids and deviations from Hooke's law. *Soviet Phys. JETP*, 16:1122–1126, 1963.

[53] A. A. Gedroits, L. K. Zarembo, and V. A. Krasilnikov. Shear waves of finite amplitude in polycrystals and single crystals of metals. *Sov. Phys. Dokl.*, 8:478–480, 1963.

[54] J. Goodman. *Mechanics applied to engineering.* Longmans, Green, and Co., London; New York, 1899.

[55] R. E. Green. Non-contact ultrasonic techniques. In *Ultrasonics*, volume 42, pages 9–16, apr 2004.

[56] Z. Guo, J. Achenbach, and S. Krishnaswamy. EMAT generation and laser detection of single lamb wave modes. *Ultrasonics*, 35(6):423–429, sep 1997.

[57] M. F. Hamilton and D. T. Blackstock. *Nonlinear acoustics*, volume 427. Academic press San Diego, 1998.

[58] S. Haupert, G. Renaud, J. Riviere, M. Talmant, P. a. Johnson, and P. Laugier. High-accuracy acoustic detection of nonclassical component of material nonlinearity. *The Journal of the Acoustical Society of America*, 130(5):2654, nov 2011.

[59] T. Hayashi and K. Kawashima. Single Mode Extraction from Multiple Modes of Lamb Wave and Its Application to Defect Detection. *JSME International Journal Series A*, 46(4):620–626, 2003.

[60] F. Hernandez-Valle and S. Dixon. Pulsed electromagnet EMAT for ultrasonic measurements at elevated temperatures. *Insight - Non-Destructive Testing and Condition Monitoring*, 53(2):96–99, feb 2011.

[61] J. Herrmann, J.-Y. Kim, L. J. Jacobs, J. Qu, J. W. Littles, and M. F. Savage. Assessment of material damage in a nickel-base superalloy using nonlinear Rayleigh surface waves. *Journal of Applied Physics*, 99(12):124913, 2006.

[62] J. Herrmann, J.-Y. Kim, L. J. Jacobs, J. Qu, J. W. Littles, and M. F. Savage. Assessment of material damage in a nickel-base superalloy using nonlinear Rayleigh surface waves. *Journal of Applied Physics*, 99(12):124913, 2006.

[63] A. Hikata and C. Elbaum. Generation of Ultrasonic Second and Third Harmonics Due to Dislocations. I. *Physical Review*, 144(2):469–477, apr 1966.

[64] S. Hill and S. Dixon. Frequency dependent directivity of periodic permanent magnet electromagnetic acoustic transducers. *NDT & E International*, 62:137–143, mar 2014.

[65] S. J. Hill. *Time-Frequency localisation of defects using broadband pulsed arrays.* PhD thesis, University of Warwick, 2014.

[66] M. Hirao and H. Ogi. An SH-wave EMAT technique for gas pipeline inspection. *NDT & E International*, 32(3):127–132, apr 1999.

[67] M. Hirao and H. Ogi. *EMATs for Science and Industry.* Springer US, Boston, MA, 2003.

[68] K. Huang. On the Atomic Theory of Elasticity. *Proceedings of the Royal Society A: Mathematical, Physical and Engineering Sciences*, 203(1073):178–194, sep 1950.

[69] S. Huang, S. Wang, W. Li, and Q. Wang. *Electromagnetic Ultrasonic Guided Waves*. Springer Series in Measurement Science and Technology. Springer Singapore, Singapore, 2016.

[70] D. Hull. *Introduction to dislocations*. Pergamon Press, Oxford: New York, 2nd ed. edition, 1975.

[71] N. Ida and J. P. A. Bastos. *Electromagnetics and Calculation of Fields*. Springer US, New York, NY, 1992.

[72] Y. Ishii and T. Ohtani. Applying Nonlinear Resonant Ultrasound Spectroscopy (NRUS) to Evaluating Fatigue Damage in a Pure Copper. *Proceedings of Symposium on Ultrasonic Electronics*, 32:209–210, 2011.

[73] J. Isla and F. Cegla. Optimization of the Bias Magnetic Field of Shear Wave EMATs. *IEEE Transactions on Ultrasonics, Ferroelectrics, and Frequency Control*, 63(8):1148–1160, aug 2016.

[74] J. Isla, M. Seher, R. Challis, and F. Cegla. Optimal impedance on transmission of Lorentz force EMATs. In *AIP Conference Proceedings 1706*, volume 1706, page 090012, 2016.

[75] J. Blitz and G. Simpson. *Ultrasonic methods of non-destructive testing*. Chapman & Hall, 1996.

[76] H. Jagodzinski. The direct observation of dislocations. *Acta Crystallographica*, 20(2):324–324, feb 1966.

[77] H. Jeong, S. Zhang, D. Barnard, and X. Li. A novel and practical approach for determination of the acoustic nonlinearity parameter using a pulse-echo method. In *AIP Conf. Proc*, volume 1706, page 060006, 2016.

[78] K.-y. Jhang. Nonlinear ultrasonic techniques for nondestructive assessment of micro damage in material: A review. *International Journal of Precision Engineering and Manufacturing*, 10(1):123–135, jan 2009.

[79] K.-Y. Jhang and K.-C. Kim. Evaluation of material degradation using nonlinear acoustic effect. *Ultrasonics*, 37(1):39–44, jan 1999.

[80] X. Jian and S. Dixon. Enhancement of EMAT and eddy current using a ferrite back-plate. *Sensors and Actuators A: Physical*, 136(1):132–136, may 2007.

[81] X. Jian, S. Dixon, and R. S. Edwards. Modelling ultrasonic generation for Lorentz force EMATs. *Insight - Non-Destructive Testing and Condition Monitoring*, 46(11):671–673, nov 2004.

[82] X. Jian, S. Dixon, R. S. Edwards, and J. Reed. Coupling mechanism of electromagnetic acoustical transducers for ultrasonic generation. *The Journal of the Acoustical Society of America*, 119(5):2693, 2006.

[83] X. Jian, S. Dixon, K. Grattan, and R. Edwards. A model for pulsed Rayleigh wave and optimal EMAT design. *Sensors and Actuators A: Physical*, 128(2):296–304, apr 2006.

[84] W. Jiang and W. Cao. Nonlinear properties of lead zirconatetitanate piezoceramics. *Journal of Applied Physics*, 88(11):6684, 2000.

[85] W. Jiang and W. Cao. Second harmonic generation of shear waves in crystals. *IEEE Transactions on Ultrasonics, Ferroelectrics and Frequency Control*, 51(2):153–162, feb 2004.

[86] J. Jiao, J. Sun, N. Li, G. Song, B. Wu, and C. He. Micro-crack detection using a collinear wave mixing technique. *NDT & E International*, 62:122–129, mar 2014.

[87] J. E. Jones. On the Determination of Molecular Fields. II. From the Equation of State of a Gas. *Proceedings of the Royal Society A: Mathematical, Physical and Engineering Sciences*, 106(738):463–477, oct 1924.

[88] J. Joule. XVII. On the effects of magnetism upon the dimensions of iron and steel bars. *Philosophical Magazine Series 3*, 30(199):76–87, feb 1847.

[89] J. Kacher and I. Robertson. Quasi-four-dimensional analysis of dislocation interactions with grain boundaries in 304 stainless steel. *Acta Materialia*, 60(19):6657–6672, nov 2012.

[90] L. Kang, S. Dixon, K. Wang, and J. Dai. Enhancement of signal amplitude of surface wave EMATs based on 3-D simulation analysis and orthogonal test method. *NDT & E International*, 59:11–17, oct 2013.

[91] L. Kang, Y. Fan, L. Chen, S. N. Ramadas, and S. Dixon. Low-power EMAT measurements for wall thickness monitoring. *Insight - Non-Destructive Testing and Condition Monitoring*, 57(6):319–323, jun 2015.

[92] L. Kang, W. Mi, C. Lv, and S. Wang. Research on weak signal detection technique for electromagnetic ultrasonic inspection system. In *2008 3rd IEEE Conference on Industrial Electronics and Applications*, pages 2394–2399. IEEE, jun 2008.

[93] L. Kang, S. Wang, T. Jiang, and G. Zhai. Optimal Design of Lamb Wave Electromagnetic Acoustic Transducers for Improving Their Excitation Performance. *Japanese Journal of Applied Physics*, 50(7):07HD01, jul 2011.

[94] K. Kawashima. Theory and numerical calculation of the acoustic field produced in metal by an electromagnetic ultrasonic transducer. *The Journal of the Acoustical Society of America*, 60(5):1089, 1976.

[95] K. Kawashima. Theory and numerical calculation of the acoustic field produced in metal by an electromagnetic ultrasonic transducer. *The Journal of the Acoustical Society of America*, 60(5):1089, 1976.

[96] K. Kawashima. Quantitative Calculation and Measurement of Longitudinal and Transverse Ultrasonic Wave Pulses in Solid. *IEEE Transactions on Sonics and Ultrasonics*, 31(2):83–93, mar 1984.

[97] K. Kawashima, O. B. Wright, and T. Hyoguchi. High Frequency Resonant Electromagnetic Generation and Detection of Ultrasonic Waves. *Japanese Journal of Applied Physics*, 33(Part 1, No. 5B):2837–2845, may 1994.

[98] J.-Y. Kim, L. J. Jacobs, J. Qu, and J. W. Littles. Experimental characterization of fatigue damage in a nickel-base superalloy using nonlinear ultrasonic waves. *The Journal of the Acoustical Society of America*, 120(3):1266, 2006.

[99] J.-Y. Kim, J. Qu, L. J. Jacobs, J. W. Littles, and M. F. Savage. Acoustic Nonlinearity Parameter Due to Microplasticity. *Journal of Nondestructive Evaluation*, 25(1):28–36, mar 2006.

[100] Y. Y. Kim and Y. E. Kwon. Review of magnetostrictive patch transducers and applications in ultrasonic nondestructive testing of waveguides. *Ultrasonics*, 62:3–19, sep 2015.

[101] I. D. Kiteley. *A Study of EMAT (Electromagnetic Acoustic Transducer) Operation on Ferromagnetic Metals.* PhD thesis, University of Warwick, 1999.

[102] R. Koch. Electromagnetic Acoustic Transducers For Use In Ultrasound Inspection Systems, 2008.

[103] J. S. Koehler. The Nature of Work-Hardening. *Physical Review*, 86(1):52–59, apr 1952.

[104] V. Korneev and A. Demčenko. Possible second-order nonlinear interactions of plane waves in an elastic solid. *The Journal of the Acoustical Society of America*, 135(2):591–598, feb 2014.

[105] G. Kossoff. The Effects of Backing and Matching on the Performance of Piezoelectric Ceramic Transducers. *IEEE Transactions on Sonics and Ultrasonics*, 13(1):20–30, mar 1966.

[106] L. Z. Krasilnikov. and V.A. *Introduction to nonlinear acoustics.* Nauka, Moscow, 1966.

[107] Y. Kusanagi, Y. Ishii, and T. Ohtani. Nonlinear ultrasonic characterization of creep damage in an Austenitic Stainless Steel. *Proceedings of Symposium on Ultrasonic Electronics*, 33:175–176, 2012.

[108] L. Kang, F. Pan, R. Su, C. Zhang, and J. Dai. A new surface-wave EMAT design of enhanced transduction efficiency. In *2014 IEEE Far East Forum on Nondestructive Evaluation/Testing*, pages 9–13. IEEE, jun 2014.

[109] L. D. Landau and E. M. Lifshitz. *Theory of Elasticity.* Pergamon Press, 1970.

[110] H. Ledbetter. Sound velocities, elastic constants: Temperature dependence. *Materials Science and Engineering: A*, 442(1-2):31–34, dec 2006.

[111] C. J. Lissenden, Y. Liu, G. W. Choi, and X. Yao. Effect of localized microstructure evolution on higher harmonic generation of guided waves. *Journal of Nondestructive Evaluation*, 33:178–186, 2014.

[112] C. J. Lissenden, Y. Liu, and J. L. Rose. Use of non-linear ultrasonic guided waves for early damage detection. *Insight - Non-Destructive Testing and Condition Monitoring*, 57(4):206–211, apr 2015.

[113] M. Liu, J.-Y. Kim, L. Jacobs, and J. Qu. Experimental study of nonlinear Rayleigh wave propagation in shot-peened aluminum platesFeasibility of measuring residual stress. *NDT & E International*, 44(1):67–74, jan 2011.

[114] M. Liu, G. Tang, L. J. Jacobs, and J. Qu. Measuring acoustic nonlinearity parameter using collinear wave mixing. *Journal of Applied Physics*, 112(2):024908, 2012.

[115] S. Liu, S. Best, S. Neild, A. J. Croxford, and Z. Zhou. Measuring bulk material nonlinearity using harmonic generation. *NDT & E International*, 48:46–53, jun 2012.

[116] Y. Liu, V. K. Chillara, and C. J. Lissenden. On selection of primary modes for generation of strong internally resonant second harmonics in plate. *Journal of Sound and Vibration*, 332(19):4517–4528, 2013.

[117] Q. Ma, J. Jiao, P. Hu, X. Zhong, B. Wu, and C. He. Excitation and detection of shear horizontal waves with electromagnetic acoustic transducers for nondestructive testing of plates. *Chinese Journal of Mechanical Engineering*, 27(2):428–436, 2014.

[118] D. MacLauchlan, S. Clark, and B. Cox. Recent advancements in the application of EMATs to NDE. *Proceedings of the 16th world conference on NDT*, pages 1154–61, 2004.

[119] K. H. Matlack, J.-Y. Kim, L. J. Jacobs, and J. Qu. Review of Second Harmonic Generation Measurement Techniques for Material State Determination in Metals. *Journal of Nondestructive Evaluation*, 34(1):273, mar 2015.

[120] K. R. McCall. Theoretical study of nonlinear elastic wave propagation. *Journal of Geophysical Research: Solid Earth*, 99(B2):2591–2600, feb 1994.

[121] K. R. McCall and R. A. Guyer. Equation of state and wave propagation in hysteretic nonlinear elastic materials. *Journal of Geophysical Research: Solid Earth*, 99(B12):23887–23897, dec 1994.

[122] M. Meo, U. Polimeno, and G. Zumpano. Detecting damage in composite material using nonlinear elastic wave spectroscopy methods. *Applied Composite Materials*, 15(3):115–126, 2008.

[123] K. Mirkhani, C. Chaggares, C. Masterson, M. Jastrzebski, T. Dusatko, A. Sinclair, R. J. Shapoorabadi, A. Konrad, and M. Papini. Optimal design of EMAT transmitters. *NDT and E International*, 37(3):181–193, 2004.

[124] H. Mohrbacher and K. Salama. The Temperature Dependence of Third-Order Elastic Constants in Metal-Matrix Composites. *Review of Progress in Quantitative Nondestructive Evaluation*, 12:2091–2097, 1993.

[125] J.-P. Monchalin. Optical Detection of Ultrasound. *IEEE Transactions on Ultrasonics, Ferroelectrics and Frequency Control*, 33(5):485–499, sep 1986.

[126] J. P. Monchalin, J. D. Aussel, R. Heon, C. K. Jen, A. Boudreault, and R. Bernier. Measurement of in-plane and out-of-plane ultrasonic displacements by optical heterodyne interferometry. *Journal of Nondestructive Evaluation*, 8(2):121–133, jun 1989.

[127] R. S. C. Monkhouse, P. W. Wilcox, M. J. S. Lowe, R. P. Dalton, and P. Cawley. The rapid monitoring of structures using interdigital Lamb wave transducers. *Smart Materials and Structures*, 9(3):304–309, jun 2000.

[128] T. J. Moran. Electromagnetic generation of electronically steered ultrasonic bulk waves. *Journal of Applied Physics*, 47(5):2225, 1976.

[129] M. B. Morlock. *Nonlinear Mixing of Two Collinear Rayleigh Waves Nonlinear Mixing of Two Collinear*. PhD thesis, Georgia Institute of Technology, 2013.

[130] M. B. Morlock, J.-Y. Kim, L. J. Jacobs, and J. Qu. Mixing of two collinear Rayleigh waves in an isotropic nonlinear elastic half-space. In *AIP Conf. Proc.*, pages 654–661, 2014.

[131] W. L. Morris, O. Buck, and R. V. Inman. Acoustic harmonic generation due to fatigue damage in high-strength aluminum. *Journal of Applied Physics*, 50(1979):6737–6741, 1979.

[132] M. F. Mueller. *Analytical investigation of internally resonant second harmonic lamb waves in nonlinear elastic isotropic plates*. PhD thesis, Georgia Institute of Technology, 2009.

[133] M. Muller, A. Sutin, R. Guyer, M. Talmant, P. Laugier, and P. A. Johnson. Nonlinear resonant ultrasound spectroscopy (NRUS) applied to damage assessment in bone. *The Journal of the Acoustical Society of America*, 118(6):3946, 2005.

[134] T. Müller. *Nonlinear Ultrasonics : Signal Processing Considerations and a Nonlinear Parameter for Rayleigh Waves*. PhD thesis, Georgia Institute of Technology, 2005.

[135] R. Murayama and K. Ayaka. Evaluation of Fatigue Specimens Using EMATs for Nonlinear Ultrasonic Wave Detection. *Journal of Nondestructive Evaluation*, 26(2-4):115–122, oct 2007.

[136] R. Murayama and K. Yamaguchi. Nonlinear Ultrasonic Wave Detection by Electromagnetic Acoustic Transducer [EMAT] for Guided Wave. *Japanese Journal of Applied Physics*, 44(6B):4385–4388, jun 2005.

[137] F. D. Murnaghan. Finite Deformations of an Elastic Solid. *American Journal of Mathematics*, 59(2):235, apr 1937.

[138] J. K. Na. Ultrasonic nonlinear properties of lead zirconate-titanate ceramics. *The Journal of the Acoustical Society of America*, 95(6):3213, 1994.

[139] J. K. Na, J. H. Cantrell, and W. T. Yost. Linear and Nonlinear Ultrasonic Properties of Fatigued 410Cb Stainless Steel. In *Review of Progress in Quantitative Nondestructive Evaluation*, pages 1347–1352. Springer US, Boston, MA, 1996.

[140] P. B. Nagy. Fatigue damage assessment by nonlinear ultrasonic materials characterization. *Ultrasonics*, 36(1-5):375–381, feb 1998.

[141] P. B. Nagy, J. Qu, and L. J. Jacobs. Finite-size effects on the quasistatic displacement pulse in a solid specimen with quadratic nonlinearity. *The Journal of the Acoustical Society of America*, 134(3):1760, 2013.

[142] A. Novak, M. Bentahar, V. Tournat, R. El Guerjouma, and L. Simon. Nonlinear acoustic characterization of micro-damaged materials through higher harmonic resonance analysis. *NDT and E International*, 45(1):1–8, 2012.

[143] H. Ogi. Field dependence of coupling efficiency between electromagnetic field and ultrasonic bulk waves. *Journal of Applied Physics*, 82(8):3940, 1997.

[144] H. Ogi, E. Goda, and M. Hirao. Increase of Efficiency of Magnetostriction SH-Wave Electromagnetic Acoustic Transducer by Angled Bias Field: Piezomagnetic Theory and Measurement. *Japanese Journal of Applied Physics*, 42(Part 1, No. 5B):3020–3024, may 2003.

[145] H. Ogi, M. Hirao, and S. Aoki. Noncontact monitoring of surface-wave nonlinearity for predicting the remaining life of fatigued steels. *Journal of Applied Physics*, 90(1):438, 2001.

[146] H. Ogi, M. Hirao, T. Honda, and H. Fukuoka. Absolute Measurement of Ultrasonic Attenuation by Electromagnetic Acoustic Resonance. In *Review of Progress in Quantitative Nondestructive Evaluation*, volume 14, pages 1601–1608. Springer US, Boston, MA, 1995.

[147] H. Ogi, M. Hirao, and T. Ohtani. Line-focusing of ultrasonic SV wave by electromagnetic acoustic transducer. *The Journal of the Acoustical Society of America*, 103(5):2411, 1998.

[148] T. Ohtani, T. Honma, Y. Ishii, M. Tabuchi, H. Hongo, and M. Hirao. Change of nonlinear acoustics in ASME grade 122 steel welded joint during creep. *Review of Progress in Quantitative Nondestructive Evaluation*, 130006:130006, 2016.

[149] T. Ohtani and Y. Ishii. Nonlinear Resonant Ultrasound Spectroscopy (NRUS) applied to fatigue damage evaluation in a pure copper. In *AIP Conf. Proc. 1474*, volume 203, pages 203–206, 2012.

[150] T. Ohtani, Y. Kusagagi, Y. Ishii, M. Tabuchi, H. Hongo, and M. Hirao. Evolution of nonlinear acoustics during creep in welded joint for high Cr ferritic heat resisting steels. In *2014 IEEE International Ultrasonics Symposium*, pages 1444–1447. IEEE, sep 2014.

[151] T. Ohtani, Y. Kusanagi, and Y. Ishii. Noncontact nonlinear resonant ultrasound spectroscopy to evaluate creep damage in an austenitic stainless steel. In *Review of Progress in Quantitative Nondestructive Evaluation*, volume 1233, pages 1227–1233, 2013.

[152] T. Ohtani, H. Ogi, and M. Hirao. Noncontact Evaluation of Surface-Wave Nonlinearity for Creep Damage in CrMoV Steel. *Japanese Journal of Applied Physics*, 48(7):07GD02, jul 2009.

[153] T. Ohtani, H. Ogi, Y. Minami, and M. Hirao. Ultrasonic attenuation monitoring of fatigue damage in low carbon steels with electromagnetic acoustic resonance (EMAR). *Journal of Alloys and Compounds*, 310(1-2):440–444, sep 2000.

[154] S. B. Palmer, J. F. Hernandez-Valle, and S. Dixon. Electromagnetic acoustic transduction using a pulsed electromagnet. In H. F. Wu, A. A. Diaz, P. J. Shull, and D. W. Vogel, editors, *Proceedings of SPIE*, volume 7294, page 72940T, mar 2009.

[155] E. Pan, J. Rogers, S. Datta, and A. Shah. Mode selection of guided waves for ultrasonic inspection of gas pipelines with thick coating. *Mechanics of Materials*, 31(3):165–174, mar 1999.

[156] W. J. Pardee and R. B. Thompson. Half-space radiation by EMATs. *Journal of Nondestructive Evaluation*, 1(3):157–181, sep 1980.

[157] C. Payan, V. Garnier, J. Moysan, and P. A. Johnson. Applying nonlinear resonant ultrasound spectroscopy to improving thermal damage assessment in concrete. *The Journal of the Acoustical Society of America*, 121(4):EL125, 2007.

[158] M. Pereira Da Cunha and J. Jordan. Improved longitudinal EMAT transducer for elastic constant extraction. In *Proceedings of the 2005 IEEE International Frequency Control Symposium and Exposition, 2005.*, volume 2005, pages 426–432. IEEE, 2005.

[159] P. A. Petcher, S. E. Burrows, and S. Dixon. Shear horizontal (SH) ultrasound wave propagation around smooth corners. *Ultrasonics*, 54(4):997–1004, 2014.

[160] R. Halmshaw. *Non-Destructive Testing.* Edward Arnold, 1991.

[161] S. Rajaram, J. Cuadra, R. Saralaya, I. Bartoli, and A. Kontsos. In situ CTE measurements and damage detection using optical metrology. *Measurement Science and Technology*, 27(2):025202, feb 2016.

[162] V. V. S. J. Rao, E. Kannan, R. V. Prakash, and K. Balasubramaniam. Fatigue damage characterization using surface acoustic wave nonlinearity in aluminum alloy AA7175-T7351. *Journal of Applied Physics*, 104(12), 2008.

[163] M. C. Remillieux, R. A. Guyer, C. Payan, and T. J. Ulrich. Decoupling Nonclassical Nonlinear Behavior of Elastic Wave Types. *Physical Review Letters*, 116(11):115501, mar 2016.

[164] G. Ren, J. Kim, and K. Y. Jhang. Relationship between second- and third-order acoustic nonlinear parameters in relative measurement. *Ultrasonics*, 56:539–544, 2015.

[165] R. Ribichini, F. Cegla, P. Nagy, and P. Cawley. Study and comparison of different EMAT configurations for SH wave inspection. *IEEE Transactions on Ultrasonics, Ferroelectrics and Frequency Control*, 58(12):2571–2581, dec 2011.

[166] R. Ribichini, F. Cegla, P. Nagy, and P. Cawley. Experimental and numerical evaluation of electromagnetic acoustic transducer performance on steel materials. *NDT & E International*, 45(1):32–38, jan 2012.

[167] RITEC Inc. RITEC SNAP System.

[168] F. R. Rollins. Interaction of ultrasonic waves in solid media. *Applied Physics Letters*, 2(8):147, 1963.

[169] J. L. Rose. *Ultrasonic Waves in Solid Media.* Cambridge University Press, 2004.

[170] J. L. Rose. The upcoming revolution in ultrasonic guided waves. In H. F. Wu, editor, *Proc. SPIE*, volume 7983, page 798302, mar 2011.

[171] J. L. Rose. *Ultrasonic Guided Waves in Solid Media.* Cambridge University Press, New York, 2014.

[172] T. H. Ruiner. *Characterization of Thermal Damage in 2205 Duplex Stainless Steel With Nonlinear Ultrasonics (NLU).* PhD thesis, Georgia Institute of Technology, 2010.

[173] A. Ruiz, N. Ortiz, A. Medina, J. Y. Kim, and L. J. Jacobs. Application of ultrasonic methods for early detection of thermal damage in 2205 duplex stainless steel. *NDT and E International*, 54:19–26, 2013.

[174] K. Salama, A. L. W. Collins, and J. J. Wang. The Determination of Tensile Stresses Using the Temperature Dependence of Ultrasonic Velocity. *Proceedings of the ARPA/AFML Review of Progress in Quantitative NDE*, (October 1979):265–268, 1981.

[175] K. Salama and C. K. Ling. The effect of stress on the temperature dependence of ultrasonic velocity. *Journal of Applied Physics*, 51(3):1505, 1980.

[176] C. B. Scruby and L. E. Drain. *Laser Ultrasonics Techniques and Applications.* CRC Press, 1990.

[177] M. Silk. *Ultrasonic transducers for nondestructive testing.* A. Hilger, Bristol, 1984.

[178] L. Siming, A. J. Croxford, S. Neild, and Z. Zhenggan. Effects of experimental variables on the nonlinear harmonic generation technique. *IEEE Transactions on Ultrasonics, Ferroelectrics and Frequency Control*, 58(7):1442–1451, jul 2011.

[179] S. Siriwitayakorn, W. G. B. Britton, and R. W. B. Stephens. Non-Linear Propagation of Shear Ultrasonic Waves in Single Crystals of Aluminium. *Acta Acustica united with Acustica*, 56(4):247–257, 1984.

[180] L. Sun. Approach to Eliminate Couplant-Effect in Acoustic Nonlinearity Measurements. In *AIP Conference Proceedings*, volume 820, pages 1386–1393. AIP, 2006.

[181] T. Suzuki, A. Hikata, and C. Elbaum. Anharmonicity Due to Glide Motion of Dislocations. *Journal of Applied Physics*, 35(9):2761, 1964.

[182] S. Thiele, J.-Y. Kim, J. Qu, and L. J. Jacobs. Air-coupled detection of nonlinear Rayleigh surface waves to assess material nonlinearity. *Ultrasonics*, 54(6):1470–1475, aug 2014.

[183] D. O. Thompson and M. A. Breazeale. Ultrasonic Waves of Finite Amplitude in Solids. *The Journal of the Acoustical Society of America*, 35(11):1884, 1963.

[184] R. Thompson. A Model for the Electromagnetic Generation and Detection of Rayleigh and Lamb Waves. *IEEE Transactions on Sonics and Ultrasonics*, 20(4):340–346, oct 1973.

[185] R. Thompson. Electromagnetic, noncontact transducers. *1973 Ultrasonics Symposium*, 1973.

[186] R. Thompson. Electromagnetic generation of Rayleigh and Lamb waves in ferromagnetic materials. *1975 Ultrasonics Symposium*, 1975.

[187] R. Thompson. Detection of Strain by Measurement of the Efficiency of the Magnetostrictive Generation of Ultrasonic Surface Waves. *1976 Ultrasonics Symposium*, pages 585–589, 1976.

[188] R. Thompson. A model for the electromagnetic generation of ultrasonic guided waves in ferromagnetic metal polycrystals. *IEEE Transactions on Sonics and Ultrasonics*, 25(1):7–15, jan 1978.

[189] R. Thompson. New configurations for the electromagnetic generation SH waves in ferromagnetic materials. *1978 Ultrasonics Symposium*, 1978.

[190] R. Thompson. Physical Principles of Measurements with EMAT Transducers. In *Ultrasonic Measurement Methods: Volume XIX: PHYSICAL ACOUSTICS*, volume 19, pages 157–200. ACADEMIC PRESS, INC., 1990.

[191] R. B. Thompson. Mechanisms of electromagnetic generation and detection of ultrasonic Lamb waves in iron-nickel alloy polycrystals. *Journal of Applied Physics*, 48(12):4942, 1977.

[192] R. B. Thompson. Generation of horizontally polarized shear waves in ferromagnetic materials using magnetostrictively coupled meander-coil electromagnetic transducers. *Applied Physics Letters*, 34(2):175, 1979.

[193] R. B. Thompson and G. A. Alers. Noncontact ultrasonic surface wave transducers and their application to nondestructive evaluation. *Proc. 9th Symposium on NDE, San Antonio*, pages 6–19, 1973.

[194] R. B. Thompson, O. Buck, and D. O. Thompson. Higher harmonics of finite amplitude ultrasonic waves in solids. *Journal of the Acoustical Society of America*, 59(5):1087–1094, 1976.

[195] C. Thring, Y. Fan, and R. Edwards. Focused Rayleigh wave EMAT for characterisation of surface-breaking defects. *NDT & E International*, 81:20–27, jul 2016.

[196] D. Torello, S. Thiele, K. H. Matlack, J. Y. Kim, J. Qu, and L. J. Jacobs. Diffraction, attenuation, and source corrections for nonlinear Rayleigh wave ultrasonic measurements. *Ultrasonics*, 56:417–426, 2015.

[197] K. Van Den Abeele and F. Windels. Characterization and Imaging of Microdamage Using Nonlinear Resonance Ultrasound Spectroscopy (NRUS): An Analytical Model. In P. Delsanto, editor, *Universality of Nonclassical Nonlinearity*, pages 369–388. Springer New York, New York, NY, 2006.

[198] I. A. Viktorov. *Rayleigh and Lamb Waves.* Springer US, Boston, MA, 1967.

[199] E. Villari. Ueber die Aenderungen des magnetischen Moments, welche der Zug und das Hindurchleiten eines galvanischen Stroms in einem Stabe von Stahl oder Eisen hervorbringen. *Annalen der Physik und Chemie*, 202(9):87–122, 1865.

[200] W. McGonnagle. *Nondestructive Testing.* Science, Gordon and Breach Publishers, 1982.

[201] S. V. Walker, J.-Y. Kim, J. Qu, and L. J. Jacobs. Fatigue damage evaluation in A36 steel using nonlinear Rayleigh surface waves. *NDT & E International*, 48:10–15, jun 2012.

[202] J. Wang, C. Li, Y. Li, and L. Yan. Optimization design of linear Halbach array. *2008 International Conference on Electrical Machines and Systems*, 0(1):5–9, 2008.

[203] S. Wang, L. Kang, Z. Li, G. Zhai, and L. Zhang. 3-D modeling and analysis of meander-line-coil surface wave EMATs. *Mechatronics*, 22(6):653–660, sep 2012.

[204] S. Wang, Z. Li, L. Kang, X. Hu, and X. Zhang. Modeling and comparison of three bulk wave EMATs. In *IECON 2011 - 37th Annual Conference of the IEEE Industrial Electronics Society*, number 5, pages 2645–2650. IEEE, nov 2011.

[205] S. Wang, Z. Li, L. Kang, and G. Zhai. Influence of coil parameters on Rayleigh waves excited by meander-line coil EMATs. *Communications in Computer and Information Science*, 355:94–103, 2013.

[206] S. Wang, Z. Li, P. Li, X. Liu, and G. Zhai. Numerical and experimental evaluation of the receiving performance of meander-line coil EMATs. *Nondestructive Testing and Evaluation*, 29(4):269–282, 2014.

[207] S. Wang, R. Su, X. Chen, L. Kang, and G. Zhai. Numerical and experimental analysis of unidirectional meander-line coil electromagnetic acoustic transducers. *IEEE transactions on ultrasonics, ferroelectrics, and frequency control*, 60(12):2657–64, dec 2013.

[208] Y. T. Wang, W. G. Britton, and R. W. Stephens. Non-linear interaction between ultrasonic shear waves and dislocations in Aluminium. *Le Journal de Physique Colloques*, 42(C5):C5–387–C5–392, oct 1981.

[209] P. J. Westervelt. Parametric End-Fire Array. *The Journal of the Acoustical Society of America*, 32(7):934, 1960.

[210] P. J. Westervelt. Parametric Acoustic Array. *The Journal of the Acoustical Society of America*, 35(4):535, 1963.

[211] H. Wheeler. Formulas for the Skin Effect. *Proceedings of the IRE*, 30(9):412–424, sep 1942.

[212] P. Wilcox, M. Lowe, and P. Cawley. The effect of dispersion on long-range inspection using ultrasonic guided waves. *NDT & E International*, 34(1):1–9, 2001.

[213] X. Maldague. *Theory and Practice of Infrared Technology for Nondestructive Testing*. J. Wiley, 2001.

[214] Y. Xie, L. Yin, Z. Liu, P. Deng, and W. Yin. A Novel Variable-Length Meander-Line-Coil EMAT for Side Lobe Suppression. *IEEE Sensors Journal*, 16(16):6279–6287, aug 2016.

[215] G. T. Yahr. Fatigue Design Curves for 6061-T6 Aluminum. *Journal of Pressure Vessel Technology*, 119(2):211–215, may 1997.

[216] W. Yost and J. Cantrell. The effects of fatigue on acoustic nonlinearity in aluminum alloys. In *IEEE 1992 Ultrasonics Symposium Proceedings*, pages 947–955. IEEE, 1992.

[217] H. Young and R. Freedman. *University physics with modern physics*. Pearson education, 2012.

[218] G. Zhai, T. Jiang, and L. Kang. Analysis of multiple wavelengths of Lamb waves generated by meander-line coil EMATs. *Ultrasonics*, 54(2):632–6, feb 2014.

[219] G. Zhai, T. Jiang, L. Kang, and S. Wang. Minimizing influence of multi-modes and dispersion of electromagnetic ultrasonic lamb waves. *IEEE transactions on ultrasonics, ferroelectrics, and frequency control*, 57(12):2725–33, dec 2010.

[220] G. Zhai, K. Wang, Y. Wang, R. Su, and L. Kang. Modeling of Lorentz forces and radiated wave fields for bulk wave electromagnetic acoustic transducers. *Journal of Applied Physics*, 114(5), 2013.

[221] H. Zhang, R. Su, S. Wang, G. Zhai, and L. Kang. Design of bulk wave EMAT using a pulsed electromagnet. *2014 IEEE Far East Forum on Nondestructive Evaluation/Testing*, pages 242–246, jun 2014.

[222] S. Zhang, X. Li, H. Jeong, and H. Hu. Modeling nonlinear Rayleigh wave fields generated by angle beam wedge transducersA theoretical study. *Wave Motion*, 67:141–159, dec 2016.

[223] Z. Zhang, P. B. Nagy, and W. Hassan. On the feasibility of nonlinear assessment of fatigue damage in hardened IN718 specimens based on non-collinear shear wave mixing. In *AIP Conf. Proc.*, volume 1706, page 060003, 2016.

[224] Y. Zheng, R. G. Maev, and I. Y. Solodov. Review / Sythèse: Nonlinear acoustic applications for material characterization: A review. *Canadian Journal of Physics*, 77(12):927–967, 1999.

[225] S. Zhou, W. Jiang, and Y. Shui. Nonlinear bulk acoustic waves in anisotropic solids: Propagation, generation, and reflection. *Journal of Applied Physics*, 78(1):39–46, 1995.

[226] S. Zhou and Y. Shui. Nonlinear reflection of bulk acoustic waves at an interface. *Journal of Applied Physics*, 72(11):5070–5080, 1992.